INFORMATION TO USERS

This manuscript has been reproduced from the microfilm master. UMI films the text directly from the original or copy submitted. Thus, some thesis and dissertation copies are in typewriter face, while others may be from any type of computer printer.

The quality of this reproduction is dependent upon the quality of the copy submitted. Broken or indistinct print, colored or poor quality illustrations and photographs, print bleedthrough, substandard margins, and improper alignment can adversely affect reproduction.

In the unlikely event that the author did not send UMI a complete manuscript and there are missing pages, these will be noted. Also, if unauthorized copyright material had to be removed, a note will indicate the deletion.

Oversize materials (e.g., maps, drawings, charts) are reproduced by sectioning the original, beginning at the upper left-hand corner and continuing from left to right in equal sections with small overlaps.

Photographs included in the original manuscript have been reproduced xerographically in this copy. Higher quality 6" x 9" black and white photographic prints are available for any photographs or illustrations appearing in this copy for an additional charge. Contact UMI directly to order.

ProQuest Information and Learning
300 North Zeeb Road, Ann Arbor, MI 48106-1346 USA
800-521-0600

UMI®

Université d'Ottawa • University of Ottawa

National Library
of Canada

Acquisitions and
Bibliographic Services

395 Wellington Street
Ottawa ON K1A 0N4
Canada

Bibliothèque nationale
du Canada

Acquisitions et
services bibliographiques

395, rue Wellington
Ottawa ON K1A 0N4
Canada

Your file Votre référence

Our file Notre référence

0-612-67982-9

Canada

In memory of my father

Adam Tadeusz Pierozynski

Abstract

Studies of the electrochemical adsorption of small organic molecules at well-ordered Pt single-crystal surfaces in the region of underpotential deposition (UPD) of H have become a major activity in current electrochemical surface science. The direction of the research described in this thesis originates from earlier work in this laboratory on the reactive chemisorption of CH_3CN at Pt single-crystal surfaces, studied by means of cyclic voltammetry and integrated adsorption current transients, coupled with *in situ* IR reflectance spectroscopy.

It was found that resonant guanidonium cations, $^+NH_2{=}C(NH_2)_2$ (G^+), have major surface-specific influences on H underpotential deposition (UPD) voltammetric profiles at Pt(hkl) surfaces. Cyclic voltammetry, adsorbate displacement by CO, adsorption charge-transient, *in situ* FTIR spectroscopy, and a.c. impedance spectroscopy techniques were employed complementarily to study the adsorption behaviour of G^+ cations at Pt single-crystal surfaces. Based on the results of adsorption charge-transients obtained by introduction of 1% solution of G^+ in 0.1 mol dm^{-3} NaOH at the Pt(111) surface, it is concluded that G^+ becomes chemisorbed on the Pt surface in a 2-electron transfer process, with resulting electrooxidation of the H's dissociated from $-NH_2$ groups upon their chemisorption.

In situ FTIR experiments were conducted in aq. 0.05 mol dm^{-3} H_2SO_4 for the purpose of identifying the molecular basis of effects of co-adsorption of G^+ on the states of adsorbed HSO_4^- anions through changes of vibrational spectra. The spectroscopic results revealed a broad band in the spectra over the 1500-1600 cm^{-1} range which was

assigned to the $>C=NH_2^+$ stretch of G^+. Supported by the voltammetric behaviour, they also provided evidence about the co-operative chemisorption of G^+ cations with the HSO_4^- ions on the Pt single-crystal surfaces, where both species are in the *chemisorbed* state at the Pt surface. This is an attractive interaction which leads to the observed substantial voltammetric shift of potential for HSO_4^- desorption towards the RHE potential.

A mechanism of this co-operative chemisorption (or ion-pairing) between the G^+ cations and the HSO_4^- (also ClO_4^- and OH^- in aq. $HClO_4$ and NaOH solutions, respectively) ions, co-adsorbed at the Pt single-crystal surfaces, is proposed. Explanations are also given for the reported, in some cases appreciable (for Pt(100) and (511) surfaces), increases that arise in the total voltammetric charges, measured within the potential range for UPD of H. No significant diffusion control for the process of adsorption of G^+ at the Pt surface was observed. Thus, the recorded response currents in the voltammograms are directly associated with *surface* electrochemical processes.

Following studies on adsorption of G^+, the behaviour of several structurally-related molecules to G^+, namely, N,N-dimethylguanidonium (DMG^+), and acetamidonium (AA^+) cations, and urea (U) was comparatively examined at respective Pt single-crystal planes, in corresponding supporting electrolytes. The observed differences in voltammetric behaviour from that recorded for G^+ are explained in terms of the ion-pairing between the G-analogues and surface-adsorbed HSO_4^- being substantially weaker than the corresponding effect for the G^+ cation. For DMG^+, the latter difference is assigned to steric effects introduced by the presence of the two *gem*-methyl groups on one of the N atoms. On the other hand, less significant interaction of AA^+ with the HSO_4^-

anion is related to the fact that a dipole-dipole rather than a cation-dipole interaction between the latter species and the bisulphate ion is indicated. In the case of urea, an analogous effect of weakening the ion-pairing is attributed to urea's low basicity and therefore, compared with guanidine, having a much lower tendency for protonation.

Oximes contain the characteristic =N-OH group arising from condensation of carbonyl groups with NH_2OH, and can undergo electrolytic reduction to primary amines. In another main part of this thesis research, examples of surface-lattice specificity of this process, coupled with electrosorption at low-index Pt single-crystal surfaces, were studied for the cases of formamidoxime (F_{NOH}) and acetaldehyde oxime (A_{NOH}) in aq. 0.5 mol dm^{-3} H_2SO_4 and 0.1 mol dm^{-3} NaOH by means of cyclic voltammetry, adsorption charge-transient and a.c. impedance spectroscopy techniques.

In H_2SO_4, both oximes undergo Faradaic reduction involving UPD H on Pt(111) where F_{NOH} dissociates, ultimately to form CO_{ads}, leading to surface poisoning, while A_{NOH} becomes reduced to ethylamine. These effects are manifested as strikingly surface-specific changes in the cyclic voltammetric profiles for these surfaces. Unlike for the case of G^+, the process of Faradaic reduction of F_{NOH} on the Pt(111) plane was found to be diffusion-controlled. At Pt(100), the behaviour of F_{NOH} implies interactive chemisorption of the species with HSO_4^- ion on the Pt surface (related to the effect also found with guanidine), which process prevails over reductive scission, the latter, however, being the principal reaction at the Pt(111) surface.

In alkaline solution, a mixed mechanism for the behaviour of F_{NOH} and A_{NOH} at the Pt(111) surface is indicated. The behaviour of F_{NOH} at the Pt(100) plane in this medium generally resembles that observed in H_2SO_4 solution.

Publications and Conference Presentations

Some of the work described in the present thesis has already been published or submitted for publication, as follows:

1. "Influence of adsorption of guanidonium cations on H UPD at Pt(*hkl*) surfaces: lattice-specific anion-mimetic effects", B. Pierozynski, S. Morin and B.E. Conway, *J. Electroanal. Chem.*, 1999, **467**, 30.
2. "FTIR spectroscopic and cyclic voltammetric study of the influence of resonant guanidonium cations on HSO_4^- adsorption in the H UPD region at Pt(111) and (100) surfaces", Boguslaw Pierozynski, Alireza Zolfaghari and Brian E. Conway, *Phys. Chem. Chem. Phys.*, 2001, **3**, 469.
3. "Specificity of electrochemical reactivity of small aliphatic oximes to geometries of Pt(111) and (100) surfaces", Boguslaw Pierozynski and Brian E. Conway, *Phys. Chem. Chem. Phys.*, in submission.

During the course of research, the work described in this thesis was presented at several conferences and symposia, as follows:

1. "Reactivity and electrosorption of functionalized small molecules at single-crystal Pt surfaces", B.E. Conway, B. Pierozynski and S. Morin, The Electrochemical Society Inc., Conference on Electrochemical Surface Processes, Boston, USA, Fall 1998.

2. “Specificity of adsorption of guanidonium cations at single-crystal Pt surfaces”, B.E. Conway and B. Pierozynski, The Electrochemical Society Inc., Canadian Section Symposium, Ottawa, Canada, May 1999.

3. “Surface-specific reactive chemisorption of resonant organic cations and anions at Pt(hkl) single-crystal electrodes”, B.E. Conway and B. Pierozynski, Bicentenary of Alessandro Volta’s Invention of the “Electric Pile”, 50 th International Society of Electrochemistry (ISE) Meeting, Pavia, Italy, 5-10 September 1999.

Acknowledgements

I would like to thank Professor Brian E. Conway, my research supervisor, for his direction, guidance and help throughout the course of this work, and for frequent discussions during the process of the research. Professor Conway was always willing and able to give professional assistance and suggestions whenever difficulties arose.

I wish to acknowledge help of Dr. Sylvie Morin for introducing me into the art of Pt single-crystal work. I would also like to thank Professor Mario Morin for sharing his knowledge of spectroscopy and all my colleagues from Professor Conway's Group, especially Dr. Alireza Zolfaghari-Hesari, for help in running FTIR measurements and Dr. Wendy Pell for numerous fruitful discussions.

Conducting this research would not have been possible without electrochemical cells and other pieces of equipment built by master glass-blower, Mr. Egon Kristof and Mr. John Hopkins, whom I thank very much for their help and professional advice.

Finally, I would like to thank my Family for their love, patience and support throughout this work.

Table of Contents

List of Tables

List of Figures

and the first, second and the third layers of atoms are denoted by 0, 1, and 2 [23, 24].

Fig. 4.9 The goniometer assembly [31]: **A**- Pt single-crystal; **B**- crystal's holder; **C**- "head" of the goniometer (**s**- screws used for positioning the crystal to the chosen angle) and **D**- cylinder used to maintain the crystal rigid during its polishing.

Fig. 5.1 Cyclic voltammograms of the surfaces of well-ordered: (a) Pt(111), (b) Pt(100) and (c) Pt(110) single-crystals in contact with 0.5 mol dm^{-3} H_2SO_4, cooled in H_2 + Ar atmosphere, after the flame cleaning procedure, recorded at a sweep rate of 50 mV s^{-1} [9].

Fig. 5.2 Modifications of the H and O adsorption-desorption voltammetric profiles for various stages of annealing of freshly polished Pt(111) electrode in contact with 0.5 mol dm^{-3} H_2SO_4. Curve 1: CV after thermal decontaminaion; Curves 2 and 3: After two successive annealings for a few seconds at a temperature between 500 and 600° C and Curve 4: After annealing for 10 seconds at a temperature between 1300 and 1400° C [16].

Fig. 5.3 A cyclic voltammogram of the well-ordered Pt(511) surface in contact with 0.5 mol dm^{-3} H_2SO_4 after flame treatment (cooled in air), recorded at a sweep rate of 50 mV s^{-1} [26].

Fig. 5.4 A cyclic voltammogram of well-ordered Pt(111) surface in contact with 0.1 mol dm^{-3} $HClO_4$ after cooling in air, recorded at a sweep rate of 50 mV s^{-1} [9].

Fig. 5.5 Cyclic voltammogram of a well-ordered Pt(111) surface in contact with 0.1 mol dm^{-3} NaOH after cooling in air, recorded at a sweep rate of 50 mV s^{-1} [29].

Fig. 5.6 (a) Voltammograms for a well-ordered Pt(111) electrode in 0.5 mol dm^{-3} H_2SO_4: curve 1, control measurement of the surface blocking by adsorbed CO (50 mV s^{-1}, sensitivity increased by a factor of 4); curve 2, stripping of adsorbed CO (20 mV s^{-1}); curve 3, recovery of the initial voltammetric

concentrations indicated; voltammograms were recorded on the third cycle.

Fig. 6.7 Cyclic voltammograms for polycrystalline Pt in 0.1 mol dm^{-3} NaOH at a sweep-rate of 0.050 V s^{-1} and in the presence of G^{+} (or G) at the three concentrations indicated; voltammograms were recorded on the third cycle.

Fig. 6.8 Cyclic voltammograms for Pt(111) in 0.5 mol dm^{-3} H_2SO_4 at a sweep-rate of 0.050 V s^{-1} and in the presence of G^{+} at the three concentrations indicated; voltammograms were recorded on the third cycle.

Fig. 6.9 Cyclic voltammograms for Pt(111) in 0.5 mol dm^{-3} H_2SO_4 at a sweep-rate of 0.050 V s^{-1} in the presence of 6x10^{-4} mol dm^{-3} G^{+} showing the effect of progressively diminishing the positive potential limit of the sweep to four values (curves 1 to 4).

Fig. 6.10 Cyclic voltammograms for Pt(111) in 0.5 mol dm^{-3} H_2SO_4 at a sweep-rate of 0.050 V s^{-1} and in the presence of DMG^{+} at the two concentrations indicated; voltammograms were recorded on the third cycle.

Fig. 6.11 Cyclic voltammograms for Pt(111) in 0.05 mol dm^{-3} H_2SO_4 at a sweep-rate of 0.050 V s^{-1} and in the presence of G^{+} at the two concentrations indicated; voltammograms were recorded on the third cycle.

Fig. 6.12 Cyclic voltammograms for Pt(111) in 0.5 mol dm^{-3} H_2SO_4 at a sweep-rate of 0.050 V s^{-1} and in the presence of U at the concentration indicated; voltammograms were recorded on the third cycle.

Fig. 6.13 Cyclic voltammograms for Pt(111) in 0.1 mol dm^{-3} $HClO_4$ at a sweep-rate of 0.050 V s^{-1} and in the presence of G^{+} at the concentrations indicated; voltammograms were recorded on the third cycle.

Fig. 6.14 Cyclic voltammograms for Pt(111) in 0.05 mol dm^{-3} KHF_2 at a sweep-rate of 0.050 V s^{-1} and in the presence of G^{+} at the concentration indicated; voltammograms were recorded on the third cycle.

Fig. 6.15 An effect of $HClO_4$ concentration on the cyclic voltammetric behaviour of Pt(111) at a sweep-rate of 0.050 V s^{-1} at the three indicated concentrations of $HClO_4$; voltammograms were recorded on the third cycle.

List of Abbreviations and Symbols

AA	-	acetamidine
AA^+	-	acetamidonium cation
AES	-	Auger Electron Spectroscopy
AFM	-	Atomic Force Microscopy
A_{NOH}	-	acetaldehyde oxime
$(A_{NOH})^+$	-	protonated acetaldehyde oxime
a.v.	-	alternating voltage
CE	-	counter electrode
CPE	-	Constant Phase Element
CV	-	cyclic voltammetry
DMG	-	N,N-dimethylguanidine
DMG^+	-	N,N-dimethylguanidonium cation
ECMS	-	Electrochemical Mass Spectrometry
EELS	-	Energy Electron Loss Spectroscopy
EMIRS	-	Electrochemically Modulated Infrared Spectroscopy
EXAFS	-	Extended X-ray Absorption Fine Structure
fcc	-	face-centred cubic
F_{NOH}	-	formamidoxime
$(F_{NOH})^+$	-	protonated formamidoxime
FRA	-	Frequency Response Analyser
FT	-	Fourier Transform
FTIR	-	Fourier Transform Infrared
G; G^o	-	guanidine; conjugate base to G^+ ion
G^+	-	guanidonium cation
HER	-	hydrogen evolution reaction
HOMO	-	highest occupied molecular orbital
IHP	-	inner Helmholtz plane
IR	-	Infrared
LEED	-	Low Energy Electron Diffraction

LUMO - lowest unoccupied molecular orbital

OER - oxygen evolution reaction

OHP - outer Helmholtz plane

OPD - overpotential deposition

PDIR - Potential Difference Infrared

PZC - potential of zero charge

PZTC - potential of zero total charge

RAIRS - Reflection-Absorption Infrared Spectroscopy

RC - resistance/capacitance circuit

RE - reference electrode

RHE - reversible hydrogen electrode

SCE - saturated calomel electrode

SECM - Scanning Electrochemical Microscopy

SNIFTIRS - Subtractively Normalised Interfacial Fourier Transform Infrared Spectroscopy

STM - Scanning Tunnelling Microscopy

TOC - total organic carbon

U - urea

U^+ - protonated urea

UHV - ultra-high vacuum

UPD - underpotential deposition

UV - ultraviolet

WE - working electrode

A - a) solution species A; b) surface area

A_{ads} - chemisorbed species A

c - a) reactant concentration; b) speed of light

c_A - concentration of species A

c_{H+} - proton concentration

c_O - oxidant concentration

c_R - reductant concentration

C - capacitance

C_D - a) differential capacitance for the diffuse layer

C_{diff} - diffusional capacitance (also termed as C_D)

C_{dl} - double-layer capacitance

C_H - differential capacitance for the region between the metal surface and the outer Helmholtz plane

CO_{ads} - adsorbed CO species

C_p - pseudocapacitance

C_{p1} - pseudocapacitance corresponding to Faradaic reduction of A_{NOH}

C_{p2} - A_{NOH} or F_{NOH} adsorption pseudocapacitance

C_{pDMG+} - DMG^+ adsorption pseudocapacitance

C_{pG+} - G^+ adsorption pseudocapacitance

C_{pH} - H adsorption pseudocapacitance

D - diffusion coefficient (constant)

D_F - diffusion coefficient for F_{NOH}

D_O - diffusion constant for oxidant

D_R - diffusion constant for reductant

e - electron charge

E - a) potential applied at the electrode; b) photon energy

E_1 - potential value 1

E_2 - potential value 2

E_{ads} - potential of adsorption

E_{Cdl} - potential drop across capacitor C_{dl}

E_{Rs} - potential drop across resistor R_S

E_f - final potential

E_i - initial potential

E_p - peak potential

$E(t)$ - instantaneous sinusoidal potential

E^{tot} - total potential difference

ΔE - a) potential difference; b) anodic/cathodic voltage separation; c) maximum amplitude in potential

$\mathrm{E_I}$ - energy of the incident beam

$\mathrm{E_R}$ - energy of the reflected beam

$\mathrm{E_V}$ - energy lost due to the interaction of the IR radiation with the surface species

E_I - incident electric vector

E_R - reflected electric vector

E_p - incident electric vector in *p* mode

E_p' - emitted electric vector in *p* mode

E_s - incident electric vector in *s* mode

E_s' - emitted electric vector in *s* mode

F - Faraday constant

g - dimensionless lateral interaction parameter, r/RT

ΔG_{ads} - Gibbs energy of adsorption

$\Delta G^0_{ads}(\theta_H)$ - standard Gibbs energy of adsorption for UPD of H

$\Delta G_E^{\neq}$ - Gibbs energy of activation

ΔG_{H_2} - Gibbs energy of bonding in the H_2 molecule

ΔG_{MH} - Gibbs energy of binding of H atoms with the metal surface

h - Planck constant

i - current

$\overrightarrow{i}$ - current in forward direction

$\overleftarrow{i}$ - current in reverse direction

i_0 - exchange current

i_p - peak current

i_p^{irrev} - peak current for an irreversible process

i_p^{rev} - peak current for a reversible process

iR - potential drop

Δi - amplitude of current

I_0 - intensity of the incident beam

I_R - intensity of the reflected beam

I_p - absorbance intensity in *p* mode

I_s - absorbance intensity in *s* mode

j - a) current density; b) $\sqrt{-1}$

j_p - peak current density

k_1 - rate constant for a forward direction of reaction

k_{-1} - rate constant for a reverse direction of reaction

K_1 - equilibrium constant, k_1/k_{-1}

K_a - acid dissociation constant

K_H - equilibrium constant for the process of UPD of H in acidic solution

L - a) inductance; b) diffusion layer thickness

M - metal site

n - a) number of electrons exchanged in the reaction; b) width of a terrace

O - oxidised species

OH_{ad} - adsorbed OH species

p - parallel polarised radiation

q - charge

q_1 - charge required to form one monolayer of the adsorbed species

q_M - charge accumulated on the metal side of the double-layer

q_S - charge accumulated on the solution side of the double-layer

q_t - charge transient difference

$q_t(E)$ - charge transient density as a function of potential

$q_t(E_{0.08V})$ - maximum value of the charge transient density recorded for H displacement

$q_t(E_{ads})$ - charge density derived from the CO adsorption transient at potential E_{ads}

Δq - accumulation of charges of opposite signs

r - pairwise energy of lateral interactions

R - a) reduced species; b) resistance; c) reflectance; d) gas constant

R_0 - reflectance at the reference potential

R_1 - a) reflectance at potential E_1; b) charge transfer resistance for reduction of A_{NOH}

R_2 - a) reflectance at potential E_2; b) charge transfer resistance for adsorption of A_{NOH} or F_{NOH}

ΔR - difference in reflectances, R_2-R_1

R_{ct} - charge-transfer resistance

R_{diff} - diffusional resistance (also termed as R_D)

R_{DMG+} - charge transfer resistance for adsorption of DMG^+

R_F - Faradaic discharge resistance

R_{G+} - charge transfer resistance for adsorption of G^+

R_H - Faradaic charge transfer resistance for UPD of H

R_S - solution resistance

s - sweep-rate

s - perpendicular polarised radiation

t - time

T - a) temperature in [K]; b) capacitance parameter, [F cm^{-2} $s^{1-\varphi}$]; c) time constant [s]

x - a) number of H_2O molecules co-ordinating Pt atom, ≈1; b) number of effectively occupied Pt sites

X - species present in the chemisorbed state on the Pt surface

X_C - capacitive reactance

$X^{z\pm}$ - charged species released to the solution

Y - admittance or reciprocal impedance, 1/Z

z - a) number of electrons exchanged in the reaction; b) ion's charge

Z - total impedance

Z′ - real component of impedance

Z″ - imaginary component of impedance

Z_{Cdl} - impedance of the C_{dl} component

Z_{Cp} - impedance of the C_p component

Z_{CPE} - impedance of the CPE component

Z_{CpH} - impedance of the C_{pH} component

Z_{Rct} - impedance of the R_{ct} component

Z_{RF} - impedance of the R_F component

Z_{RH} - impedance of the R_H component
Z_W - Warburg impedance
α - transfer coefficient
β - barrier symmetry factor
ϕ - phase angle
ϕ_M - potential of metal
φ - dimensionless parameter, $-1 \leq \varphi \leq 1$
Φ - electron work function of metal
σ - expression determined by the diffusion parameters of the system
ψ_1 - potential at the inner limit of the diffuse layer (OHP)
ψ_2 - potential at the limit for specifically adsorbed ions (IHP)
ψ_S - potential of solution
θ - fractional coverage by an adsorbate
θ_A - fractional coverage by A_{ads}
θ_{G+} - fractional coverage by G^+
θ_H - fractional coverage by H
θ_U - fractional coverage by U
ω - a) angular frequency; b) rotation rate [rpm]
ν - frequency
$\bar{\nu}$ - wavenumber
λ - wavelength
$\delta+/\delta-$ - partial positive/negative charge

Chapter 1

Introduction

1.1 Electrochemical surface science

Much of the work described in this thesis has involved studies on chemisorption and reactivity of small molecular ions, corresponding neutral molecules co-adsorbed with H and inorganic ions, at well-ordered, single-crystal surfaces of Pt. This is an area of electrochemical research now referred to as "electrochemical surface science" involving so-called "electrosorption" (see section 1.1.2 below and Chapter 2). Electrochemical procedures are uniquely sensitive and selective for such studies, especially when complemented by *in situ* surface FTIR spectroscopy, also employed in the present work.

Electrochemistry can be defined as "study of chemical systems involving charged particles in solutions or melts, and charge transfer processes between ions or molecules at metal electrode interfaces". *Electrochemical surface science* relates aspects of *electrochemistry* to modern *surface science*, the latter involving study of solid surfaces in contact with a gas phase or, more commonly with ultra-high vacuum (UHV). As practically all electrochemical processes occur at interfaces between an electronic and an ionic conductor, it is important to introduce here the concept of the electrical double-layer [1].

1.1.1 Origin of the electrical double-layer

The electrical double-layer or, as it is also called, the "electrified interface", can be described as the array of charged particles and oriented dipoles that is usually set up between two immiscible media in which charges can arise. Thus, the double-layer is a consequence of the meeting of two phases at a boundary. If these materials contain electrons or ions, a potential difference arises from the electrification of the two sides of the boundary due to charge separation. Moreover, if they contain particles with permanent dipoles, or molecules in which dipoles can be induced, a contribution to the interfacial (sometimes called "inter-phasial") potential difference across the boundary arises from a net orientation of such dipoles [2-4]. A general review of different double-layer systems has been given by Parsons in ref. 5 and earlier by Grahame in ref. 4.

The electrochemical concept of the double-layer is narrower than that described above, because it usually refers to metal/solution interfaces. Generally, the electrical double-layer can be described as a system consisting of electrons (in the case of metals and electronic conductors), a layer of adsorbed ions and a diffuse layer consisting of an ionic atmosphere, where ions of one sign are in excess in relation to the ions of the other sign, depending on the electrode potential in relation to the potential of zero charge. In addition, the double-layer may contain a thin layer of neutral molecules, usually of the solvent (with or without oriented dipoles).

The first model of the electrical double-layer was proposed in 1879 by Helmholtz, in which he considered the behaviour of the double-layer as that of a parallel-plate condenser (see Fig. 1.1a), where ϕ_M and ψ_S represent potential of metal, and solution, respectively. This simple model was then extended by Gouy and by Chapman, taking account of the effect of the thermal distribution of ions. A later and more complete model was proposed by Stern in 1924, who took into consideration both the Helmholtz approach and Gouy's ion distribution effect [2, 3, 6], see Fig. 1.1b below.

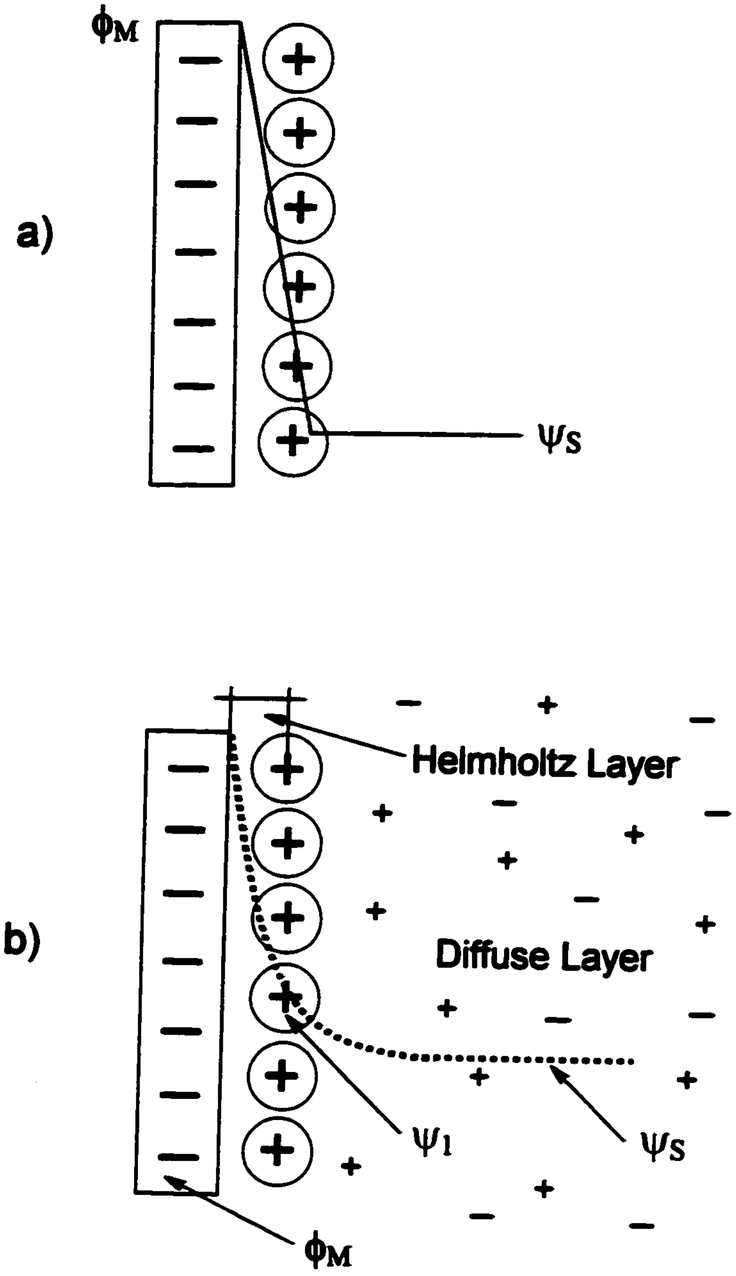

Fig. 1.1 Earliest models of the electrical double-layer by: a) Helmholtz; b) Stern [3].

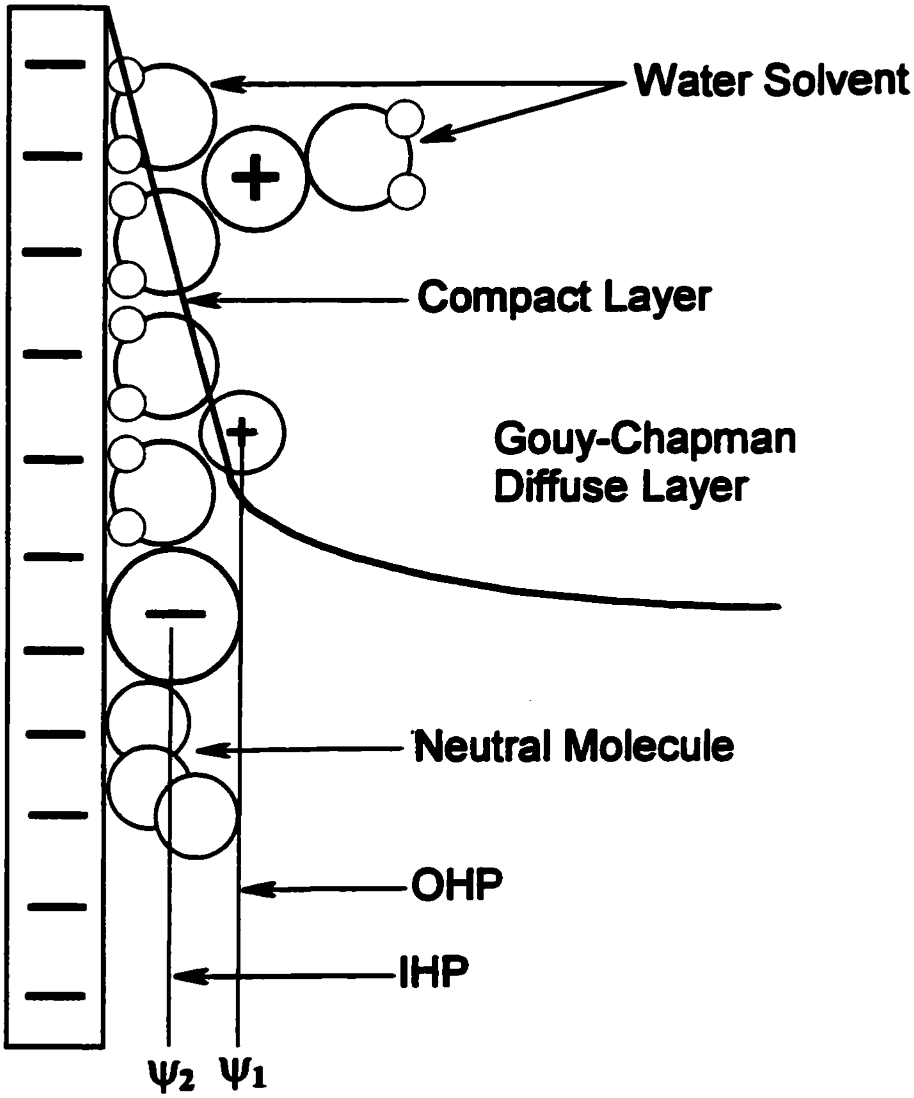

Fig. 1.2 Grahame model of the electrical double-layer [3].

Further studies by Grahame [2, 3] resulted in a new model of the double-layer structure. In this latter model, three regions of potential drop were clearly distinguished, as shown in Fig. 1.2. The first zone, limited by a plane at potential ψ_2, involves specifically adsorbed ions. The second zone is confined between planes having potentials ψ_2 and ψ_1, where the latter value determines an inner limit of the diffuse layer. The third zone commences where the potential is ψ_1 and progresses across the diffuse layer, where finally the average potential of the solution, ψ_S is reached. The inner layer of ions is called the "inner Helmholtz plane" (IHP) and the second layer, limited by the potential ψ_1, is known as the "outer Helmholtz plane" (OHP) [2, 3].

A substantially modified approach, involving distribution of solvent dipoles in the double-layer, was proposed by Bockris, Devanathan and Müller [6]. In this model, a layer of strongly adsorbed solvent dipoles is envisaged with cations remaining in their hydration shells. Only specifically adsorbed anions are able to penetrate the layer of solvent [2, 3, 6] and become in contact with the metal surface plane with which electronic interaction can arise.

All described models of the electrical double-layer allow *no Faradaic charge transfer* to take place in either direction across the double-layer. The charges are separated and an electrostatic equilibrium is attained; then the double-layer behaves like a condenser. Thus, hypothetically, the metal itself behaves as a so-called *ideally polarised electrode*.

In such a system, the charge accumulated on the metal side, q_M, is equal and opposite to the charge on the solution side of the double-layer, q_S; that is:

$$q_M = -q_S \tag{1.1}$$

The double-layer capacitance, C_{dl}, corresponds to the extent of accumulation of charges, Δq, of opposite signs in relation to the potential difference, ΔE, across the interface. If C_{dl} is not constant with changing E, a differential capacitance is defined, according to the equation:

$$C_{dl} = \frac{dq}{dE} \tag{1.2}$$

This total differential capacitance of the double-layer can be decomposed into two components: the differential capacitance of the region between the metal surface and the outer Helmholtz plane, C_H, and that for the diffuse layer, C_D. Thus, the total capacitance of the double-layer is equal to the capacitance of two capacitors connected in series, as represented by the equation below:

$$\frac{1}{C_{dl}} = \frac{1}{C_H} + \frac{1}{C_D} = \frac{C_H + C_D}{C_H C_D} \tag{1.3}$$

This relation corresponds to the total potential difference across the double-layer being represented by two distinct contributions, one across the compact Helmholtz layer and the other across the diffuse layer.

1.1.2 Definition and nature of electrosorption

So-called *electrosorption*, observable at electrodes, can be defined in terms of *chemisorption*. At metals, *chemisorption* arises when there is some degree of specific electronic interaction between the adsorbate and the substrate metal, usually involving an electron donor/acceptor surface process. In many cases, the adsorption process involves scission of the adsorbate molecule - so-called “dissociative chemisorption” into two or more adsorbed radicals [1, 7].

Electrosorption is a special case of *chemisorption* where "dissociative chemisorption", e.g. of H_2 as 2 MH_{ads}, takes place with coupled Faradaic charge transfer or some extent of partial charge transfer which, at electrodes, is accessible to experimental measurement in charge-transient experiments. In regular *chemisorption*, the extent of partial charge transfer is not directly determinable but is indirectly indicated by the change of surface dipole moment with coverage, related to the coverage-dependence of the metals' electronic work function.

In cases of *electrosorption* or redox processes, where Faradaic charge transfer takes place, a so-called "pseudocapacitance", C_p, arises which can be defined formally as was C_{dl} previously in equation 1.2. Pseudocapacitances are on the order of 500-1000 μF cm^{-2} [8], while double-layer capacitances are much smaller, usually on the order of 15-50 μF cm^{-2} [4, 8]. Note that pseudocapacitance arises with some extent of Faradaic charge transfer but *not* proceeding in a continuous manner like with electrolytic generation of H_2.

1.2 The role of the electrode-potential variable

The electronic work function, Φ, of a metal M is the critical energy required to lift an electron from the bulk metal (from its Fermi level) into vacuum, at zero kinetic energy. Correspondingly, the so-called "Fermi energy level" is that which is half populated at temperatures $T > 0$ K, and is an average energy level of an electron in a conduction band of the metal electrode [1, 2, 6, 9].

The situation at electrodes is importantly different from the case of regular chemisorption since the work function, Φ, is directly variable with electrode potential [3, 10], according to the equation:

$$\Phi_E = \Phi_{E=0} \pm eE \tag{1.4}$$

so that the electron-affinity of metal surfaces ($-\Phi$) can be controlled by variation of electrode potential: hence the chemisorption energy and the surface dipole moment can be potential dependent.

In other words, in order for a charge-transfer process to occur, the energy level corresponding to the Fermi level in the metal must be matched with suitable vacant (LUMO) or occupied (HOMO) orbitals in the reactant. Thus, an applied potential is normally required to modify the electron work function, Φ, to some value $\Phi_{E=0} \pm eE$ for e.g. electron transfer to take place at the potential, E, usually by tunnelling [10]. Moreover, rates of such *electrocatalytic* processes (characterised by a potential-dependence of the rate of an electrode reaction) can usually be varied over a wide range by change of applied electrode potential. This is because the Gibbs energy of activation, $\Delta G_E^{\neq}$, can be varied by changing the work function, according to the equation:

$$\Delta G_E^{\neq} = \Delta G_{E=0}^{\neq} \pm \beta EF \tag{1.5}$$

where β is a barrier symmetry factor, analogous to the Brønsted coefficient, as in the Tafel equation [10] for a discharge-controlled electrode process.

Nevertheless, despite the fact that under UHV conditions, one cannot conceivably utilise the electrode potential variable to control the chemisorption energy of an adsorbate, a number of surface-science techniques, for example AES, LEED, EELS, STM and AFM, have been successfully applied to study electrode interfaces and species adsorbed upon them by means of a solution → vacuum transfer system.

1.3 Importance of studies at well-ordered single-crystal surfaces

A single-crystal is an array of atoms, well-ordered on a long-range scale in a metal crystal. For metals such as Au, Ag, Cu and Pt, atoms crystallise in the face-centred cubic (fcc) lattice arrangement, which is generated by repetition of a unit cell pattern. The use of such well-ordered, highly-defined, single-crystal surfaces is of major importance as it allows the relationship between surface structure and reactivity to be characterised. The origin of specificity of surface reactions and electrosorption processes to various surface geometries lies in several factors. Most importantly, the electron work function depends on the surface structure at an atomic level, being in this sense an anisotropic quantity. Thus, the most densely packed (smoothest) surfaces have highest work functions, while those roughest on the atomic scale (stepped surfaces) exhibit lowest work functions.

By analogy to the work function, a similar relationship to surface geometry arises for the potential of zero charge (*PZC*), i.e. a characteristic potential for a given interface at which the electrode charge is zero [1, 2, 6]. In fact, the *PZC* for an electrode surface is directly related to its Φ value. Hence, the most densely packed planes are expected to have the most positive, while the atomically roughest faces should have the most negative values of *PZC*. In the absence of specific adsorption of ions, the potential of zero charge can be determined as the potential at which the differential double-layer capacitance reaches its minimum, representing, almost entirely, the contribution to the capacitance from the diffuse part of the double-layer, C_D, see e.g. ref. 6.

Some other factors responsible for existence of specificity of surface reactions to the surface geometries can also be mentioned, as: a) changes in surface geometry lead to differences in the double-layer structure, which may affect the process of adsorption of anionic species; and b) adsorption on planes of various geometries leads to different geometries of co-ordination of adsorbed species which, in some cases, cause 2-dimensional reconstruction of the fine layer of metal atoms.

1.4 References

1. W. Schmickler, "*Interfacial Electrochemistry*", Oxford University Press, Inc., New York, 1996.
2. J.O'M. Bockris and A.K.N. Reddy, "*Modern Electrochemistry*", vol. 2, Plenum Press, New York, 1970.
3. B.E. Conway, "*Theory and Principles of Electrode Processes*", the Ronald Press Company, New York, 1965.
4. D.C. Grahame, *Chem. Rev.*, 1947, **47**, 441.
5. R. Parsons, *Chem. Rev.*, 1990, **90**, 813.
6. J.O'M. Bockris and S.U.M. Khan, "*Surface Electrochemistry: a molecular level approach*", Plenum Press, New York, 1993.
7. R.I. Masel, "*Principles of Adsorption and Reaction on Solid Surfaces*", Wiley Interscience, John Wiley & Sons, Inc., New York, 1996.
8. B.E. Conway, V. Birss and J. Wojtowicz, *J. Power Sources*, 1997, **66**, 1.
9. G.A. Samorjai, "*Introduction to Surface Chemistry and Catalysis*", Wiley Interscience, John Wiley & Sons, Inc., New York, 1994.
10. B.E. Conway and B.V. Tilak, *Adv. Catalysis*, 1992, **38**, 1.

Chapter 2

Examples of Electrosorption Processes

2.1 Experimental methods for their study

A considerable variety of experimental techniques is available for the study of electrode processes. While purely electrochemical techniques have been extensively used for some years for studies of electrosorption and electrocatalytic processes, and have yielded important information on the nature of such processes, they are not, by themselves, adequate for chemical identification of the involved species.

Hence, much interest has centred, in recent years, on complementary techniques that can provide more information of a "chemical" type about processes at and species adsorbed on electrode surfaces. Spectroscopic and electron-microscopic techniques are now widely used in electrochemical surface science because they allow the electrode surface to be examined at the microscopic or molecular level. Both can be carried out *in situ*, when they can be employed directly in conjunction with electrochemical methods or *ex situ*, when high-energy photo-electron spectroscopy or diffraction techniques, are available, as used in the study of solid electrode surfaces under ultra-high vacuum (UHV) conditions.

For studies at single-crystal surfaces, especially of noble metals, a number of *in situ* techniques can be employed. Methods such as *in situ* FTIR, EXAFS, STM or its modification, SECM, provide valuable information, related to that obtained by AES, LEED, ECMS or other UHV-based techniques, and are complementary to the basic electrochemical procedures. It is not in the scope of this thesis to review the above-mentioned group of techniques, although more detailed information can be found in refs. 1-3.

In the present chapter, some of the most commonly used techniques in electrochemical surface science, especially for the characterisation of behaviour at Pt single-crystal electrodes, the subject of the present research, will be reviewed.

2.1.1 Cyclic voltammetry

Cyclic voltammetry or linear sweep voltammetry, commonly abbreviated to CV, is one of the most versatile electroanalytical techniques available to the electrochemist. It is the most widely used electrochemical method for studies at single-crystal electrodes. This is because it provides excellent resolution of various processes occurring at different potentials and good facility for quantitative analysis of the results obtained. In the study of single-crystal surfaces (e.g. of Pt), cyclic voltammetry provides characteristic "finger-prints" corresponding to different crystallographic orientations of the surfaces (see Chapter 5).

Information about electrode processes is obtained from the current (i) vs. electrode potential (E) profiles, called cyclic voltammograms [4-7], which arise in response to a linearly changing potential in time, applied to the electrode under investigation. Thus, the potential, E, of the working electrode is swept between two defined limits, linearly with time, t, at a constant sweep-rate, s (V s^{-1}), according to the equation:

$$E = E_i + st \tag{2.1}$$

or

$$\frac{dE}{dt} = s \tag{2.2}$$

where E_i is some initial potential that may be held constant for some period of time. The method can employ either a single sweep (half cycle) between the initial potential, E_i, and the final potential, E_f, or a scan may be programmed to give a repetitive current response of the electrode by varying the potential between E_i and E_f (usually within ± 2 V), forward and backward in a continuous manner.

The current, i, or current-density, j, vs. potential, E, profile resulting from the potential sweep gives an electrical representation of the process(es) taking place at the electrode surface (Fig. 2.1). The current response, i, to the applied potential, E, can be expressed as the first derivative of charge, q, with respect to time:

$$i = \frac{dq}{dt} = \frac{dq}{dE}\frac{dE}{dt} \tag{2.3}$$

Since dq/dE = C (capacitance) and also dE/dt = s, the current response can be represented by the equivalent formula:

$$i = Cs \tag{2.4}$$

giving directly and conveniently the capacitance of the electrode interface. The total charge, q, passed between two potential limits E_1 and E_2 can be evaluated from the following equation:

$$dq = idt \tag{2.5}$$

by integration between the two potential limits, according to the equations shown below:

$$q = \int_{E_1}^{E_2} dq = q(E_2) - q(E_1) \tag{2.6}$$

$$q = \int_{E_1}^{E_2} i\,dt = \int_{E_1}^{E_2} \frac{i}{s}\,dE = \int_{E_1}^{E_2} C\,dE \tag{2.7}$$

where C may be a function of potential, C = f(E). For surface processes, such as the so-called underpotential deposition of H, fractional coverages, θ, may be determined using the formula:

$$\theta = \int \frac{dq}{q_1} = \int \frac{i(t)}{q_1}\,dt \tag{2.8}$$

where q_1 is the charge required to form *one* monolayer of the adsorbed species.

In the investigation of adsorption processes at electrode surfaces by means of cyclic voltammetry, it is possible to determine surface coverage down to about 3% of a monolayer (θ=0.03) of an electroactive species formed by Faradaic electron transfer, e.g. desorption of adsorbed H, or OH and O species in a step such as:

$$H_2O + M + e^- \Leftrightarrow M-H_{ads} + OH^- \tag{2.9}$$

Reversibility and irreversibility of electrode surface processes

One of the fundamental aspects of the cyclic voltammetry technique is the possibility of examining the reversibility and irreversibility of surface processes. Fig. 2.2 shows four schematic diagrams of the principal types of observable CV profiles.

A *reversible* electroreduction and reoxidation surface process which is *not* governed by diffusion to and/or from the electrode surface is represented by a symmetrical anodic/cathodic pair of current-response peaks, as shown in Fig. 2.2a. In an ideal case, the anodic/cathodic voltage separation (ΔE) for this system is close to zero. A surface electrosorption process such as:

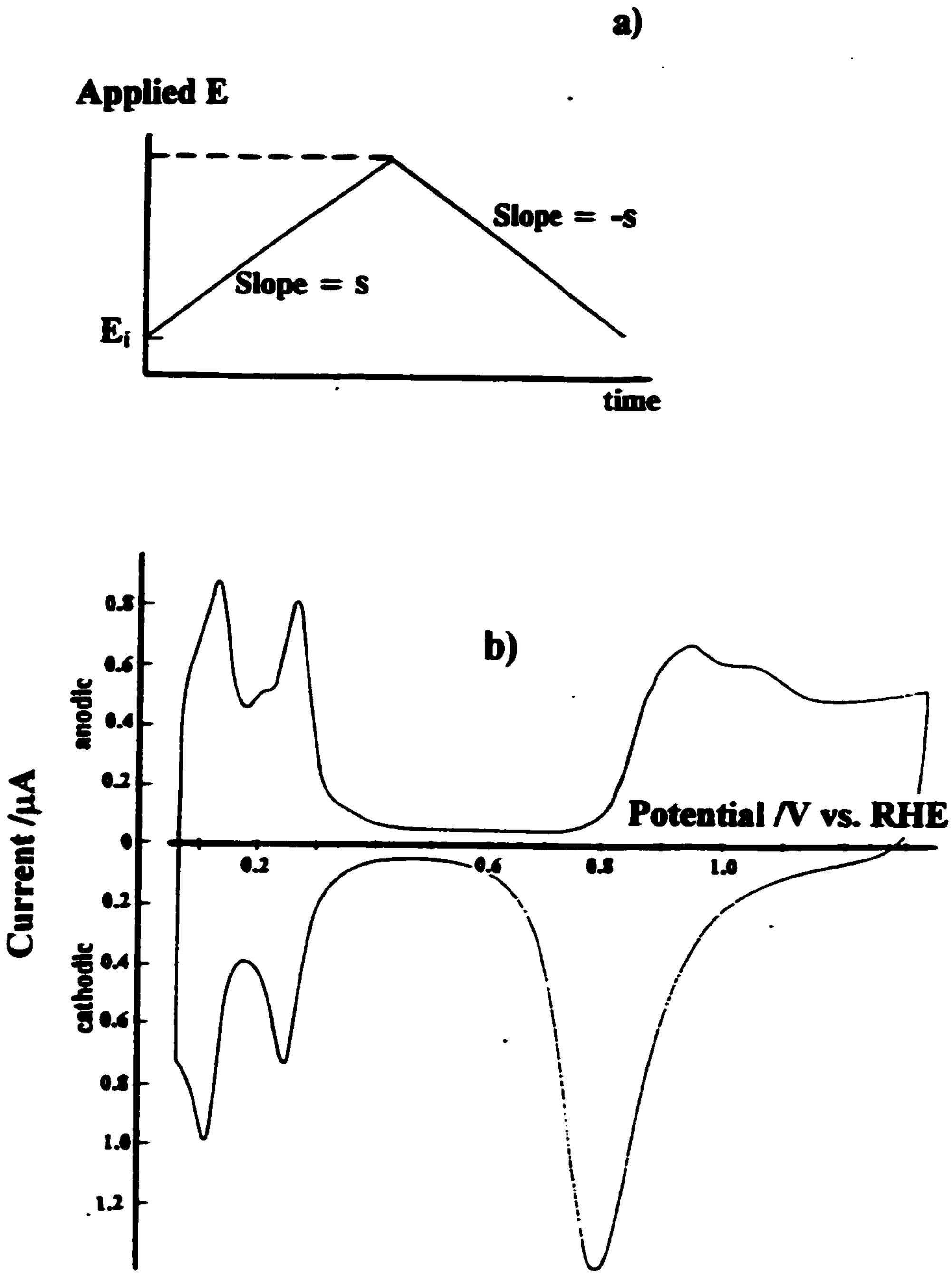

Fig. 2.1 a) Schematic diagram of a cyclic potential sweep; b) Resulting current-response (cyclic voltammetric profile) for a polycrystalline Pt electrode, obtained in aqueous 0.5 mol dm^{-3} H_2SO_4 solution, at a sweep rate s=0.050 V s^{-1} [8].

$$\underset{(1-\theta_A)c_A}{M + A} + \underset{E}{ne^-(\text{in } M)} \underset{k_{-1}}{\overset{k_1}{\Leftrightarrow}} \underset{\theta_A}{M-A_{ads}} \qquad \textbf{(2.10)}$$

is at equilibrium when the forward rate of reaction equals that for the reverse process, $\vec{i} = \overleftarrow{i}$. Then a potential-sweep experiment generates a reversible cyclic voltammetric profile, as shown in Fig. 2.2a. The surface charge-transfer process occurs by electron transfer between a metal site M and a solution species A (at a concentration of c_A). This leads to the formation of a chemisorbed species MA_{ads}, up to a limiting fractional coverage θ_A=1. The net Faradaic current, i, can be expressed in the form of a Butler-Volmer equation [9-12]:

$$i = nF\left[k_1 c_A(1-\theta_A)\exp\left(\frac{-\alpha nFE}{RT}\right) - k_{-1}\theta_A \exp\left(\frac{(1-\alpha)nFE}{RT}\right)\right] \qquad \textbf{(2.11)}$$

where k_1 and k_{-1} are the rate constants for the forward and reverse directions of the reaction, respectively, E is the metal/solution potential difference, α is the transfer coefficient, θ_A the fractional coverage by A_{ads}, $(1-\theta_A)$ is the corresponding fraction of free sites of M available at which the process 2.10 can occur, and n is the number of electrons transferred in the reaction [9]. A negative sign in the argument of the exponent in equation 2.11 is conventionally taken for a cathodic (reductive) process. At equilibrium, the forward and reverse current terms in equation 2.11 are equal (so i=0) and each is called the exchange current, i_0.

The electrochemical *Langmuir isotherm* for the process 2.10 can be represented by the following equation:

$$\frac{\theta_A}{1-\theta_A} = K_1 c_A \exp\left(\frac{-nFE}{RT}\right) \qquad \textbf{(2.12)}$$

where $K_1 = k_1/k_{-1}$ and $\alpha=1$. Equation 2.12 results from extracting $\theta_A/(1-\theta_A)$ from equation 2.11, for the equilibrium condition, $i=0$. A process represented by equation 2.12 has, effectively, a potential-dependent equilibrium constant and a corresponding potential-dependent standard Gibbs energy (from K_1).

The Langmuir isotherm is the simplest adsorption equilibrium expression based on the assumptions that every adsorption site is equivalent and that the particles bind randomly to the surface, i.e. independently of whether or not nearby sites are occupied. The increase of coverage of the species starts from $\theta=0$ and is limited by completion of one full monolayer on the substrate surface, $\theta=1$. Both the coverage and the Gibbs energy of adsorption, ΔG_{ads}, are potential dependent and (for the Langmuir case) the latter does not involve lateral interaction effects [14-17]. K_1 contains the standard value of ΔG_{ads}, defined for c_A (or activity of A) =1 and $\theta_A=0.5$.

Srinivasan and Gileadi [9] derived equations which relate current to potential as a function of sweep-rate for the type of surface process shown in 2.10. In the reversible case, the peak current, i_p, and peak potential, E_p, are given by the equations:

$$i_p = -\frac{q_1 nF}{4RT} s \qquad \textbf{(2.13)}$$

$$E_p = -\frac{RT}{nF} \ln K_1 \qquad \textbf{(2.14)}$$

Here, the peak current is directly proportional to the sweep-rate and the peak potential is independent of s. The quantity: $q_1 nF/4RT$ is the maximum adsorption pseudocapacitance

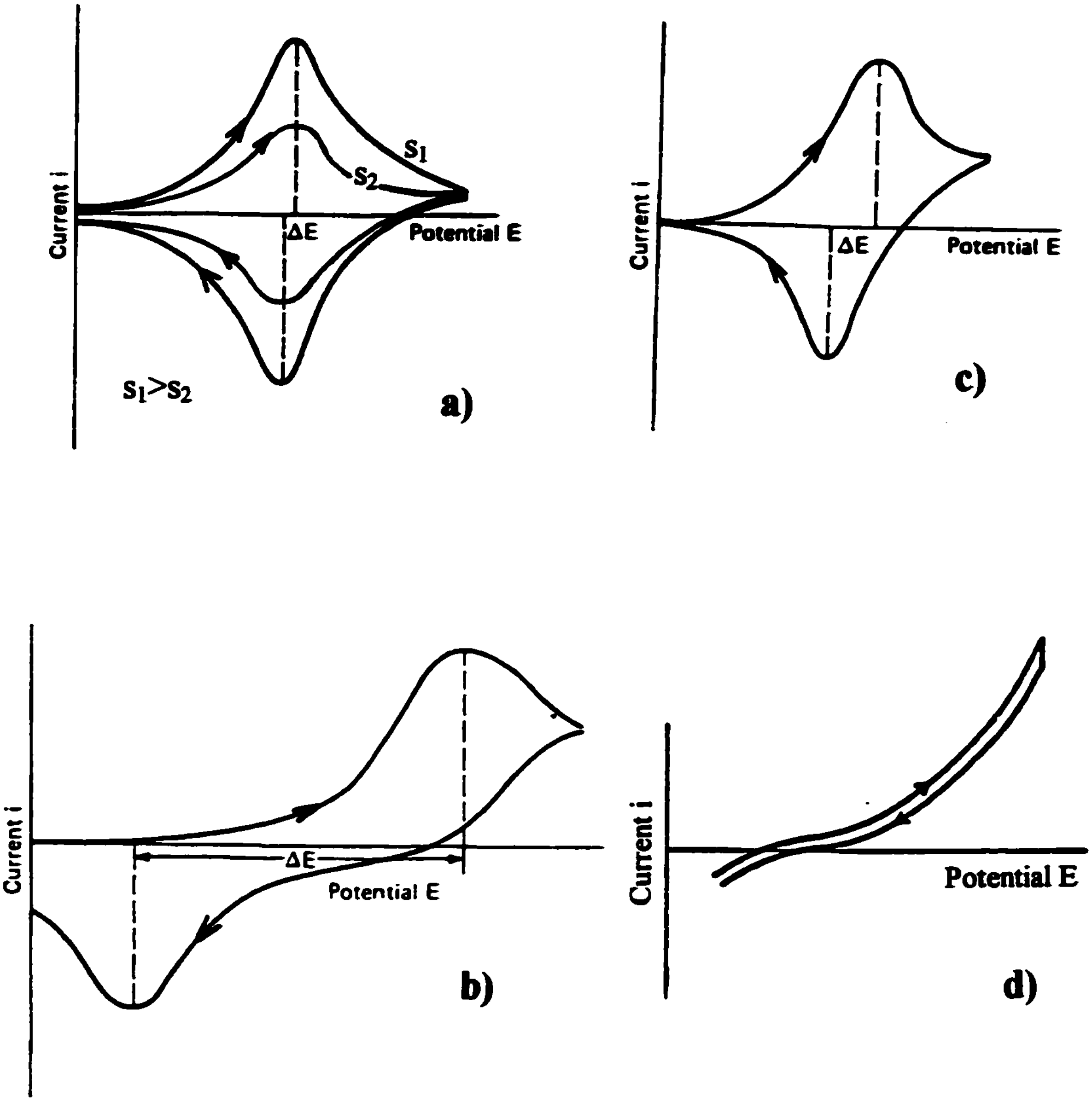

Fig. 2.2 Schematic diagrams of principal types of observable CV profiles: a) Reversible electroreduction and reoxidation surface process; b) Quasi-reversible surface process; c) Reversible surface process under diffusion control; d) Continuous Faradaic process not involving a surface species; [7, 13].

(when θ_A=0.5). For all values of coverage, the pseudocapacitance, C_p, can be obtained from the equation:

$$C_p = \frac{q_1 nF}{RT} \theta_A (1-\theta_A) \qquad (2.15)$$

For a *quasi-reversible* surface process, the positive and negative-going current peaks are separated to an extent dependent on s and the shape of the peak is less sharp at its summit, as shown in Fig. 2.2b.

A completely *irreversible* electrode process produces a single peak on one direction of sweep. In this case, the reaction proceeds at a rate almost equal to its forward rate, i.e. as $k_1 \gg k_{-1}$. For this condition, the back reaction rate is negligible, so that equation 2.11 simplifies to:

$$i = nFk_1 c_A (1-\theta_A) \exp\left(\frac{-\alpha nFE}{RT}\right) \qquad (2.16)$$

For this case, the derived [9] peak cathodic current and potential are obtained from the equations:

$$i_p = -(1-\theta_A) \frac{q_1 nF}{RT} s \qquad (2.17)$$

and

$$E_p = -\frac{RT}{nF}\left(\ln \frac{q_1 nF}{k_1 RT} + \ln s\right) \qquad (2.18)$$

The peak current is again proportional to the sweep-rate, s. The peak potential, on the other hand, is now a linear function of the natural logarithm of the sweep-rate [9], corresponding to a Tafel-like relation involving an overvoltage in the s-dependent E_p.

Sweep-rate dependence of current in relation to diffusion control

The reaction rate of the electrode process can be under ohmic, activation (i.e. the reaction kinetics are determined by the rate of formation of an activated complex) or diffusion control. For a reversible or irreversible electrochemical reaction:

$$O + ne^- \Leftrightarrow R \tag{2.19}$$

the process may be diffusion-controlled at sufficiently low reagent concentration or (and) when a large enough rate constant is involved.

The kinetic behaviour of a *reversible* surface process under *diffusion control* is shown in Fig. 2.2c. Here, a significantly asymmetric pair of current peaks is observable, i.e. the anodic and cathodic peak potentials do not have the same value along the range of potential in the sweep since a concentration gradient of R in the reverse direction from that generated with O in the cathodic sweep must be established to reoxidise R to O. For an *irreversible* process, however, the cathodic and anodic peak potentials will differ more and their difference will increase with ln s. For the reversible case, the peak potential, E_p, is independent of the potential sweep-rate, s. The kinetic behaviour of an *irreversible* Faradaic process which does *not* involve a surface adsorbed species is shown in Fig. 2.2d.

Under diffusion control, application of Fick's laws with the appropriate boundary conditions leads to equations for the peak current, i_p, [18-22] which varies linearly with the square-root of the sweep-rate, $s^{1/2}$, according to the equations:

$$i_p^{rev} = (2.69x10^5)n^{3/2}Ac_A(Ds)^{1/2} \tag{2.20}$$

for a reversible process and

$$i_p^{irrev} = (2.99x10^5)\alpha^{1/2}n^{3/2}Ac_A(Ds)^{1/2} \tag{2.21}$$

for a completely irreversible process, where A is the surface area (cm^2), D the diffusion coefficient ($cm^2\ s^{-1}$) and c_A is the concentration of species A ($mol\ cm^{-3}$). Note that under both conditions i_p is *square-root* in s, which provides a diagnostic characteristic for diffusion control.

2.1.2 *A.c. impedance spectroscopy*

A.c. impedance spectroscopy is a technique employing modulation of current at an electrode by a small sinusoidal alternating voltage (a.v.) (<10 mV) signal. Application of such a sinusoidal potential modulation signal to an electrode:

$$E(t) = \Delta E \sin \omega t \tag{2.22}$$

where ω is the angular frequency ($2\pi f$) in Rad/s, E is the instantaneous and ΔE is the maximum amplitude, produces a current response, i, in a sinusoidal form of the same frequency, but different in amplitude, Δi and phase, φ, from the potential [6, 23]:

$$i = \Delta i \sin(\omega t + \phi) \tag{2.23}$$

An electrode interface exhibits a (double-layer) capacitance, C_{dl}. Since such a capacitance, C, relates the charge, q, residing on the plates of the capacitor to the potential, E, across its plates:

$$q = CE \quad \text{and} \quad i = \frac{dq}{dt} \quad \Rightarrow \quad i = C\frac{dE}{dt} \tag{2.24}$$

Thus, equation 2.23 can be rewritten for alternating voltage conditions as:

$$i = \omega \Delta E C \cos \omega t \tag{2.25}$$

Replacing 1/ωC by the symbol X_C [6, 23] (called the capacitive reactance), an equation similar in form to Ohm's law for a resistor (i = E/R) is obtained:

$$i = \frac{\Delta E}{X_C} \sin(\omega t + \frac{\pi}{2}) \tag{2.26}$$

where R is replaced by X_C and the phase angle between the current and potential is $\pi/2$. In the case of a purely resistive circuit, the phase angle between the current and potential is zero (Fig. 2.3a). However, in the case of the capacitance, the resulting current and the applied potential are out of phase by 90°, as shown in Fig. 2.3b. Introducing complex notation in which magnitudes on the ordinate axis are multiplied by $j = \sqrt{-1}$, current and potential can be regarded as phasors (i.e. rotating vectors) and:

$$E(t) = -jX_C i(t) \tag{2.27}$$

An ideally polarisable electrode can be represented by a circuit containing a solution resistance, R_S, in series with a double-layer capacitance component, C_{dl}. For a resistor and a capacitor connected in series, the sum of the potential drops across each element must be equal to the total potential difference of E^{tot}, thus:

$$E^{tot} = E_{R_S} + E_{C_{dl}} \tag{2.28}$$

$$E^{tot} = iR_S + (-jX_{C_{dl}} i) \tag{2.29}$$

$$E^{tot} = i(R_S - jX_{C_{dl}}) \tag{2.30}$$

$$E^{tot} = iZ \tag{2.31}$$

where $Z = (R_S - jX_{C_{dl}})$ is called the *impedance*. The impedance of this circuit can be decomposed into its real, $Z' = R_S$, and imaginary, $Z'' = -jX_{C_{dl}}$, components. Hence, the total impedance, Z, of this circuit is represented by the equation [6, 23, 24]:

$$Z = Z' + Z'' \tag{2.32}$$

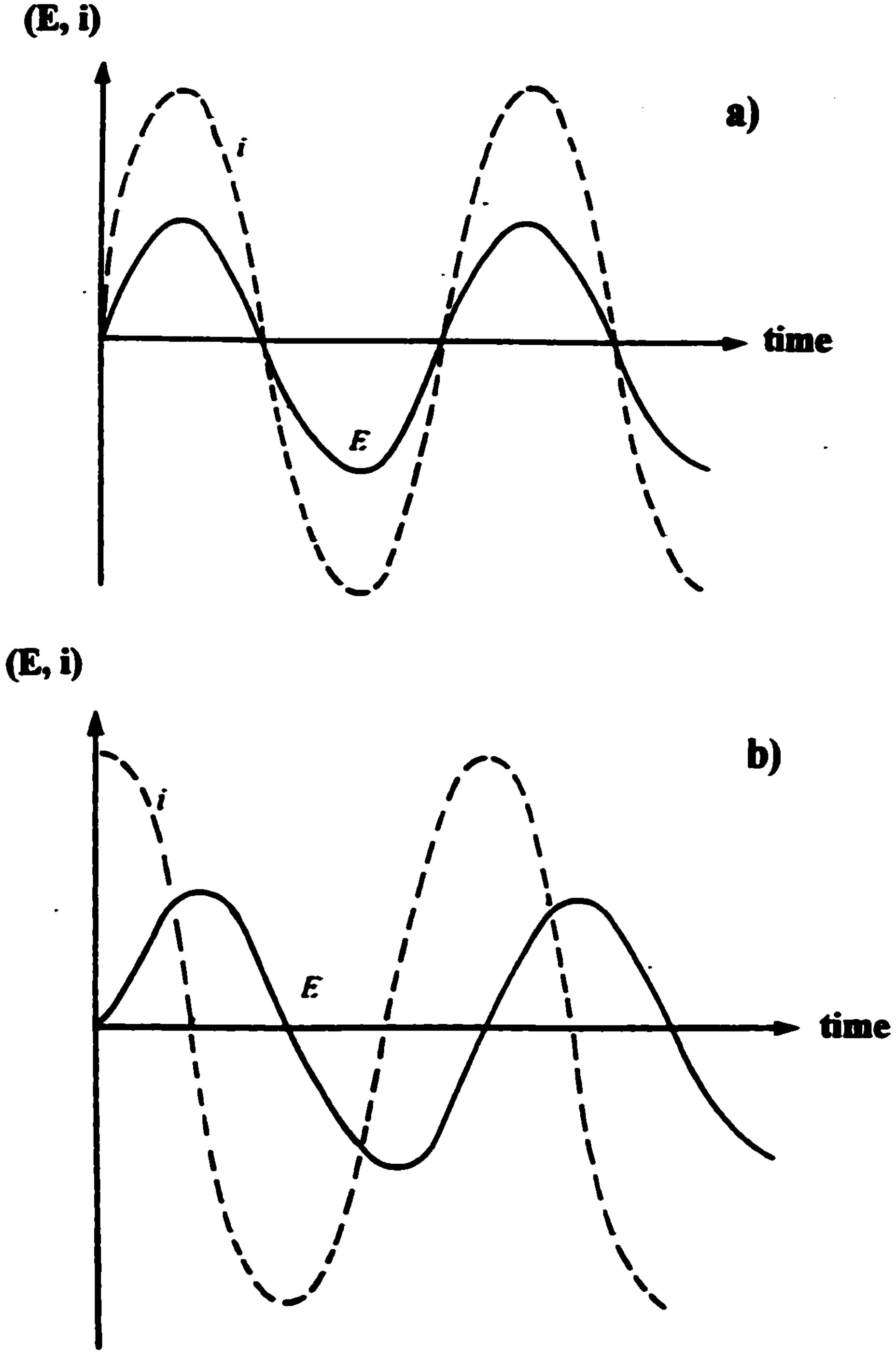

Fig. 2.3 Equivalent representations in phasor and time axis form of current response and applied potential in a) A purely resistive circuit where the phase angle is zero; b) A circuit with capacitive reactance, showing a 90° phase angle [6, 23].

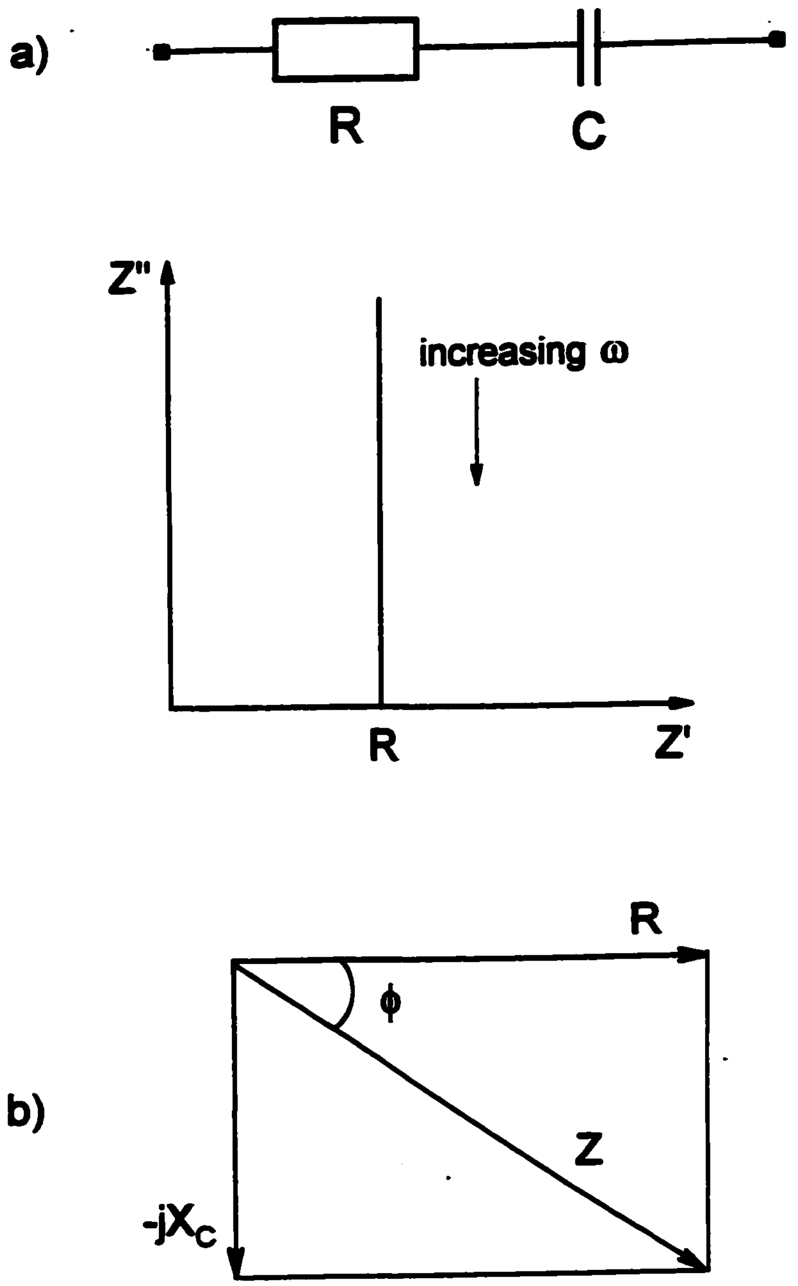

Fig. 2.4 a) Equivalent circuit for a series RC connection for an ideally polarised electrode and the corresponding Nyquist impedance representation for this circuit; b) Complex-plane diagram showing the total impedance, Z, obtained by vector addition of resistive, R, and capacitive, $-jX_C$ components [6, 23].

The above circuit can be modelled by the equivalent RC series circuit with the corresponding complex-plane impedance (or Nyquist) diagram, as shown in Fig. 2.4a. Note, that the real and imaginary components are directly separable. The result is a vertical line; the real part of the impedance, Z', is frequency independent while the imaginary part, $Z'' = (1/j\omega C \equiv -j/\omega C)$, tends to zero at high frequencies. When the potential is measured with respect to the current, the phase shift of a capacitor is negative with respect to a resistor ($\phi=0$); thus, the convention for presentation is to plot the negative of the imaginary vs. the positive real axis. The total impedance, Z, is obtained by vector addition and the phase angle, ϕ, represented in the complex plane diagram (Fig. 2.4b), is obtained simply from the following equation [6]:

$$\tan\phi = \frac{X_C}{R} = \frac{1}{\omega RC} \tag{2.33}$$

When a Faradaic current passes due to an electron-transfer process (e.g. a redox reaction), the electrode equivalent circuit contains a potential-dependent charge-transfer resistance element, R_{ct}, in parallel with the double-layer capacitance, C_{dl}, as shown in Fig. 2.5a. The reciprocal impedance (or so-called *admittance*, $Y = 1/Z$), of such a combination is calculated [24] as:

$$Y = \frac{1}{Z} = \frac{1}{Z_{R_{ct}}} + \frac{1}{Z_{C_{dl}}} = \frac{1}{R_{ct}} + j\omega C_{dl} = \frac{(1 + j\omega R_{ct} C_{dl})}{R_{ct}} \tag{2.34}$$

The real and imaginary components of the impedance can be separated by multiplying top and bottom of equation 2.34 by the complex conjugate of the numerator:

$$\frac{1}{Z} = \frac{(1 + j\omega R_{ct} C_{dl})}{R_{ct}} \frac{(-1 + j\omega R_{ct} C_{dl})}{(-1 + j\omega R_{ct} C_{dl})} = \frac{(-1 - \omega^2 R_{ct}^2 C_{dl}^2)}{R_{ct}(j\omega R_{ct} C_{dl} - 1)} \tag{2.35}$$

When the impedance, Z, is required, the result is:

$$Z = \frac{R_{ct}}{(\omega^2 R_{ct}^2 C_{dl}^2 + 1)} - j\frac{\omega R_{ct}^2 C_{dl}}{(\omega^2 R_{ct}^2 C_{dl}^2 + 1)} = Z' + Z'' \qquad (2.36)$$

so that the real and imaginary parts become separated. Also, both parts are frequency dependent. Since Z" in equation 2.36 is:

$$Z'' = -j\frac{\omega R_{ct}^2 C_{dl}}{(\omega^2 R_{ct}^2 C_{dl}^2 + 1)} \qquad (2.37)$$

then, by replacing ω by the Z′ function term, a relation between Z" and Z′ follows as:

$$Z''^2 = (R_{ct} - Z')Z' \Rightarrow Z''^2 + \left(Z' - \frac{R_{ct}}{2}\right)^2 - \left(\frac{R_{ct}}{2}\right)^2 = 0 \qquad (2.38)$$

As may be seen in the Nyquist spectrum of Fig. 2.5b, the above expression is simply the equation for a semicircle passing through the origin with diameter R_{ct}, centred at $R_{ct}/2$. The charge-transfer resistance, R_{ct}, may be read directly from the diameter of the semicircle and C_{dl} can be calculated from the semicircle's maximum, since $\omega_{max}=1/R_{ct}C_{dl}$, where $R_{ct}C_{dl}$ is the time constant for the given parallel combination [6, 23, 24]. Another way in which impedance results may be represented is in terms of the phase angle, ϕ, (or $\log|Z|$) vs. frequency, ω, plot (the so-called Bode plot). This kind of plot, corresponding to the Nyquist diagram shown in Fig. 2.5b, has a characteristic inflection point, as shown in Fig. 2.5c.

Since the a.c. impedance technique is capable of scanning a very wide frequency range (10^6-10^{-4} Hz), it is often possible to resolve more complicated combinations of RC circuits provided that the relative values of their time constants are sufficiently large.

For a process involving an adsorbed intermediate, such as UPD of H, where the Faradaic discharge resistance for electrosorption of H, R_F, is accompanied by a corresponding Faradaic pseudocapacitance, C_p, the equivalent circuit is as shown in Fig. 2.6a. It gives rise to a Nyquist plot having the form shown in Fig. 2.6b. The admittance of such a circuit is as follows [24]:

$$\frac{1}{Z}=\frac{1}{Z_{R_F}+Z_{C_p}}+\frac{1}{Z_{C_{dl}}}=\frac{1}{R_F-\frac{j}{\omega C_p}}+j\omega C_{dl} \Rightarrow \tag{2.39}$$

$$\Rightarrow \frac{1}{Z}=\frac{\omega C_p}{R_F\omega C_p-j}+j\omega C_{dl} \tag{2.40}$$

After separating the real and imaginary components, the admittance takes the following form:

$$\frac{1}{Z}=\frac{R_F\omega^2 C_p^2}{R_F^2\omega^2 C_p^2+1}+j\left(\frac{\omega C_p}{R_F^2\omega^2 C_p^2+1}+\omega C_{dl}\right) \tag{2.41}$$

Solution resistance, R_S, is significant in all ion-conducting media; thus, practically it has always to be included in the equivalent circuits, see Fig. 2.6. It defines the high-frequency limit of the impedance plot and normally behaves as a pure resistor. The solution resistance is added in series with the vectorial combination of C_{dl} and R_F, or other circuit elements, and simply shifts the spectra along the real, Z', axis. It can be then read as the high-frequency intercept with that axis.

In many cases, when a Faradaic process takes place at the electrode, allowance must be made for diffusional effects associated with consumption of solution species involved in the electrode reaction, leading to a concentration gradient. Then, a diffusional impedance element, called the *Warburg impedance*, must be included in the equivalent

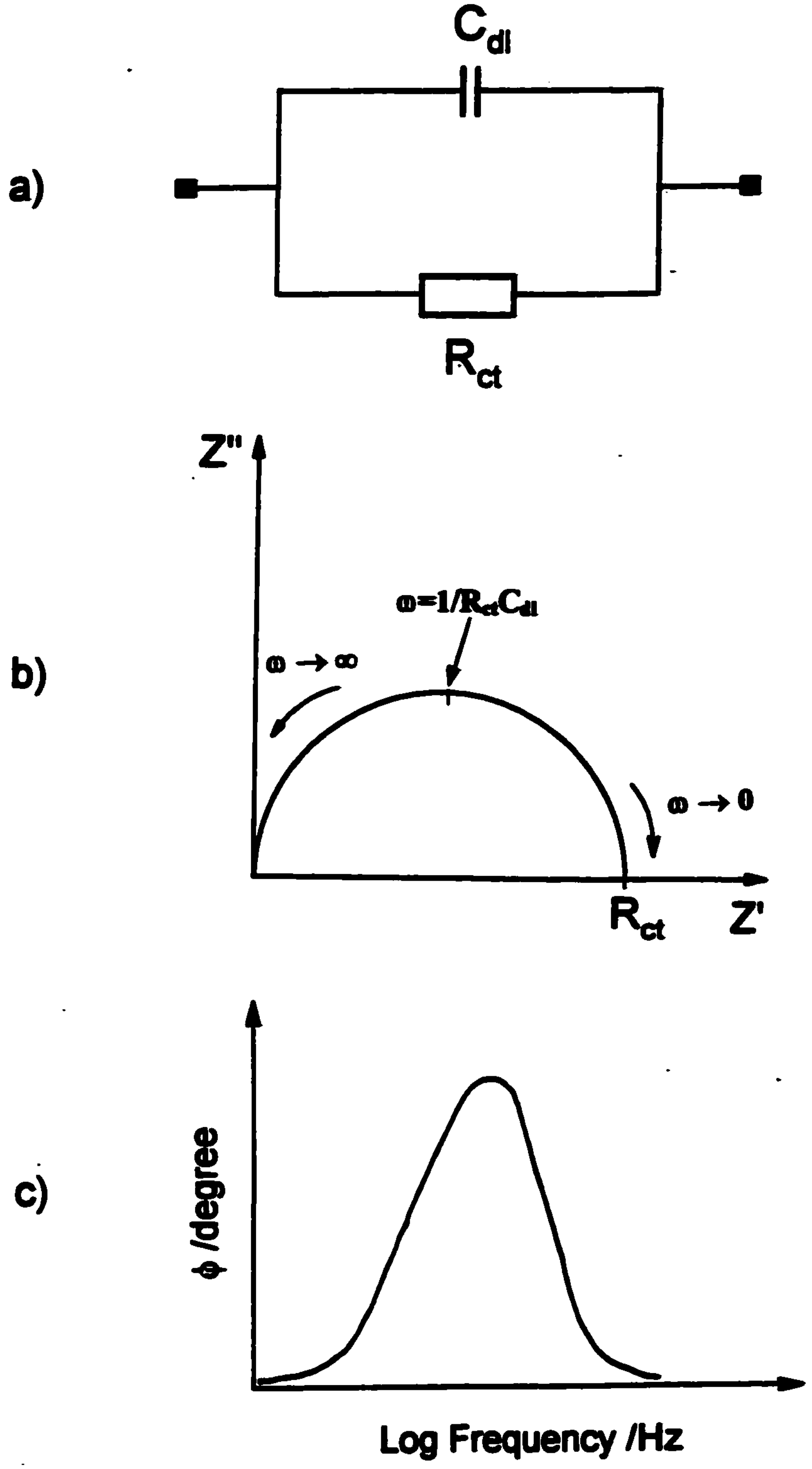

Fig. 2.5 a) Equivalent circuit for an electrode reaction with double-layer capacitance, C_{dl}, in parallel with a Faradaic charge-transfer resistance, R_{ct}; b) Complex-plane Nyquist diagram for a parallel $R_{ct}C_{dl}$ circuit; c) Bode phase-angle plot for a parallel $R_{ct}C_{dl}$ circuit [6].

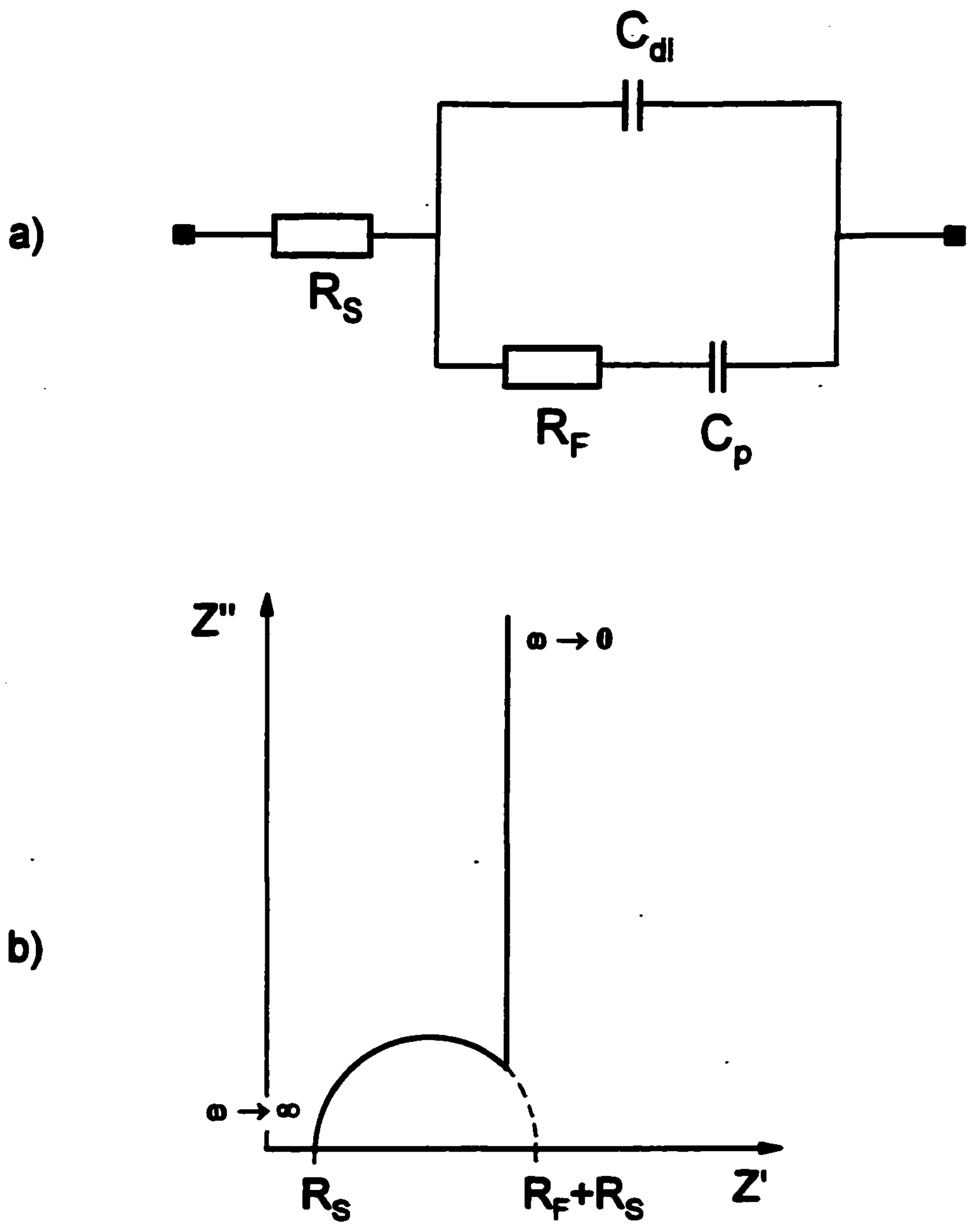

Fig. 2.6 a) Equivalent circuit for an adsorption process such as UPD of H, exhibiting Faradaic pseudocapacitance, C_p, charged via a Faradaic resistance, R_F, in a parallel combination with the double-layer capacitance, C_{dl}, jointly in series with an uncompensated solution resistance, R_S; b) Nyquist representation for this circuit [25, 26].

circuit [6, 23, 24] to represent this situation, as shown in Fig. 2.7a. It is comprised of capacitance, C_{diff}, and resistance, R_{diff}, components in parallel, each of which is dependent on the reciprocal of square-root of frequency, $\omega^{-1/2}$. This kind of equivalent circuit gives rise to a Nyquist diagram of the form shown in Fig. 2.7b. The ohmic part is determined by the finite mobility of ions in a field or of molecules in a concentration gradient and the capacitative part by the fluctuating quantity of material available for reaction in the periodically changing diffusion layer. Since both capacitative and ohmic components of the Warburg impedance term depend on the reactant concentration, c, and frequency, ω, in the same way, the combination exhibits a phase angle of 45° at sufficiently low angular frequencies. The Warburg line, of slope 45°, seems to tend to infinity as ω becomes smaller (see Fig. 2.7b); however, it will ultimately curve, either back down to the real axis for Faradaic reactions or, for capacitive responses, upwards, giving finally a vertical line tending to infinity as $\omega \rightarrow 0$.

Analysis of the equivalent circuit for a Faradaic reaction involving solution mass-transfer effects leads to the following equation for the Warburg impedance term, Z_W [6, 24]:

$$Z_W = \sigma\omega^{-1/2} - j\sigma\omega^{-1/2} \quad \textbf{(2.42)}$$

where

$$\sigma = \frac{RT}{n^2F^2\sqrt{2}}\left(\frac{1}{c_O\sqrt{D_O}} + \frac{1}{c_R\sqrt{D_R}}\right) \quad \textbf{(2.43)}$$

for a redox process involving a concentration of oxidant, c_O, and of reductant, c_R, in an n-electron reaction, where D_O and D_R quantities are diffusion constants for the oxidant and reductant, respectively.

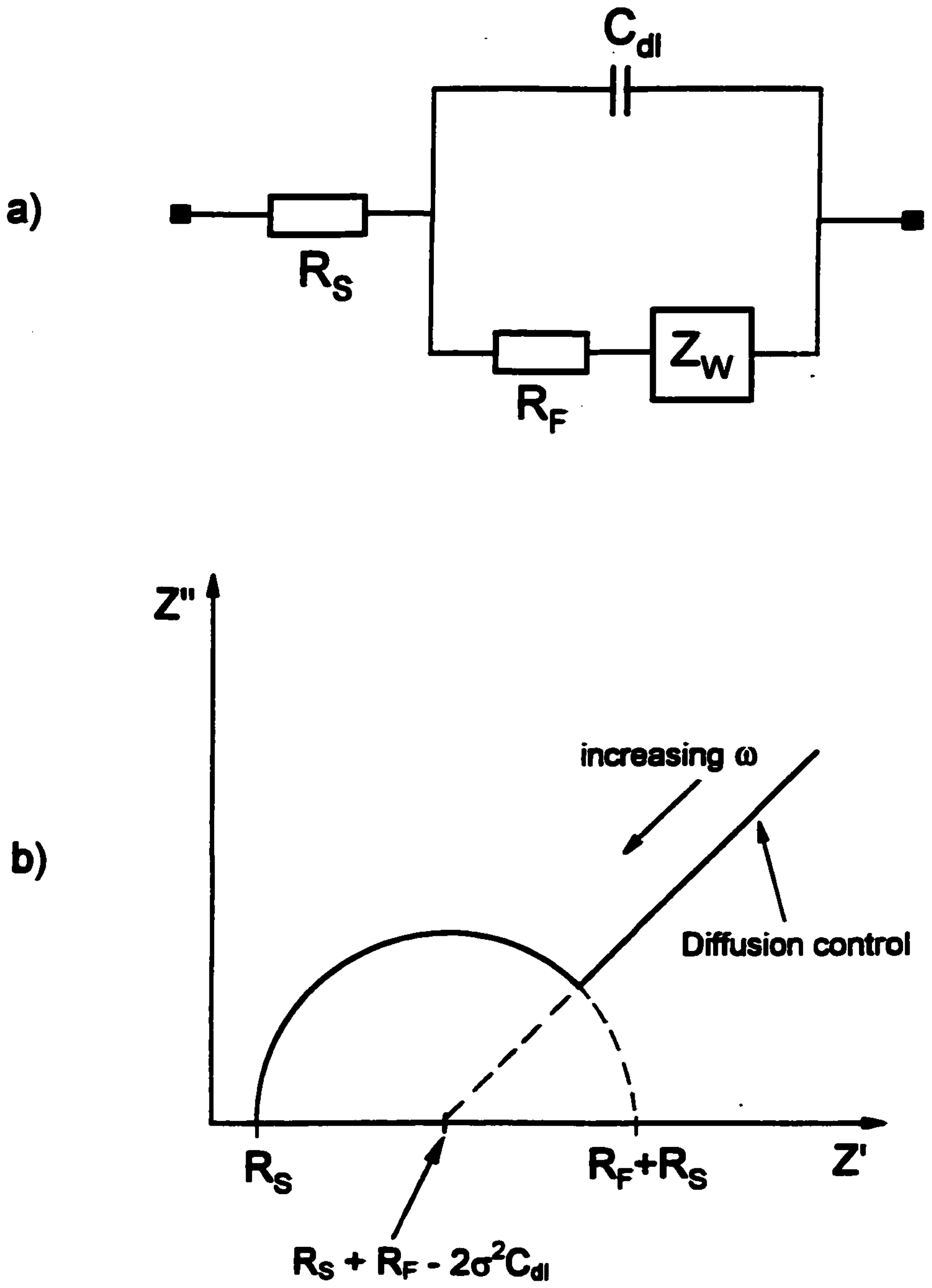

Fig. 2.7 a) Equivalent circuit for an electrode reaction with double-layer capacitance, C_{dl}, in parallel with a charge-transfer resistance, R_F, with uncompensated solution resistance, R_S, and a diffusional Warburg impedance term, Z_W; b) Complex-plane Nyquist diagram for this circuit [6].

At low frequencies, the total impedance, Z, characterising the behaviour of the equivalent circuit shown in Fig. 2.7a, reduces to the form [6]:

$$Z = R_S + R_F + \sigma\omega^{-1/2} - j\left(\sigma\omega^{-1/2} + 2\sigma^2 C_{dl}\right) \qquad \textbf{(2.44)}$$

and the Warburg line, when extended to the real axis, has an intercept of: $R_S+R_F-2\sigma^2C_{dl}$. On the other hand, at high frequencies, where the Warburg impedance is negligible in relation to R_F, the total impedance can be written as in equation 2.36, for the parallel combination of R_F and C_{dl} elements.

In the case of inhomogeneous surfaces, displaying surface defects, porosity, etc., the impedance response can be modelled by an equivalent circuit containing a so-called *Constant Phase Element* (CPE), as shown in the simple model in Fig. 2.8a. The corresponding Nyquist diagram for this circuit is shown in Fig. 2.8b. Here, the capacitive line shows deviation from an ideal response (see Fig. 2.4a for comparison), which is related to the inhomogeneous distribution of current caused by surface irregularities. Moreover, for the equivalent circuit normally giving rise to the semicircle (Fig. 2.5b), when a CPE component is included, a depressed (rotated) semicircle results [27]. In practice, when the latter is experimentally observed, the equivalent circuit and its analysis requires inclusion of a CPE element.

For a series RC connection, the angle of inclination of the capacitive line to the Z′ axis, observed in the impedance spectrum (Fig. 2.8b), is independent of angular frequency, ω, and is modelled by substituting the capacitance by a parameter T, given in F cm^{-2} $s^{1-\varphi}$. The impedance of the CPE component is described [27] by:

$$Z_{CPE} = \frac{1}{T(j\omega)^{\varphi}} \qquad \textbf{(2.45)}$$

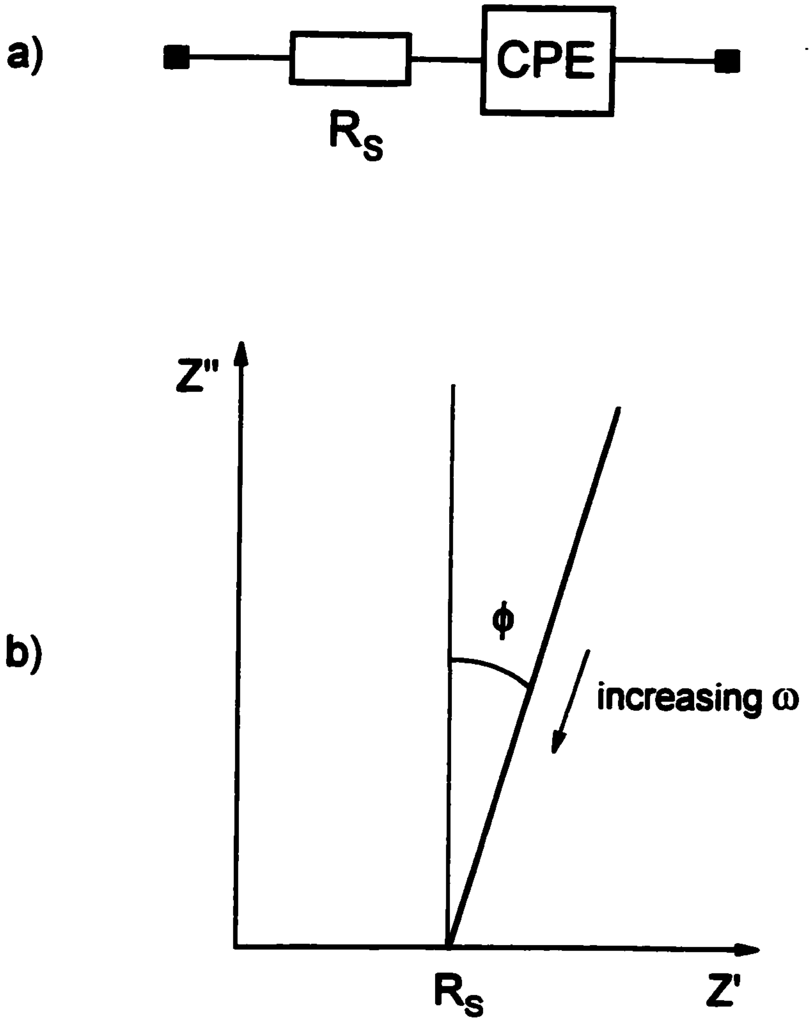

Fig. 2.8 a) Equivalent circuit for an inhomogeneous, ideally polarisable electrode; b) Complex-plane Nyquist diagram for this circuit [23].

where exponent φ is a dimensionless parameter $(-1 \leq \varphi \leq 1)$ which determines the constant phase angle in the complex-plane plot, as $(\pi/2)\varphi$.

2.1.3 In situ FTIR spectroscopy

In situ techniques, in which the structural integrity of the electrode-solution interface is maintained, are of special interest in surface electrochemistry. Among others, *in situ* IR spectroscopy is one of the most important and has been applied in a significant section of the present work. Infrared spectroscopy measurements at electrodes have been attempted since about 1966 [28]. However, only when the technique was improved (largely by Bewick and Robinson) by utilising a monochromator [29] and a signal-averaging procedure, were first meaningful results on adsorbed molecules at electrodes obtained by Neugebauer et al. in 1981 [30]. Especially, a new era in IR spectroscopy at electrode surfaces started when the Fourier Transform (FT) technique was employed to enhance the signal intensity [31]. The detection of infrared absorbances by submonolayers of species at an electrode-solution interface requires a high level of selectivity and sensitivity, which has been achieved by using thin-layer infrared-electrochemical cells and by modulating the electrode potential or the state of polarisation of the infrared radiation. This is required in order to distinguish the IR absorption characteristics of the adsorbate film from the usually stronger background absorption of bulk solvent water.

A particularly powerful tool for research on adsorbed layers on metal surfaces is Reflection-Absorption Infrared Spectroscopy (RAIRS). The RAIRS method consists in modulating the polarisation state of the incident IR light (in *s* and *p* polarisation) and recording the difference in the absorbance intensity (I_p-I_s) as a function of electrode potential. Fig. 2.9 illustrates the incident and reflected electric vectors of the *s* and *p* components of the infrared radiation, where *p* refers to parallel polarised and *s* (senkrecht) to perpendicular polarised radiation with respect to the plane of incidence. At the point of contact with the surface, the *p*-polarised radiation has a net combined amplitude that is almost twice that of the incident radiation (through the vector summation of E_p and E_p'). However, for the *s*-polarised radiation, the incident, E_s, and emitted, E_s', electric vectors undergo a 180 degree phase-shift with respect to each other and thus the net amplitude of the IR radiation parallel to the surface plane is zero (Fig. 2.9) [32-34].

Since only radiation having a *p*-component (parallel to the plane of incidence and hence perpendicular to the surface plane) may experience finite interaction with the surface (or species adsorbed on it), the only vibrations that are active are those having a component of the dynamic surface dipole oriented in the direction normal (perpendicular) to the surface plane. According to this "surface selection rule" for reflection IR spectroscopy, *s*-polarised radiation does not interact with the species adsorbed on the surface [32, 34].

There are two types of RAIRS infrared experiments that can be conducted: a) Electrochemically Modulated Infrared Spectroscopy (EMIRS) and b) Subtractively Normalised Interfacial Fourier Transform Infrared Spectroscopy (*SNIFTIRS*).

EMIRS involves relatively rapid (*ca.* 1-100 Hz) alternation of electrode potential between the two values, E_1 and E_2, such that the electrochemistry is modulated to produce a periodic change in the IR energy absorbed. This is measured as a relative change in the reflectivity of the electrode: $\Delta R/R$, where $\Delta R = R_2 - R_1$, and R_1 and R_2 refer

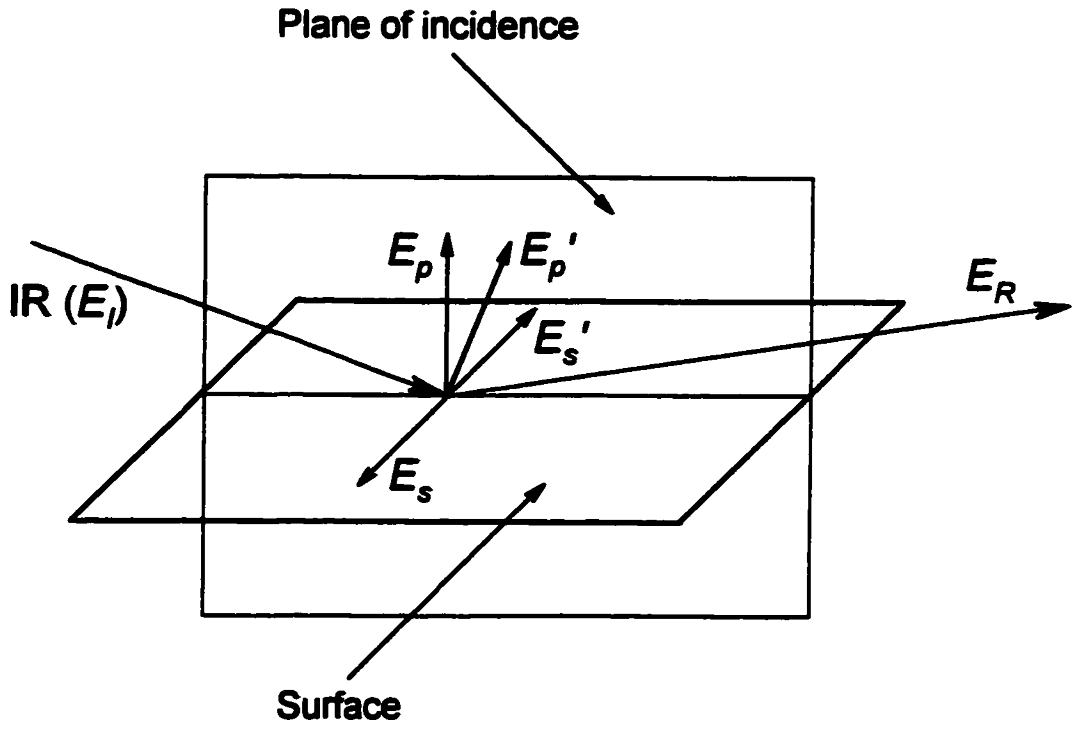

Fig. 2.9 Schematic representation of the plane of incidence, showing the incident, E_I, and reflected, E_R, electric vectors, and the definition of *s* and *p*-polarised radiation in the RAIRS experiment [34].

to the reflectance at the E_1 and E_2 potential values, respectively. The reflectance, R, is a ratio between the intensities of the reflected, I_R, and incident, I_0, beams:

$$R = \frac{I_R}{I_0} \qquad (2.46)$$

A grating monochromator is used to achieve the frequency (wavenumber) identification in EMIRS [32, 33].

In the *SNIFTIRS* method, utilising Fourier transform analysis, all the light from the source falls onto the detector at any instant, leading to an increased signal level. The frequency identification is achieved by the Fourier frequency analysis of the periodic signal at the detector. *SNIFTIRS* involves recording a series of interferometer scans, sequentially, at the two modulation potential values. To increase the signal-to-noise ratio, the so-called "interferograms" are obtained over a large number of frequency scans, e.g. 100, and then averaged [1, 32-34]. The interferograms obtained at the two potential values are then subtracted from each other to yield the Potential Difference Infrared (PDIR) spectra [35]. The spectra are usually shown as normalised differential reflectance data ($\Delta R/R_0$), where $\Delta R = R - R_0$, taking R as the reflectance at the sample and R_0 that at the reference potential.

The surface infrared experiments involve interactions of photons with surface species which result in energy transfer to (or from) the adsorbed species on the surface via vibrational excitations (or de-excitations). The discrete energies transferred correspond to vibrational quanta and analysis of these energies according to their frequencies and intensities provides the means of determining the structure of the surface species [34]. Thus, when absorption of infrared radiation occurs at the surface, the reflected beam has decreased intensity compared with that of the incident beam:

$$E_R = E_I - E_V \tag{2.47}$$

where E_R and E_I are the energies of the reflected and incident beams, and E_V is the energy lost due to the interaction of the IR radiation with the surface species. The energy loss is related to the frequency, ν, (or wavenumber, $\bar{\nu}$) as:

$$E_V = h\nu = h\frac{c}{\lambda} = hc\bar{\nu} \tag{2.48}$$

Thus, from infrared spectra, $\Delta R/R_0 = f(\bar{\nu})$, the characteristic wavenumbers (cm^{-1}) or group frequencies, corresponding to different modes of vibration for molecules or groups of atoms can be obtained. By analysis of such wavenumbers, thus obtained, the adsorbed species can not only be identified, but also its surface bonding geometry, intermolecular interactions, etc., can be determined [32, 33]. The infrared-active vibrational energy transitions usually lie in the region *ca.* 100-4,000 cm^{-1} of the electromagnetic spectrum.

2.2 UPD of H at Pt

So-called underpotential deposited (UPD) species arise (e.g. as in equations 2.9 and 2.50 later) when an electrochemical reaction produces first, on a suitable substrate adsorbent metal, a two-dimensional array of ad-species at potentials more positive or less positive than those for the respective thermodynamically reversible processes of bulk crystal or gas formation of the same element. The latter, so-called overpotential deposition (OPD) processes, require an overpotential for initial nucleation of the bulk phase. Thus, an underpotential-electrodeposition process leads not to formation of the bulk phase of some element but to a monolayer or submonolayer array of chemisorbed atoms of the same element, on the metal electrode substrate. This phenomenon normally occurs when the Gibbs energy for deposition of the ad-atom array is ***more negative*** (more favourable) than that for the corresponding three-dimensional bulk-phase formation of the element [25, 36, 37]. Cathodic UPD processes, such as deposition of ad-atoms of metals or H thus occur at potentials more positive (or less negative) than those for the respective bulk element deposition. On the other hand, for anodic processes, e.g. OH and O deposition, the UPD arises at less positive potentials than for the bulk oxide formation or O_2 evolution, as observed at Au, Pt, Pd, Rh, Ir and Ru [8, 25, 38-43].

One of the most fundamental and important subjects in surface electrochemistry is the phenomenon of UPD of H on metal substrates. The study of UPD of H at the catalytic noble (or semi-noble) metals (Pt, Rh, Ir, Ru and Pd) [4, 35, 44-49], especially at well-ordered single-crystal surfaces of Pt [50-52], has established a major activity in the field of electrochemical surface science. Since all the experiments conducted in the work described in this thesis were performed on polycrystalline or single-crystal Pt surfaces using aqueous acid or alkaline solutions, attention is given principally to UPD of H at Pt.

The first observation of UPD of H at Pt can be traced to the work of Frumkin and Slygin in 1935 [53]. However, Will and Knorr [4], by applying the cyclic voltammetry technique, were first to point out that electrosorption of H at polycrystalline Pt occurs apparently in two principal states, between 0.05 and 0.35 V, RHE, before the electrode potential becomes extended into the double-layer charging region. Thus, they were first to conclude that such a surface must comprise different types of adsorption sites. In order to characterise the nature of those sites, Will [54] investigated Pt single-crystal surfaces of (111), (100) and (110) orientations and concluded that two or three adsorption states can be simultaneously present on each plane, however in different surface fraction ratios.

Similar results were obtained by Conway et al. [55, 56]. However, later it appeared that the crystals used had facets of various orientations. The third, so-called "anomalous" state (observable in aqueous H_2SO_4 at potentials positive to the two principal adsorption states) was recognised and attributed to HSO_4^- ion adsorption [51, 57-59]. The above-mentioned sub-monolayer states are distinguished by having well-resolvable electrode potentials and each state is often characterised by Langmuir adsorption. Furthermore, the distribution and energies of the resolvable states depend on the geometry of the host lattice.

Because of the above, observation of UPD of H (and other UPD processes) is most satisfactorily studied by means of cyclic-voltammetry, which provides excellent resolution of multi-state deposition and desorption in a single cyclic sweep of potential, down to sub-monolayer levels of coverage. Further information on characterisation of different states of UPD of H and the anomalous adsorption states that arise in different supporting electrolytes, at various Pt single-crystal surfaces, will be given in Chapter 5.

The process of UPD of H at Pt (and similarly at e.g. Ir and Rh) occurs at potentials *positive* to the H_2 reversible potential, when the Gibbs energy of binding of H atoms with the metal surface is numerically greater than half the Gibbs energy of bonding in the H_2 molecule [25], thus:

$$|\Delta G|_{MH} > \frac{1}{2}|\Delta G|_{H_2} \qquad \textbf{(2.49)}$$

The relation between the currents for UPD of H, as observed in cyclic voltammetry experiments (e.g. see refs. 50 and 51, on H cathodic deposition and anodic desorption), and the continuous currents resulting from the cathodic H_2 evolution reaction (HER), when the reversible potential is exceeded in the negative direction, is illustrated in Fig. 2.10. The overpotential deposition (OPD) process, which results in cathodic H_2

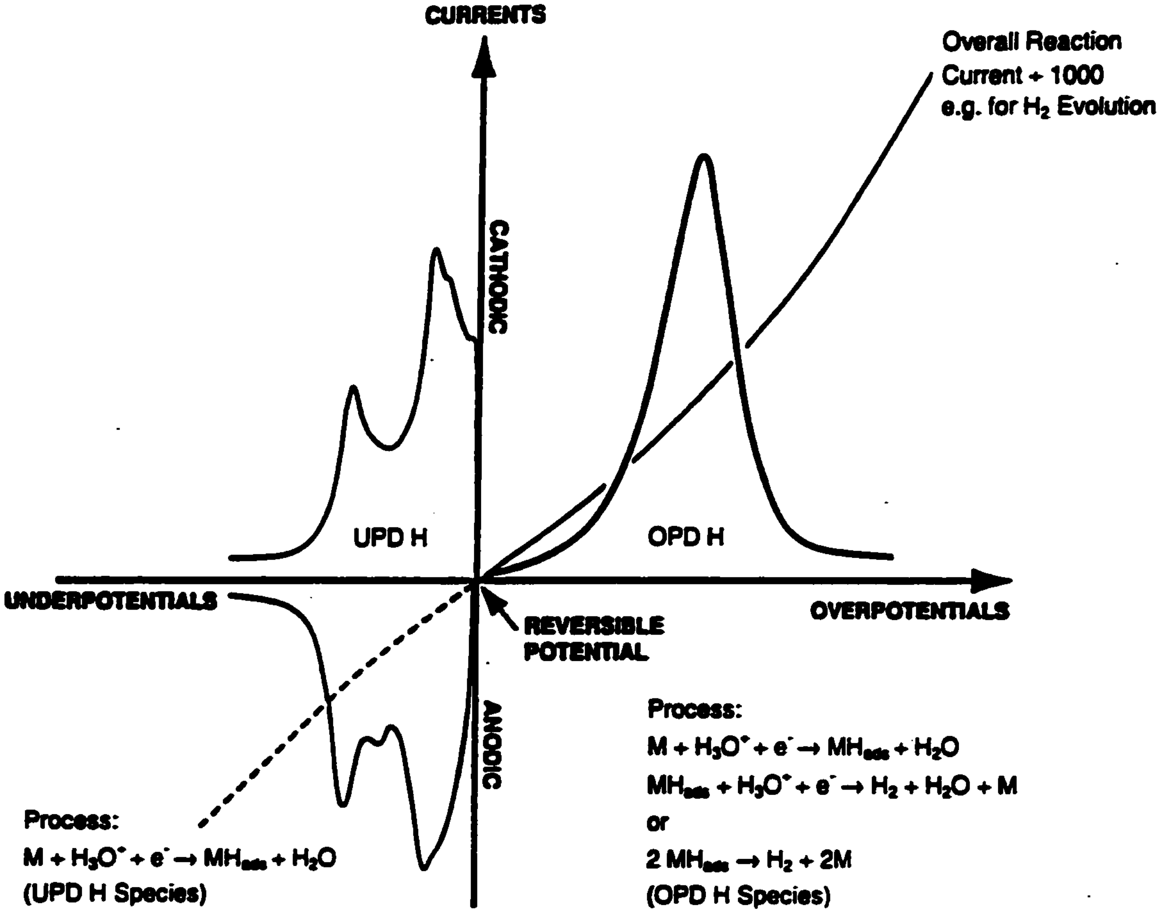

Fig. 2.10 Relation between UPD currents for H deposition and desorption, and overall H_2 evolution currents (OPD) at potentials negative to the H_2 reversible potential [25].

evolution, can pass much larger currents than the UPD process. This is because the rates of the Faradaic reactions involved in the OPD process are not limited by approach to full monolayer coverage by the adsorbed H intermediate, as is the case for the process of UPD of H. Continuous desorption of electrosorbed H takes place, forming H_2.

In acidic solution, the process of UPD of H at Pt is represented by the reaction:

$$\begin{array}{ccccccc} H_3O^+ & + & Pt & + & e^-(\text{in Pt}) & \Leftrightarrow & Pt-H_{ads}+H_2O \\ c_{H^+} & & (1-\theta_H) & & E & & \theta_H \end{array} \qquad (2.50)$$

where E is the applied potential, c_{H+} the proton concentration, θ_H the fraction of site occupancy for adsorbed H and $1\text{-}\theta_H$ is the corresponding fraction of free sites of Pt, available for adsorption, where $0 \leq \theta_H \leq 1$. The analogous UPD of H from alkaline or neutral medium is represented by the reaction:

$$H_2O+Pt+e^- \Leftrightarrow Pt-H_{ads}+OH^- \qquad (2.51)$$

where H_2O is now the source of protons for discharge.

The electrochemical Langmuir isotherm for the UPD of H process in equation 2.50 can be represented by an equation similar to 2.12:

$$\frac{\theta_H}{1-\theta_H}=K_H c_{H^+} \exp\left(\frac{-FE}{RT}\right) \qquad (2.52)$$

where K_H is an equilibrium constant for this process. Again, as previously explained in section 2.1.1, the pseudocapacitance, C_p, associated with the UPD of H process, is represented by the equation:

$$C_p=\frac{q_1F}{RT}\theta_H(1-\theta_H) \qquad (2.53)$$

where q_1 is the charge for monolayer deposition of H. The maximum adsorption pseudocapacitance arises when θ_H=0.5, thus:

$$C_p^{max} = \frac{q_1 F}{4RT} \tag{2.54}$$

An evaluation of the enthalpy and the Gibbs energy of adsorption for UPD H can be made by analysis of the temperature dependence of potentials of the current peaks in cyclic voltammetry of Pt electrodes, over the potential range for UPD of H.

Following the procedure of Conway et al. [60], Zolfaghari and Jerkiewicz [61-65] determined the standard entropies and enthalpies of UPD of H at polycrystalline and (111) Pt single-crystal surfaces, as a function of coverage. The above calculations were based on determined Gibbs energies of adsorption for the UPD of H process as a function of H coverage and temperature.

The Gibbs energy was found [65, 66] to increase linearly (it becomes less-negative) with increase of H coverage on the surface:

$$\Delta G^0_{ads}(\theta_H) = \Delta G^0_{ads}(\theta_H = 0) + r\theta_H \tag{2.55}$$

where $\Delta G^0_{ads}(\theta_H)$ is the standard Gibbs energy of adsorption for UPD, taking account of its dependence on H coverage. $\Delta G^0_{ads}(\theta_H=0)$ is the value of the standard Gibbs energy at θ_H=0 and r is the pairwise energy of lateral interactions. Since ΔG^0_{ads} becomes less negative upon increase of θ_H, the lateral interactions between the H ad-atoms must be repulsive [66]. Hence, in the latter case, the electrochemical Frumkin isotherm for the process of UPD of H has to be used [10, 67, 68] and is:

$$\frac{\theta_H}{1-\theta_H} = K_H c_{H^+} \exp(g\theta_H) \exp\left(\frac{-EF}{RT}\right) \tag{2.56}$$

where g = r/RT is a dimensionless lateral interaction parameter, reflecting the variation of apparent standard Gibbs energy of adsorption with coverage. When $g>0$, the pseudocapacitance, C_p, is diminished at all θ_H and potentials, E. C_p values become stretched over a wider potential range for larger values of the g parameter. Similar behaviour is also observed for variation of θ_H with increasing values of g [68]. In other words, as H coverage increases, it becomes more and more difficult to accommodate further H atoms successively on the metal surface, due to significant repulsive interactions between the atoms or surface Pt-H dipoles.

2.3 Adsorption of anions and their influence on H adsorption at Pt

A complete characterisation of different adsorption states at polycrystalline Pt in H_2SO_4 and at principal-index, Pt single-crystal surfaces in three principal (H_2SO_4, $HClO_4$ and NaOH) supporting electrolytes, will be given in Chapter 5. However, it is important to introduce already here a discussion of the phenomenon of co-adsorption of anions with H at Pt, as observed over the potential range for UPD of H.

The idea that the third, so-called "anomalous" (or unusual) adsorption state, observed at Pt (especially at the (111) plane) in aqueous H_2SO_4, could be attributed to adsorption of bisulphate (HSO_4^-) or sulphate (SO_4^{2-}) ions was first introduced by Scherson and Kolb [69] and developed later by Al Jaaf-Golze et al. [57]. The existence of such an adsorption state was found to be intrinsic to the well-ordered Pt(111) surface and to be dependent on its long-range order [51]. The unusual adsorption state at Pt(111) is represented by appearance of a characteristic pair of spikes, observed in the cyclic voltammogram of a well-ordered surface, on positive and negative-going sweeps, at *ca.*

0.44 V, RHE in 0.5 mol dm^{-3} H_2SO_4 (see Fig. 5.1a in section 5.2 of Chapter 5, later). Various authors observed that, for a given concentration of sulphate ion, variation of pH had no effect on the potential of that unusual adsorption state. Conversely, at constant pH, the above adsorption state is shifted towards less positive potentials with increasing sulphate concentration [51, 70, 71]. The latter effect, corresponding to strengthening of the specific adsorption of the anions, gives an indication about the anionic character of the anomalous adsorption state. However, only displacement charge-transient experiments [72-74], conducted by Clavilier et al. using CO as a competitive adsorption probe [75, 76], allowed quantitative evaluation of charges and surface coverages corresponding to adsorption of anionic species in H_2SO_4, at principal Pt single-crystal planes (see section 5.6 of Chapter 5 for details on this technique).

The nature of the adsorbed species was finally revealed by application of the *in situ* FTIR spectroscopy technique [77-80]. From such works, it is now evident that in H_2SO_4 solution, it is the HSO_4^- ion that is the predominantly adsorbed anionic species on Pt at potentials negative to that for the initial stage of Pt oxide formation [77]. Experiments with radio-labelled ^{35}S-containing sulphate ions [59, 81-84] showed that HSO_4^- ion adsorption at Pt continues significantly into the OH/O oxide formation potential region, before competitive desorption is established. The potential range for the desorption of the HSO_4^- ions, on the other hand, largely depends on the ion concentration (activity) in solution.

Anions which are very strongly adsorbed on Pt can compete with the HSO_4^- ions for adsorption sites. They also have a significant effect on UPD of H. Thus, in the presence of such anions as Cl^-, Br^- or I^-, the H UPD current response profiles become displaced towards the H_2 reversible potential, but with the same charges being passed [85-87]. Then the voltammograms in the UPD of H potential region appear to be "squeezed", resulting in narrower peaks with increased heights (currents). This arises because UPD of H does not commence until substantial anion desorption has taken place at negatively displaced potentials. The extents of the above shifts of the current-response voltammetric peaks strongly depends on the concentration of such specifically co-adsorbing halide anions [85-86] and their lone-pair donicity.

It is significant that UPD of H and adsorption of anionic species (including H_2SO_4, $HClO_4$ and NaOH electrolytes), on various Pt single-crystal surfaces, can overlap, which means that anionic species are still present on some parts of the Pt surface, while UPD of H commences on others. Markovic et al. [88] suggest that the only exception in aqueous NaOH solutions is the Pt(111) surface. Here, the region of UPD of H is separated from that for adsorption of OH^- anions at more positive potentials by a double-layer charging region. Similar behaviour is also found in $HClO_4$ solutions. Thus, in both cases, the Pt(111) surface shows two very well-defined zones (see Figs. 5.4 and 5.5 in sections 5.4 and 5.5 of Chapter 5, respectively). The zone located at lower potentials is associated with weakly adsorbed hydrogen and the characteristic "butterfly" current-response region, observed at higher potentials (*ca.* 0.6-0.9 V, RHE), corresponds to adsorption of hydroxyl ions (or possibly ClO_4^- in $HClO_4$). The assignment of the above-mentioned "butterfly" region in $HClO_4$ has been controversial for a number of years. Nevertheless, substantial similarities between the voltammograms for Pt(111) in aqueous NaOH and $HClO_4$ solutions have led most researchers to the conclusion that at least a significant fraction of the charge passed reversibly in the "butterfly" region for Pt in

$HClO_4$ may be due to OH (or O) deposition and desorption [89, 90]. In such systems, with well-defined separation of H and OH^- adsorption states, the specific adsorption of anions, e.g. Br^- or I^- has practically no effect on UPD of H [89], although at other planes such effects do arise.

2.4 Electrosorption of OH and O species at Pt

Among gas evolution processes, one of the most extensively examined is the O_2 evolution reaction (OER). The OER process at Pt (and other noble metals) is preceded by UPD of OH and O species, which leads to formation of a monolayer of Pt oxide and occurs at potentials negative to the reversible potential for oxygen evolution [25]. Hence, the latter takes place on a completed monolayer film of oxide. An analogous situation arises for cathodic H_2 evolution at polycrystalline Pt: thus, the latter process involving OPD H takes place on a full monolayer of UPD H.

In the case of polycrystalline Pt, studied in aqueous H_2SO_4, a monolayer of OH species is generated by 1.1 V, RHE and a surface oxide of nominal stoichiometry PtO is formed by 1.4 V. According to ref. 8, a transition from the PtOH monolayer to the PtO structure is achieved through the rearranged Pt/OH state, including a proton interchange reaction [25]. Once the rearranged state of the oxide has been formed, the reduction of surface oxide proceeds at less positive potentials than its initial formation, thus a characteristic hysteresis is observed, e.g. see refs. 4 and 25. Oxide films, thicker than one monolayer of OH or O, can eventually be formed at Pt by prolonged potential cycling between the oxide formation region and that for UPD of H [42] or by holding the potential beyond *ca.* 1.1 V, RHE.

A significant difference of the mechanism for the OER between acid and alkaline solutions arises from the difference of source of OH or O species, which are H_2O at acid pH values and $OH^-_{(aq.)}$ in alkaline media. Previously, the "butterfly" peak observed at Pt(111) in aqueous NaOH solutions, over the potential range 0.6-0.9 V, was tentatively assigned to strongly adsorbed H [89, 91]. However, most authors now agree that this "butterfly" region (see Fig. 5.5, later) corresponds to the process of reversible adsorption-desorption of OH^- ions [88, 90, 92, 93]. As pointed out by Drazic et al. [93], the OH^- electrosorption process takes place before the oxide layer formation starts and proceeds with a complete single electron-transfer step. However, it is not a simple OH^- ion discharge, but rather a reaction involving substitution of H_2O molecules by adsorbed OH:

$$\mathrm{Pt}-(\mathrm{H_2O})_x + \mathrm{OH}^- \Leftrightarrow \mathrm{Pt}-\mathrm{OH} + x\mathrm{H_2O} + e^- \tag{2.57}$$

where $x \approx 1$. In addition, it may be suggested that the oxidation process observed at more positive potentials (*ca.* 0.9-1.2 V), as shown e.g. in ref. 90, corresponds to formation of a film of one O atom per Pt surface atom. Since the Pt(111) surface is the only one low index plane where the UPD of H region is broadly separated from that for adsorption of the OH^- ions (by the double-layer charging region), Markovic et al. [88] suggested that, in NaOH, for both the (110) and (100) planes, the OH^- electrosorption process immediately follows that for UPD of H. The two states, a reversibly and irreversibly electroadsorbed OH_{ad}, are actually distinguished by these authors. On the contrary, in works by Morallon et al. [91] and Marinkovic et al. [92], it is implied that the UPD of H and OH^- electrosorption processes are broadly separated at the above two planes. Thus, electroadsorption of oxygen-like species would take place over the high potential range, as at the Pt(111) surface.

2.5 UPD of metal adatoms

Similarly to UPD of H, the phenomenon of UPD of foreign metal ad-atoms on a metal substrate can take place at potentials positive to the respective reversible potentials for their bulk deposition. UPD monolayers tend to be formed by deposition of low work-function metals onto high work-function substrates [25, 94].

The most extensively studied system appears to be UPD of Cu on low index faces of Au, especially on the Au(111) plane, e.g. in aqueous $H_2SO_4/CuSO_4$ solutions [94, 95]. In the latter case, three different structures can be distinguished. The first, at most positive potentials, is the bare Au(111) surface. The next overlay structure, formed between 0.1 and 0.2 V vs. Cu^0/Cu^{2+}, is a $(\sqrt{3} \times \sqrt{3})$ R 30° adlattice, formed due to co-adsorption of HSO_4^- (or SO_4^{2-}) anions with UPD Cu atoms, where the coverage by bisulphate (or sulphate) is 1/3 and that by Cu is 2/3. Finally, a (1x1) Cu monolayer is formed just prior to its bulk deposition [94, 96]. On the other low Miller index planes of Au, Cu (as shown by STM) does not form such well-ordered ad-layers as on the (111) substrate surface. Other systems studied on Au substrates involve UPD of Ag, Pb, Bi, Tl, Cd and Hg [94].

UPD systems on Pt substrates, usually on the (111) plane, include Ag, Pb, Cu [94] and Sn [97]. UPD of Cu on Pt(111) reveals significant structure-similarities to those observed on the Au(111) substrate. STM studies of UPD on Pt surfaces in supporting electrolytes containing relatively high concentrations of Cl^-, Br^- or I^- ions, reveal strong influence of their co-adsorption on the observed surface structure [94]. In addition to Au and Pt, much work has been done on Ag surfaces, especially UPD of Pb on Ag(111) and (100) surfaces [94].

2.6 Adsorption and reactivity; "reactive chemisorption" of small molecules: CH_3CN, CH_3OH and HCOOH

2.6.1 Reactive chemisorption of CH_3CN

In the early 1970s, Conway et al. [72-74] commenced studies on electrosorption and reactivity of nitriles, especially of acetonitrile, CH_3CN, at polycrystalline Pt in 0.5 mol dm^{-3} aqueous H_2SO_4. They found that CH_3CN became adsorbed on Pt in the double-layer charging region. Two possibilities were originally proposed, namely: a) a donative and b) an associative chemisorption reaction:

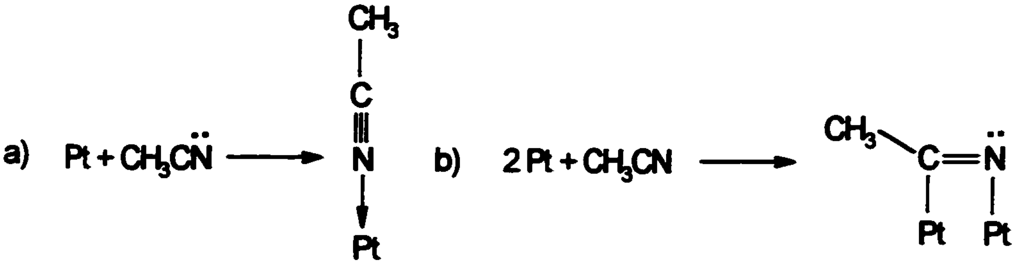

$$\text{a)}\ \mathrm{Pt} + \mathrm{CH_3C\ddot{N}} \longrightarrow \mathrm{CH_3{-}C{\equiv}N{\rightarrow}Pt} \qquad \text{b)}\ 2\,\mathrm{Pt} + \mathrm{CH_3CN} \longrightarrow \mathrm{CH_3{-}C(Pt){=}\ddot{N}(Pt)} \qquad (2.58)$$

Of special interest was that, in the chemisorbed state (without desorption of the adsorbate species from the electrode surface), the species underwent an almost reversible reduction/reoxidation in a two electron-transfer process, over the potential range 0.05-0.7 V, RHE. The above chemisorptive behaviour was later termed "reactive chemisorption" [71]. The CH_3CN/Pt system was the first "chemically modified electrode" to receive such detailed study [73].

Simultaneously, a new effect of "anodic H displacement" was discovered. It was found that when CH_3CN is added to an initially CH_3CN-free H_2SO_4 solution (in the H UPD region), an anodic current transient arises. This current transient is due to displacement of previously adsorbed H by the CH_3CN molecules introduced on to the surface from solution:

$$\mathrm{xCH_3CN + xPt\,H \;\Leftrightarrow\; xPt\,CH_3CN + xH^+ + xe^-} \qquad \textbf{(2.59)}$$

where one CH_3CN molecule occupies effectively x sites, previously occupied by UPD H. Process 2.59 was referred to as the "anodic hydrogen displacement effect". The above technique of adsorption charge displacement, with its further and later modifications (using CO as the displacing probe) for the study of the adsorption states of H and anions on Pt single-crystal electrodes, will be discussed in detail in section 5.6 of Chapter 5.

Following these early studies on adsorption of CH_3CN at polycrystalline Pt, Morin et al. examined the phenomenon of reactive chemisorption of CH_3CN at Pt single-crystal surfaces of (111), (100), (110) and (311) orientations, studied by means of cyclic voltammetry and integrated adsorption current transients [71] and more recently by means of *in situ* FTIR spectroscopy [98]. In the former work, it was demonstrated that the reactivity of CH_3CN is highly specific to the geometrical and corresponding electronic properties of these planes. A two-stage mechanism for the surface reactivity was proposed. It was concluded from the displacement charge transient experiments that CH_3CN can suffer Faradaic reduction on chemisorption (but the product remains chemisorbed), and that the sign and magnitude of the observed charge transient is potential dependent [71]. Moreover, the mechanism of reactive chemisorption of CH_3CN on Pt, as originally proposed [71, 73, 74], was confirmed by *in situ* FTIR studies [98].

2.6.2 Oxidation of CH_3OH and HCOOH

The possibility of using methanol, CH_3OH, and hydrocarbons as fuel reactants in fuel cells has attracted much attention with regard to the mechanisms of oxidation of such molecules at noble metals [25, 99]. Such mechanisms, as will be seen later (section 6.6 of

Chapter 6), are relevant to part of the present work involving oximes.

Electrooxidation of CH_3OH at Pt in acid electrolyte is initiated by the dissociative chemisorption reaction [25, 100]:

$$6\,Pt + CH_3OH \;\Rightarrow\; Pt_3COH + 3\,Pt\,H \qquad \textbf{(2.60)}$$

Further oxidation leads (as a side-reaction) to formation of strongly adsorbed CO, linearly or bridge-bonded to the Pt surface [25, 100, 101]:

$$Pt_3COH \;\Rightarrow\; Pt.CO + 2\,Pt + H^+ + e^- \qquad \textbf{(2.61)}$$

Hence, oxidation of methanol can become self-poisoned by an intermediate product of its anodic oxidation reaction at the electrode, and thus PtCO appears to be responsible for the surface deactivation [25]. The conversion of the latter adsorbate to form the final product, CO_2, requires attack on the adsorbed carbon species by an oxygen-containing species. This process is usually slow and strongly dependent on the nature of that species [100].

Similarly, electrooxidation of formic acid, HCOOH (also of formaldehyde, HCHO), at polycrystalline and single-crystal Pt surfaces [25, 99, 102-106], was found to lead to formation of chemisorbed CO on the electrode surface in a side-reaction. Major support for this arises from the direct observations of adsorbed CO by *in situ* IR reflection spectroscopy [25, 101]. The main reaction sequence for HCOOH electrooxidation at Pt is [25, 103-106]:

$$HCOOH + 2\,Pt \;\Rightarrow\; Pt\,H + Pt.COOH \qquad \textbf{(2.62)}$$

coupled with

$$Pt\,H \;\Rightarrow\; Pt + H^+ + e^- \qquad \textbf{(2.63)}$$

and

$$\mathrm{Pt.COOH} \Rightarrow \mathrm{Pt} + \mathrm{CO_2} + \mathrm{H^+} + \mathrm{e^-} \qquad \textbf{(2.64)}$$

The surface poisoning CO species probably arises as a by-product in the process of electroreduction of the adsorbed HCOOH molecule by H:

$$\mathrm{Pt.COOH} + 2\mathrm{H^+} + 2\mathrm{e^-} \Rightarrow \mathrm{Pt.CHO} + \mathrm{H_2O} \qquad \textbf{(2.65)}$$

and

$$\mathrm{Pt.CHO} \Rightarrow \mathrm{Pt.CO} + \mathrm{H^+} + \mathrm{e^-} \qquad \textbf{(2.66)}$$

It is these effects of an adsorbed CO species that are of major importance in contemporary and earlier fuel-cell work as they lead to diminution of electro-oxidation activity of Pt electrocatalyst surfaces.

2.7 References

1. J.O'M. Bockris and S.U.M. Khan, "*Surface Electrochemistry: a molecular level approach*", Plenum Press, New York, 1993, **1**.
2. A. Zangwill, "*Physics at Surfaces*", Cambridge University Press, New York, 1988.
3. R. Varma and J.R. Selman (Eds.), "*Techniques for characterization of electrodes and electrochemical processes*", John Wiley and Sons, New York, 1991.
4. F.G. Will and C.A. Knorr, *Z. Elektrochem.*, 1960, **64**, 258.
5. P. Delahay, "*New Instrumental Methods in Electrochemistry*", Robert E. Krieger, Huntington, New York, 1980.
6. Southampton Electrochemistry Group, "*Instrumental Methods in Electrochemistry*", Ellis Horwood, Chichester, 1985.

7. D. Linden (Ed. in chief), "*Handbook of Batteries*", McGraw-Hill, Inc., 2nd ed., New York, 1995.

8. H. Angerstein-Kozlowska, B.E. Conway and W.B.A. Sharp, *J. Electroanal. Chem.*, 1973, **43**, 9.

9. S. Srinivasan and E. Gileadi, *Electrochim. Acta*, 1966, **11**, 321.

10. H. Angerstein-Kozlowska, J. Klinger and B.E. Conway, *J. Electroanal. Chem.*, 1977, **75**, 45 and 61.

11. H. Angerstein-Kozlowska and B.E. Conway, *J. Electroanal. Chem.*, 1979, **95**, 1.

12. D.A. Harrington and B.E. Conway, *Electrochim. Acta*, 1987, **32**, 1703.

13. B.E. Conway and H. Angerstein-Kozlowska in Proc. Symposium on "*Electrocatalysis on Non-Metallic Surfaces*", A.D. Franklin (Ed.), U.S. Department of Commerce, National Bureau of Standards, U.S. Government Printing Office, Washington D.C., 1976, 107.

14. I. Langmuir, *J. Am. Chem. Soc.*, 1916, **38**, 1145.

15. I. Langmuir, *J. Am. Chem. Soc.*, 1916, **38**, 2221.

16. I. Langmuir, *Trans. Faraday Soc.*, 1921, **17**, 621.

17. K.J. Laidler, "*Chemical Kinetics*", Harper and Row, New York, 1987.

18. J.E.B. Randles, *Trans. Faraday Soc.*, 1948, **44**, 327.

19. P. Delahay, and G. Perkins, *J. Phys. Coll. Chem.*, 1951, **55**, 586 and 1146.

20. R.S. Nicholson and I. Shain, *Anal. Chem.*, 1964, **36**, 706.

21. R.S. Nicholson and I. Shain, *Anal. Chem.*, 1965, **37**, 178 and 190.

22. R.S. Nicholson, *Anal. Chem.*, 1965, **37**, 1351.

23. A.J. Bard and L.R. Faulkner, "*Electrochemical Methods: fundamentals and*

applications", John Wiley and Sons, Inc., New York, 1980.

24. J. Ross Macdonald (Ed.), "*Impedance Spectroscopy. Emphasizing Solid Materials and Systems*", John Wiley and Sons, New York, 1987.
25. B.E. Conway and B.V. Tilak, *Adv. Catalysis*, 1992, **38**, 1.
26. S. Morin, H. Dumont and B.E. Conway, *J. Electroanal. Chem.*, 1996, **412**, 39.
27. A. Lasia in Proc. Symposium on "*Electrochemistry and Materials Science of Cathodic H Absorption and Adsorption*", B.E. Conway and G. Jerkiewicz (Eds.), The Electrochemical Society, Pennington, NJ, 1995, **94-21**, 261.
28. W.W. Hansen, T. Kuwena and R.A. Osteryoung, *Anal. Chem.*, 1966, **38**, 1809.
29. A. Bewick and J. Robinson, *J. Electroanal. Chem.*, 1975, **60**, 163.
30. M. Neugebauer, G. Nauer, N. Brinda-Knopik and G. Gidaly, *J. Electroanal. Chem.*, 1981, **122**, 237.
31. S. Pons, T. Davidson, A. Bewick and P.P. Schmidt, *J. Electroanal. Chem.*, 1982, **125**, 237.
32. A. Bewick in "*Trends in Interfacial Electrochemistry*", A.F. Silva (Ed.), D. Reidel Publishing Company, Dordrecht, 1986, 331.
33. K. Ashley and S. Pons, *Chem. Rev.*, 1988, **88**, 673.
34. M.E. Pemble in "*Surface Analysis-The Principal Techniques*", J.C. Vickerman (Ed.), John Wiley and Sons, New York, 1997, Chapter 7, 267.
35. R.J. Nichols in "*Adsorption of Molecules at Metal Electrodes*", J. Lipkowski and P.N. Ross (Eds.), VCH Publishers, New York, 1992, Chapter 7.
36. B.E. Conway in "*Interfacial Electrochemistry. Theory, Experiment and Applications*", A. Wieckowski (Ed.), Marcel Dekker, Inc., New York, 1999,

Chapter 9, 131.

37. G. Jerkiewicz and A. Zolfaghari in Proc. Symposium on *"Electrochemistry and Materials Science of Cathodic H Absorption and Adsorption"*, B.E. Conway and G. Jerkiewicz (Eds.), The Electrochemical Society, Pennington, NJ, 1995, **94-21**, 31.

38. D. Gilroy and B.E. Conway, *Can. J. Chem.*, 1968, **46**, 875.

39. W. Visscher and M. Blielevens, *Electrochim. Acta*, 1974, **19**, 387.

40. W. Visscher and M. Blielevens, *J. Electroanal. Chem.*, 1973, **47**, 363.

41. J.M. Oten and W. Visscher, *J. Electroanal. Chem.*, 1979, **118**, 118.

42. S. Hadzi-Jordanov, M. Vukovic, H. Angerstein-Kozlowska and B.E. Conway, *J. Electrochem. Soc.*, 1978, **125**, 1471.

43. M. Wohlfahrt-Mehrens and J. Heitbaum, *J. Electroanal. Chem.*, 1987, **237**, 251.

44. A. Hubbard, R. Ishikawa and J. Katekara, *J. Electranal. Chem.*, 1978, **86**, 271.

45. B.E. Conway, F.C. Ho, H.A. Kozlowska and W. Sharp, *J. Vac. Sci. Technol.*, 1977, **14**, 351.

46. A. Bewick and J.W. Russell, *J. Electranal. Chem.*, 1982, **142**, 337.

47. M. Elam and B.E. Conway, *J. Electrochem. Soc.*, 1988, **135**, 1678.

48. M. Enyo in *"Comprehensive Treatise of Electrochemistry"*, B.E. Conway and J.O'M. Bockris, (Eds.), Plenum Press, New York, 1983, 7, Chapter 5, 241.

49. L.J. Wan, T. Suzuki, K. Sashikata, J. Okada, J. Inukai and K. Itaya, *J. Electranal. Chem.*, 2000, **484**, 189.

50. J. Clavilier, K. El Achi, M. Petit, A. Rodes and M.A. Zamakhchari, *J. Electroanal. Chem.*, 1990, **295**, 333.

51. J. Clavilier, A. Rodes, K. El Achi and M.A. Zamakhchari, *J. Chim. Phys.*, 1991, **88**, 1291.

52. N. Furuya and S. Motoo, *J. Electroanal. Chem.*, 1979, **98**, 189.

53. A.N. Frumkin and B. Slygin, *Acta Physicochim. URSS*, 1935, **3**, 791.

54. F.G. Will, *J. Electrochem. Soc.*, 1965, **112**, 481.

55. H. Angerstein-Kozlowska, W.B.A. Sharp and B.E. Conway in Proc. Symposium on *"Electrocatalysis"*, The Electrochemical Society, 1974, 94.

56. B.E. Conway, *"Chemistry in Canada"*, 1976, **28**, 8.

57. K. Al Jaaf-Golze, D.M. Kolb and D. Scherson, *J. Electroanal. Chem.*, 1986, **200**, 353.

58. J.M. Feliu, J.M. Orts, R. Gomez, A. Aldaz and J. Clavilier, *J. Electroanal. Chem.*, 1994, **372**, 265.

59. M. Gamboa-Aldeco, E. Harrero, P. Zelenay and A. Wieckowski, *J. Electroanal. Chem.*, 1993, **348**, 451.

60. B.E. Conway, H.A. Kozlowska and W.B.A. Sharp, *Trans. Faraday Soc.*, 1977, **19**, 1373.

61. A. Zolfaghari and G. Jerkiewicz, *J. Electroanal. Chem.*, 1997, **422**, 1.

62. G. Jerkiewicz and A. Zolfaghari, *J. Electrochem. Soc.*, 1996, **143**, 1240.

63. G. Jerkiewicz and A. Zolfaghari, *J. Phys. Chem.*, 1996, **100**, 8454.

64. A. Zolfaghari and G. Jerkiewicz, *J. Electroanal. Chem.*, 1997, **420**, 11.

65. A. Zolfaghari, M. Chayer and G. Jerkiewicz, *J. Electrochem. Soc.*, 1997, **144**, 3034.

66. A. Zolfaghari and G. Jerkiewicz in Proc. Symposium on *"Electrochemical Surface*

Science of Hydrogen Adsorption and Absorption", G. Jerkiewicz and P. Marcus (Eds.), The Electrochemical Society, Pennington, NJ, 1997, **97-16**, 133.

67. B.E. Conway and E. Gileadi, *Trans. Faraday Soc.*, 1962, **58**, 2493.

68. B.E. Conway, H. Angerstein-Kozlowska and H.P. Dhar, *Electrochim. Acta*, 1974, **19**, 455.

69. D.A. Scherson and D.M. Kolb, *J. Electroanal. Chem.*, 1984, **176**, 353.

70. J. Clavilier, K. El Achi and A. Rodes, *Chem. Phys.*, 1990, **141**, 1.

71. S. Morin and B.E. Conway, *J. Electroanal. Chem.*, 1994, **376**, 135.

72. B. MacDougall, B.E. Conway and H.A. Kozlowska, *J. Electroanal. Chem.*, 1971, **32**, App. 15.

73. H.A. Kozlowska, B.R. MacDougall and B.E. Conway, *J. Electroanal. Chem.*, 1972, **39**, 287.

74. B.E. Conway, B. MacDougall and H.A. Kozlowska, *J. Chem. Soc., Faraday Trans. I*, 1972, **68**, 1566.

75. J. Clavilier, R. Albalat, R. Gomez, J.M. Orts, J.M. Feliu and A. Aldaz, *J. Electroanal. Chem.*, 1992, **330**, 489.

76. J. Clavilier, R. Albalat, R. Gomez, J.M. Orts and J.M. Feliu, *J. Electroanal. Chem.*, 1993, **360**, 325.

77. P.W. Faguy, N. Markovic, R.R. Adzic, C.A. Fierro and E.B. Yeager, *J. Electroanal. Chem.*, 1990, **289**, 245.

78. F.C. Nart, T. Iwasita and M. Weber, *Electrochim. Acta*, 1994, **39**, **No.**7, 961.

79. T. Iwasita and F.C. Nart, *J. Electroanal. Chem.*, 1990, **295**, 215.

80. T. Iwasita, F.C. Nart, A. Rodes, E. Pastor and M. Weber, *Electrochim. Acta*, 1995, **40**, **No.1**, 53.

81. P. Zelenay, M. Gamboa-Aldeco and A. Wieckowski, *J. Electroanal. Chem.*, 1993, **357**, 307.

82. S. Thomas, Y-E. Sung, H.S. Kim and A. Wieckowski, *J. Phys. Chem.*, 1996, **100**, 11726.

83. W. Savich, S-G. Sun, J. Lipkowski and A. Wieckowski, *J. Electroanal. Chem.*, 1995, **388**, 233.

84. A. Wieckowski, P. Zelenay and K. Varga, *J. Chim. Phys.*, 1991, **88**, 1247.

85. D.M. Novak and B.E. Conway, *J. Chem. Soc., Faraday Trans.* I, 1981, 77, 2341.

86. S. Gilman and M.W. Breiter, *J. Electrochem. Soc.*, 1962, **109**, 1099.

87. B.E. Conway, Y. Phillips and S.Y. Qian, *J. Chem. Soc., Faraday Trans.*, 1995, **91(2)**, 283.

88. N.M. Markovic, S.T. Sarraf, H.A. Gasteiger and P.N. Ross, Jr., *J. Chem. Soc., Faraday Trans.*, 1996, **92**, 3719.

89. E. Morallon, J.L. Vasquez and A. Aldaz, *J. Electroanal. Chem.*, 1992, **334**, 323.

90. H. Kita, S. Ye, A. Aramata and N. Furuya, *J. Electroanal. Chem.*, 1990, **295**, 317.

91. E. Morallon, J.L. Vasquez and A. Aldaz, *J. Electroanal. Chem.*, 1990, **288**, 217.

92. N.S. Marinkovic, N.M. Markovic and R.R. Adzic, *J. Electroanal. Chem.*, 1992, **330**, 433.

93. D.M. Drazic, A.V. Tripkovic, K.D. Popovic and J.D. Lovic, *J. Electroanal. Chem.*, 1999, **466**, 155.

94. A.A. Gewirth and B.K. Niece, *Chem. Rev.*, 1997, **97**, 1129.

95. D. Kolb, *Z. Phys. Chem. N.F.*, 1987, **154**, 179.

96. M.F. Toney, J.N. Howard, J. Richer, G.L. Borges, J.G. Gordon, O.R. Melroy, Y. Dennis and L.B. Sorensen, *Phys. Rev. Lett.*, 1995, **75**, 4472.

97. S.H. Overbury, D.R. Mullins, M.T. Paffett and B.E. Koel, *Surf. Sci.*, 1991, **254**, 45.

98. S. Morin, B.E. Conway, G.J. Edens and M.J. Weaver, *J. Electroanal. Chem.*, 1997, **421**, 213.

99. W. Vielstich, *"Fuel Cells: Modern Processes for the Electrochemical Production of Energy"*, (translation from German by D.J.G. Ives), Chichester, Wiley-Interscience, New York, 1970.

100. A. Hamnett, in *"Interfacial Electrochemistry, Theory, Experiment and Applications"*, A. Wieckowski (Ed.), Marcel Dekker, Inc., New York, 1999, Chapter 47, 843.

101. A. Bewick, *J. Electroanal. Chem.*, 1983, **150**, 481.

102. M.W. Breiter, *Electrochim. Acta*, 1963, **8**, 457.

103. H. Angerstein-Kozlowska, B. MacDougall and B.E. Conway, *J. Electrochem. Soc.*, 1973, **120**, **No.6**, 756.

104. R.R. Adzic, W.E. O'Grady and S. Srinivasan, *J. Electrochem. Soc.*, 1981, **128**, **No.9**, 1913.

105. R.R. Adzic, W.E. O'Grady and S. Srinivasan, *Surf. Sci.*, 1980, **94**, L.191.

106. G.Q. Lu, A. Crown and A. Wieckowski, *J. Phys. Chem. B*, 1999, **103**, 9700.

Chapter 3

Aims of the Work and Systems Examined

3.1 Origin of the research and its aims

Practically all electrochemical processes occur at the interfaces of metals or semiconductors. Use of single-crystal surfaces, especially of Pt and Au, with highly specific surface geometries, provides the opportunity to study the dependence of particular co-ordinations of the electrode's surface atoms by adsorbates, determined by the surface's lattice geometry. Differences in surface geometry may also lead to changes in kinetic pathways or activation energies for electrosorption processes and also to differences of surface electronic properties, e.g. the electronic work function, Φ.

An initial aim of the research project was to find an interesting and possibly as unique a surface electrochemical process as that referred to as "reactive chemisorption", discovered [1-5] in the case of acetonitrile (and other nitriles), previously studied at polycrystalline and single-crystal Pt surfaces in this laboratory. The examples found were guanidine, $NH{=}C(NH_2)_2$ (G), and its protonated form, $^+NH_2{=}C(NH_2)_2$ (G^+), together with their structurally-related analogues, N,N-dimethylguanidine (DMG), acetamidine (AA) and urea (U).

The above led the author to explore in detail the mechanism of interaction of G^+ cations with UPD H and surface adsorbed anions, and to investigate further the influence of the latter's type (HSO_4^-, ClO_4^- and OH^-) and its concentration (for HSO_4^- ion) on the above type of adsorption process.

Complementarily, the author then investigated the behaviour of two small aliphatic oximes, acetaldehyde oxime (A_{NOH}) and formamidoxime (F_{NOH}) at several Pt single-crystal surfaces. Although the choice of these substances was based on their chemical simplicity and relationships to the other adsorbates, their investigation at Pt surfaces also offered the opportunity for study the adsorption processes coupled with a continuous Faradaic reduction current which arises in the case of oximes.

3.2 Systems studied

The adsorption behaviour of guanidonium cations (G^+) was examined at polycrystalline and single-crystal Pt surfaces having (111), (100), (110) and (511) orientations, in three supporting electrolytes: aqueous 0.5 mol dm^{-3} H_2SO_4, 0.1 mol dm^{-3} $HClO_4$ and 0.1 mol dm^{-3} NaOH. In addition, the effects of changes of concentration of G^+ at the Pt planes studied were examined in all three electrolytes; also the effects on the adsorption behaviour of G^+ by HSO_4^- ions co-adsorbed from progressively diluted H_2SO_4, were examined. Cyclic voltammetry, *in situ* FTIR spectroscopy and a.c. impedance spectroscopy techniques were employed to conduct the above experiments.

Analogous investigations were performed in the presence of adsorbates structurally-related to G^+, viz. N,N-dimethylguanidonium (DMG^+) and acetamidonium (AA^+) cations, and comparatively urea (U). Examination of the behaviour of the latter molecule was restricted to Pt(111) and (100) surfaces in 0.5 mol dm^{-3} H_2SO_4 and 0.1 mol dm^{-3} NaOH media.

Finally, the electrochemical reactivity of acetaldehyde oxime (A_{NOH}) and formamidoxime (F_{NOH}) was investigated at three low-index Pt single-crystal planes in 0.5 mol dm^{-3} H_2SO_4 and 0.1 mol dm^{-3} NaOH electrolyte media by means of cyclic voltammetry and a.c. impedance spectroscopy.

3.3 References

1. B. MacDougall, B.E. Conway and H.A. Kozlowska, *J. Electroanal. Chem.*, 1971, **32**, App. 15.
2. H.A. Kozlowska, B.R. MacDougall and B.E. Conway, *J. Electroanal. Chem.*, 1972, **39**, 287.
3. B.E. Conway, B. MacDougall and H.A. Kozlowska, *J. Chem. Soc., Faraday Trans. I*, 1972, **68**, 1566.
4. S. Morin and B.E. Conway, *J. Electroanal. Chem.*, 1994, **376**, 135.
5. S. Morin, B.E. Conway, G.J. Edens and M.J. Weaver, *J. Electroanal. Chem.*, 1997, **421**, 213.

Chapter 4

Experimental

This chapter contains all the information concerning the choice of experimental methods and instrumentation employed in the course of this work. The design of electrochemical cells, the specifications of the water solvent and chemicals used, and the preparation and voltammetric characterisation of platinum single-crystal electrodes are described in some detail.

4.1 Instrumentation and data processing

The following electroanalytical and spectroscopic techniques were employed during the course of this work: cyclic voltammetry, a.c. impedance spectroscopy and *in situ* FTIR spectroscopy.

4.1.1 Cyclic voltammetry

Cyclic voltammetry experiments were conducted at 295 K using an HA-501 potentiostat/galvanostat which controls potentials and monitors current responses. An HB-104 function generator (Hokuto Denko, Ltd., Japan) provided the required linearly-varying, time-dependent, input potential to the potentiostat. Voltammograms were recorded and collected digitally on a Nicolet-310 digital oscilloscope (Nicolet Instrument Corporation). Data collected on the oscilloscope were then transferred to an IBM-compatible PC for further digital processing.

The voltammetric polarisations were conducted over controlled ranges of the working-electrode potential, usually in the H UPD region or at more positive potentials at the Pt electrode surfaces and usually at a sweep-rate s of 50 mV s^{-1}. In some experiments, s was varied in order to examine the role, if any, of diffusion processes in determining the response currents.

4.1.2 Adsorption and displacement-charge transients

Based on the anodic H displacement effect [1-3], described in section 2.6 of Chapter 2 in the present work, the CO adsorption replacement technique (with carbon monoxide used as a competing adsorbent probe) was employed to study the adsorption behaviour of G^+ (or G) at the Pt(111) and (100) surfaces in 0.5 mol dm^{-3} H_2SO_4 and 0.1 mol dm^{-3} NaOH supporting electrolytes. Experiments were performed at room temperature, in the way previously described in the literature [4-6]. Transients were recorded at potentials ranging from 0.08 to 0.60 V (RHE), in the presence of $1x10^{-3}$ mol dm^{-3} G^+ (or G). Details are given in Chapters 5 and 6.

In addition to the CO adsorption displacement transients, charge displacement transients were recorded at the Pt(111) plane, at constant electrode potential, by injecting 100 μL amounts of 1 weight % solution of guanidine carbonate in 0.5 mol dm^{-3} H_2SO_4, to an initially G^+-free 0.5 mol dm^{-3} H_2SO_4 solution. Here, guanidine itself was used as the adsorbent competing with pre-adsorbed H and HSO_4^- species on the Pt surface. Moreover, similar experiments at the (111) surface were performed by injecting guanidine carbonate, urea and formamidoxime to 0.1 mol dm^{-3} NaOH, within the potential range of double-layer charging. Thus, in the latter cases, no interference from the adsorbed H or OH^- species could have arisen. Further details are written in Chapter 6.

4.1.3 Impedance spectroscopy

The system used for impedance measurements consisted of a Solartron 1255 HF Frequency Response Analyser (FRA) in conjunction with a SI 1287 Solartron Electrochemical Interface. The instruments were controlled by *ZPlot* software for Windows, version 2.0 (Scribner Associates, Inc., 1997). The generator provided an output signal of known amplitude (5 mV) and the frequency range was typically swept between $1.0\text{x}10^5$ to $1\text{x}10^{-1}$ Hz. Data analysis was performed with *ZView* software, where the impedance spectra were fitted by means of a complex, non-linear, least-squares immitance fitting program, *LEVM 6*, written by J. Ross Macdonald in ref. 7.

4.1.4 In situ FTIR spectroscopy

Vibrational FTIR spectroscopy experiments were performed in a thin-layer electrochemical-FTIR cell, allowing for ultra-delicate adjustment of the Pt single-crystal to the prism's surface (see a diagram of the thin-layer cell in Fig. 4.3, later). The cell had a 60° CaF_2 trapezoidal prism fitted at its bottom. This design allows a very thin electrolyte layer (< 5 μm) to be examined and simultaneously enables electrochemical and modulation voltammetry measurements to be made by means of the hanging solution-meniscus technique. The infrared spectrometer used was a Nicolet Magma 550 with an MCT/A detector. A ZnSe wire-grid polariser was employed to obtain *p* and *s*-polarised light. In order to maintain controlled but varied electrochemical conditions, cyclic voltammograms were recorded at a sweep-rate of 50 mV s^{-1}, directly at the Pt crystal in the FTIR cell, both prior to and following the spectral measurements. An EG&G model 173 potentiostat/galvanostat and a 175 universal programmer (Princeton

Applied Research) were used.

4.1.5 FTIR measurements and procedures

The FTIR measurements were performed at room temperature in the Subtractively Normalised Interfacial Fourier Transform Infrared Spectroscopy (*SNIFTIRS*) mode (referred to in Chapter 3), where a series of interferometer scans was sequentially recorded at two potential values between which modulation was applied. The resulting two spectra were then subtracted [8, 9] to yield the differential infrared spectra. Here, the spectrum acquired at the lowest positive potential was taken as the background (reference curve) for the series of spectra recorded at increasing potential values. The spectra are shown in the present work as normalised differential reflectance data ($\Delta R/R_0$), where $\Delta R = R - R_0$, taking R as the reflectance at the sample potential and R_0 that at the reference potential. Generally, the spectra were obtained from processing 200 or 500 scans, with a spectral resolution of 8 cm^{-1} and an amplification factor of the detector signal, 4. Digital processing of the spectral results was conducted by means of *Omnic* for Windows software, version 2.1 (Nicolet Instrument Corporation, 1994).

4.2 Electrochemical and FTIR cells

Two electrochemical cells, made all of Pyrex glass, were used during the course of this work: one for cyclic voltammetric studies and the other primarily for a.c. impedance measurements.

The cell used for voltammetric studies in the present work is shown in Fig. 4.1 and comprises three electrodes: the single-crystal working electrode (equipped with flexible adjustment) in a central part, the RHE as reference and the Pt counter electrode, both in separate compartments.

The cell, which was mainly used for a.c. impedance measurements, is shown in Fig. 4.2. It is also a three-compartment design but where the working electrode section is designed for rotating-electrode experiments. A glass cup attached at the top of the cell could be filled with water, so that a Teflon cap fastened to the rotating electrode could be immersed in it. This design creates a gas seal and hence prevents the main compartment of the cell from becoming contaminated by atmospheric oxygen. By replacing the rotating electrode assembly with the pyrex-glass made cover having a 29/32 mm joint, this cell could still be used for stationary measurements. Special care was taken to minimise the iR drop by locating the Luggin capillary at the centre of the cell. Also, a 0.5 mm diameter Pt wire was installed between and within the tip of the Luggin capillary and the RHE reference compartment. This arrangement (allowing for significant elimination of iR potential drop) was essential for the fast responses required for a.c. impedance spectroscopy.

A diagram of the thin-layer cell used for combined *in situ* FTIR and electrochemical measurements is shown in Fig. 4.3 and follows earlier designs in the literature [9, 10].

Prior to each experiment, the electrochemical cells were taken apart and soaked in hot sulphuric acid for at least 2 hours. After having been cooled to about 40° C, the cells were thoroughly rinsed with Millipore ultra-pure water. An identical procedure was applied for cleaning all the glassware used to prepare supporting electrolytes and other solutions.

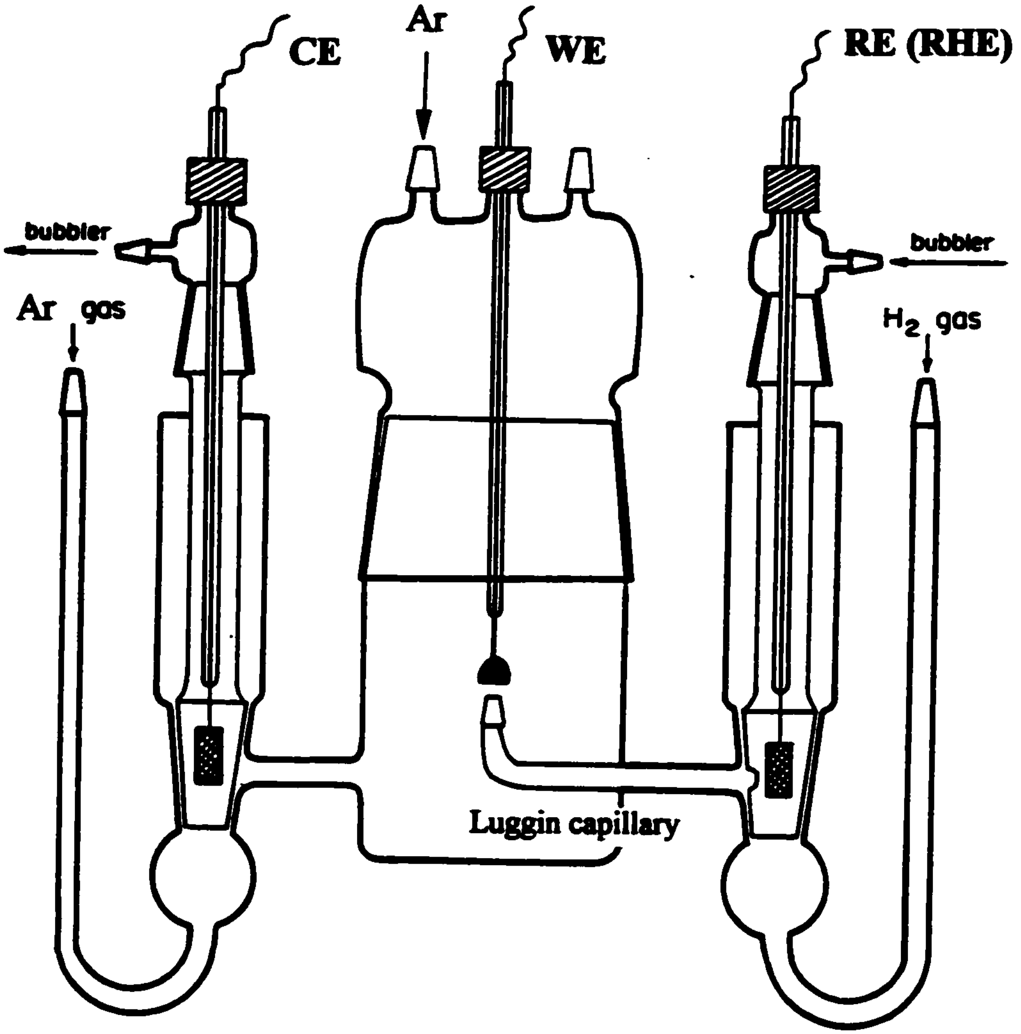

Fig. 4.1 A diagram of the electrochemical cell used in this work for cyclic voltammetric measurements.

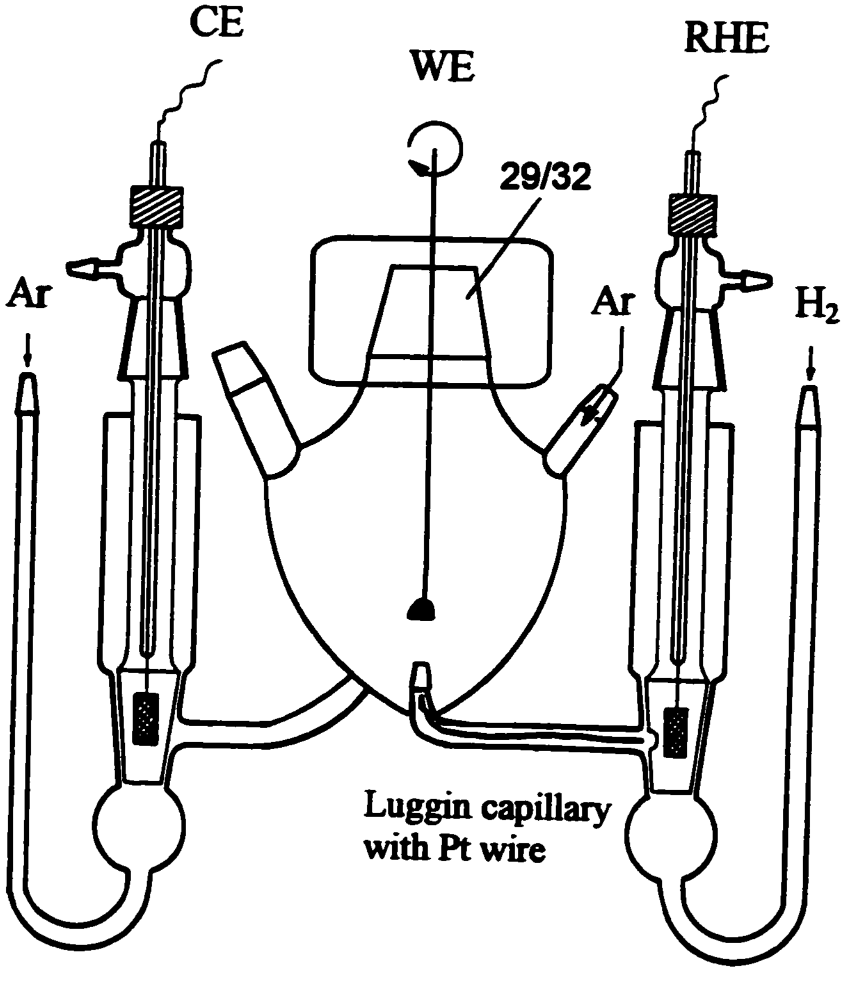

Fig. 4.2 A diagram of the electrochemical cell used in the present work for a.c. impedance measurements.

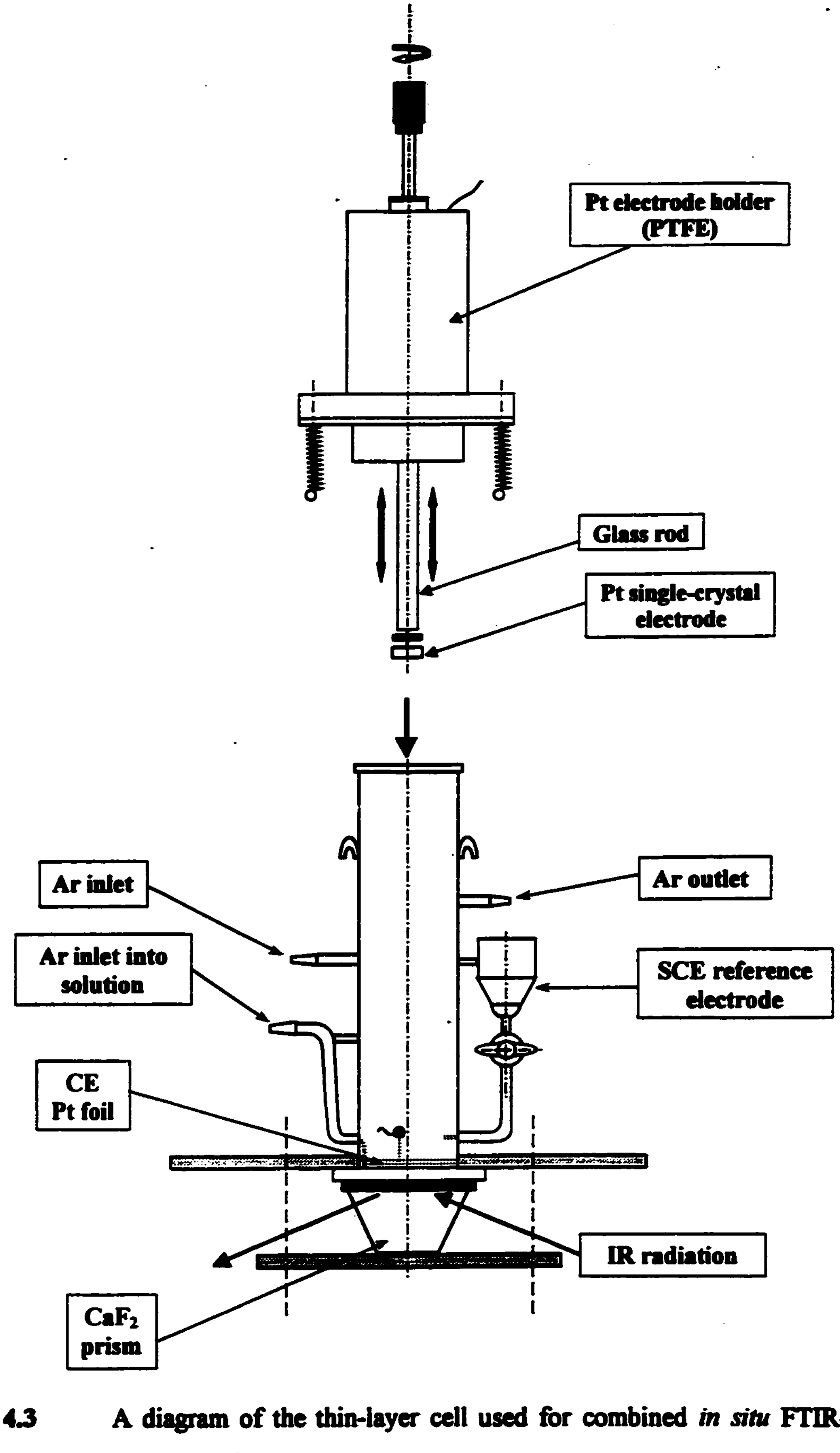

Fig. 4.3 A diagram of the thin-layer cell used for combined *in situ* FTIR-cyclic voltammetric measurements.

4.3 Reference and counter electrodes

The reversible hydrogen electrode, (RHE), H^+/H_2 (Pt), was used throughout this work. Hence, all the potentials, if not stated otherwise, are given on the RHE scale. The RHE was made of platinised Pt(99.99% purity, 100 mesh, Johnson Matthey Inc.) gauze attached to a Pt wire and sealed in soft or pyrex glass. Before its use, this electrode was cleaned in hot sulphuric acid. Just prior to and during the experiments, purified H_2 gas (as described in more detail in section 4.5) was continuously bubbled into the reference compartment of the electrochemical cell in the usual way. For combined *in situ* FTIR-electrochemical measurements, performed with the thin-layer cell, a saturated calomel electrode (SCE) was used instead.

Generally, two counter electrodes were used in this work, one was a Pt gauze, with the same characteristics as that used to make the reference electrode and the other was made of a coiled Pt wire (0.5 mm diameter, 99.9998% purity, Johnson Matthey Inc.). Prior to their use, the counter electrodes were cleaned in hot sulphuric acid or, in the case of the coiled wire, it could also be flame-annealed. The thin-layer *in situ* FTIR cell was equipped with a counter electrode made of Pt foil.

4.4 Choice of compounds as adsorbates

In previous works from this laboratory, the phenomenon of "reactive chemisorption" of nitriles, especially of acetonitrile, $CH_3C{\equiv}N$, was reported for adsorption at polycrystalline and single-crystal Pt surfaces [1-3, 11, 12].

These studies led the author of this thesis to examine the electrosorption behaviour at Pt of guanidine (G) and N,N-dimethylguanidine (DMG) which contain an imine-type

>C=N bond, related to the -C≡N function. In acidic solutions, these adsorbates become converted to the corresponding *onium*-type ions in which the cation structure is stabilised by resonance between three canonical forms leading, e.g., to guanidine being one of the strongest non-inorganic bases known in aqueous solution (see their unprotonated and protonated structures **I** to **IV** in Fig. 4.4). Choice of DMG was not arbitrary, as the two *gem* methyl groups bonded to one of the N atoms could significantly affect its adsorption behaviour at Pt surface and modify the resonance energy and steric properties of its cation (Fig. 4.4).

Another adsorbate molecule, structure-related to G, is acetamidine (AA) where one of the $-NH_2$ groups in G is substituted by $-CH_3$. Acetamidine was chosen on account of its significantly reduced resonance in the acetamidonium cation, AA^+, resulting from protonation. The corresponding formulae for AA and AA^+ are shown as structures **V** and **VI** in Fig. 4.5. Similarly, urea (U) which also exhibits close structure-similarities to G, was proposed for examination comparatively at Pt surfaces (see its chemical formula as structure **VII** in Fig. 4.5). In the latter case, the presence of the C=O bond significantly lowers the basicity of urea compared with that of G, and thus its tendency for protonation in solution, giving a 2-site resonant cation.

In order to support the proposed protonated forms of guanidine and its analogues in Figs. 4.4 and 4.5, a concept of relative proton affinities could also be introduced into discussion. In other words, based on the relative basicity of groups (=NH, $-NH_2$, $-CH_3$ and >C=O), a charge site location in the protonated molecules can be predicted.

Finally, it is well-known [13-15] that oximes, organic compounds with a characteristic =N-OH group, undergo electrolytic reduction at e.g. Hg or Pb cathodes to

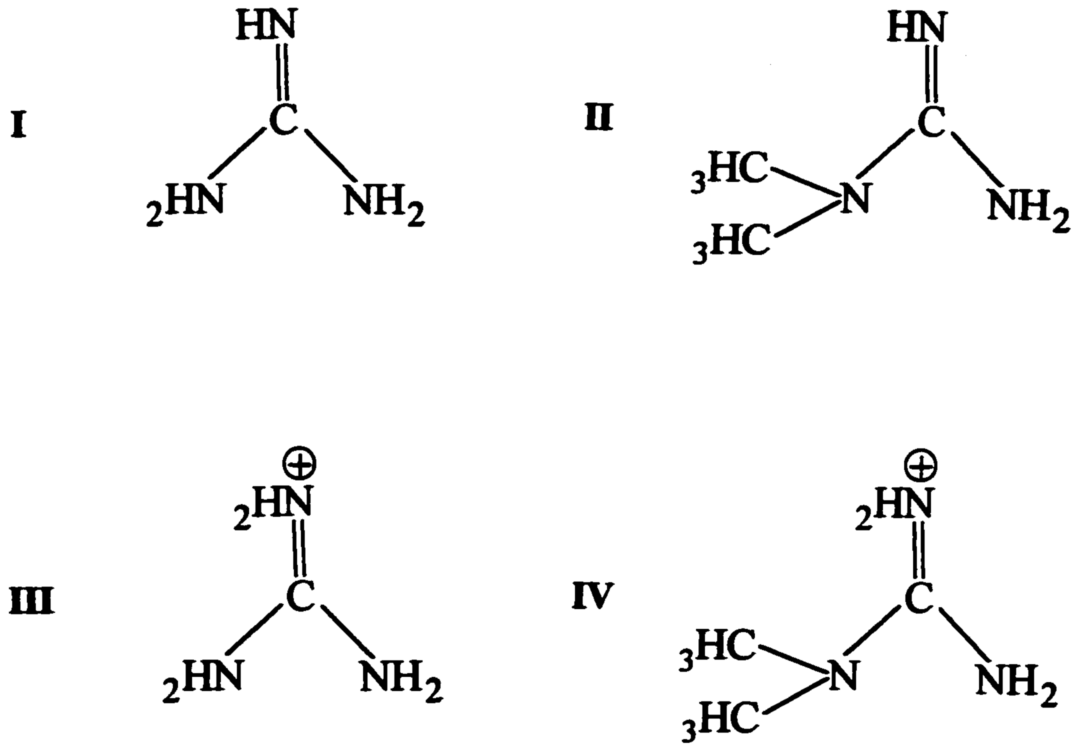

Fig. 4.4 Chemical structures of nonprotonated (I, II) and corresponding protonated (III, IV) forms of G and DMG.

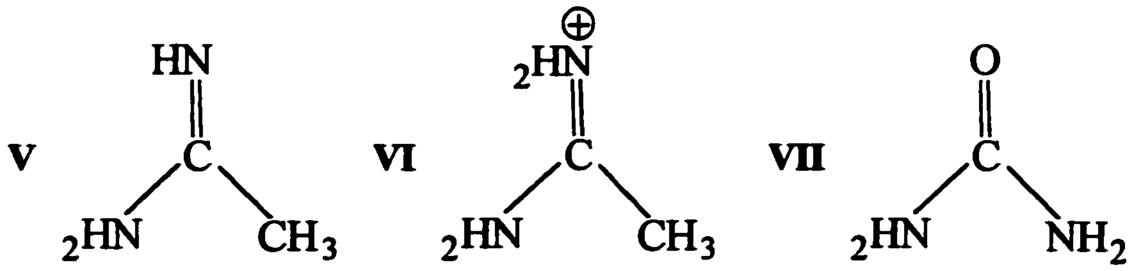

Fig. 4.5 Chemical structures of nonprotonated (V) and protonated (VI) forms of AA, and of U (VII).

form primary amines in acidic and neutral solutions. However, no studies on reactivity of oximes at Pt single-crystal electrodes have been reported in the literature. Thus, it was of interest to examine the reactivity and adsorption of oximes in the presence of UPD H and how this reactivity would be influenced by Pt surface geometry. Two small aliphatic oximes: formamidoxime (F_{NOH}) and acetaldehyde oxime (A_{NOH}), belonging to the group of *aldoximes*, were therefore chosen (see their chemical formulae as structures **VIII** and **IX** in Fig. 4.6 below) for the above purpose of examination of their structure-specific adsorption and reactivity.

The oximes were chosen because they offer the possibility of examination of surface-specific Faradaic reduction (electrocatalysis in the reduction) coupled with surface-specific adsorption, in contrast to G or DMG which do not undergo Faradaic reduction under the conditions employed in the present programme of experiments.

VIII

$$NH_2-CH=N-OH$$

Formamidoxime

IX

$$CH_3-CH=N-OH$$

Acetaldehyde oxime

Fig. 4.6 Chemical structures of F_{NOH} (VIII) and A_{NOH} (IX).

4.5 Water solvent and chemicals

All supporting electrolytes were prepared using a Milli-Q UV Plus ultra-pure water purification system (Millipore). The *QPAK* purification package, employing nuclear-grade ion-exchange resins contained in this system, allows inorganic ions to be gettered up to a resistivity of 18.2 MΩ cm. After passing through the *QPAK* purification unit, water is circulated through the UV chamber which photo-oxidises trace organic substances and destroys traces of bacteria that could be present. These trace organics are then removed by the "polisher" cartridge. This combination reduces the total organic carbon (TOC) to 5 ppb. The final Millipak 40 filter provides a 0.22 μm filtration, just before water is delivered to the point of use [16]. The Milli-Q UV Plus system provides up to 1.5 litres per minute of ultra-pure water on demand for the most critical analytical, electrochemical and biotechnological applications [16].

Aqueous 0.05 and 0.5 mol dm^{-3} H_2SO_4 acid solutions were made up from sulphuric acid of the highest purity available (Seastar Chemicals). Also, 0.05, 0.1 and 1.0 mol dm^{-3} aqueous solutions of $HClO_4$ were prepared from perchloric acid (Seastar Chemicals), also of the highest purity commercially available. Finally, aqueous 0.1 mol dm^{-3} alkaline supporting electrolyte solutions were made up from 99.996% (AESAR) NaOH pellets. Use of the above chemicals of highest purity available allowed us to obtain very good reproducibility and quality of cyclic voltammetric profiles for various single-crystal Pt planes compared with a number of those previously reported in the literature [17-22]. Aqueous 0.05 and 0.5 mol dm^{-3} supporting electrolyte solutions used for a special comparative study with KHF_2 were made from the 99% material (Sigma).

Dilute solutions of G^+ were made up in the above supporting electrolytes at concentrations typically about $6x10^{-5}$ to $3x10^{-3}$ mol dm^{-3}, from 99% guanidine carbonate salt (Aldrich). N,N-dimethylguanidine sulphate (Fluka, ≥ 98%) salt was used to prepare N,N-dimethylguanidonium solutions in the above supporting electrolytes, at concentrations about $6x10^{-5}$ to $3x10^{-3}$ mol dm^{-3} DMG^+.

Acetamidine was only available in the form of its hydrochloride salt (Fluka, ≥ 97%). Therefore, to enable electrochemical studies to be conducted in the absence of the otherwise strongly adsorbing Cl^- ion, its chemical form was changed to acetamidine sulphate by means of an exhaustive ion-exchange procedure. A strongly basic, Dowex-1-chloride (50-100 mesh), ion-exchange resin (Aldrich), previously completely converted to its sulphate form until no turbidity could be detected in a nephelometric test with $AgNO_3$, was employed.

Dilute solutions of urea (Aldrich, 99%) were made up in 0.05 and 0.5 mol dm^{-3} H_2SO_4 and 0.1 mol dm^{-3} NaOH supporting electrolytes at concentrations typically about $6x10^{-5}$ to $3x10^{-3}$ mol dm^{-3}.

Finally, acetaldehyde oxime (Fluka, ~99% "purum") and formamidoxime (Sigma, 99%) were used to prepare solutions in 0.5 mol dm^{-3} H_2SO_4 and 0.1 mol dm^{-3} NaOH supporting electrolytes, at a maximum concentration of about $1x10^{-3}$ mol dm^{-3} A_{NOH} (or F_{NOH}). The above solutions of adsorbates in supporting electrolytes were prepared by injecting G, DMG, AA, U, A_{NOH} and F_{NOH} from 1 wt.% stock solutions into a known volume of supporting electrolyte already in the electrochemical cell, using a 10 or a 100 μL microsyringe (Hamilton).

Carbon monoxide of ultra-high purity grade (Air Products) was used to perform adsorbate displacement current-transient experiments. The CO was introduced in the gas atmosphere of the cell, as a mixture of CO with Ar, and then was allowed to diffuse to the metal/solution interface (see section 5.6 of Chapter 5 for further details).

High purity H_2 gas (Air Products), passed through a gas purification line, was used for the reversible H reference electrode (RHE). The method for H_2 purification involved: passing the gas first through a drying agent, $Mg(ClO_4)_2$, then a molecular sieve (BDH type 4A), then through an oven containing Cu turnings and palladized azbestos at *ca.* 600 K to remove traces of oxygen, and eventually the H_2 was purged through activated charcoal traps in liquid N_2.

Atmospheric oxygen was removed from solutions before each experiment by bubbling with high-purity, research grade Ar (Air Products). During the experiments, the gas flow was kept above the solutions.

4.6 Preparation of single-crystal surfaces of Pt and their characterisation

4.6.1 Crystallographic information

In the research reported in this thesis, Pt single-crystal surfaces of the following crystallographic orientations were used: (111), (100), (110) and (511). The choice of three low-Miller index planes, which are the smoothest on the atomic scale, was made because the (111), (100) and (110) surfaces are located at the extremities (apices) of the stereographic triangle [23, 24] for the face-centred cubic (fcc) system in which platinum crystallises (see Fig. 4.7). Major structural differences between the above faces are responsible for leading to the largest differences in their adsorptive or catalytic behaviour in comparison with corresponding properties of a polycrystalline electrode. On the other hand, the (511) Miller notation represents a *stepped*, 3[100]x[111], surface which offers short, 3-atom-wide (100) terraces and monoatomic steps of (111) configuration and is thus located on the line connecting the (111) and (100) apices of the stereographic triangle, as shown in Fig. 4.7. The (110) plane, however, can also be represented by the terrace/step notation as: 2[111]x[111], indicating that it is the surface with 2-atom-wide terraces and monoatomic wide steps, both having (111) configuration and co-ordination.

Assuming that the metal atoms are just hard spheres, any face can be represented by a ball model [23-25]. Such models for (111), (100), (110) and (511) planes in the fcc system are shown in Fig. 4.8 from which it is clear that each surface displays different types of sites. Thus, the (111) surface has a three-fold symmetry with two types of non-equivalent hollow sites; the (100) plane has four-fold symmetry, and the (110) and stepped (511) surfaces have a significant increase in the number of types of sites available in comparison with the (111) and (100) surfaces. Introduction of stepped, atomically "rough", surfaces is very important as it enables the electrochemical characterisation of surface structure, particularly that concerning the effect of long-range order on the (111) and (100) atomically flat surface domains [18], to be made.

4.6.2 Determination of crystallographic orientation

High-purity Pt wire (99.9995%, Johnson Matthey) 1 mm in diameter, was used to make the single-crystals. Firstly, monocrystalline spherical beads of platinum were obtained by melting the extremity of this wire, using a gas-oxygen flame [26]. To eliminate any gross surface impurities, prior to its use, the wire was rinsed with acetone and then etched in *aqua regia*. Once a drop of melted platinum *ca.* 3 mm in diameter was

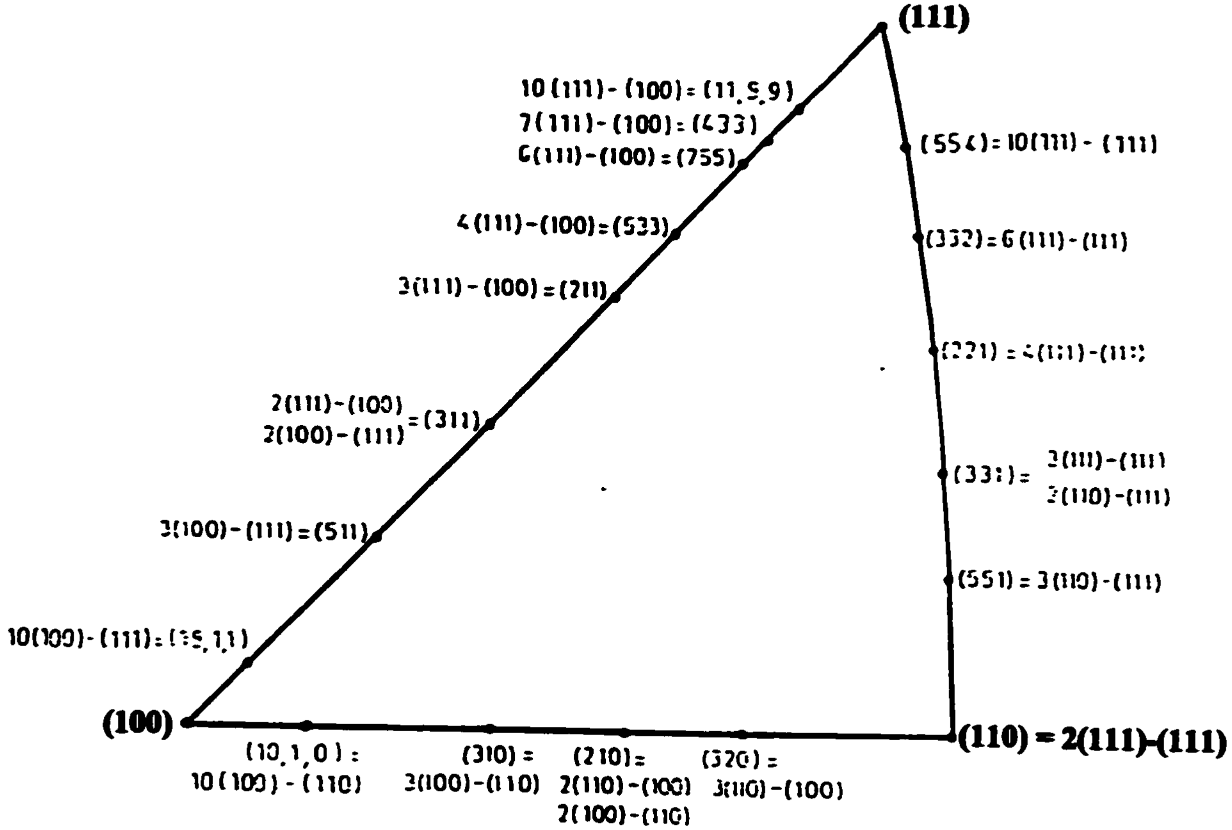

Fig. 4.7 Unit projected stereographic triangle for the fcc structure. Miller indices and terrace/step notations are given [23, 24].

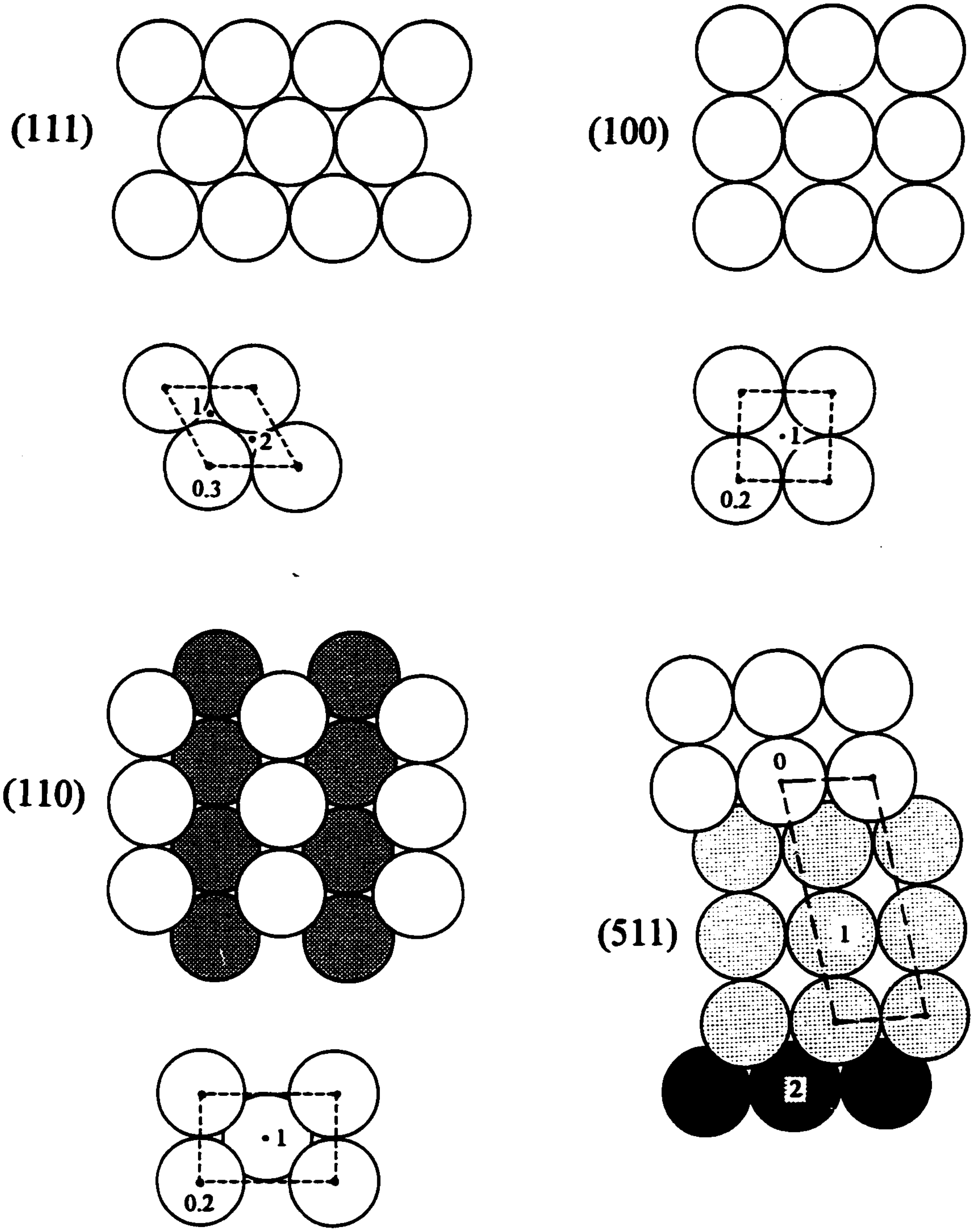

Fig. 4.8 Ball models for four faces of the fcc system. Diagrams are drawn looking normally at the model. The unit cell-boundary is marked with a dotted line and the first, second and the third layers of atoms are denoted by 0, 1, and 2 [23, 24].

obtained, the flame was very slowly lowered to ensure proper recrystallisation and allow time for diffusion of possible metal impurities to the surface. At that time, oxygen from air can catalytically oxidise any carbonaceous and sulphurous impurities [27]. The resulting metal bead displays small but significant flat areas, equally spaced (90° apart), corresponding to the face of the fcc cube. These flat areas are of the (111) crystallographic orientation [28].

Monocrystalline beads of Pt, thus obtained, were then aligned to the chosen crystallographic orientation using the back-reflection, von Laue X-ray diffraction method [29, 30], in the way described by Hamelin for Au and Ag single-crystals in ref. 30. An Enraf Nonius Delft, Diffractis model 581, X-ray diffractometer (Holland) was used. The equipment consisted of an X-ray generator, a von Laue back-reflection camera with a film holder, a pin-hole collimator and a goniometer. The goniometer assembly [31], shown in Fig. 4.9, consisted of the Pt single-crystal, **A**, and a holder, **B**, made from polyamide, placed in the "head" of the goniometer, **C**. The "head", mostly made from stainless steel, was designed to fit with very good precision into a cylinder of stainless steel, **D**, for the purpose of polishing the aligned crystals (Fig. 4.9). The crystal was secured in the holder by epoxy resin, **E** (Epofix, Struers). The distance between the single-crystal face and the X-ray direct exposure (Kodak) film was 6 (± 0.1) cm. The X-rays were generated using a Cu tube and applying a voltage of 30 kV at a current of 20 mA; the exposure time was usually about 30 min.

The back-reflection von Laue diffraction method is much used for orientation of single-crystals, particularly those having the fcc structure. The interpretation of the von Laue diffraction patterns is greatly facilitated by the use of the Greninger chart [32]. The alignment procedure for single-crystals is quite complex and is explained in detail in ref. 30. However, it is important to point out that in order to interpret the cubic pattern one looks for the three most important spots on this pattern. These are the low-index reflections (111), (100) or (110) which are quite dark spots arising at the intersections of several prominent zone lines. Alignment of the crystal to a specifically selected orientation consists in reading angular relations on the back-reflection film using the Greninger chart and a table of the angles between the different faces [30] for a crystal positioned at 6 cm from the X-ray film.

4.6.3 Polishing and final preparation

Once the orientation of the crystal was completed, the crystal was then cut and polished along the chosen crystallographic orientation, according to the procedure described in ref. 31. For this purpose, the goniometer assembly was placed in the cylinder **D** (Fig. 4.9) in order to keep the crystal in the proper position. Then, the resin and crystal were ground flat on fine-grade silicon carbide paper (Struers, Denmark) of 1200, 2400 and 4000 grades, until about half of the sphere was removed. The above procedure was followed by polishing the surface using 1 micron diamond paste (Metadi II, Buehler, USA), then 0.25 and 0.1 micron polycrystalline diamond suspensions (Metadi Supreme, Buehler, USA) on a soft polishing cloth. Such polished surfaces were mirror-like and did not show any scratches. Finally, an X-ray pattern was taken again to check for deviations from alignment caused by the polishing procedures. Only those crystals oriented within 1° were used to conduct experiments.

Larger Pt(111) and (100) single-crystals (*ca.* 8 mm diameter, 2 mm thick) were

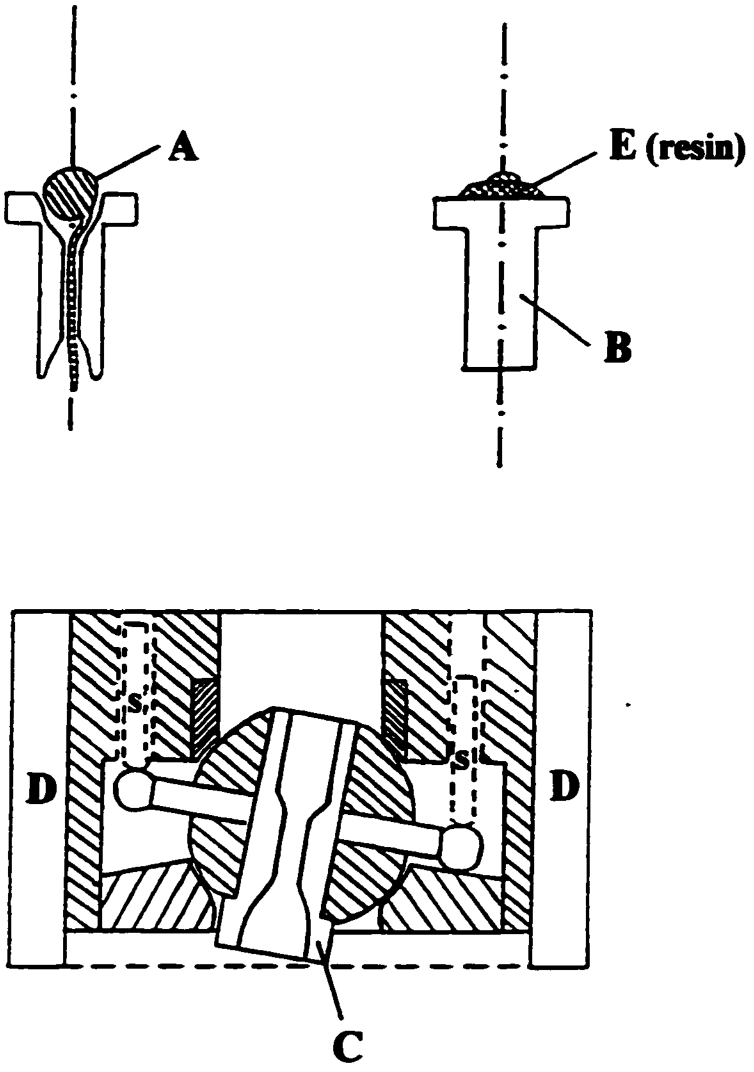

Fig. 4.9 The goniometer assembly [31]: A- Pt single-crystal; B- crystal's holder; C- "head" of the goniometer (s- screws used for positioning the crystal to the chosen angle) and D- cylinder used to maintain the crystal rigid during its polishing.

used for the combined *in situ* FTIR and CV experiments. They were obtained from Johnson Matthey (99.999% purity). These crystals were realigned, if needed, to their (111) or (100) orientations and polished by applying the same procedures as those described above for preparation of small Pt single-crystal electrodes.

Properly oriented Pt single-crystals were removed from the holder by dissolving the remaining resin in chloroform. The monocrystals were then spot-welded to a 0.5 mm diameter Pt wire, partly sealed in soft or pyrex glass. Finally, a 0.5 mm Ag wire was used to provide an electrical contact between the Pt wire and the working electrode connector. In order to provide an electrical contact and support in the FTIR cell, two pieces of 0.5 mm Pt wire were originally (before alignment) spot-welded to the large Pt crystals used for the *in situ* FTIR-CV measurements.

The electrodes were then annealed according to the procedures described in sections 5.2.1 and 5.3.4 of Chapter 5 below. A polyoriented Pt electrode, having multi-oriented facets, used for comparative experiments, was a spherical single-crystal bead.

4.7 References

1. B. MacDougall, B.E. Conway and H.A. Kozlowska, *J. Electroanal. Chem.*, 1971, **32**, App. 15.
2. H.A. Kozlowska, B.R. MacDougall and B.E. Conway, *J. Electroanal. Chem.*, 1972, **39**, 287.
3. B.E. Conway, B. MacDougall and H.A. Kozlowska, *J. Chem. Soc., Faraday Trans. I*, 1972, **68**, 1566.
4. J. Clavilier, J.M. Orts, R. Gomez, J.M. Feliu and A. Aldaz in *Proc. Symposium on*

"Electrochemistry and Materials Science of Cathodic H Absorption and Adsorption", B.E. Conway and G. Jerkiewicz (Eds.), The Electrochemical Society, Pennington, N.J., 1995, **94-21**, 167.

5. J. Clavilier, R. Albalat, R. Gomez, J.M. Orts, J.M. Feliu and A. Aldaz, *J. Electroanal. Chem.*, 1992, **330**, 489.
6. J. Clavilier, R. Albalat, R. Gomez, J.M. Orts and J.M. Feliu, *J. Electroanal. Chem.*, 1993, **360**, 325.
7. J.R. Macdonald, *Electrochim. Acta*, 1990, **35**, 1483.
8. R.J. Nichols in *"Adsorption of Molecules at Metal Electrodes"*, J. Lipkowski and P.N. Ross (Eds.), VCH Publishers, New York, 1992, Chapter 7.
9. A. Bewick in *"Trends in Interfacial Electrochemistry"*, A.F. Silva (Ed.), D. Reidel Publishing Company, Dordrecht, 1986, 331.
10. K. Ashley and S. Pons, *Chem. Rev.*, 1988, **88**, 673.
11. S. Morin and B.E. Conway, *J. Electroanal. Chem.*, 1994, **376**, 135.
12. S. Morin, B.E. Conway, G.J. Edens and M.J. Weaver, *J. Electroanal. Chem.*, 1997, **421**, 213.
13. M.M. Baizer and H. Lund, *"Organic Electrochemistry. An Introduction and a Guide"*, Marcel Dekker, Inc., New York, 1983.
14. R.M. Elofson and J.G. Atkinson, *Can. J. Chem.*, 1956, **34**, 4.
15. A.J. Fry, *"Synthetic Organic Electrochemistry"*, John Wiley & Sons, Inc., New York, 1999.
16. *"Milli-Q UV Plus Operating and Maintenance Manual"*, Millipore Corporation, 2nd edition, USA, 1990.

17. J. Clavilier, K. El Achi, M. Petit, A. Rodes and M.A. Zamakhchari, *J. Electroanal. Chem.*, 1990, **295**, 333.

18. J. Clavilier, A. Rodes, K. El Achi and M.A. Zamakhchari, *J. Chim. Phys.*, 1991, **88**, 1291.

19. N. Furuya and S. Motoo, *J. Electroanal. Chem.*, 1979, **98**, 189.

20. E. Morallon, J.L. Vasquez and A. Aldaz, *J. Electroanal. Chem.*, 1992, **334**, 323.

21. E. Morallon, J.L. Vasquez and A. Aldaz, *J. Electroanal. Chem.*, 1990, **288**, 217.

22. N.S. Marinkovic, N.M. Markovic and R.R. Adzic, *J. Electroanal. Chem.*, 1992, **330**, 433.

23. J.F. Nichols, *"An Atlas of Models of Crystal Surfaces"*, Gordon and Breach, New York, 1965.

24. Hamelin, *Portugaliae Electrochimica Acta*, 1987, **5**, 77.

25. E.A. Wood, *"Crystal Orientation Manual"*, Columbia University Press, New York, 1963.

26. J. Clavilier and R. Pineaux, *C.R. Acad. Sci.*, Paris, 1965, **260**, 891.

27. J. Clavilier and J.P. Chauvineau, *J. Electroanal. Chem.*, 1978, **100**, 461.

28. G. Lehmpfuhl and Y. Uchida, *Surf. Sci.*, 1990, **235**, 295.

29. C.S. Barret and T.B. Massalski, *"Structure of Metals: Crystallographic Methods, Principles and Data"*, McGraw Hill, London, 1966.

30. A. Hamelin in *"Modern Aspects of Electrochemistry"*, B.E. Conway, J.O'M. Bockris and R.E. White (Eds.), Plenum Press, New York, 1985, **16**, Chapter 1.

31. A. Hamelin, S. Morin, J. Richer and J. Lipkowski, *J. Electroanal. Chem.*, 1990, **285**, 249.

32. A.B. Greninger, *Trans. AIME*, 1935, **117**, 61.

Chapter 5

Characterisation of Voltammograms for Pt Single-Crystal Electrodes over the Potential Range for UPD of H

The process of underpotential deposition (UPD) of H on Pt single-crystals, where H atoms become reversibly adsorbed on the Pt surface at potentials positive to the H_2 reversible potential, has been extensively studied since the beginning of the 1980's. At that time, a new and very reliable procedure for final preparation of low-index Pt single-crystals by flame annealing was reported by Clavilier et al. [1-4].

5.1 Interpretation of adsorption states at polycrystalline Pt in 0.5 mol dm^{-3} H_2SO_4

As previously reported in a number of papers (see e.g. refs. 5-8), a cyclic voltammogram of polycrystalline Pt wire in 0.5 mol dm^{-3} H_2SO_4, over the potential range for UPD of H, is characterised by the presence of two principal, reversible adsorption states. The first, centred at 0.11 V, corresponds to adsorption on (110) sites and a second one, centred at 0.26 V, principally to adsorption on sites of (100) geometry. In addition, a voltammogram of a polyoriented, single-crystal bead Pt electrode, exhibits small contributions, centred at 0.43 V, from currents at (111) facets [6] and also some contribution from HSO_4^- electrosorption at facets of various orientations.

5.2 Interpretation of adsorption states at Pt(111) in 0.5 mol dm^{-3} H_2SO_4

A cyclic voltammogram for a well-ordered Pt(111) surface in 0.5 mol dm^{-3} H_2SO_4, recorded at a sweep rate of 50 mV s^{-1} and cooled in H_2 + Ar mixture, is shown in Fig. 5.1a [9]. The voltammogram features two distinguishable potential regions. Firstly, at low potentials over the range 0.06 to 0.32 V, the surface is covered by chemisorbed H. Secondly, at potentials more positive than 0.32 V, another, so-called "butterfly" region, appears. The latter region has also been termed "unusual" or "anomalous", as it was observed at relatively high potentials and appeared to be sensitive to the nature of anions present in the electrolyte.

As in the review in 1991 by Clavilier et al. [9], initially the unusual adsorption states were thought to be associated with adsorption of strongly bonded H, significantly different in energy from the weakly bonded H, adsorbed at lower potentials. However, the latter was not consistent with the fact that these states were intrinsic features of a well-ordered Pt(111) electrode and were dependent on H_2SO_4 concentration. Simultaneously, two other hypotheses for the origin of the anomalous adsorption states were considered. A first interpretation in terms of surface defects suggested that the unusual states correspond to adsorption of H having high energy of bonding on surface defects (Pt ad-atoms or clusters of ad-atoms), which become generated by the thermal treatment of the surface. These defects could be eliminated after a few cycles into the oxygen adsorption-desorption potential range, resulting in the progressive elimination of the supposed unusual states. This latter conclusion was contradicted by the preliminary LEED studies by Aberdam et al. [10] of thermally treated Pt(111), before and after cycling in the oxygen adsorption-desorption region. The above work clearly demonstra-

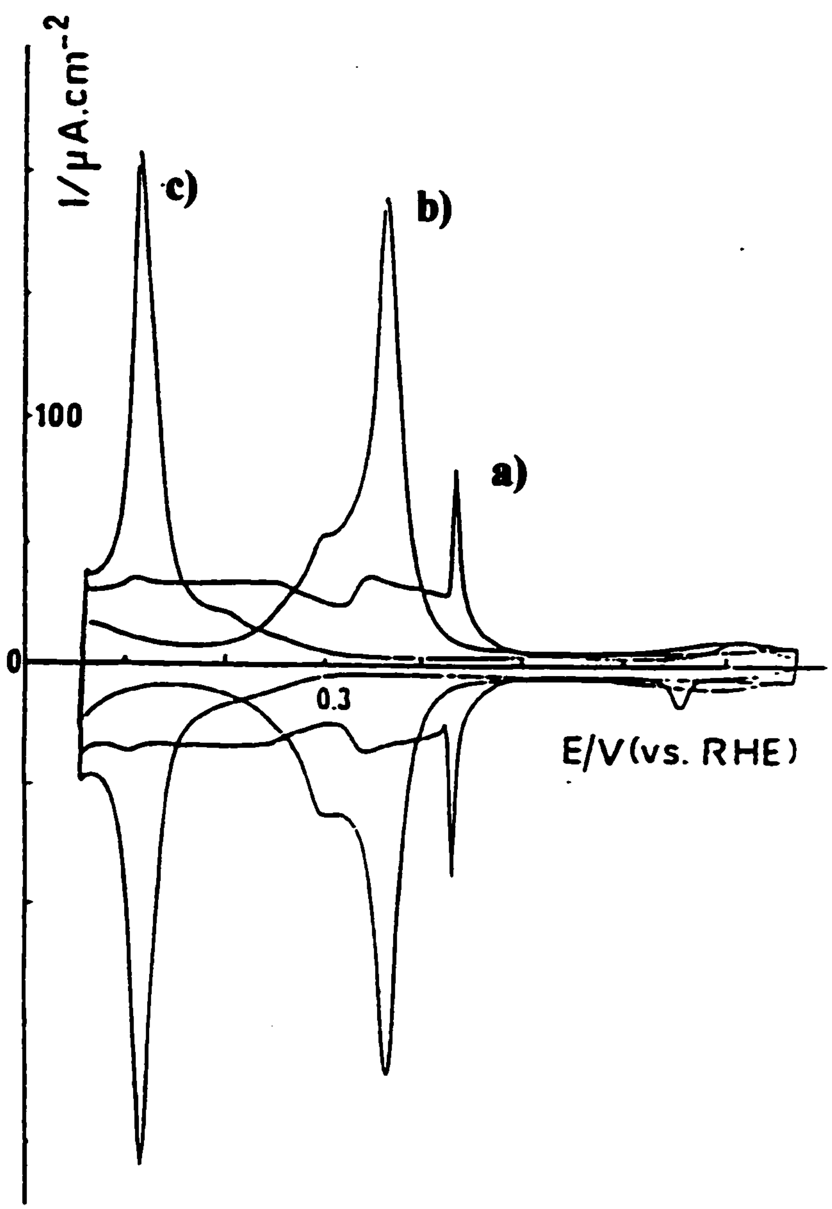

Fig. 5.1 Cyclic voltammograms of the surfaces of well-ordered: (a) Pt(111), (b) Pt(100) and (c) Pt(110) single-crystals in contact with 0.5 mol dm^{-3} H_2SO_4, cooled in H_2 + Ar atmosphere, after the flame cleaning procedure, recorded at a sweep rate of 50 mV s^{-1} [9].

ted that cycling in the oxygen adsorption-desorption region caused micro-roughening, involving the presence of atomic steps on the surface. Similar observations were reported by Itaya et al. [11], based on *in situ* STM experiments.

On the other hand, Wagner and Ross [12] interpreted the unusual adsorption states as due to effects of surface impurities or to a process of reversible OH adsorption. The former interpretation was supported by the ease with which these states were eliminated after a few cycles of oxidation and reduction of the Pt surface. The surface impurities hypothesis was, however, ruled out by its authors when, by means of coupled UHV-electrochemistry experiments [13], they showed that existence of the anomalous adsorption states depended on the long-range order of the Pt(111) surface. Thus, again, these states were found to be intrinsic to the well-ordered (111) plane.

As mentioned in section 2.3 of Chapter 2, the idea that the unusual adsorption states, observed at Pt(111) in H_2SO_4, correspond to adsorption-desorption of HSO_4^- or SO_4^{2-} ions, was originally introduced by Scherson and Kolb [14] in 1984. Since then, the presence of specifically adsorbed HSO_4^- on Pt(111) surface has been proven by means of various techniques, most importantly by *in situ*-FTIR spectroscopy, the charge-transient, CO adsorption replacement method (see sections 2.3 of Chapter 2 and 5.6 in this Chapter for further details, respectively) and by STM [15] techniques.

The mean electric charge measured for the well-ordered Pt(111) surface (as for that shown in voltammogram of Fig. 5.1a) between 0.06 and 0.76 V was found to be about 240 $\mu C\ cm^{-2}$ [2, 6, 16], after subtracting the double-layer charge contribution. For the reason that the total charge measured from the voltammetric profile contains a significant contribution from charging the electrical double-layer, such corrections are necessary and can be done by subtracting from the calculated total charge, the value obtained by integration of the voltammetric profile under the dashed lines, as shown as an example in Fig. 5.1a. The value of 240 $\mu C\ cm^{-2}$ apparently complies very well with the calculated value of 243 $\mu C\ cm^{-2}$ for an ideal (111) plane [2], with a coverage formally of one H atom per Pt surface atom (for a Pt atom density of 1.5×10^{15} atoms cm^{-2}). However, the surface concentration of HSO_4^-, adsorbed on Pt(111) at potentials positive to 0.32 V, attains its maximum value equivalent to 1/3 of H monolayer coverage with the formation of a $(\sqrt{3} \times \sqrt{3})\ R30^{\circ}$ (three-fold co-ordination) bisulphate pattern; see e.g. refs. 15 and 17. Correspondingly, the adsorbed H present on the Pt(111) surface occupies 2/3 of a monolayer over the potential range 0.06-0.32 V [9, 18], where UPD H atoms occupy three-fold octahedral (or tetrahedral) hollow sites; see ref. 19 and other papers cited in this work (also see section 5.6 in the present Chapter, later).

5.2.1 Thermal reordering of the Pt(111) surface after metallographic polishing

The flame-annealing treatment was performed directly after the polishing procedure (see section 4.6.3 of Chapter 4) had been completed. The treatment consisted of several steps and allows complete reordering of the perturbed Pt surface after metallographic preparation [16].

Firstly, the freshly polished (111) oriented sample undergoes decontamination by exposing it for a few seconds to the gas-oxygen flame, at temperature just above 100° C. The CV of such a decontaminated surface looks very similar to that of a polyoriented Pt (see Fig. 5.2, curve 1). The above indicates that the three low-index structures are present at the surface and no preferential site distribution is observed. In other words, the surface

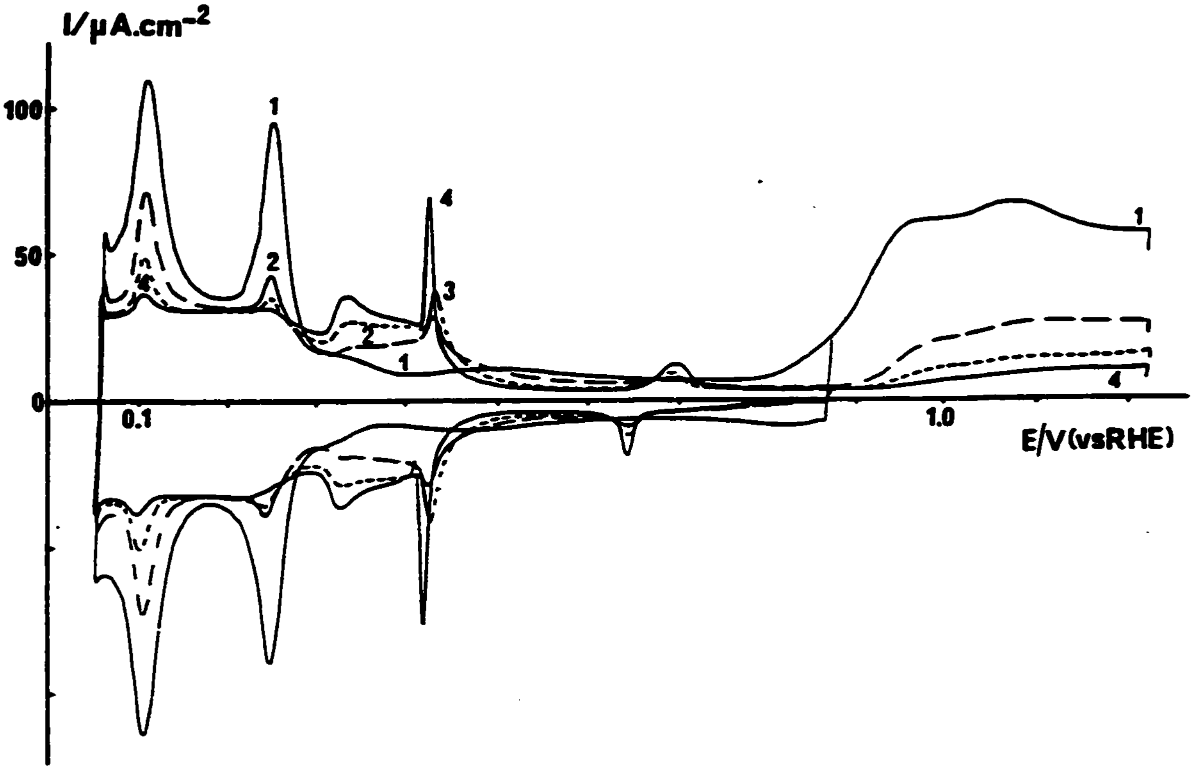

Fig. 5.2 Modifications of the H and O adsorption-desorption voltammetric profiles for various stages of annealing of freshly polished Pt(111) electrode in contact with 0.5 mol dm^{-3} H_2SO_4. Curve 1: CV after thermal decontaminaion; Curves 2 and 3: After two successive annealings for a few seconds at a temperature between 500 and 600° C and Curve 4: After annealing for 10 seconds at a temperature between 1300 and 1400° C [16].

contains only very narrow (*ca.* three atomic rows) (111) terraces. The main two peaks observed in the voltammogram (Fig. 5.2, curve 1) correspond to randomly distributed (100) and (110) steps of different heights.

The result of such reordering of the decontaminated (111) surface by gradually increasing the temperature of the crystal and the time of annealing, is shown in Fig. 5.2 (curves 2 to 4) [16]. It can be seen in this Figure that the current peaks at 0.11 and 0.26 V, corresponding to H adsorption at (110) and (100) orientations, simultaneously decrease while the adsorption states between 0.3 and 0.5 V, corresponding to the (111) geometry, increase. Thus, the (100) and (110) surface defects become progressively eliminated as the size of the (111) ordered domains, increases. Also, at each stage of the annealing procedure (Fig. 5.2), the CV profile is modified with a dramatic decrease in the current for O adsorption. This indicates that electrochemical adsorption of the latter species occurs preferentially on the less-ordered surface domains, i.e. at crystalline defects. A well-ordered (111) surface is already obtained after annealing for 10 seconds at 1300-1400° C; however, the ultimate stage of reordering is obtained after 15 minutes of annealing at 1300° C. Then, the mean electric charge measured between 0.06 and 0.76 V is 243 $\mu C\ cm^{-2}$, after subtracting the double-layer charge contribution [16].

Right after the flame annealing procedure, the hot (111) crystal was cooled in air and then quenched in ultra-pure H_2O, similarly to the treatment of polycrystalline Pt electrodes. As the (111) orientation was not found to be sensitive to the presence of O_2 [16], the procedure of cooling in a non-oxidising mixture of H_2 + Ar was not employed with new Pt(111) surfaces.

The well-ordered Pt(111) plane in 0.5 mol dm^{-3} H_2SO_4 is characterised by the absence of the adsorption state at 0.11 V and 0.26 V, but the presence of a very sharp peak at 0.43 V (on both positive- and negative-going sweeps) and flatness of the current profile, i.e. the low level of CV currents, over the potential range where otherwise adsorption of oxygen species takes place on Pt.

In summary, the cyclic voltammogram provides a very characteristic fingerprint for the well-ordered (111) crystallographic orientation, based on which the quality of the surface obtained and types of defects present, can be precisely evaluated. In the present work, the Pt(111) electrodes were subjected to the same thermal reordering process which was electrochemically monitored at its every stage. The main goal was to obtain the same CV shape and total electric charge as for those reported in the literature [6, 9, 16].

5.3 Interpretation of adsorption states at Pt(100), (110) and (511) surfaces in 0.5 mol dm^{-3} H_2SO_4

5.3.1 Pt(100)

A cyclic voltammogram of a well-ordered Pt(100) surface in 0.5 mol dm^{-3} H_2SO_4, recorded at a sweep rate of 50 mV s^{-1} and cooled in H_2 + Ar mixture, is shown in Fig. 5.1b [9]. It is characterised by strong H adsorption states with appearance of a symmetrical current peak on negative- and positive-going sweeps, at *ca.* 0.36 V. Like that of the (111) orientation, the (100) plane exhibits long-range ordering, resulting in an atomically flat surface with wide (100) terraces. The above can be supported by the presence of only a small peak at *ca.* 0.28 V, which otherwise (with decreasing dimensions of (100) surface ordered domains) becomes significantly intensified.

The mean electric charge measured between 0.15 and 0.76 V was found to be about 205-215 μC cm^{-2}, after subtracting the double-layer charge contribution [4, 16, 20, 21]; this value fits very well with the charge evaluated for a (1x1) structure (209 μC cm^{-2}), assuming one H atom per surface Pt atom [22]. The above charge comprises two components: that for UPD of H and that for HSO_4^- adsorption with partial charge-transfer, with H atoms being adsorbed on four–fold sites [19]. On the other hand, HSO_4^- ions [23] are mostly adsorbed in two-fold co-ordination at the (100) surface, which means that upon adsorption of the bisulphate ion on the (100) plane, one electron is transferred per two occupied Pt atoms. Evaluated by the CO adsorption replacement technique [24], the surface concentration of the HSO_4^- ions adsorbed on Pt(100) was found to reach 0.26 of an equivalent monolayer of adsorbed H. Correspondingly, close to a full monolayer (θ_H=0.94) of H is present on the (100) surface, near the threshold potential for onset of the HER.

5.3.2 Pt(110)

A voltammogram for a well-ordered Pt(110) surface in 0.5 mol dm^{-3} H_2SO_4, recorded at a sweep rate of 50 mV s^{-1} and cooled in H_2 + Ar mixture, is shown in Fig. 5.1c [9]. It is characterised by strong H adsorption states with appearance of a symmetrical current peak on negative- and positive-going sweeps, at *ca.* 0.12 V. The mean electric charge measured between 0.06 and 0.76 V was found to be about 218 μC cm^{-2}, after subtracting the double-layer charge contribution [25].

Moreover, evaluated by the CO adsorption replacement technique [24], the hydrogen maximum coverage is estimated to be again close to the full monolayer value (θ_H=0.97) for H, where the charge equivalent for the Pt(110)-(1x1) structure with one H atom adsorbed per surface Pt atom, is 147 μC cm^{-2} [24]. On the other hand, the surface concentration of the HSO_4^- ions adsorbed on Pt(110) was found to reach a coverage equivalent to about 0.43 of a monolayer of adsorbed H. This is the highest value amongst those for all the three low-index planes.

5.3.3 Pt(511)

Finally, a cyclic voltammogram for a well-ordered Pt(511) surface in 0.5 mol dm^{-3} H_2SO_4, again recorded at a sweep rate of 50 mV s^{-1} and cooled in H_2 + Ar mixture, is shown in Fig. 5.3 [26]. The voltammogram of this high index, 3(100)x(111) surface, features two well-distinguished regions in the H UPD potential range: a pair of reversible current peaks, respectively at 0.26 for a cathodic and 0.33 V for an anodic process, and a part of a relatively broad peak between 0.05 and 0.2 V. The very sharp current peak, observed at 0.26 V, can be attributed [26, 27] to adsorption-desorption of H on (100) terraces.

The mean electric charge measured between 0.06 and 0.76 V is 245 μC cm^{-2}, after subtracting the double-layer charge contribution (as integrated from the voltammogram in Fig. 1 of ref. 26). This charge comprises two components: one corresponding to adsorption on (100) terraces and the second to adsorption on (111) step sites. The charge contribution for the three-atom wide (100) terraces at Pt(511) surface was evaluated [27] from the hard-sphere model as 161 μC cm^{-2}, after subtracting the double-layer charge contribution.

For the high-index planes having terrace widths n>7, the fractions of charges assigned and measured for the unusual adsorption states on terraces are expected to follow those corresponding to adsorption of anionic species on low-index surfaces, as pointed out by Clavilier et al. in ref. 9, for the surfaces vicinal to the (111) index of geometry. However, for surfaces such as the Pt(511) plane, which do not feature long-range, two-dimensional ordering, the charge ratios for usual and unusual adsorption states on terraces no longer correspond to those at low-index planes.

5.3.4 Thermal reordering of Pt(100), (110) and (511) surfaces after metallographic orientation

The same flame annealing treatment for successive surface reordering as that applied to the (111) plane (see section 5.2.1 above) was employed with the above three Pt single-crystal surfaces. However, a final stage of preparation (unlike that for the (111) orientation) involved the procedure of annealing the electrodes in H_2 + Ar mixture, followed by quenching the crystals in ultra-pure H_2O. The above procedure of surface preparation was originally proposed by Motoo and Furuya [28], who suggested that thermal treatment in non-oxidising atmospheres (H_2 + Ar) favours migration of surface atoms towards their equilibrium positions. Thus, the long-range ordering on the surface tends to become restored. The above procedure is believed to lead to unreconstructed surfaces and, at the same time, prevents the formation of adsorbed oxygen species on the Pt surface.

Nevertheless, the response to the conditions of thermal preparation (cooling in air or in H_2 + Ar mixture) for the above three surfaces, significantly varies from that for the

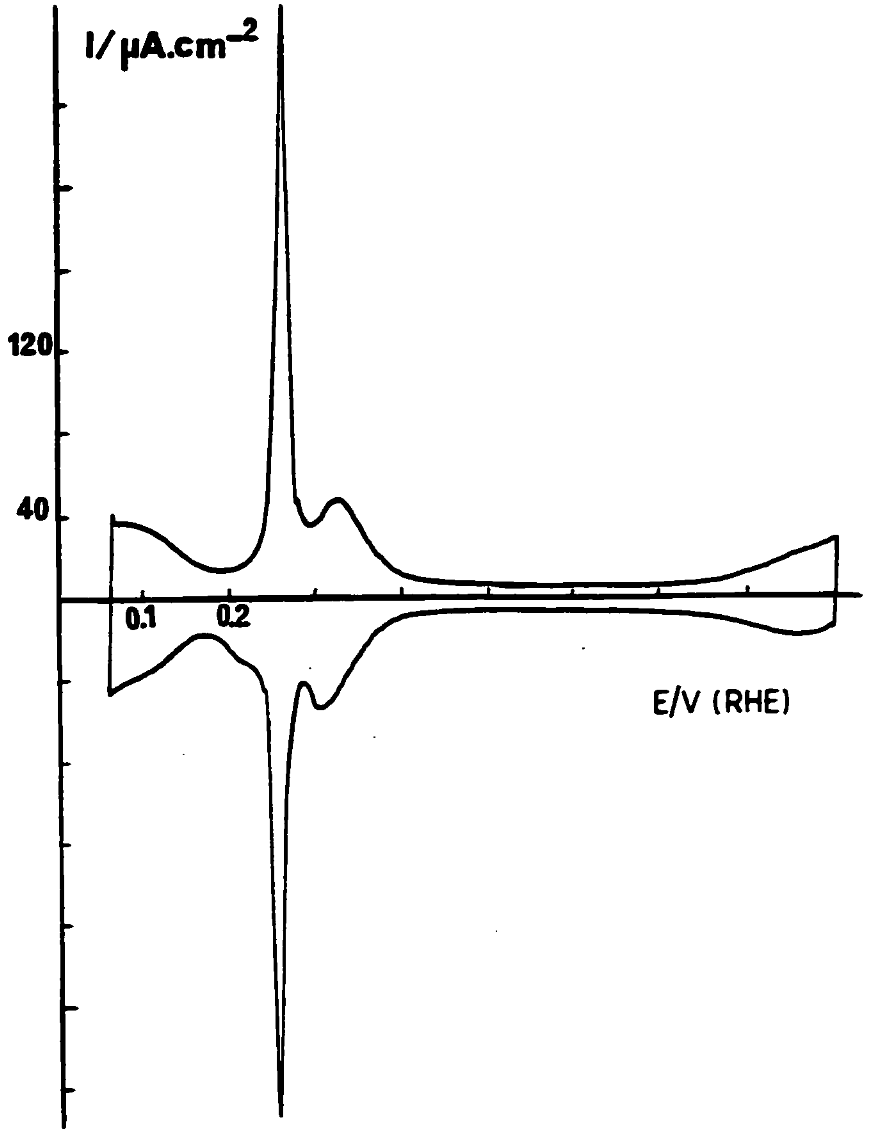

Fig. 5.3 A cyclic voltammogram of the well-ordered Pt(511) surface in contact with 0.5 mol dm^{-3} H_2SO_4 after flame treatment (cooled in air), recorded at a sweep rate of 50 mV s^{-1} [26].

(111) plane. The Pt(100) surface is very sensitive to the conditions of surface preparation but, although perturbed by a few cycles of oxygen adsorption-desorption (or by the preparation procedure of cooling in air), it can be restored to its long-range ordered state by a "fast cycling" electrochemical procedure [9, 16]. The above procedure consists in applying repetitive polarisation cycles to the sample, between 0.06 and 1.0 V, at a sweep rate between 50 and 200 V s^{-1}, for 60 seconds [16]. Similarly to Pt(100), the Pt(110) and (511) surfaces are also sensitive to the surface preparation procedure. However, no electrochemical treatment (such as the fast cycling procedure for the (100) plane in H_2SO_4) is known to improve their terrace long-range ordering.

The same pre-treatments for surface preparation (cooling in air and H_2 + Ar mixture) were employed with respective Pt single-crystal electrodes studied in the two other principal supporting electrolytes ($HClO_4$ and NaOH), as well as in KHF_2 (see Chapter 6).

5.4 Interpretation of adsorption states at Pt in 0.1 mol dm^{-3} $HClO_4$

5.4.1 Pt(111)

A cyclic voltammogram of a well-ordered Pt(111) surface in contact with 0.1 mol dm^{-3} $HClO_4$ is shown in Fig. 5.4. It is characterised by the presence of two well-separated regions over the potential ranges: 0.06-0.40 V and 0.55-0.87 V vs. RHE, as reported in a number of previously published papers [2, 6, 9]. As already mentioned in section 2.3 of Chapter 2, the region located at lower potentials corresponds to adsorption-desorption processes of weakly adsorbed, UPD H. On the other hand, the characteristic "butterfly", here a major feature observed over the 0.55-0.87 V range, corresponds to reversible adsorption of anionic species (ClO_4^- and/or OH^-). A significant part of the charge passed in this butterfly region is due to adsorption-desorption of the latter anion, as suggested by most authors [9, 12, 29-31]. In relation to the well-known progression of the HSO_4^- adsorption region to more positive potentials with dilution of H_2SO_4, the butterfly region observed in aqueous $HClO_4$ is suggestive of weaker chemisorption of ClO_4^- than that of HSO_4^- ion [6, 32].

The mean electric charge measured between 0.06 and 0.87 V is 249 $\mu C\ cm^{-2}$, after subtracting the double-layer charge contribution (as evaluated by Armand and Clavilier [33]), whereas the maximum charge for UPD of H, obtained by the CO adsorption replacement technique [34] conducted at 0.08 V, is 152 $\mu C\ cm^{-2}$.

5.4.2 Pt(100), (110) and (511) surfaces

The processes of UPD of H and that corresponding to the adsorption of anionic species, are not separated by a double-layer charging region at the above three Pt surfaces, unlike the behaviour at the Pt(111) plane. Characteristic (usual and unusual) adsorption states are observed over the following potential ranges: 0.06-0.70 V at Pt(100), 0.06-0.35 V at Pt(110) and 0.06-0.45 V at the (511) surfaces, where behaviour at the latter plane is similar to that observed at its vicinal index surfaces [6, 9, 34, 35].

For the Pt(100) surface, a mean electric charge of 258 $\mu C\ cm^{-2}$, measured between 0.06 and 0.76 V, was obtained, as before, after subtracting the double-layer charge contribution [22]. The above charge is greater by about 23% than that obtained in 0.5 mol dm^{-3} H_2SO_4, for the (100) plane in the (1x1) structure [4, 16, 20, 21]. This was hypothetically assigned by Clavilier et al. [9] to the effect of surface reconstruction to the

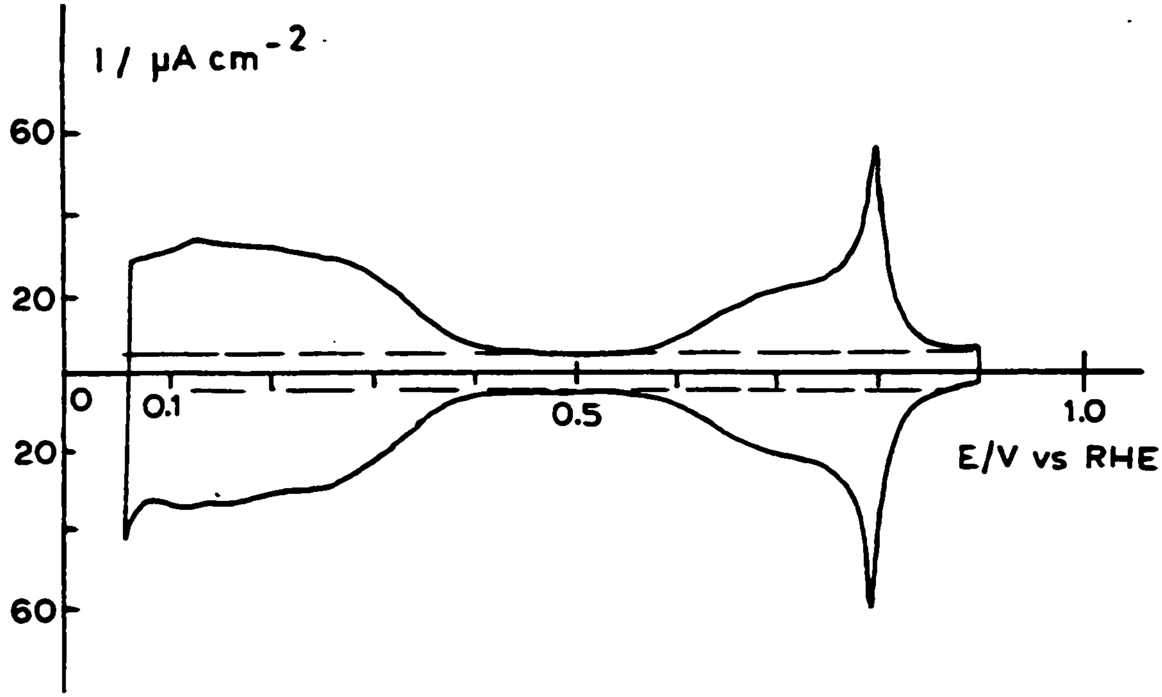

Fig. 5.4 A cyclic voltammogram of well-ordered Pt(111) surface in contact with 0.1 mol dm^{-3} $HClO_4$ after cooling in air, recorded at a sweep rate of 50 mV s^{-1} [1].

Pt(100) hexagonal or (5x20) structure in $HClO_4$ solution.

For the Pt(110) surface, the maximum coverage for UPD H, evaluated by the CO adsorption replacement technique [34] gave a charge transient at 0.085 V, corresponding to *ca.* 0.99 of an equivalent monolayer of H, where the charge equivalent for Pt(110) in the (1x1) structure with one H atom per surface Pt atom is 147 μC cm^{-2}. Correspondingly, the surface concentration of anionic (ClO_4^-) species was found to be about 0.26 of an equivalent monolayer of H.

5.5 Interpretation of adsorption states at Pt in 0.1 mol dm^{-3} NaOH

5.5.1 Pt(111)

A cyclic voltammogram of a well-ordered Pt(111) surface in contact with 0.1 mol dm^{-3} NaOH is shown in Fig. 5.5. As for the case of aqueous $HClO_4$, the voltammogram is characterised by the presence of two well-separated regions over the potential ranges 0.06-0.40 V and 0.60-0.90 V vs. RHE, as reported in a number of previously published papers [29, 31, 36-38]. Again, the region located at lower potentials corresponds to adsorption-desorption processes of weakly adsorbed hydrogen (UPD of H). On the other hand, the butterfly region observed over the 0.60-0.90 V range, as argued by most authors, corresponds to reversible adsorption-desorption of OH^- ions [31, 37-39] (for more details see section 2.4 of Chapter 2).

The mean electric charge measured between 0.06 and 0.90 V, after subtracting the double-layer charge contribution, as before, is 268 μC cm^{-2}, as provided by the results of Morallon et al. [36]. The above charge is the sum of 112 μC cm^{-2}, corresponding to the first, low potential zone and 156 μC cm^{-2}, corresponding to the high potential, "butterfly" region (0.60-0.90 V). Thus, the above charges give a maximum coverage by UPD H of about 0.46 of a monolayer of H and that corresponding to OH species of 0.64 of an equivalent monolayer of H. However, somewhat different mean charge values have also been reported for this surface [29, 37].

5.5.2 Pt(100), (110) and (511) surfaces

The voltammogram of the Pt(100) surface is characterised by the presence of four reversible current peaks at: 0.28, 0.39, 0.47 and 0.56 V, as shown e.g. in refs. 31, 36-38. Two peaks observed at lower potentials were assigned by Morallon et al. [36] to weakly adsorbed H (possibly on steps, as suggested by Marinkovic et al. [37]) and two others, located at higher potentials, to strongly bonded H (probably on (100) terrace sites [37]). On the other hand, in their recent work, Markovic et al. [38], assigned the peaks located at potentials positive to 0.45 V to formation of reversibly and irreversibly deposited OH types of species on the Pt surface (see section 2.4 of Chapter 2 for more details). The mean electric charge measured between 0.14 and 0.62 V, after subtracting the double-layer charge contribution, is 207 μC cm^{-2} [36], which very well matches the geometrically expected value of 209 μC cm^{-2} for monolayer coverage on the (1x1) surface structure.

The voltammogram of a Pt(110) surface is characterised by the presence of one principal, reversible adsorption current peak, centred at 0.32 V, as shown e.g. in refs. 31, 36-38. The mean electric charge measured between 0.05 and 0.50 V, after subtracting, as usual, the double-layer charge contribution, is 220 μC cm^{-2}, as found by Marinkovic et al.

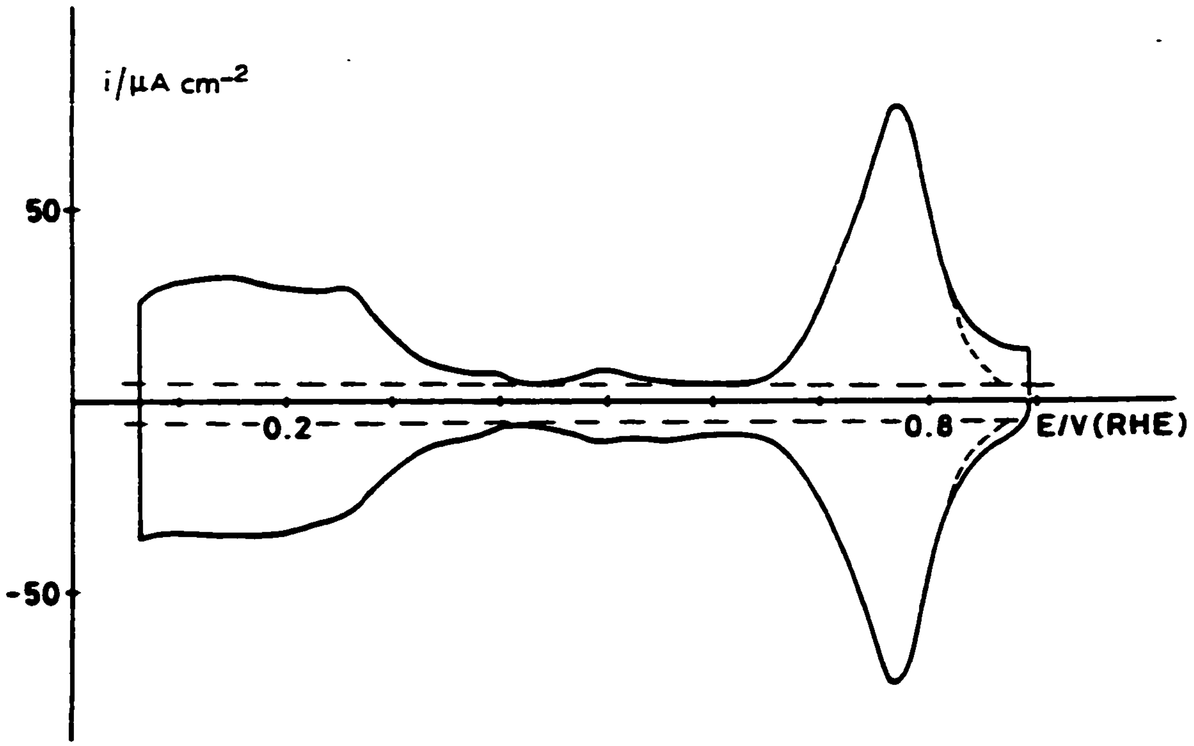

Fig. 5.5 Cyclic voltammogram of a well-ordered Pt(111) surface in contact with 0.1 mol dm^{-3} NaOH after cooling in air, recorded at a sweep rate of 50 mV s^{-1} [36].

[37]. This charge is much greater than the geometrically expected value of 147 μC cm^{-2}, corresponding to the (1x1) surface structure. This result indicates that the charge integrated over 0.05-0.50 V comprises two components: one for UPD of H and the other for OH adsorption-desorption processes [38]. However, a smaller mean charge of 140-145 μC cm^{-2} has also been reported [36] for the Pt(110) surface in aqueous NaOH.

Finally, the voltammogram of the Pt(511) surface in 0.1 mol dm^{-3} NaOH is characterised by the presence of one principal, reversible adsorption peak, centred at 0.42 V, on the positive- and at 0.37 V on the negative-going scan [31], corresponding to adsorption on the (100) terraces of the stepped surface.

5.6 Displacement chemisorption charge transients

As was already mentioned in section 2.6 of Chapter 2, the technique for adsorption charge displacement originated from the discovery of the "anodic H displacement effect" by Conway et al. [5, 40, 41]. The latter effect is based on the anodic displacement of H, chemisorbed on polycrystalline Pt, by addition of a competing adsorbent (in their paper CH_3CN) to an initially CH_3CN-free, H_2SO_4 solution, in the H UPD region.

Based on the above-mentioned method, a related electrochemical procedure for examination of adsorbed species, the "CO adsorption replacement technique", was developed by Clavilier and co-workers [24, 34, 42]. It allowed electrochemical characterisation of the nature of the species present on the Pt surface by measuring the current transient that arises upon adsorption of carbon monoxide on an initially clean electrode surface, being in contact with the electrolyte solution and maintained at a constant potential. The strongly adsorbed CO replaces any previously adsorbed species on the surface, such as H or/and HSO_4^- or ClO_4^- ions. Thus, below a potential at which CO starts being oxidised to CO_2, it could be used as a neutral probe in the replacement process. The above method has been employed to study the region of UPD of H at low-index and stepped surfaces of Pt in various electrolyte media, such as: H_2SO_4 [24], $HClO_4$ [34] and also in $H_2C_2O_4$, NaCl, CH_3COONa, and with KBr added to an $HClO_4$ supporting electrolyte solution [43]. This procedure has been applied in the present work.

The basis of the procedure is that most electrosorbed species are chemisorbed with a substantial extent of charge transfer related to their "electrosorption valency". Then, when they are competitively desorbed by a neutral molecule, CO, the desorption must take place by (a measurable) charge-transfer in a direction opposite to that accompanying the prior adsorption process. This replacement process, giving rise to transient currents, can be schematically represented by the following equation:

$$\mathrm{Pt}-\mathrm{X}_{\mathrm{ads}}+(\mathrm{CO})_{\mathrm{sol}} \xrightarrow{E=E_{\mathrm{ads}}} \mathrm{Pt}-\mathrm{CO}_{\mathrm{ads}}+\mathrm{X}^{z\pm} \pm z e^{-} \qquad (5.1)$$

where charged species released to the solution ($X^{z\pm}$) may be regarded as a reaction product. X represents the species present in a chemisorbed state on the platinum electrode surface.

As an example from ref. 24, Fig. 5.6 shows current-density vs. time transients corresponding to CO adsorption experiments on a well-ordered Pt(111) electrode in 0.5 mol dm^{-3} H_2SO_4, recorded at two potentials: 0.08 V (b) and 0.50 V (c) vs. RHE. The adsorption current transient recorded at 0.08 V is anodic (+161 $\mu C\ cm^{-2}$) while that obtained at 0.50 V is cathodic (-92 $\mu C\ cm^{-2}$), which clearly indicates that the nature of the species being replaced by CO is different at these two potentials. Thus, at 0.08 V, H becomes desorbed in an *anodic* oxidation process, as in refs. 5, 40 and 41. Correspondingly, introduction of CO at 0.50 V leads to *cathodic* desorption of HSO_4^- species from the Pt surface. From integration of the charge under the current transient, the maximum H coverage near the onset of the HER is estimated to be near 2/3 of an H monolayer for the well-ordered Pt(111). Accordingly, the maximum coverage by HSO_4^- (estimated from the cathodic current transient recorded at 0.50 V) comes out to be about 1/3 of an equivalent monolayer of adsorbed H.

By an interpolation procedure, a plot of charge transient densities, $q_t(E)$, as a function of potential allows estimation of the "potential of zero total charge" (*PZTC*), the potential corresponding to zero desorption charge [$q_t(E_{ads})=0$], as shown in Fig. 5.7. Furthermore, integration of the charges under the voltammograms compares very well with those obtained from the charge transient differences, q_t, expressed by equation 5.2:

$$q_t = q_t(E_{0.08V}) - q_t(E_{ads}) \qquad \textbf{(5.2)}$$

where $q_t(E_{0.08V})$ corresponds to the maximum charge of the charge transient recorded for H displacement and $q_t(E_{ads})$ to the charge derived from the CO adsorption transient recorded at any potential more positive than 0.08 V [24].

An alternative adsorbate replacement agent to CO was found to be iodine [42, 44]. The application of iodine as a neutral probe has one significant advantage over CO - it allows the adsorbate replacement measurements to be conducted up to more positive potentials, thus enabling it to be applied e.g. to Pt(111) in $HClO_4$ solutions; otherwise, at such potentials, CO can become electro-oxidised at Pt.

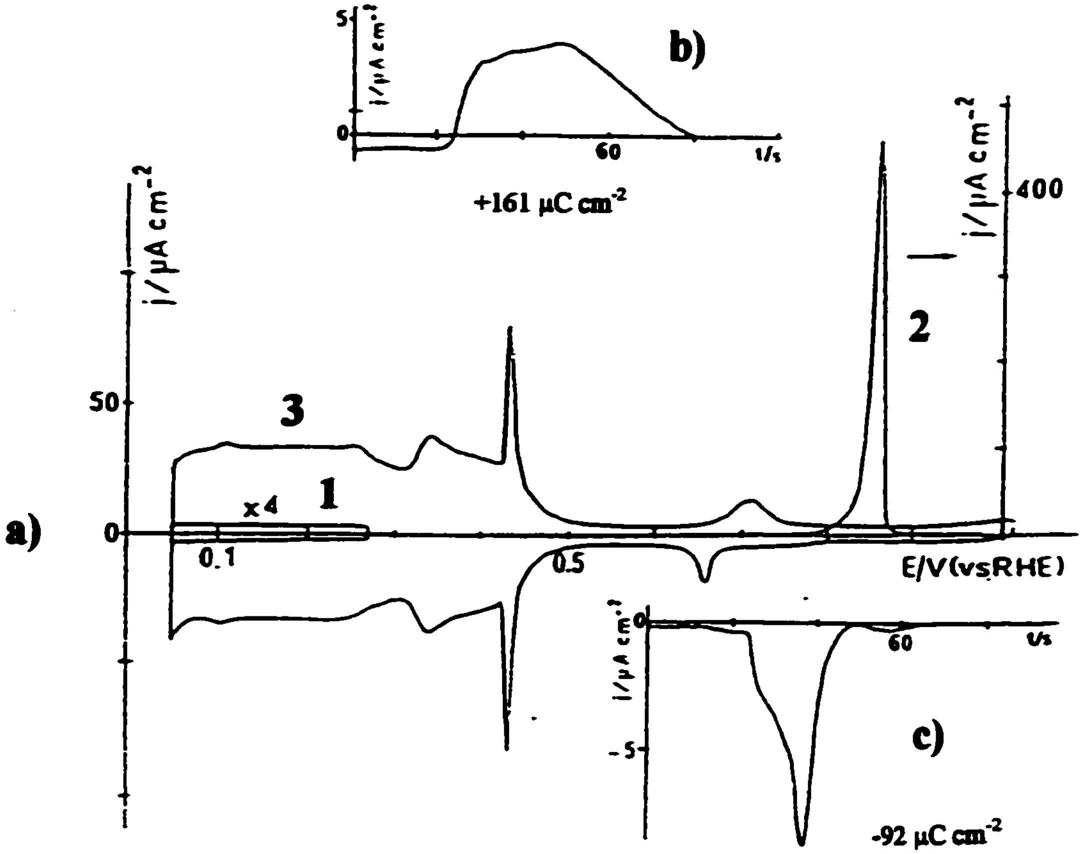

Fig. 5.6 (a) Voltammograms for a well-ordered Pt(111) electrode in 0.5 mol dm^{-3} H_2SO_4: curve 1, control measurement of the surface blocking by adsorbed CO (50 mV s^{-1}, sensitivity increased by a factor of 4); curve 2, stripping of adsorbed CO (20 mV s^{-1}); curve 3, recovery of the initial voltammetric profile (50 mV s^{-1}). (b) and (c): Current density vs. time transients for E_{ads}=0.08 and 0.50 V, respectively [24].

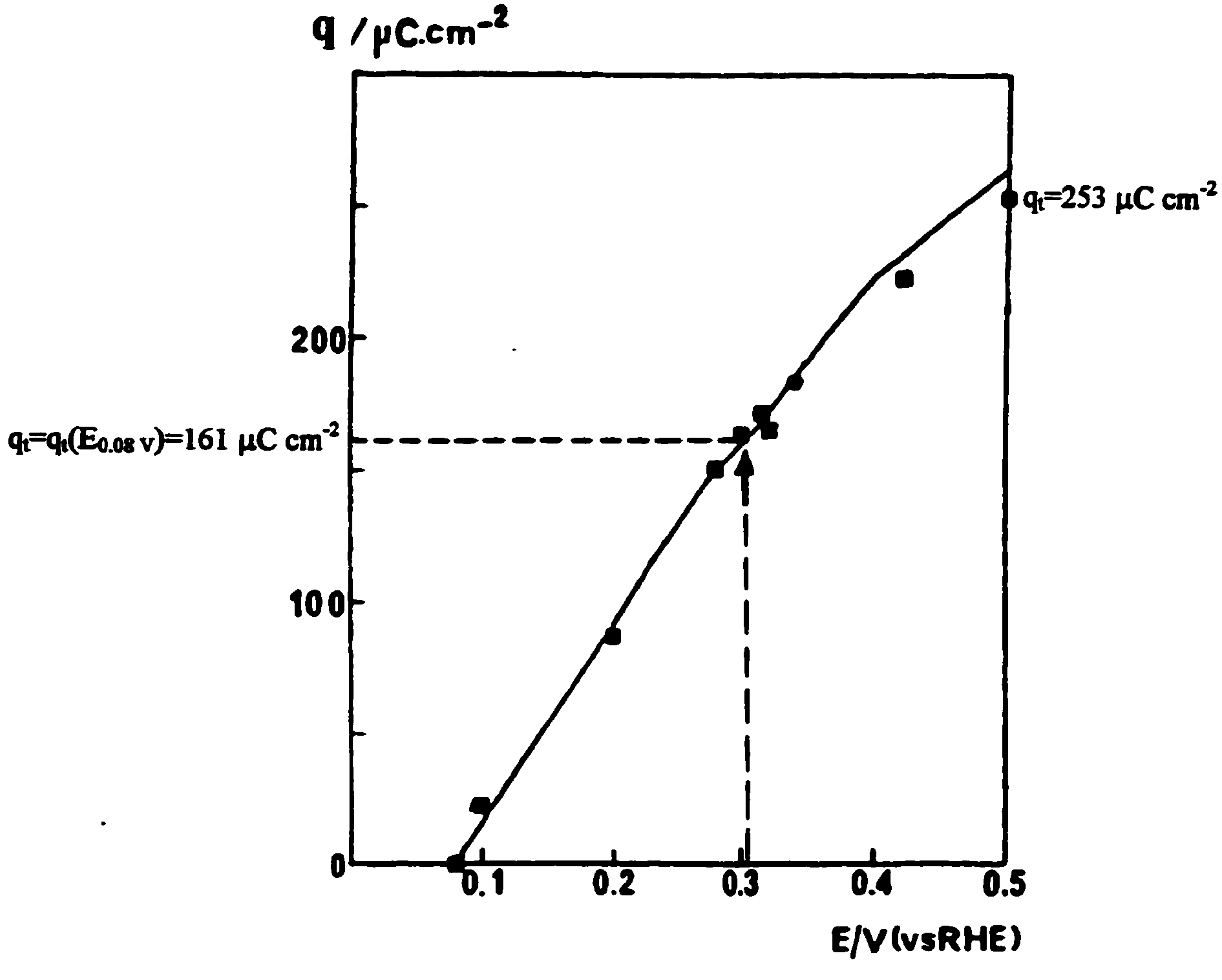

Fig. 5.7 Plots of the charge densities, q, obtained from voltammogram integration (solid line) and those obtained from transient charge differences (q_t) vs. electrode potential for well-ordered Pt(111) surface, cooled in air. The experimentally determined potential of zero total charge (*PZTC*) for this surface is indicated [24].

5.7 References

1. J. Clavilier, R. Faure, G. Guinet and R. Durand, *J. Electroanal. Chem.*, 1980, **107**, 205.
2. J. Clavilier, *J. Electroanal. Chem.*, 1980, **107**, 211.
3. J. Clavilier, R. Durand, G. Guinet and R. Faure, *J. Electroanal. Chem.*, 1981, **127**, 281.
4. J. Clavilier, D. Armand and B.L. Wu, *J. Electroanal. Chem.*, 1982, **135**, 159.
5. H.A. Kozlowska, B.R. MacDougall and B.E. Conway, *J. Electroanal. Chem.*, 1972, **39**, 287.
6. S. Morin and B.E. Conway, *J. Electroanal. Chem.*, 1994, **376**, 135.
7. F.G. Will and C.A. Knorr, *Z. Elektrochem.*, 1960, **64**, 258.
8. H. Angerstein-Kozlowska, B.E. Conway and W.B.A. Sharp, *J. Electroanal. Chem.*, 1973, **43**, 9.
9. J. Clavilier, A. Rodes, K. El Achi and M.A. Zamakhchari, *J. Chim. Phys.*, 1991, **88**, 1291.
10. D. Aberdam, C. Corotte, D. Dufayard, R. Durand, R. Faure and G. Guinet, "*Le vide, les couches minces*" (Suppl. Proc. 4 th Int. Conf. Solid Surfaces, Cannes), 1980, 622.
11. K. Itaya, S. Sugawara, K. Sashikata and N. Furuya, *J. Vac. Sci. Technol. A*, 1990, **8**, 515.
12. F.T. Wagner and P.N. Ross, *J. Electroanal. Chem.*, 1983, **150**, 141.
13. F.T. Wagner and P.N. Ross, *J. Electroanal. Chem.*, 1988, **250**, 301.
14. D.A. Scherson and D.M. Kolb, *J. Electroanal. Chem.*, 1984, **176**, 353.

15. A.M. Funtikov, U. Stimming and R. Vogel, *J. Electroanal. Chem.*, 1997, **428**, 147.

16. J. Clavilier, K. El Achi, M. Petit, A. Rodes and M.A. Zamakhchari, *J. Electroanal. Chem.*, 1990, **295**, 333.

17. S. Thomas, Y.E. Sung, H.S. Kim and A. Wieckowski, *J. Phys. Chem.*, 1996, **100**, 11726.

18. B.E. Conway and G. Jerkiewicz, *Electrochim. Acta*, 2000, **45**, 4075.

19. G. Jerkiewicz and A. Zolfaghari in Proc. Symposium on *"Electrochemistry and Materials Science of Cathodic H Absorption and Adsorption"*, B.E. Conway and G. Jerkiewicz (Eds.), The Electrochemical Society, Pennington, NJ, 1995, **94-21**, 31.

20. C.L. Scortichini, F.E. Woodward and C.N. Reilley, *J. Electroanal. Chem.*, 1982, **139**, 265.

21. F.T. Wagner and P.N. Ross, *Surf. Sci.*, 1985, **160**, 305.

22. A. Rodes, K. El Achi, M.A. Zamakhchari and J. Clavilier, *J. Electroanal. Chem.*, 1990, **284**, 245.

23. T. Iwasita, F.C. Nart, A. Rodes, E. Pastor and M. Weber, *Electrochim. Acta*, 1995, **40, No.1**, 53.

24. J. Clavilier, J.M. Orts, R. Gomez, J.M. Feliu and A. Aldaz in *Proc. Symposium on "Electrochemistry and Materials Science of Cathodic H Absorption and Adsorption"*, B.E. Conway and G. Jerkiewicz (Eds.), The Electrochemical Society, Pennington, N.J., 1995, **94-21**, 167.

25. D. Armand and J. Clavilier, *J. Electroanal. Chem.*, 1989, **263**, 109.

26. J. Clavilier, D. Armand, S.G. Sun and M. Petit, *J. Electroanal. Chem.*, 1986, **205**, 267.

27. M.A. Climent, M.J. Valls, J.M. Feliu, A. Aldaz and J. Clavilier, *J. Electroanal. Chem.*,

1992, **326**, 113.

28. S. Motoo and N. Furuya, *J. Electroanal. Chem.*, 1984, **172**, 339.

29. E. Morallon, J.L. Vasquez and A. Aldaz, *J. Electroanal. Chem.*, 1992, **334**, 323.

30. K. Al Jaaf-Golze, D.M. Kolb and D.A. Scherson, *J. Electroanal. Chem.*, 1986, **200**, 353.

31. H. Kita, S. Ye, A. Aramata and N. Furuya, *J. Electroanal. Chem.*, 1990, **295**, 317.

32. J. Clavilier, K. El Achi and A. Rodes, *Chem. Phys.*, 1990, **141**, 1.

33. D. Armand and J. Clavilier, *J. Electroanal. Chem.*, 1989, **270**, 331.

34. J. Clavilier, R. Albalat, R. Gomez, J.M. Orts, J.M. Feliu and A. Aldaz, *J. Electroanal. Chem.*, 1992, **330**, 489.

35. N.M. Markovic, N.S. Marinkovic and R.R. Adzic, *J. Electroanal. Chem.*, 1988, **241**, 309.

36. E. Morallon, J.L. Vasquez and A. Aldaz, *J. Electroanal. Chem.*, 1990, **288**, 217.

37. N.S. Marinkovic, N.M. Markovic and R.R. Adzic, *J. Electroanal. Chem.*, 1992, **330**, 433.

38. N.M. Markovic, S.T. Sarraf, H.A. Gasteiger and P.N. Ross, Jr., *J. Chem. Soc., Faraday Trans.*, 1996, **92**, 3719.

39. D.M. Drazic, A.V. Tripkovic, K.D. Popovic and J.D. Lovic, *J. Electroanal. Chem.*, 1999, **466**, 155.

40. B. MacDougall, B.E. Conway and H.A. Kozlowska, *J. Electroanal. Chem.*, 1971, **32**, App. 15.

41. B.E. Conway, B. MacDougall and H.A. Kozlowska, *J. Chem. Soc., Faraday Trans. I*, 1972, **68**, 1566.

42. J. Clavilier, R. Albalat, R. Gomez, J.M. Orts and J.M. Feliu, *J. Electroanal. Chem.*, 1993, **360**, 325.

43. J.M. Orts, R. Gomez, J.M. Feliu, A. Aldaz and J. Clavilier, *Electrochim. Acta*, 1994, **39, No.11/12**, 1519.

44. E. Herrero, J.M. Feliu, A. Wieckowski and J. Clavilier, *Surf. Sci.*, 1995, **325**, 131.

Chapter 6

Results and Discussion

6.1 Adsorption behaviour of G^+, DMG^+, AA^+ and U in relation to co-adsorption of HSO_4^- and other anions, and to UPD of H at various Pt single-crystal planes

This section of Chapter 6 is devoted to cyclic voltammetric characterisation of the process of adsorption of the resonant guanidonium cation and its structure-related analogues (N,N-dimethylguanidonium, acetamidonium and urea) on polycrystalline and four, well-ordered, single-crystal surfaces of Pt. All the experimental and other related details were given in Chapters 3 and 4.

Study of the surface chemistry of electrode processes and electrosorption, from the modern point of view, requires systematic, comparative experiments on well-ordered surfaces (in the present work, of Pt) having different but related lattice orientations, e.g. the principal index planes and derived stepped surfaces. Additionally, various concentrations of selected, structurally-related adsorbates should be studied in conjunction with supporting electrolytes containing different simple anions. Such experiments provide the structure of the present research. However, purely electrochemical experimentation is rarely sufficient to provide chemical structural details of surface-electrochemical processes. Hence, in the present work, complementary FTIR spectroscopic studies have been applied to the elucidation of the 2-dimensional interactions between HSO_4^- and G^+, and U. The latter aspects of the research are presented and discussed in section 6.3 of this thesis.

The combination of such experiments leads unavoidably to a panoply of results between which useful comparisons can be made and contrasts drawn. It is therefore useful to recall the summary of systems studied and the respective conditions involved, as given in section 3.2 of Chapter 3. The reader should also note, in the material which follows, that in the cases where voltammograms were found to be quite similar for two analogous adsorbates, e.g. G^+ and DMG^+, only the voltammogram for one type is actually presented in order to maintain brevity in the description of the results and reference to figure numbers. However, for the above types of example, comparisons and similarities between such cases are recorded in the text.

6.1.1 Adsorption behaviour at polycrystalline Pt

The purpose of this section of the work was simply to provide a background to the full studies at selected single-crystal Pt surfaces and thus to recognise, by contrast, the surface specific adsorption effects that arise at the latter type of Pt surfaces. At polycrystalline surfaces, a variety of poorly defined effects can arise owing to complexities and variations of the surfaces but it is not one of the purposes of the work described in this thesis to address such aspects.

6.1.1.1 Behaviour in H_2SO_4

The adsorption behaviour of the guanidonium cation (G^+), at three concentrations of G^+ in aq. 0.5 mol dm^{-3} H_2SO_4 at a Pt poly-oriented single-crystal, which exhibits mainly (110) and (100) facets, is illustrated by the series of voltammograms shown in Fig. 6.1. A major effect is revealed as a shift of the current-potential profile towards the

H_2 reversible potential (RHE) at the (100) plane facets, especially observable at the highest concentration, 3×10^{-3} mol dm^{-3}, of G^+ in solution. A significant increase of response current-density in this potential region is also observed. Conversely, only small changes are detected over the potential ranges corresponding to the (110) and (111) surface orientations.

On the contrary, in the presence of the N,N-dimethylguanidonium cation DMG^+, which is closely related in structure to G^+, only minor effects are observed over potential ranges corresponding to either of the two, principally exposed, surface orientations. However, some small but observable blocking of adsorption sites on both surfaces can be observed, especially at higher concentrations (6×10^{-4} mol dm^{-3}) of DMG^+; see Fig. 6.2 below.

The corresponding cyclic voltammetric behaviour of the acetamidonium cation at polycrystalline Pt, at two concentrations, is shown in Fig. 6.3. Again, as for G^+, the presence of AA^+ leads to a significant shift of the voltammetric profile towards the RHE potential, over the range corresponding to the (100) plane. Moreover, a substantial increase of voltammetric charge over a potential range *ca.* 0.20-0.45 V/RHE, is observed.

In relation to the effects demonstrated with G^+ at Pt, it was important to establish if there were significant effects of G^+ at a "non-catalytic" surface, e.g. of Au, where no UPD of H arises. An experiment conducted with 6×10^{-4} mol dm^{-3} G^+ in 0.5 mol dm^{-3} H_2SO_4 at a clean, polycrystalline Au electrode gave no charge-transfer (chemisorption) currents in the overall cyclic voltammogram nor any continuous Faradaic reduction or oxidation currents, over a range of 0.07 to 1.20 V, RHE (see Fig. 6.4).

6.1.1.2 Behaviour in $HClO_4$

A cyclic voltammogram for a polycrystalline Pt electrode in 0.1 mol dm^{-3} $HClO_4$, over the H UPD range, exhibits two reversible adsorption states. The first state, centred at *ca.* 0.13 V, again corresponds to adsorption of H on (110) sites and a second, broad peak, centred at *ca.* 0.30 V, to adsorption of H on sites of (100) geometry (see Fig. 6.5 below).

The specific difference between the adsorption effects of G^+ (at two concentrations) in 0.1 mol dm^{-3} $HClO_4$ at Pt(100) and (110) surfaces is again nicely illustrated by the behaviour at polycrystalline Pt in Fig. 6.5. Thus, only over the (100) region does G^+ have substantial observable effects; there being practically none over the (110) region.

The adsorption behaviour of DMG^+ closely resembles the above-described behaviour of the G^+ molecule-ion and so does that of AA^+ (Fig. 6.6). However, in the latter case, the new peaks observable over the (100) adsorption region, are much sharper and the shift of the current-potential profile towards the RHE potential is much more pronounced than in the first two cases, viz. G^+ and DMG^+.

6.1.1.3 Behaviour in NaOH

A cyclic voltammogram for polycrystalline Pt in 0.1 mol dm^{-3} NaOH, over the potential range for UPD of H, again exhibits two adsorption states. The first, quite reversible state, centred at *ca.* 0.27 V, corresponds to adsorption on (110) sites and a second, less reversible peak, centred on the negative-going sweep at *ca.* 0.37 V, can be assigned to adsorption on sites of (100) geometry (see Fig. 6.7 below).

The adsorption behaviour of guanidine, at three concentrations of G (or G^+, since guanidine, with $pK_a \approx 13.6$ [1], remains appreciably, *ca.* 80%, ionised in 0.1 mol dm^{-3}

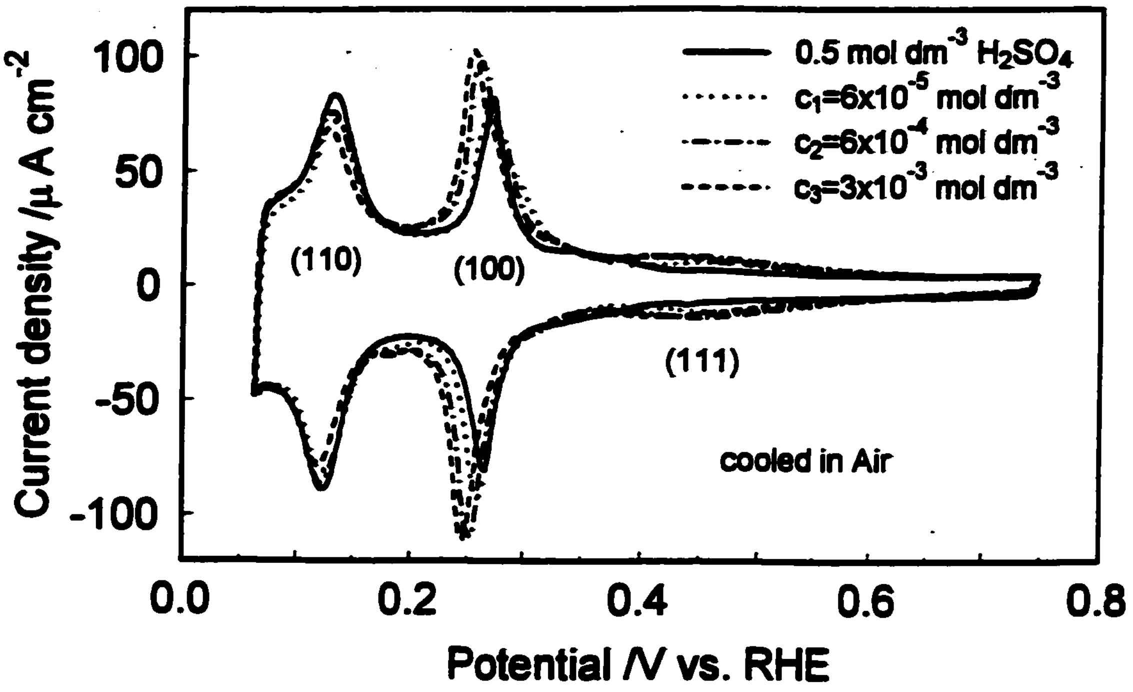

Fig. 6.1 Cyclic voltammograms for polycrystalline Pt in 0.5 mol dm^{-3} H_2SO_4 at a sweep-rate of 0.050 V s^{-1} and in the presence of G$^+$ at the three concentrations indicated; voltammograms were recorded on the third cycle.

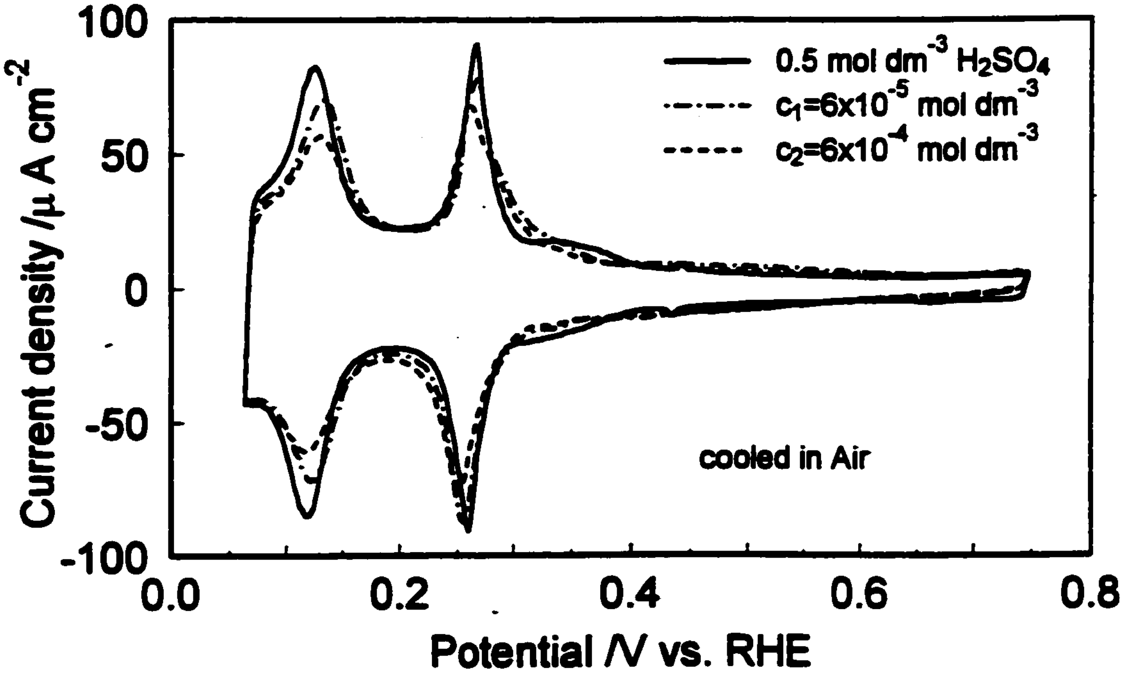

Fig. 6.2 Cyclic voltammograms for polycrystalline Pt in 0.5 mol dm^{-3} H_2SO_4 at a sweep-rate of 0.050 V s^{-1} and in the presence of DMG$^+$ at the two concentrations indicated; voltammograms were recorded on the third cycle.

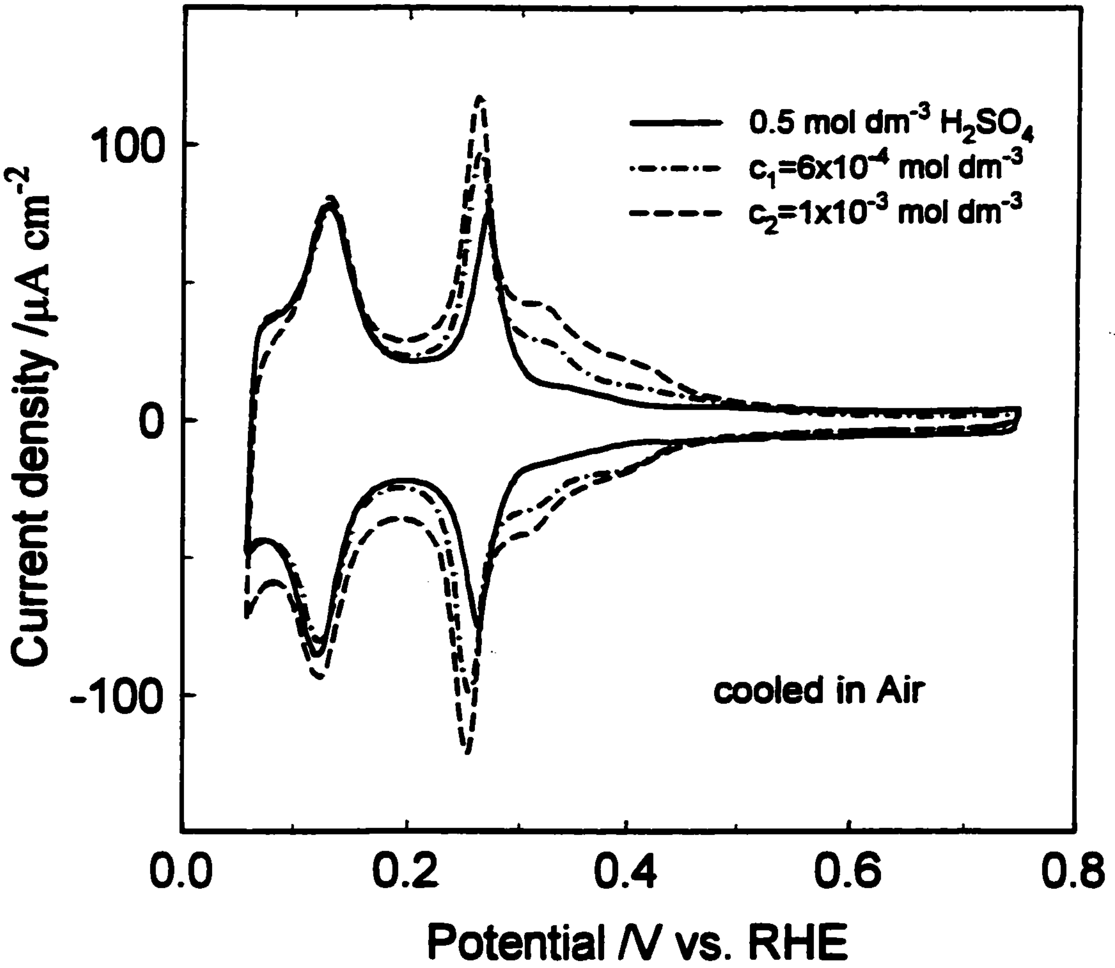

Fig. 6.3 Cyclic voltammograms for polycrystalline Pt in 0.5 mol dm^{-3} H_2SO_4 at a sweep-rate of 0.050 V s^{-1} and in the presence of AA$^+$ at the two concentrations indicated; voltammograms were recorded on the third cycle.

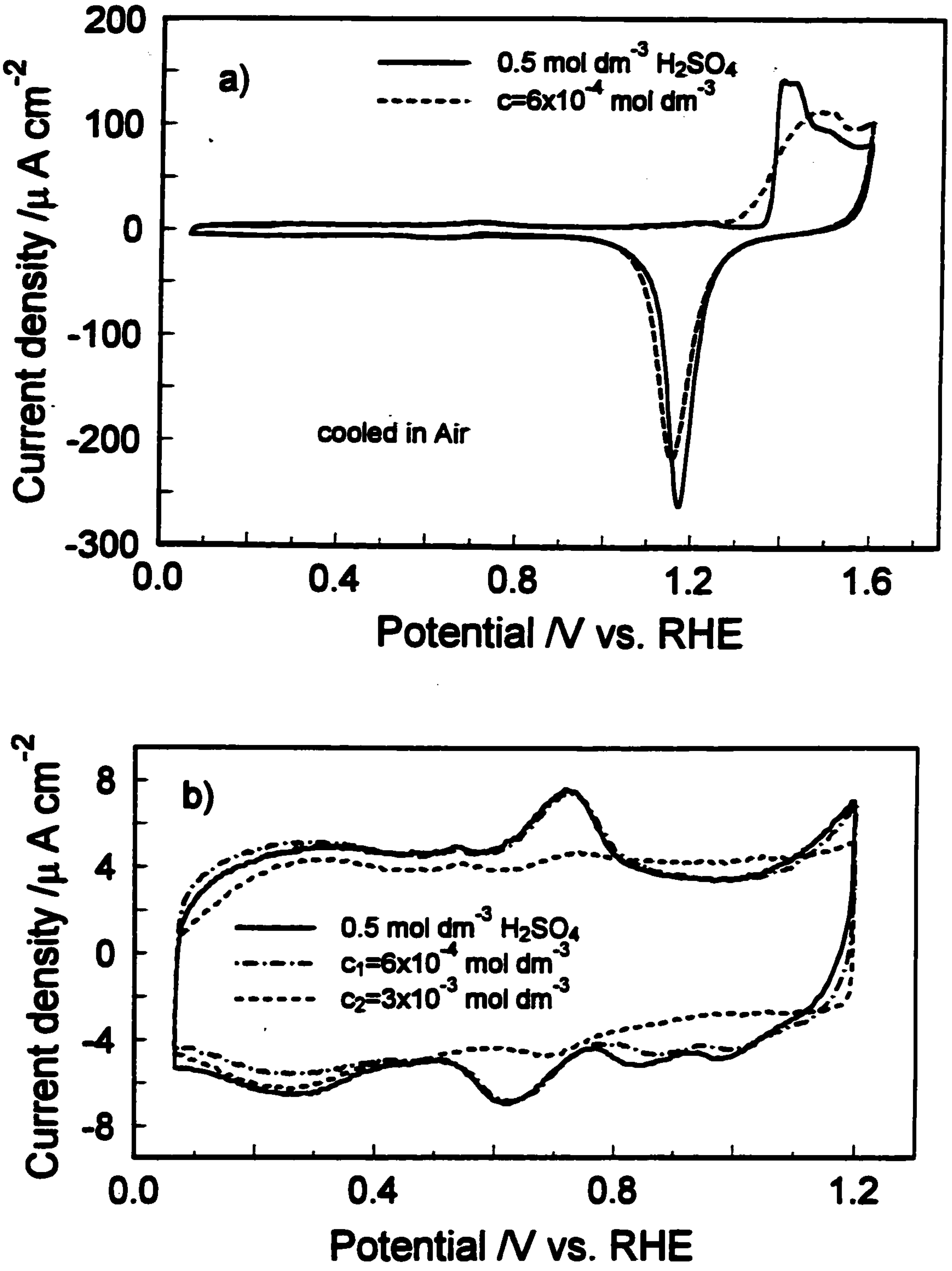

Fig. 6.4 a) Cyclic voltammograms for polycrystalline Au in 0.5 mol dm^{-3} H_2SO_4 at a sweep-rate of 0.050 V s^{-1} and in the presence of G^+ at the concentration indicated; voltammograms were recorded on the third cycle; b) As in (a), but double-layer charging region shown, at the two concentrations of G^+, indicated.

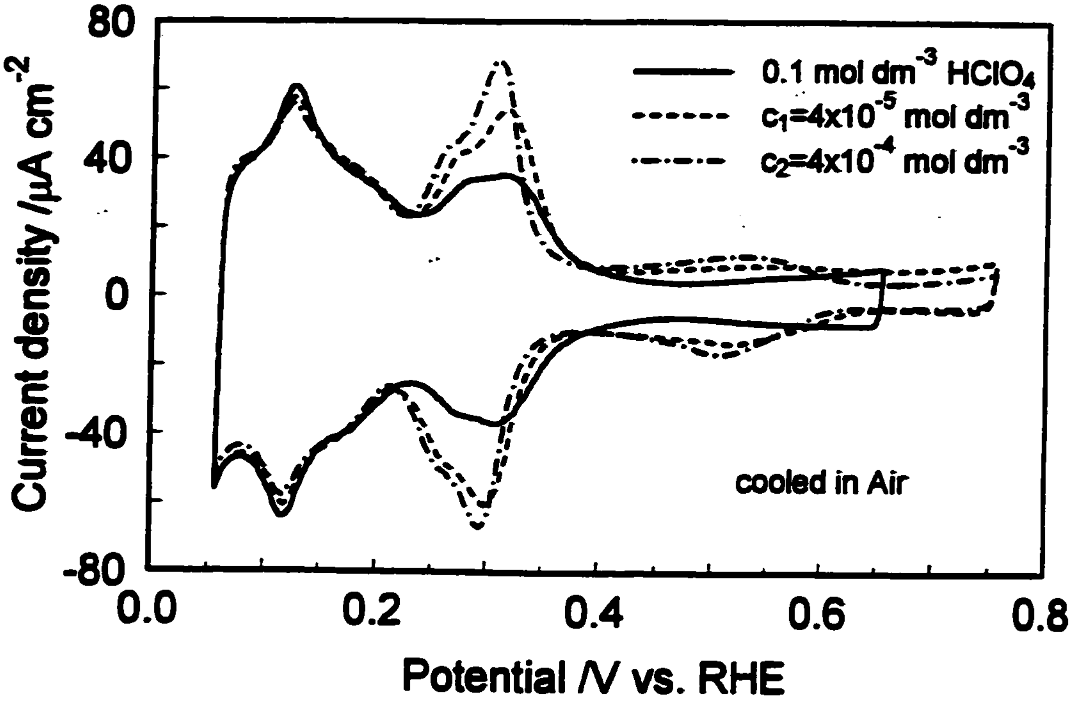

Fig. 6.5 Cyclic voltammograms for polycrystalline Pt in 0.1 mol dm^{-3} HClO$_4$ at a sweep-rate of 0.050 V s^{-1} and in the presence of G$^+$ at the two concentrations indicated; voltammograms were recorded on the third cycle.

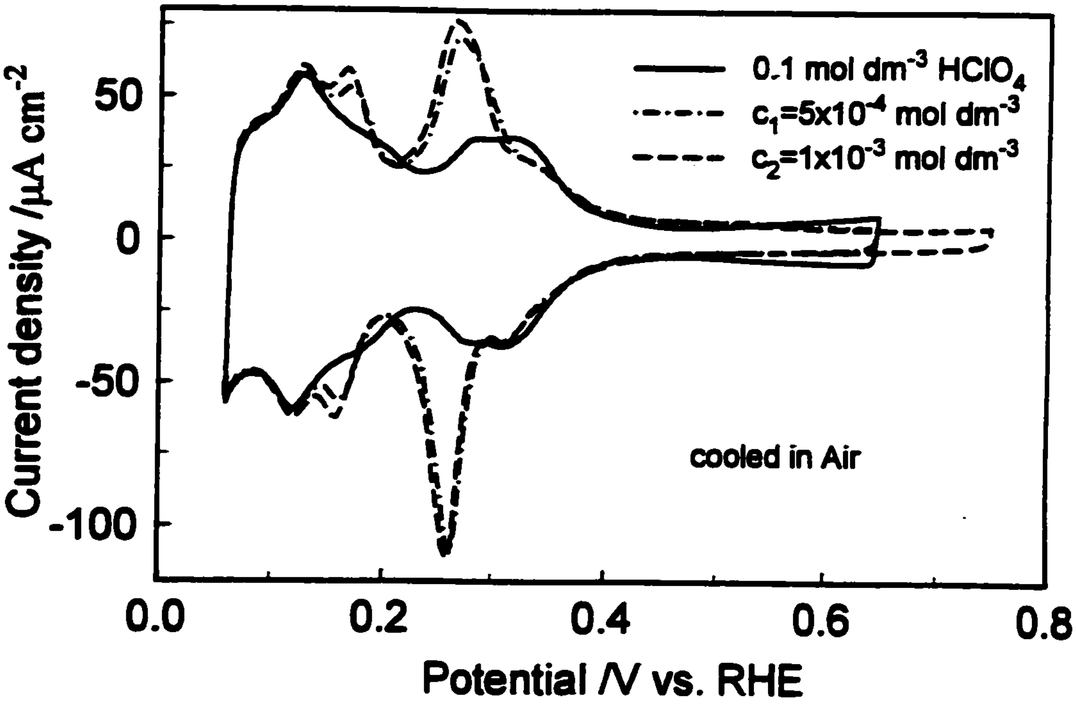

Fig. 6.6 Cyclic voltammograms for polycrystalline Pt in 0.1 mol dm^{-3} HClO$_4$ at a sweep-rate of 0.050 V s^{-1} and in the presence of AA$^+$ at the two concentrations indicated; voltammograms were recorded on the third cycle.

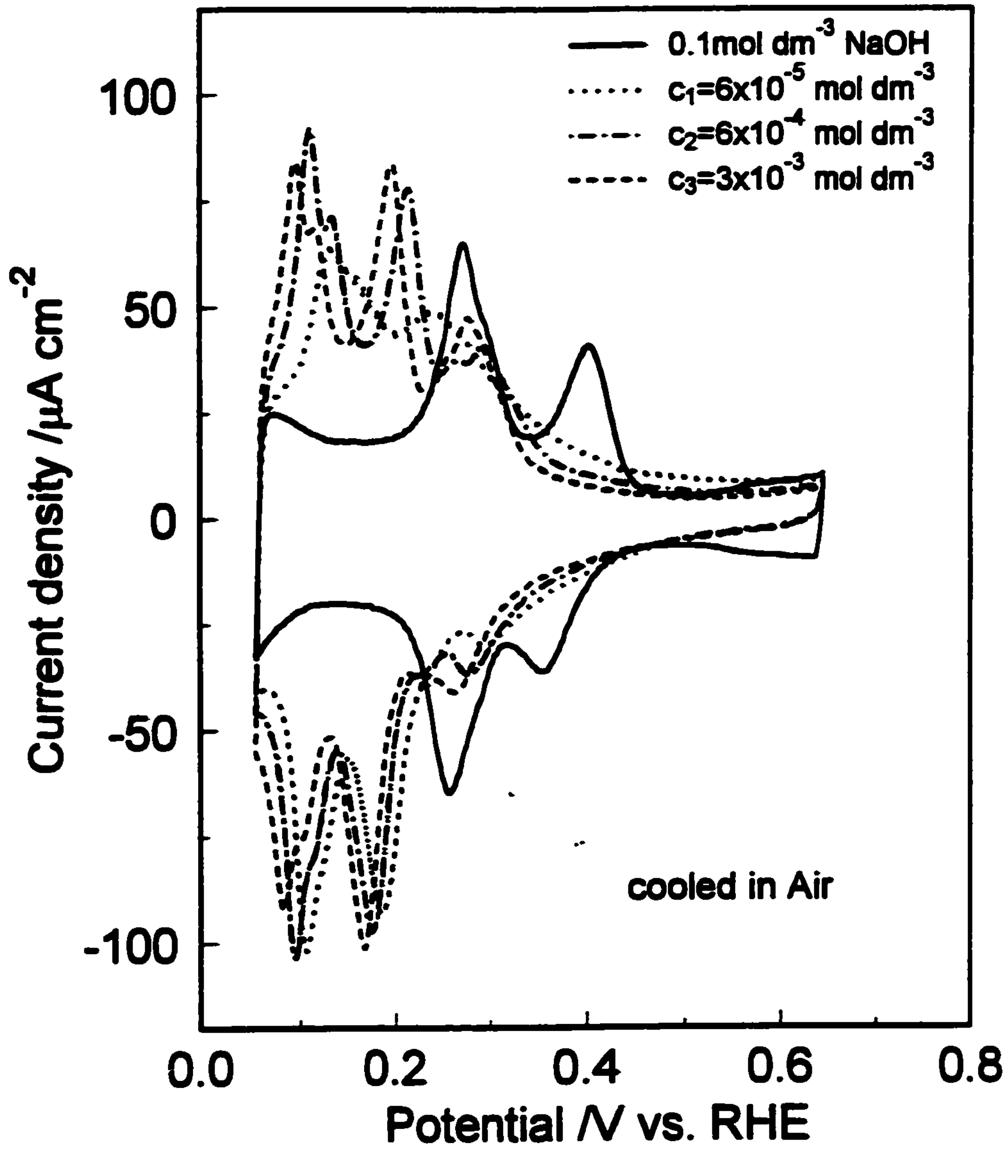

Fig. 6.7 Cyclic voltammograms for polycrystalline Pt in 0.1 mol dm^{-3} NaOH at a sweep-rate of 0.050 V s^{-1} and in the presence of G^{+} (or G) at the three concentrations indicated; voltammograms were recorded on the third cycle.

NaOH solution) at polycrystalline Pt in 0.1 mol dm^{-3} NaOH, is illustrated by the voltammograms shown in Fig. 6.7. A major effect observed here is a shift of the current-potential profile towards the RHE potential at both (100) and the (110) planes, unlike the behaviour in H_2SO_4 and $HClO_4$ solutions. Moreover, a characteristic "squeezing" of the CV profiles on the potential axis results in an overall increase of current-density values in the voltammogram. Similar, although less pronounced, changes were recorded in the presence of DMG and AA. Note that pK_a values for these molecules appear to be unavailable.

6.1.2 Adsorption behaviour at the Pt(111) surface

6.1.2.1 Behaviour in H_2SO_4

The adsorption behaviour of G^+ (at three concentrations) at the Pt(111) surface in aq. 0.5 mol dm^{-3} H_2SO_4 is shown in Fig. 6.8 and is of particular interest. The phenomenology of the effects of G^+ at Pt(111) is characterised by the potential range for UPD of H being "squeezed" and also appreciably negatively shifted towards the RHE potential, as mainly observed on the negative-going sweep. The CV current-response is displaced from the HSO_4^- adsorption region and, from part of that due to UPD of H, split into two clear peaks, D_1 and D_2 (Fig. 6.8), the charges for which are equal (within 5%) to the charge displaced from the regions marked C_1 and C_2.

Over the return positive-going sweep, the UP-H ionisation profile is hardly changed until a potential of *ca.* 0.33 V is reached when passage of positive charge reappears in the HSO_4^- electrosorption region of the voltammogram. Striking effects are found in the presence of 6x10^{-4} mol dm^{-3} G^+, but the above behaviour is qualitatively the same for two other concentrations of G^+, $6x10^{-5}$ and $3x10^{-3}$ mol dm^{-3}. It has to be noted that, in a number of experiments, in addition to recording voltammograms on the third cycle, for the (111) and other Pt(hkl) surfaces studied, cycling was continued for up to 10 min. The voltammograms remained virtually superimposable (regardless of the concentration of G^+), indicating absence of effects of any accumulated impurities.

Based on the results shown in Fig. 6.8, it is seen that, in the presence of G^+, the potential for HSO_4^- desorption has been shifted appreciably (by about 200 mV) towards the RHE potential. Hence, there must exist an attractive (stabilising adsorption) interaction between the chemisorbed HSO_4^- and G^+ ions on the Pt surface.

Thus, it is suggested that, as oxidative desorption of H into solution becomes completed on the positive-going sweep, HSO_4^- and G^+ both become chemisorbed on the Pt(111) surface. In the adsorbed state, it is proposed[1] that a co-operative interaction (ion-pairing) between these two species arises on account of a chemical interaction (cation with a lone-pair donor), providing the basis of a mechanism for stabilisation of HSO_4^- ion adsorption (as shown in structure XI in section 6.2 later), corresponding to the observed (Fig. 6.8) anion-like shift of the H UPD process to less positive potentials, i.e. similar to that caused by adsorption of Cl^-, Br^- or I^- on UPD of H at Pt [2, 3], but for different reasons. However, unlike the latter anions, G^+ at $6x10^{-4}$ mol dm^{-3} leads to increase of the mean voltammetric charge by *ca.* 8% after subtracting the double-layer charge contribution (see Table 6.1, later).

The peaks D_1 and D_2, observed on the negative-going sweep, suggest that significant quantities of HSO_4^- and also of G^+ become desorbed over the potential range 0.27 →

---

[1] More direct support for this mechanism is given on a chemical-structure basis in section 6.3, where FTIR spectroscopic studies on HSO_4^- and G^+, and U adsorption, are described.

0.08 V, RHE, and remain desorbed on the return, positive-going sweep, over the UP-H ionisation range up to *ca.* 0.33 V. It is suggested that the first cathodic current peak on the negative-going sweep (Fig. 6.8) is partly due to HSO_4^-/G^+ desorption and the second (D_2) corresponds to a significant component of UPD of H (see the effects of CO described in section 6.4 later), shifted to less positive potentials by the displacement of the HSO_4^- region. Thus, a significant fraction of the adsorbed HSO_4^- and G^+ ions has to become desorbed before UP-deposited H atoms can be accommodated on the Pt surface.

The basis of the interpretation of the effect of G^+ in shifting the HSO_4^- part of the (111) profile is supported by the behaviour shown in Fig. 6.9. Here, voltammograms are shown for Pt(111) in 0.5 mol dm^{-3} H_2SO_4 containing G^+ at a concentration of $6x10^{-4}$ mol dm^{-3} taken from four, successively diminishing (curves 1 to 4), positive reversal potentials of the sweep. Evidently, only at the several potentials taken within the HSO_4^- adsorption region, down to the least positive potential of the HSO_4^- profile, does the G^+ give rise to the new peaks D_1 and D_2 on the cathodic scan. Reversal of the positive-going sweep just at the onset of the HSO_4^- electrosorption profile gives a negative-going j-V profile, almost typical of UPD of H at Pt(111). The above behaviour must therefore be associated with displacement of the HSO_4^- response to less positive potentials.

The comparative adsorption behaviour of DMG^+ (at two concentrations), at the Pt(111) surface in 0.5 mol dm^{-3} H_2SO_4 is shown in Fig. 6.10. Here, the charge passed over the HSO_4^- region is simply over a smaller potential range, thus “squeezing” the j *vs.* V profile with a sharpened region, positive to the H UPD potential range. The cathodic and anodic charges passed remain within 5% the same, and the UPD H region also remains almost unaltered.

These results provide a striking example of structure-specificity of the adsorption behaviour of two functionally similar compounds. In the presence of DMG^+, a related, although substantially weaker interaction with the Pt(111) surface-adsorbed HSO_4^- species than that for G^+, is observed. The implied weaker chemisorptive interaction for DMG^+ is probably related to steric effects, where the *gem*-methyl groups on one of the N atoms introduce geometrical difficulties and possibly steric repulsions influencing the accommodation of DMG^+ ions on the Pt surface (see section 6.2 of this Chapter and Table 6.1 for charge analysis, later).

Moreover, close similarities to the behaviour of DMG^+ in 0.5 mol dm^{-3} H_2SO_4 can be found for G^+ studied at a lower concentration of HSO_4^- anions (0.05 mol dm^{-3} H_2SO_4). In this case (see Fig. 6.11), desorption of the latter species takes place over a relatively higher positive potential range (*ca.* 0.5-0.3 V/RHE), compared with that in 0.5 mol dm^{-3} H_2SO_4 solution. This implies that interaction of the G^+ cations with the Pt(111) surface strongly depends on the chemisorptive behaviour of the co-adsorbed HSO_4^- anions on this surface.

The cyclic voltammograms for the Pt(111) surface in 0.5 mol dm^{-3} H_2SO_4 in the presence of AA^+ are qualitatively similar to those observed in the presence of DMG^+ (see Fig. 6.10). This suggests that, for AA^+ (as also for DMG^+) weaker chemisorptive interaction with HSO_4^- arises than that for the G^+ cation. Here, the ion-pairing between the AA^+ species and HSO_4^- is substantially diminished because the CH_3 group cannot carry a positive charge (as does $={}^+NH_2$ in protonated G). However, a dipole-dipole interaction between the $CH_3^{\delta+}$ and $OH^{\delta-}$ groups would be sufficient for existence of significant electrostatic interaction between the species on the surface (see also section

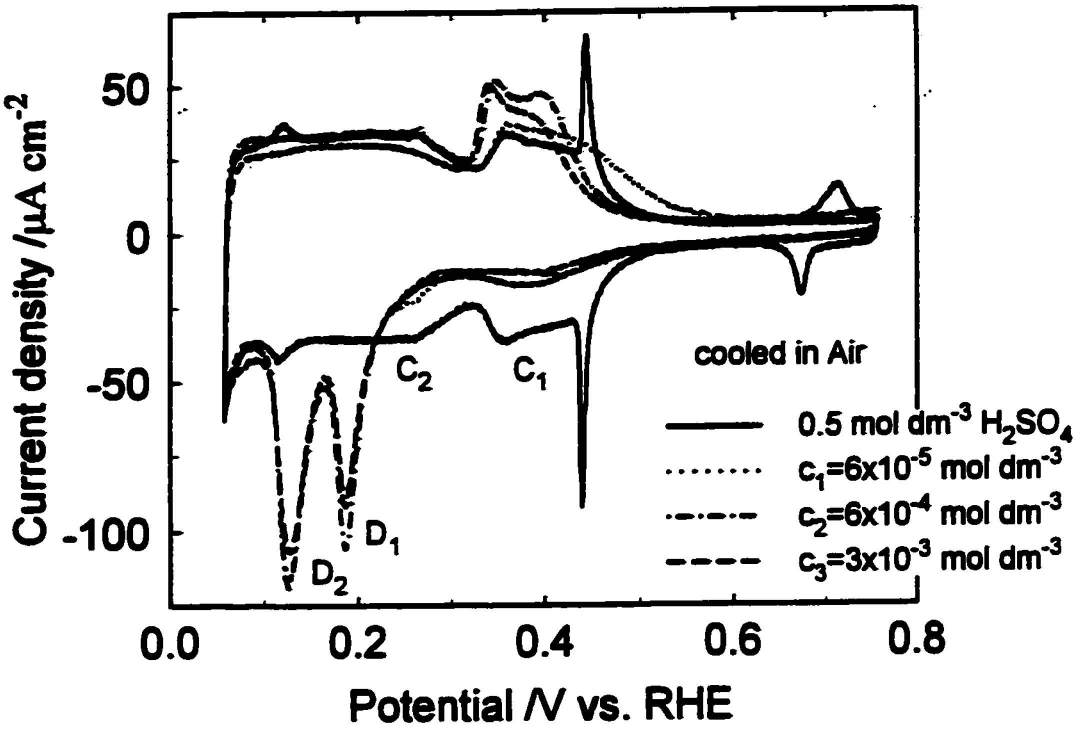

Fig. 6.8 Cyclic voltammograms for Pt(111) in 0.5 mol dm^{-3} H_2SO_4 at a sweep-rate of 0.050 V s^{-1} and in the presence of G$^+$ at the three concentrations indicated; voltammograms were recorded on the third cycle.

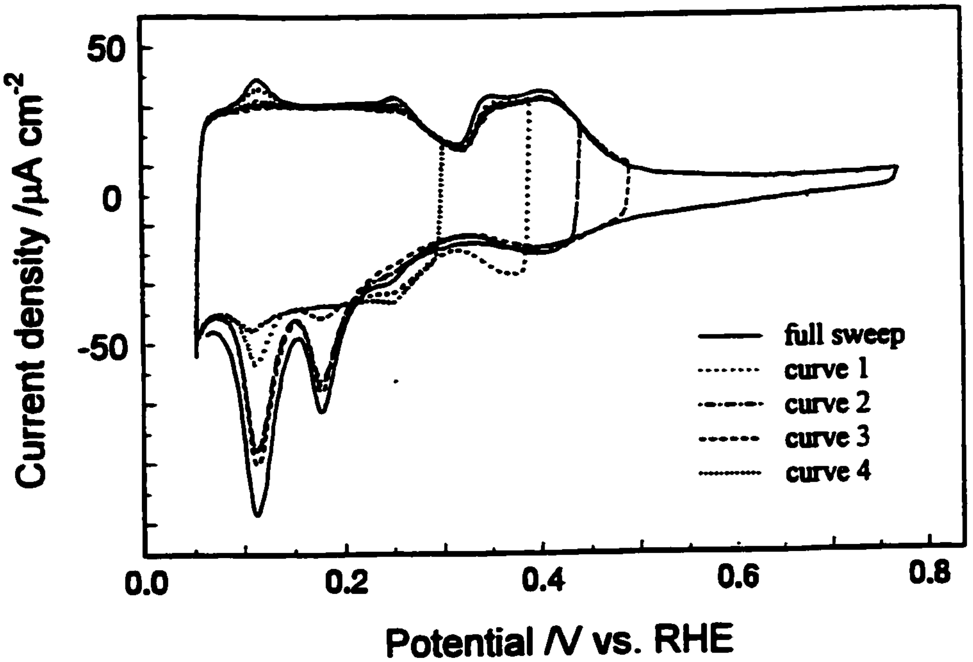

Fig. 6.9 Cyclic voltammograms for Pt(111) in 0.5 mol dm^{-3} H_2SO_4 at a sweep-rate of 0.050 V s^{-1} in the presence of 6x10^{-4} mol dm^{-3} G$^+$ showing the effect of progressively diminishing the positive potential limit of the sweep to four values (curves 1 to 4).

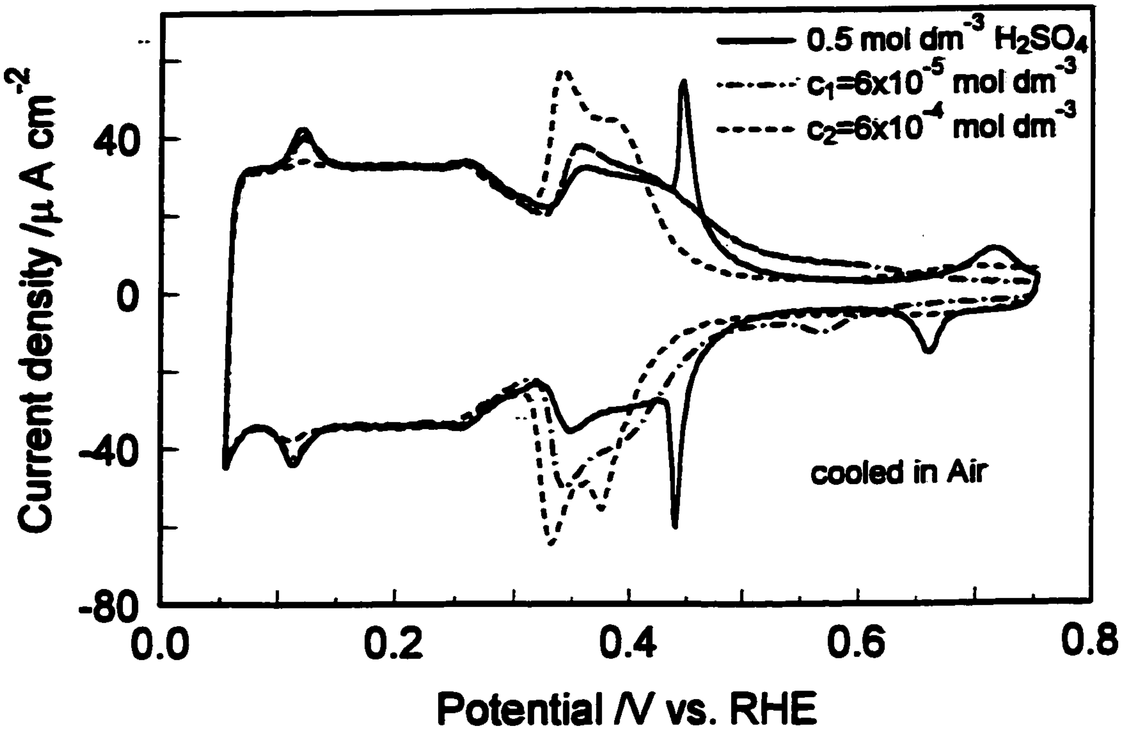

Fig. 6.10 Cyclic voltammograms for Pt(111) in 0.5 mol dm^{-3} H_2SO_4 at a sweep-rate of 0.050 V s^{-1} and in the presence of DMG$^+$ at the two concentrations indicated; voltammograms were recorded on the third cycle.

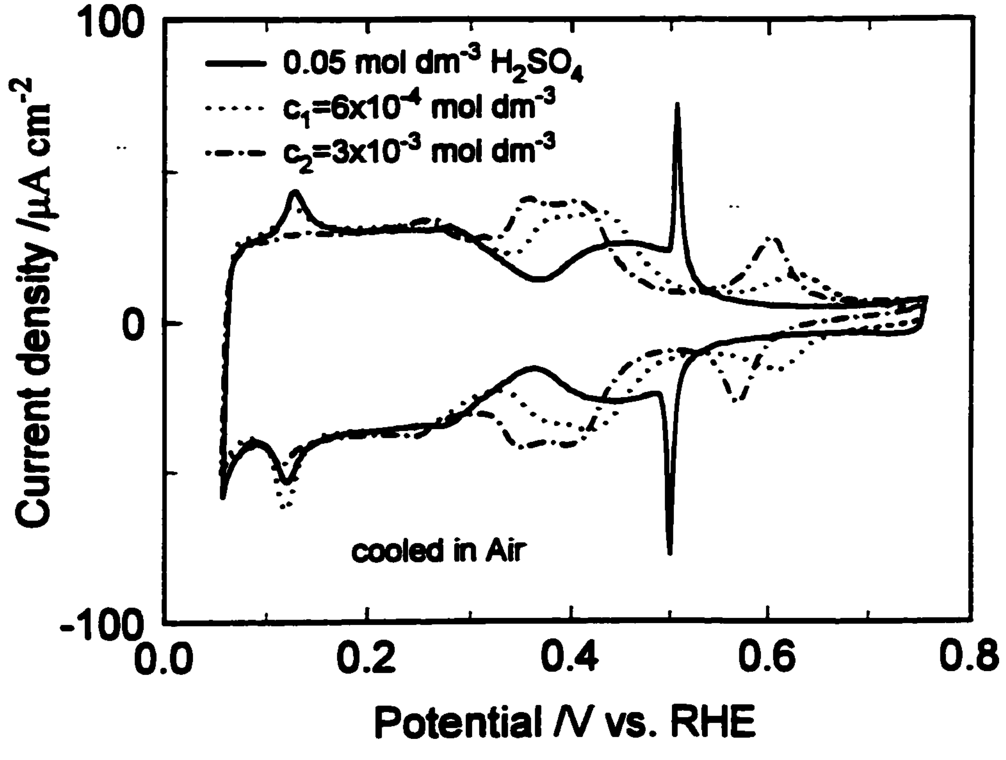

Fig. 6.11 Cyclic voltammograms for Pt(111) in 0.05 mol dm^{-3} H_2SO_4 at a sweep-rate of 0.050 V s^{-1} and in the presence of G$^+$ at the two concentrations indicated; voltammograms were recorded on the third cycle.

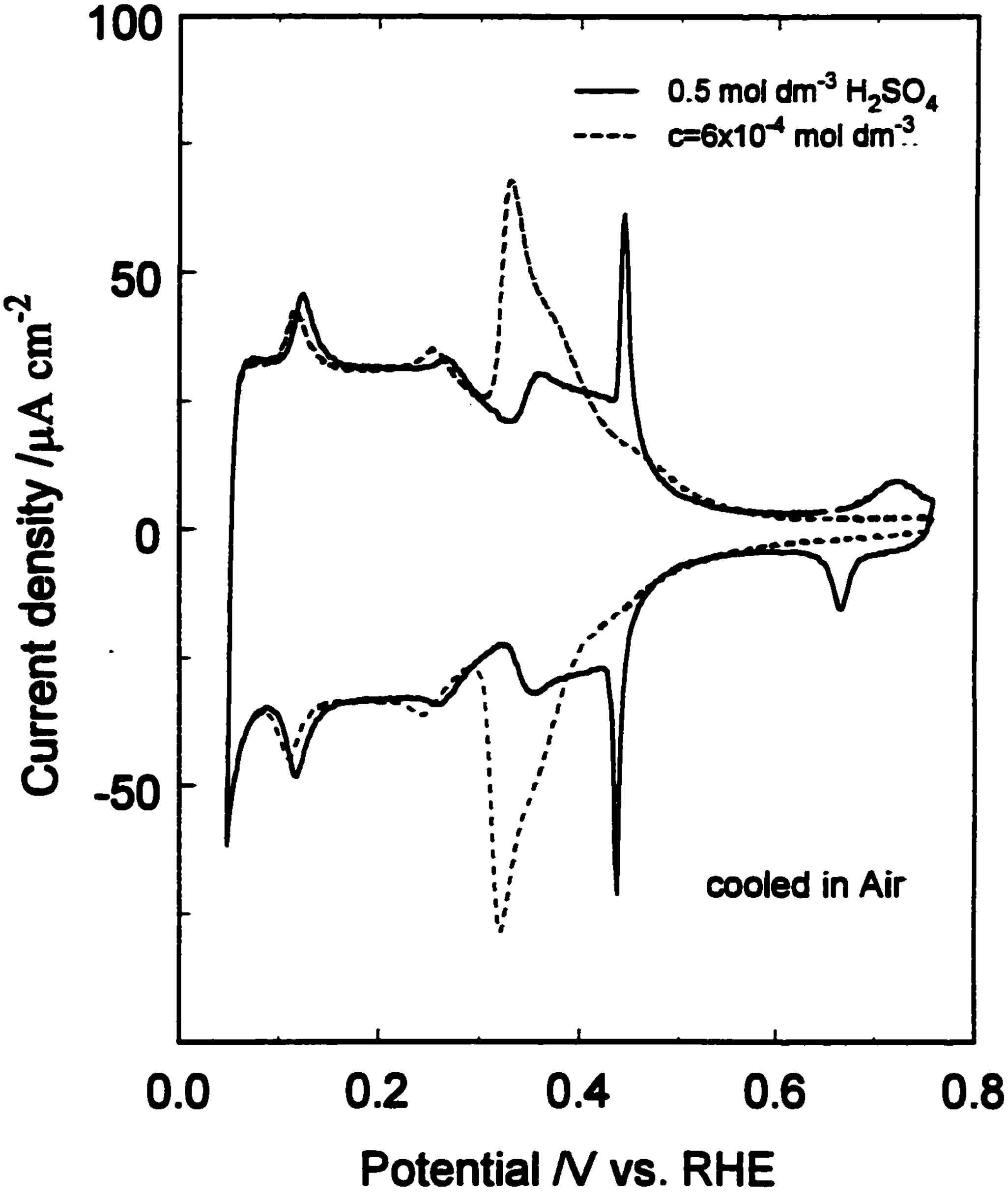

Fig. 6.12 Cyclic voltammograms for Pt(111) in 0.5 mol dm^{-3} H_2SO_4 at a sweep-rate of 0.050 V s^{-1} and in the presence of U at the concentration indicated; voltammograms were recorded on the third cycle.

6.2 of this Chapter and Table 6.1 for charge analysis, later). Additionally, upon adsorption of AA^+, some repulsion of the partial positive charge (formally, each N atom carries $^1/_2$ of the effective charge) from the positively charged Pt surface could arise. Nevertheless, the latter effect does not seem to be significant.

Comparative CV experiments on adsorption of U in relation to that of G^+ were obviously desirable on account of the close structural relation between U and G. In order to make meaningful comparisons with the effects of G^+, a comparative series of CV experiments was performed in the presence of urea. The resulting behaviour of U at the Pt(111) surface in 0.5 mol dm^{-3} H_2SO_4 is shown in Fig. 6.12. Close similarities to the behaviour of DMG^+ (see Fig. 6.10) and AA^+ are observed. The reason why urea, compared with G^+ at the Pt(111) surface, exhibits less significant interaction with adsorbed HSO_4^- is to be attributed to its much lower basicity and hence tendency for protonation (only about 10% of molecules [4] at pH≈1 exist as U^+).

6.1.2.2 Behaviour in $HClO_4$

It is well known that the voltammogram for Pt(111) in aq. $HClO_4$ differs in a major way from that in aq. H_2SO_4. The second "butterfly" region, adjacent to that for UPD H processes seen in H_2SO_4 solution, becomes widely separated, appearing over a more positive potential range, 0.55 → 0.85 V, RHE, as seen in Fig. 6.13. In relation to the known [5, 6] progression of the HSO_4^- region to more positive potentials with dilution of H_2SO_4, the second, well separated, "butterfly" region seen in aq. $HClO_4$ is suggestive of ClO_4^- adsorption, weaker than that of HSO_4^-. This receives some support from the work of Ye et al. [7] where the influence of H_3PO_4 on the "bisulphate" region in 0.5 mol dm^{-3} H_2SO_4 and the "butterfly" region in 0.5 mol dm^{-3} $HClO_4$, was reported.

However (as already mentioned in section 2.3 of Chapter 2), this has been a controversial assignment as at least a significant fraction of the charges, reversibly passed, may be due to OH (or O) deposition and desorption (see e.g. refs. 8 and 9). This is supported by the substantial similarity of voltammograms for Pt(111) in aq. NaOH (see Fig. 6.17 later in section 6.1.2.3) to those in aq. $HClO_4$.

In order to elucidate further the significance of this region, experiments were conducted using 0.05 mol dm^{-3} KHF_2 solution, as used by Nart et al. [10]. Bifluoride ion, F-H···F$^-$, which is in equilibrium with F$^-$ and HF, does not tend to become chemisorbed. Thus, based on its cyclic voltammetric behaviour (Fig. 6.14), which is very similar to that in NaOH and $HClO_4$, it is suggested that the adsorbed species giving the reversible cathodic/anodic currents within the potential range *ca.* 0.6-0.9 V, RHE in KHF_2 is OH$^-$, as has been supposed (cf. refs. 8, 9) for ClO_4^- solutions. Moreover, the effects of G$^+$ on the voltammogram in KHF_2 compare very well with those recorded in 0.1 mol dm^{-3} $HClO_4$ (compare Fig. 6.14 with Fig. 6.13).

Additionally, a series of experiments was performed at various (0.05, 0.1 and 1.0 mol dm^{-3}) concentrations of $HClO_4$. The results showed practically *no shift* in potential of the "butterfly" peak (Fig. 6.15), unlike the previously known result that increasing concentration of H_2SO_4 causes progressive shifts of the current profile peak for HSO_4^- on Pt(111) [5, 6]. Hence, it is proposed that a significant fraction of the charges involved in the "butterfly" peak, observed in $HClO_4$ at the Pt(111) surface, is associated with OH adsorption and desorption processes, rather than with ClO_4^- ion. The latter conclusion is in agreement with that made in the previous paragraph and with the literature cited.

Fig. 6.13 also shows the effects of G^+ (at two concentrations) on the voltammogram for Pt(111) in the 0.1 mol dm^{-3} aq. $HClO_4$. There is a major shift of charge from the "butterfly" region (0.55 to 0.85 V) to the potential range for double-layer charging, with appearance of almost reversible current peaks associated with appreciable (*ca.* 115 μC cm^{-2}) anodic and cathodic charges, measured in the presence of $4x10^{-4}$ mol dm^{-3} G^+ in solution (see Table 6.1). On the other hand, the UPD H region is almost unaffected by the presence of G^+ (contrast the behaviour in H_2SO_4, Fig. 6.8). Due to the weaker adsorption of ClO_4^- (or OH^-) than that of HSO_4^-, it is suggested that the charge accumulated in the double-layer charging region corresponds almost entirely to the chemisorbed G^+ cations. As the surface becomes blocked by adsorbed G^+, understandably, only small further charge is observed over the potential region 0.75-0.88 V. This charge (*ca.* 20 μC cm^{-2}) could be assigned to co-adsorption of ClO_4^- ions or OH^- deposition and desorption [8, 9].

In aq. $HClO_4$, the adsorption behaviour of DMG^+ closely resembles that of G^+. It has to be recalled here that adsorption of the above molecules on the (111) plane occurs in the relative absence of anionic species (over the potential range for the double-layer charging). For this reason, presence of the two methyl groups on one of the N atoms in DMG^+ does not affect (compared with G^+) the accommodation of DMG^+ ions on the Pt(111) surface. In the case of AA^+ (Fig. 6.16), however, the voltammetric charge is displaced more towards the H_2 reversible potential and a pair of reversible, and sharp, peaks (especially on the cathodic-going sweep) appears right at the positive end of the H UPD profile.

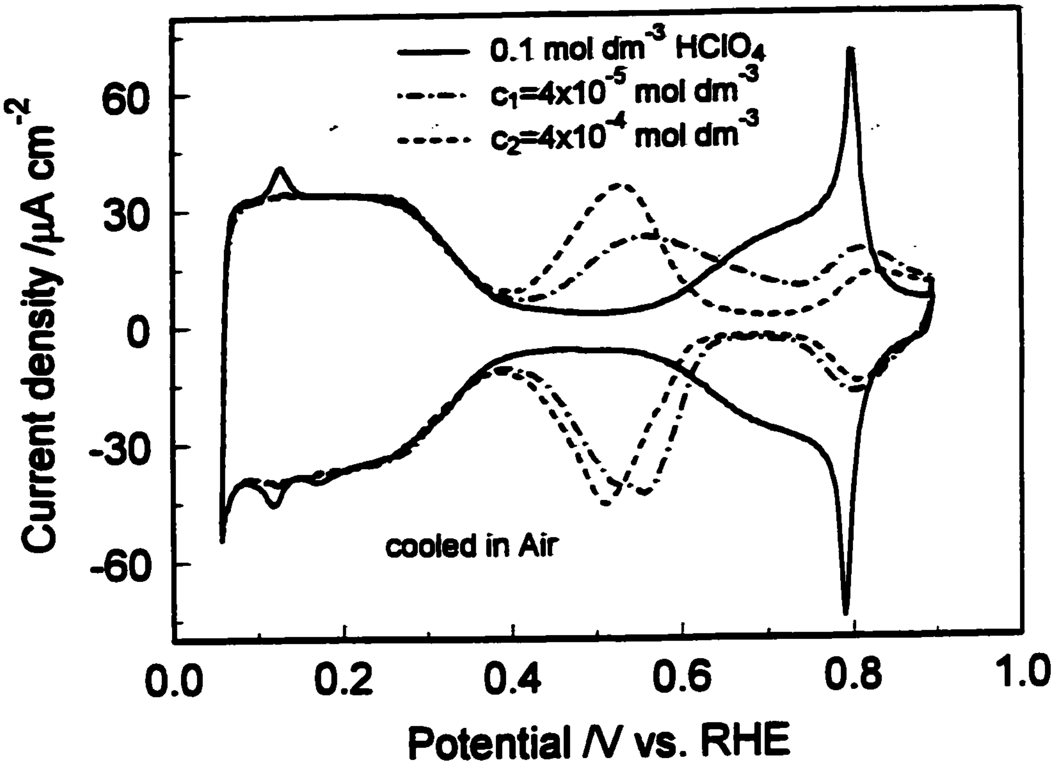

Fig. 6.13 Cyclic voltammograms for Pt(111) in 0.1 mol dm^{-3} HClO$_4$ at a sweep-rate of 0.050 V s^{-1} and in the presence of G$^+$ at the concentrations indicated; voltammograms were recorded on the third cycle.

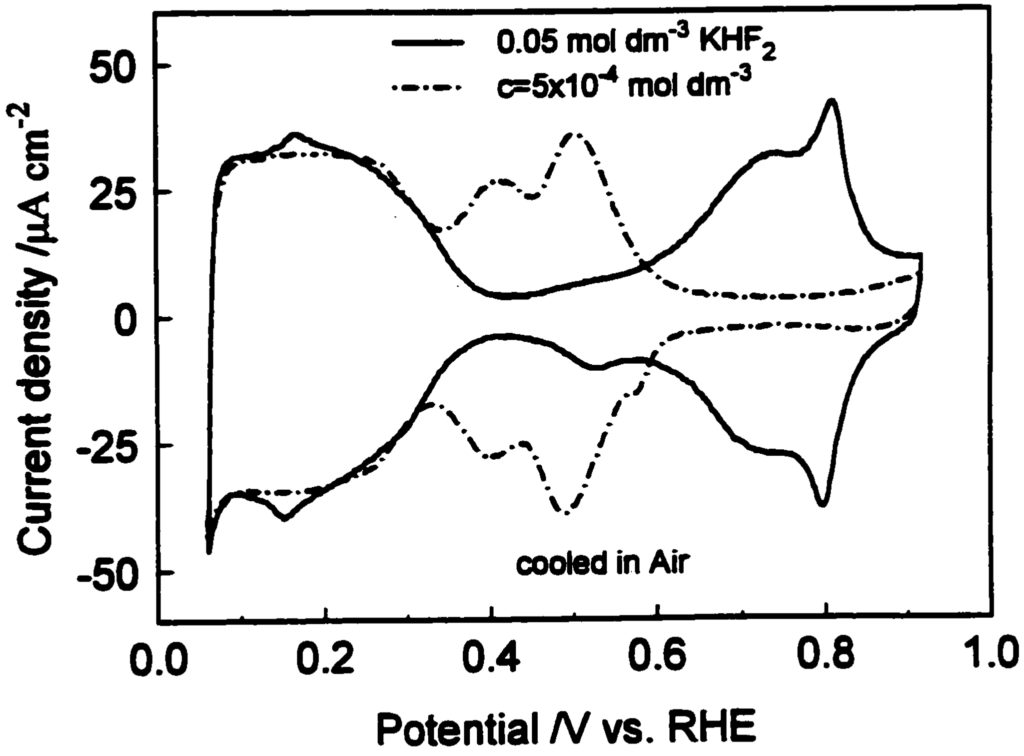

Fig. 6.14 Cyclic voltammograms for Pt(111) in 0.05 mol dm^{-3} KHF$_2$ at a sweep-rate of 0.050 V s^{-1} and in the presence of G$^+$ at the concentration indicated; voltammograms were recorded on the third cycle.

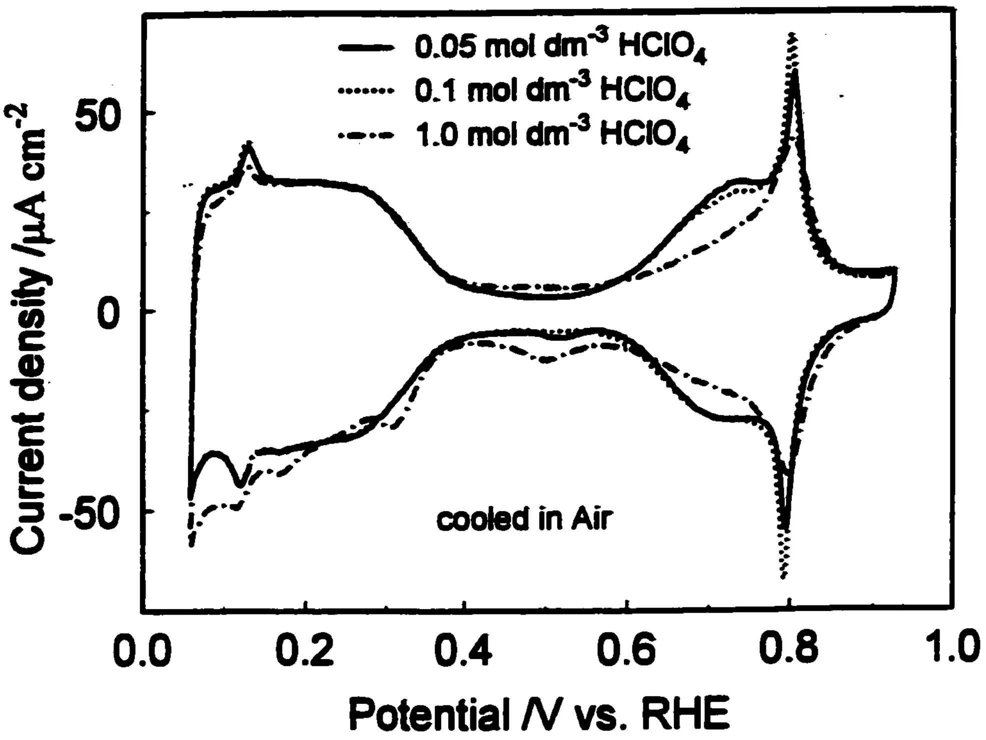

Fig. 6.15 An effect of HClO$_4$ concentration on the cyclic voltammetric behaviour of Pt(111) at a sweep-rate of 0.050 V s^{-1} at the three indicated concentrations of HClO$_4$; voltammograms were recorded on the third cycle.

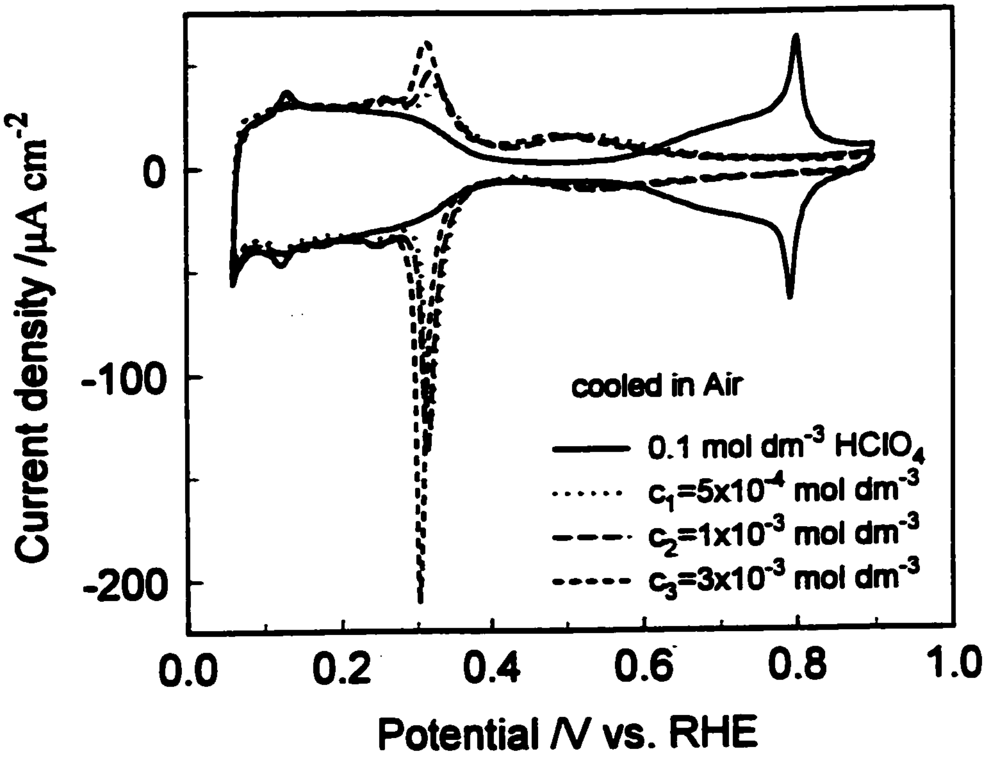

Fig. 6.16 Cyclic voltammograms for Pt(111) in 0.1 mol dm^{-3} HClO$_4$ at a sweep-rate of 0.050 V s^{-1} and in the presence of AA$^+$ at the concentrations indicated; voltammograms were recorded on the third cycle.

6.1.2.3 Behaviour in NaOH

Initially, it was assumed that a comparison between adsorption behaviour of guanidine in acid and alkaline solutions might have led to distinction between the effects of the ion G^+ and its conjugate base, G^0. However, the ionisation equilibrium requires (as already mentioned in section 6.1.1.3) that, even in 0.1 mol dm^{-3} aq. NaOH, guanidine remains substantially in the cationic form since it is such a strong base.

Nevertheless, comparative experiments in 0.1 mol dm^{-3} aqueous NaOH are still of considerable interest since the voltammograms for Pt(hkl) surfaces in pure alkaline solutions are themselves appreciably different from those in H_2SO_4 owing to the lack of the well-known HSO_4^- adsorption effects.

The adsorption behaviour of G^+ or G (at three concentrations) at the Pt(111) surface in 0.1 mol dm^{-3} NaOH is shown in Fig. 6.17. Here, substantial changes in the voltammetric profiles are also observed. The "butterfly" region at *ca.* 0.6-0.9 V is completely suppressed in the presence of 5×10^{-4} mol dm^{-3} G^+ and a new region (*ca.* 0.25-0.6 V), with relatively sharp peaks, appears just at the positive end of the UPD H zone. This result is qualitatively similar to that observed in 0.1 mol dm^{-3} $HClO_4$. Here, also the UPD H region itself remains almost unchanged, suggesting that G^+ adsorption commences only beyond the underpotential-H ionisation zone. The charge accumulated over the potential range 0.25-0.60 V (*ca.* 170 μC cm^{-2} at the concentration of 3×10^{-3} mol dm^{-3} G^+, see Table 6.1), is (presumably) entirely due to the adsorption/desorption of the G^+ cations on the Pt(111) surface. Then, after G^+ has become adsorbed, the surface remains practically blocked for OH formation so that only a very small charge can then be passed over the original, more positive, "butterfly" region (*ca.* 0.6-0.9 V). Thus, in

NaOH, G^+ (possibly also as G^0) becomes adsorbed on the Pt(111) plane in the absence of significant adsorption of OH groups, as is also the case in $HClO_4$.

For comparison with previously shown Fig. 6.9, Fig. 6.18 shows the voltammetric behaviour at the Pt(111) surface in 0.1 mol dm^{-3} NaOH containing 6x10^{-4} mol dm^{-3} G^+ species over two restricted ranges of potential. It is seen that a pair of reversible peaks (as also observed in Fig. 6.17) arises independently of whether polarisation had or had not been taken into a higher potential range, e.g. to 0.9 V. The two corresponding peaks, here denoted as P_1 and P_2, remain present on the voltammogram upon cycling over the narrow potential range *ca.* 0.20-0.45 V, thus indicating that over the latter potential range, G^+ undergoes reversible adsorption/desorption processes on the Pt surface.

The adsorption behaviour of DMG^+ in 0.1 mol dm^{-3} NaOH closely resembles that of G^+ (see Fig. 6.19); however, at the corresponding concentration of 3x10^{-3} mol dm^{-3} of DMG^+, only a charge of 122 μC cm^{-2} passes over the potential range 0.26-0.50 V (compare with 170 μC cm^{-2} for G^+). At the same time, a charge of 55 μC cm^{-2} (see Table 6.1) is accumulated in the "butterfly" region, over the potential range *ca.* 0.65-0.90 V. The latter charge corresponds to the reversible formation of OH species on the Pt surface. The above behaviour fully supports the idea that accommodation of DMG^+ on the Pt(111) surface (relative to that of G^+) is significantly restricted by its molecular geometry.

The corresponding behaviour of AA^+ and U is illustrated by the cyclic voltammograms in Figs. 6.20 and 6.21, respectively. While voltammograms for the former species qualitatively resemble those of G^+, for the latter (U) molecule, the voltammetric charge beyond that for the UPD of H is mostly accumulated over the potential range for double-

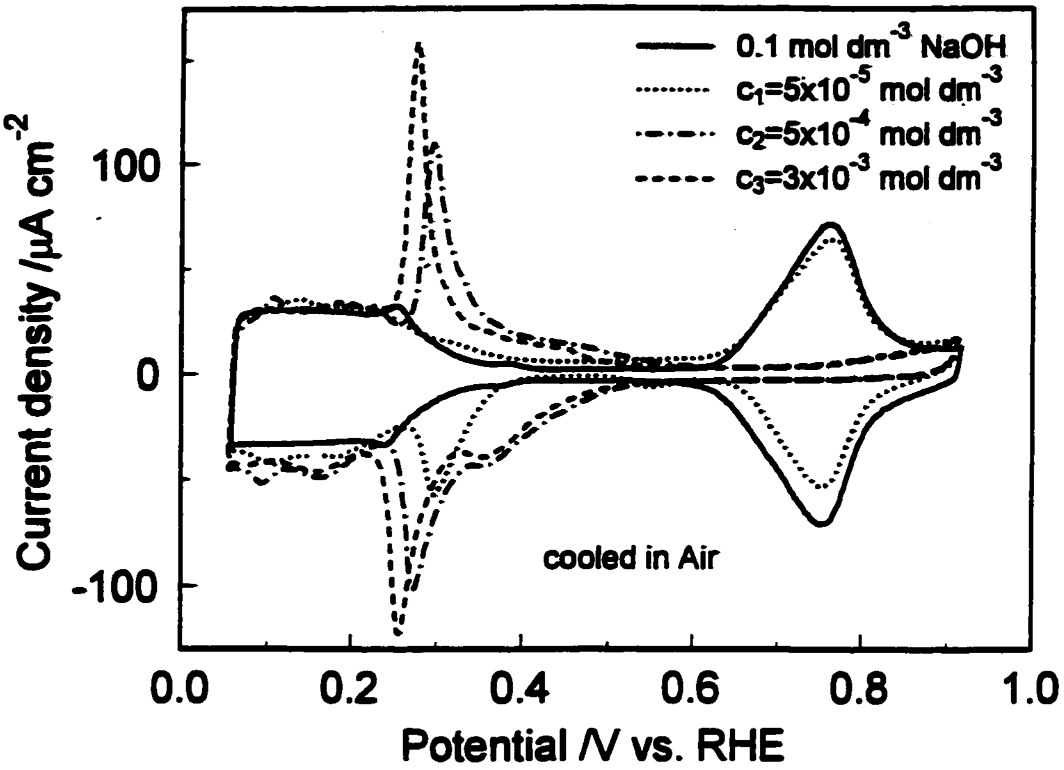

Fig. 6.17 Cyclic voltammograms for Pt(111) in 0.1 mol dm^{-3} NaOH at a sweep-rate of 0.050 V s^{-1} and in the presence of G^{+} at the concentrations indicated; voltammograms were recorded on the third cycle.

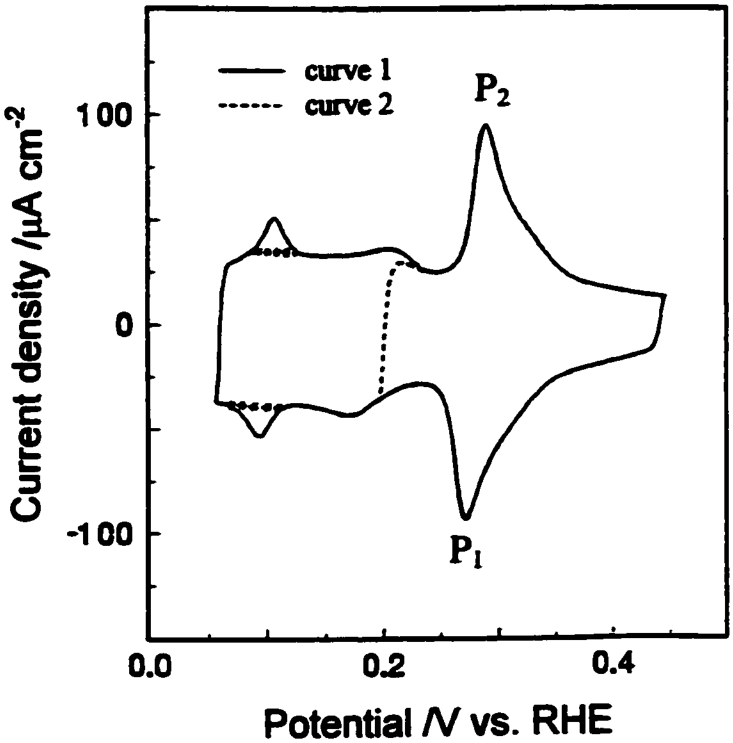

Fig. 6.18 Cyclic voltammograms for Pt(111) in 0.1 mol dm^{-3} NaOH at a sweep-rate of 0.050 V s^{-1} in the presence of 6x10^{-4} mol dm^{-3} G^{+} with sweep reversed at 0.44 V and limited to the range 0.20-0.44 V, curves 1 and 2.

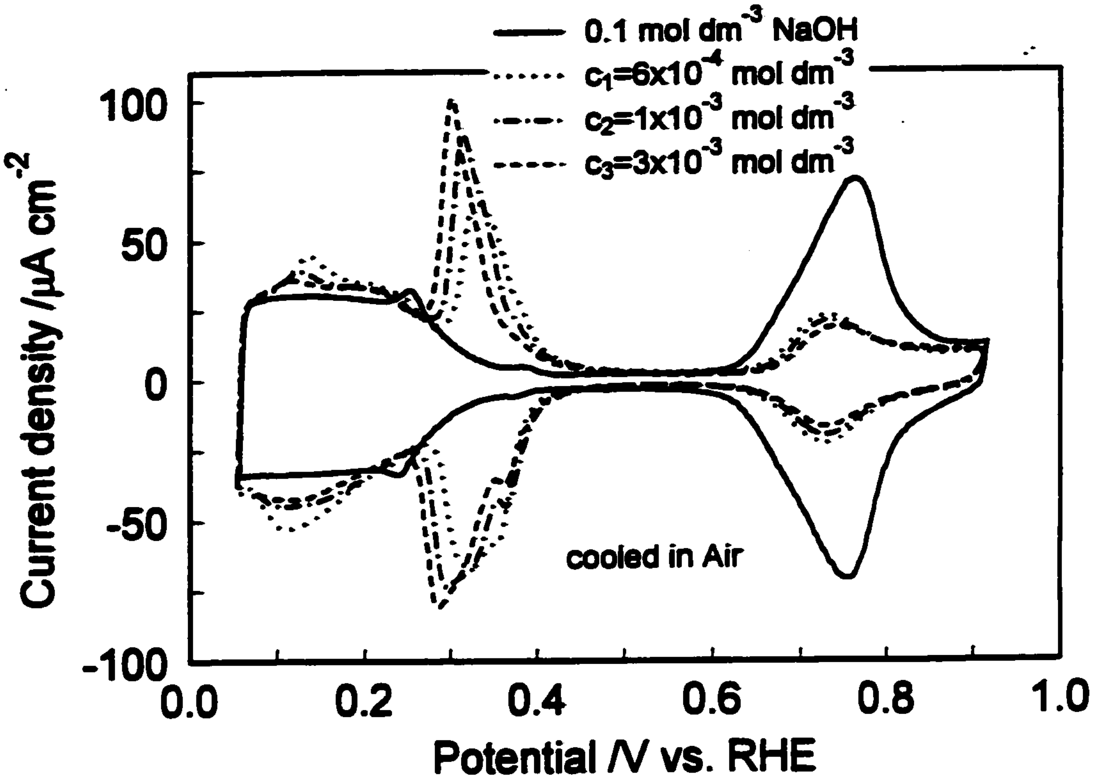

Fig. 6.19 Cyclic voltammograms for Pt(111) in 0.1 mol dm^{-3} NaOH at a sweep-rate of 0.050 V s^{-1} and in the presence of DMG^{+} at the concentrations indicated; voltammograms were recorded on the third cycle.

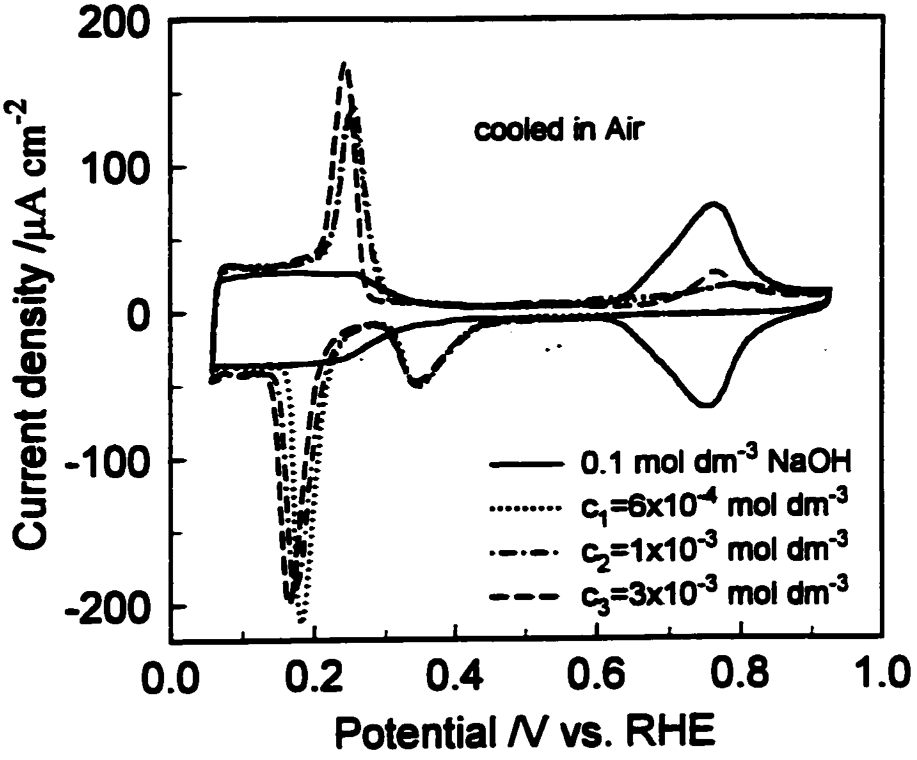

Fig. 6.20 Cyclic voltammograms for Pt(111) in 0.1 mol dm^{-3} NaOH at a sweep-rate of 0.050 V s^{-1} and in the presence of AA^{+} at the concentrations indicated; voltammograms were recorded on the third cycle.

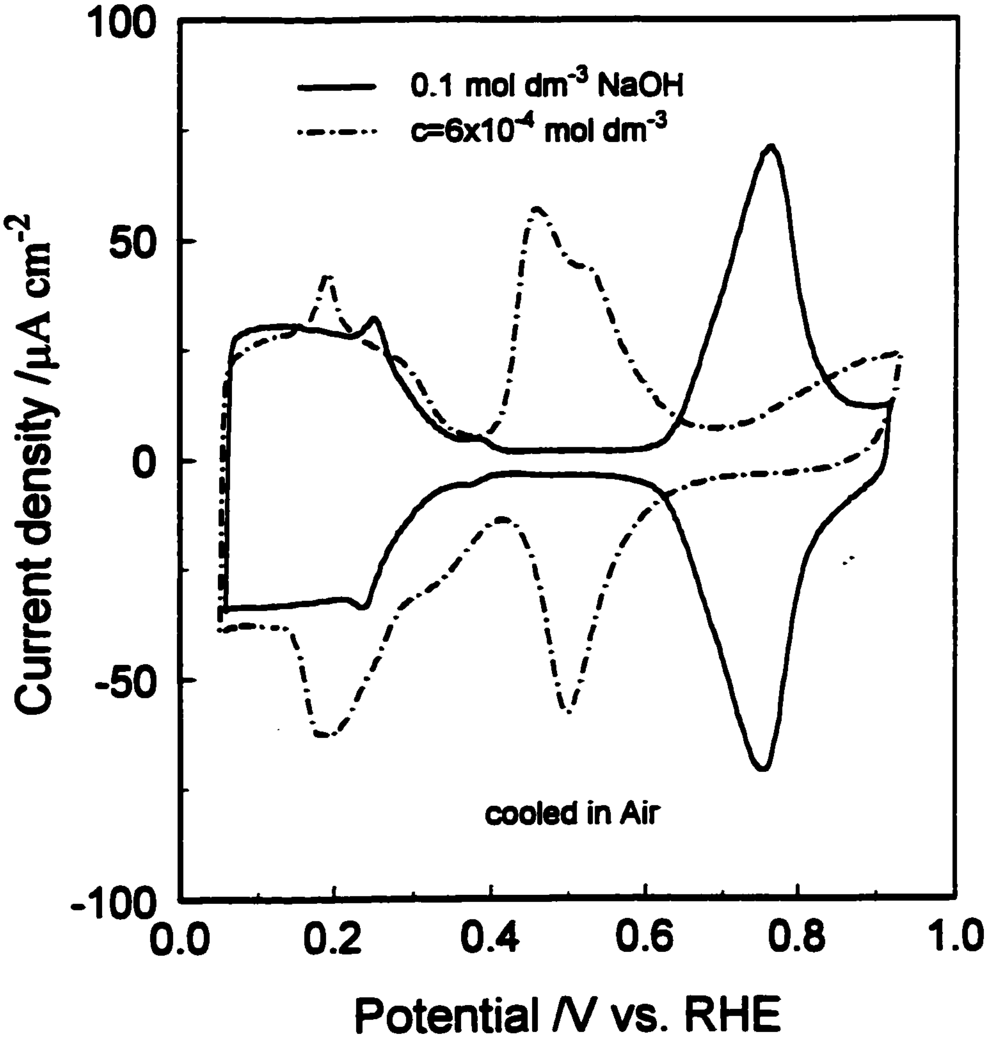

Fig. 6.21 Cyclic voltammograms for Pt(111) in 0.1 mol dm^{-3} NaOH at a sweep-rate of 0.050 V s^{-1} and in the presence of U at the concentration indicated; voltammograms were recorded on the third cycle.

layer charging.

6.1.3 Adsorption behaviour at the Pt(100) surface

6.1.3.1 Behaviour in H_2SO_4

The behaviour of G^+ (at three concentrations) at the Pt(100) plane in 0.5 mol dm^{-3} H_2SO_4 is shown in Fig. 6.22. Like the behaviour at the (111) surface, the most significant effect here is that G^+ causes a substantial shift of both (anodic and cathodic) current-response peaks towards the H_2 reversible potential, by *ca.* 0.10-0.12 V. In terms of the proposed mechanism of the effect of G^+ (due to ion-pairing with HSO_4^- in the chemisorbed state), the above result is consistent with the mechanism proposed for the Pt(111) surface. However, HSO_4^- ion exhibits only two-fold co-ordination at the Pt(100) surface [11] (compared with three-fold co-ordination at the (111) plane). Also, the coverage of the Pt(100) plane by the HSO_4^- ions corresponds only to about 25% of the total electric charge measured from the voltammogram [12]. Consequently, a significant fraction of sites on the (100) surface is available for co-adsorption of G^+, after H has become desorbed. The latter situation leads to an increase of charge by 26% in the presence of $6x10^{-4}$ mol dm^{-3} G^+ in solution (see Table 6.2), compared with *ca.* only 8% at the (111) plane.

Comparison of the effects of DMG^+ (Fig. 6.23), AA^+ and U (Fig. 6.24) at the Pt(100) surface shows that they are quite similar, apart from some small but perceptible details, to those of G^+, unlike at the (111) plane. It seems that the geometry and electronic properties of the Pt(111) surface are sufficiently different from those of the (100) plane to promote a major difference of the adsorption and ion-pairing behaviour of DMG^+, AA^+

and U vis-à-vis G^+, co-adsorbed with HSO_4^- in the case of the Pt(111) surface.

6.1.3.2 Behaviour in $HClO_4$

The behaviour of G^+ (at two concentrations) at the Pt(100) surface in 0.1 mol dm^{-3} $HClO_4$ is shown in Fig. 6.25. In this case, again, there is an appreciable redistribution of anodic and cathodic charges towards the RHE potential with simultaneous "compression" of the charge response over narrower current peaks. Taking into account the close similarities of the above-mentioned voltammogram to that for Pt(100) in 0.5 mol dm^{-3} H_2SO_4, we can anticipate, in $HClO_4$, the same type of interfacial interaction of the G^+ species at the Pt(100) plane as that observed in H_2SO_4 solution. The recorded smaller increase of the total voltammetric charge (*ca.* 8% at the concentration of $4x10^{-4}$ mol dm^{-3} G^+, see Table 6.2) may be related to different site-occupancy by the ClO_4^- anions (from that by HSO_4^-) on the Pt(100) surface (see also section 6.2 later).

The adsorption behaviour of DMG^+ and AA^+ (Fig. 6.26) at the Pt(100) surface closely resembles that of the G^+ molecule-ion.

6.1.3.3 Behaviour in NaOH

The adsorption behaviour of G^+ (at three concentrations) at the Pt(100) surface in 0.1 mol dm^{-3} NaOH is shown in Fig. 6.27. Here, major shifts of charge distribution take place from a broad, four-peaked, cyclic voltammogram, similar to those observed in the presence of G^+ in $HClO_4$ and H_2SO_4 solutions. In a work by Morallon et al. [13], it is implied that all four peaks observed in the voltammogram of Pt(100) in NaOH correspond to different states of adsorbed H. A similar conclusion was made by

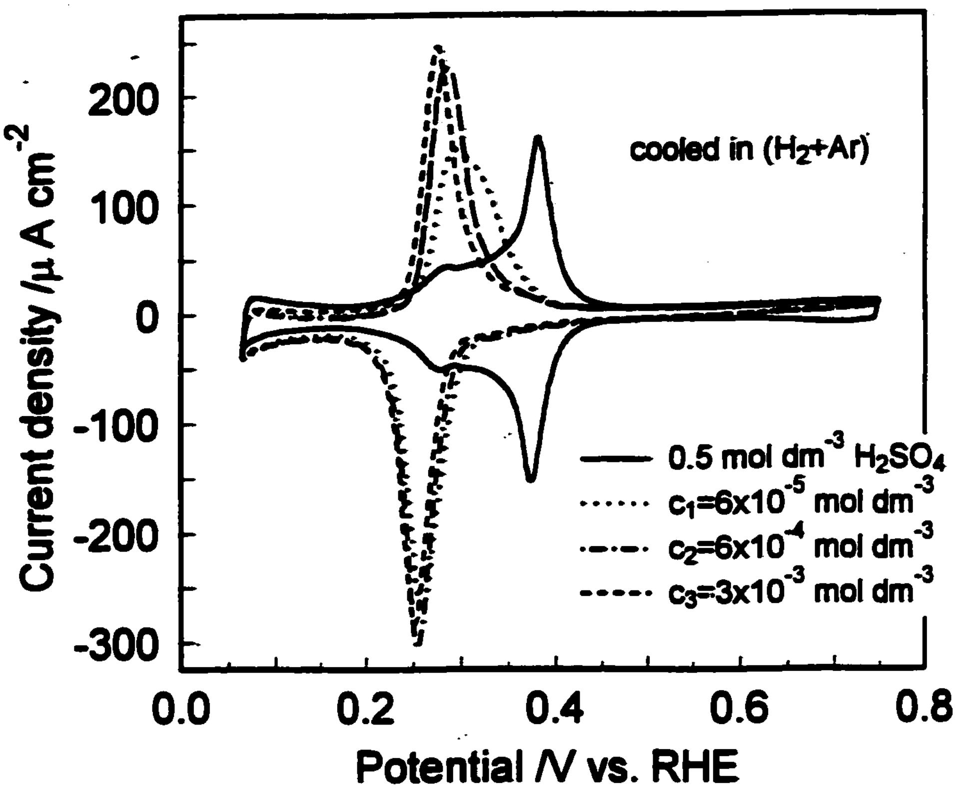

Fig. 6.22 Cyclic voltammograms for Pt(100) in 0.5 mol dm^{-3} H_2SO_4 at a sweep-rate of 0.050 V s^{-1} and in the presence of G^+ at the concentrations indicated; voltammograms were recorded on the third cycle.

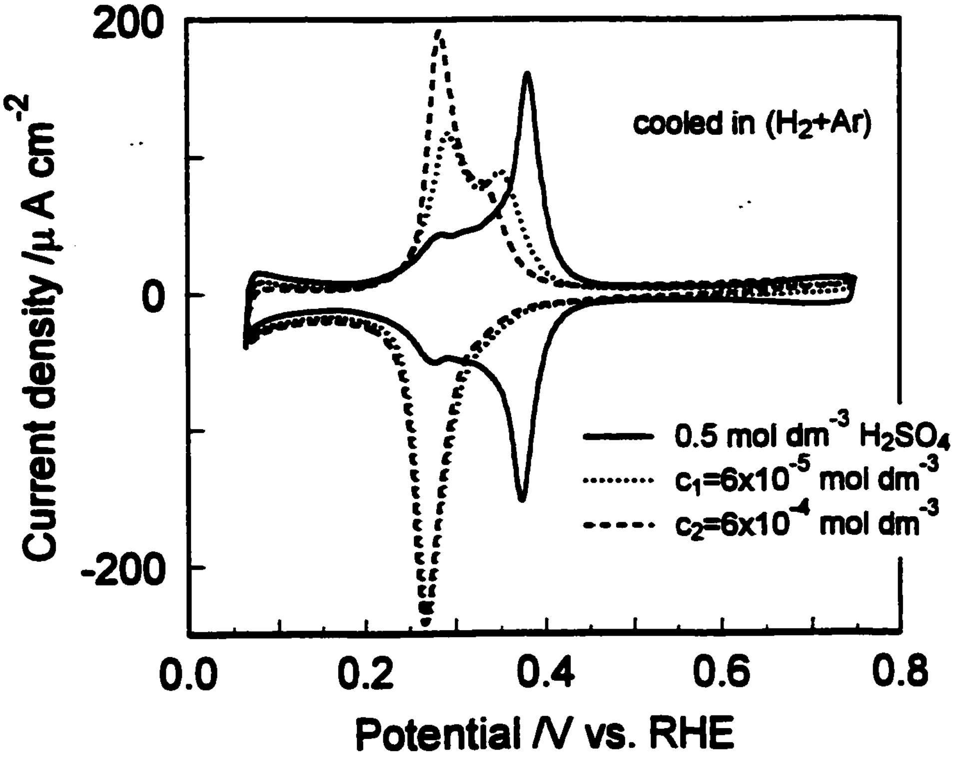

Fig. 6.23 Cyclic voltammograms for Pt(100) in 0.5 mol dm^{-3} H_2SO_4 at a sweep-rate of 0.050 V s^{-1} and in the presence of DMG^+ at the concentrations indicated; voltammograms were recorded on the third cycle.

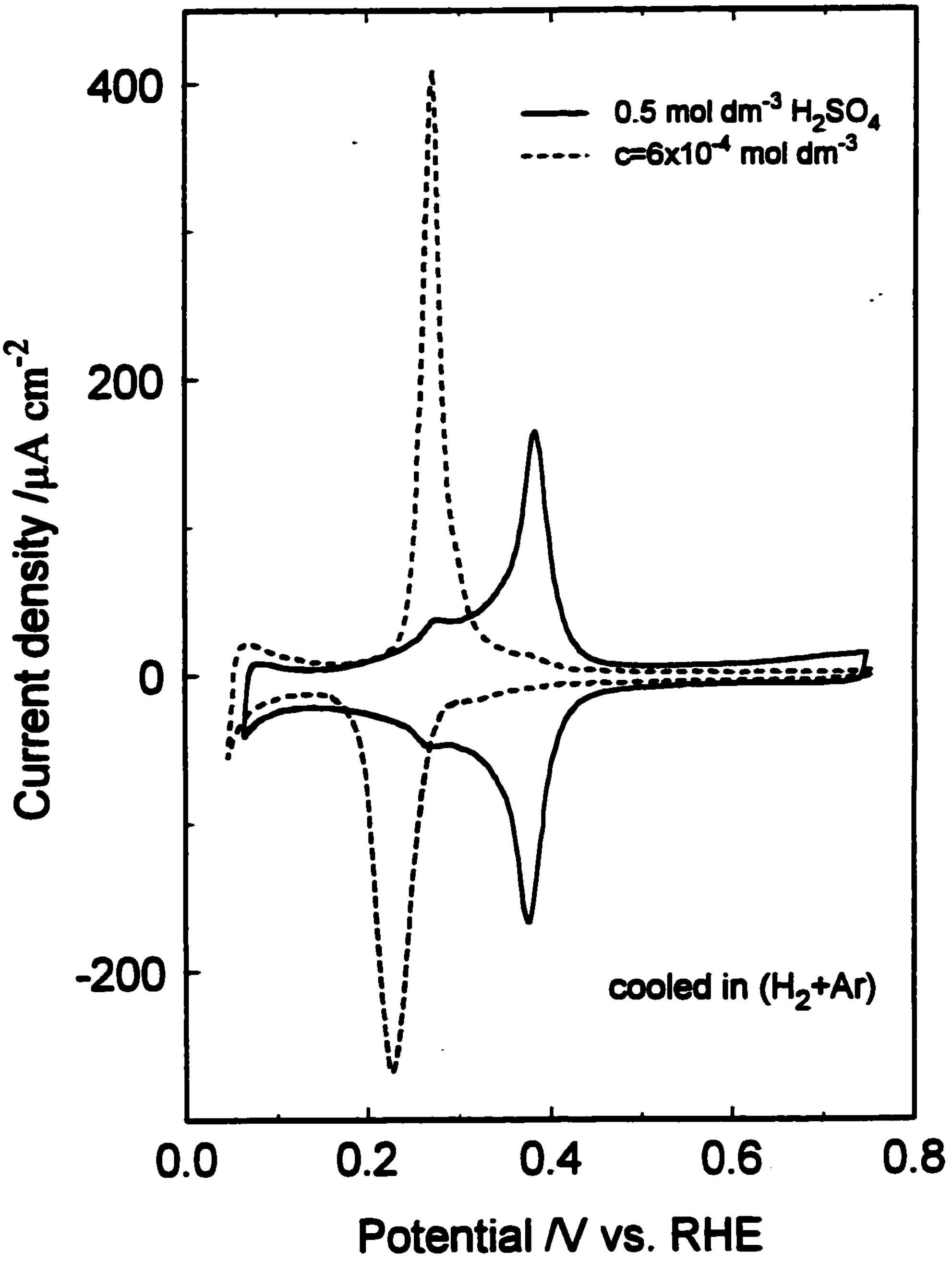

Fig. 6.24 Cyclic voltammograms for Pt(100) in 0.5 mol dm^{-3} H_2SO_4 at a sweep-rate of 0.050 V s^{-1} and in the presence of U at the concentration indicated; voltammograms were recorded on the third cycle.

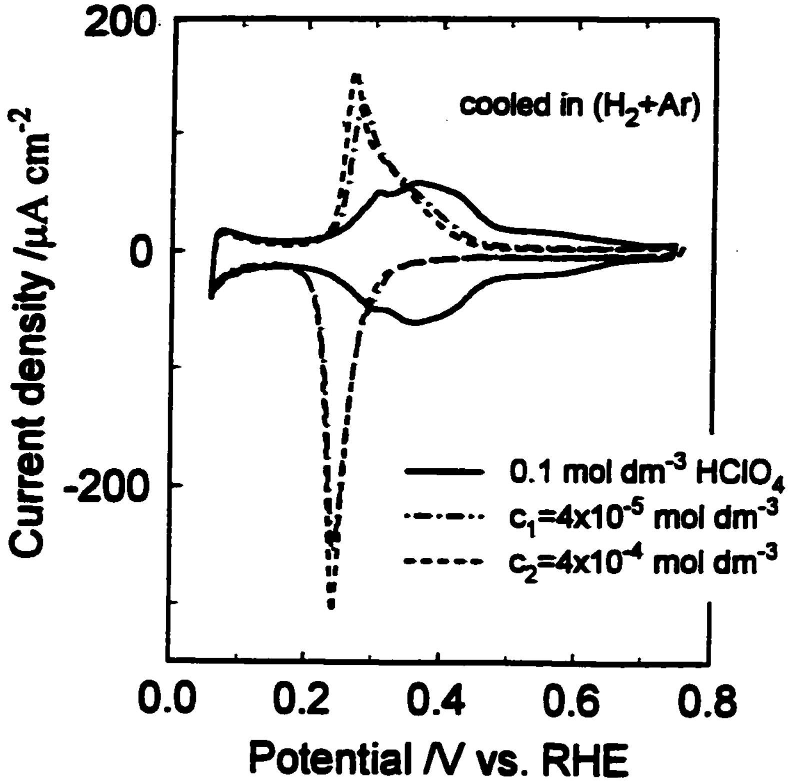

Fig. 6.25 Cyclic voltammograms for Pt(100) in 0.1 mol dm^{-3} $HClO_4$ at a sweep-rate of 0.050 V s^{-1} and in the presence of G$^+$ at the concentrations indicated; voltammograms were recorded on the third cycle.

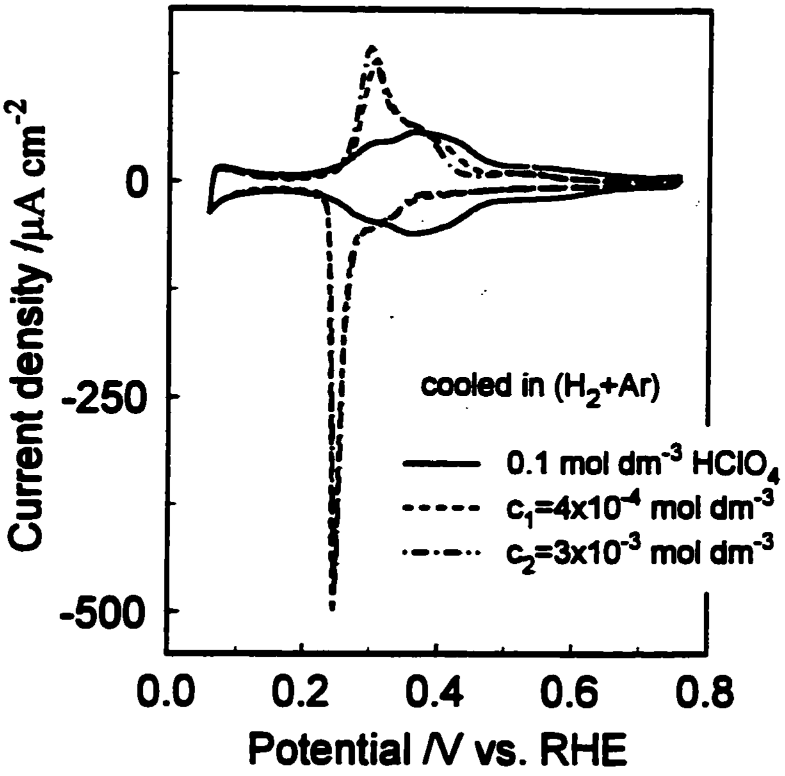

Fig. 6.26 Cyclic voltammograms for Pt(100) in 0.1 mol dm^{-3} $HClO_4$ at a sweep-rate of 0.050 V s^{-1} and in the presence of AA$^+$ at the concentrations indicated; voltammograms were recorded on the third cycle.

Marinkovic et al. [14]. However, Markovic et al. [15] suggest that in NaOH, for both the Pt(100) and (110) planes, on the positive-going sweep, desorption of H is immediately followed by adsorption of oxygen-like species (OH_{ad}). At the Pt(100) surface, these two processes supposedly overlap, with OH_{ad} being formed on some parts of the surface, while UPD H is still present on other parts [15], depending on potential.

Thus, in the case of the Pt(100) plane in NaOH, a similar mechanism of interaction of G^+ with the surface species can be suggested, although it is proposed here that G^+ undergoes a co-operative chemisorption with the hydroxyl anion, instead of with HSO_4^- in sulphuric acid. The electrostatic interaction between adsorbed G^+ and $OH^{(\delta-)}$ leads to stabilisation of the adsorption of OH^-. Thus, the cyclic voltammetry profile (see Fig. 6.27) is again significantly shifted towards the RHE potential. The increase of the total voltammetic charge by *ca.* 21% in this case (at the concentration of $3x10^{-3}$ mol dm^{-3} G^+, see Table 6.2) may be related to the fact that the reversibly-adsorbed hydroxy species, formed within the potential range 0.45-0.70 V, may not co-ordinate to the Pt surface in the same way as that at potentials beyond 0.70 V where the OH electrosorption is irreversible [15]; hence, the OH species adsorbed over the studied range of potential may tend to populate only the more strongly adsorbing sites.

Again, like in $HClO_4$, in NaOH the adsorption behaviour of DMG^+, AA^+ (Fig. 6.28) and of U (Fig. 6.29) at the Pt(100) surface closely resembles that of the G^+ species.

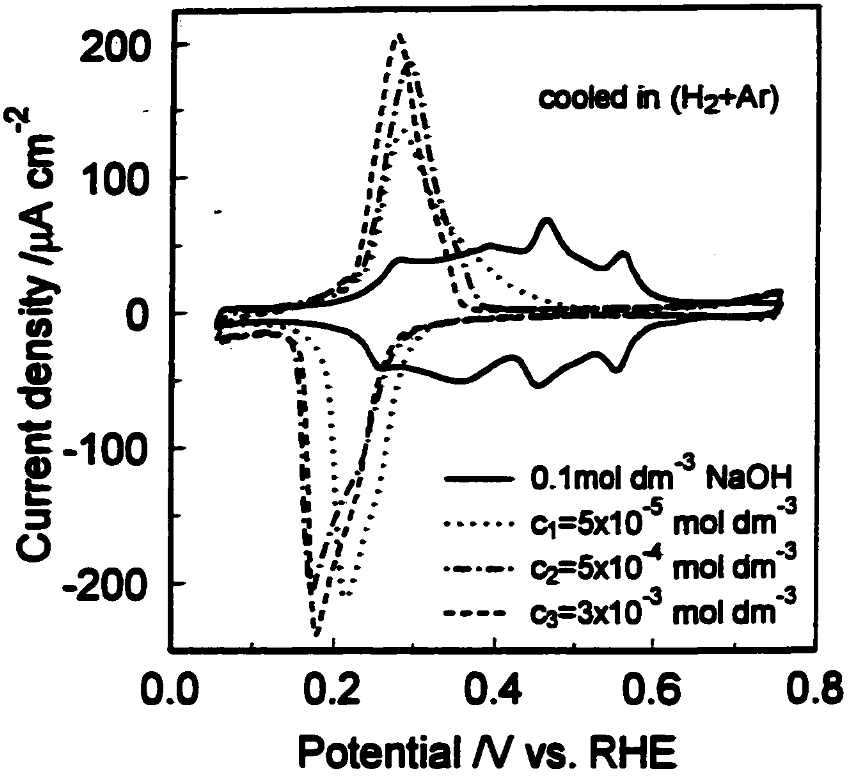

Fig. 6.27 Cyclic voltammograms for Pt(100) in 0.1 mol dm^{-3} NaOH at a sweep-rate of 0.050 V s^{-1} and in the presence of G^{+} at the concentrations indicated; voltammograms were recorded on the third cycle.

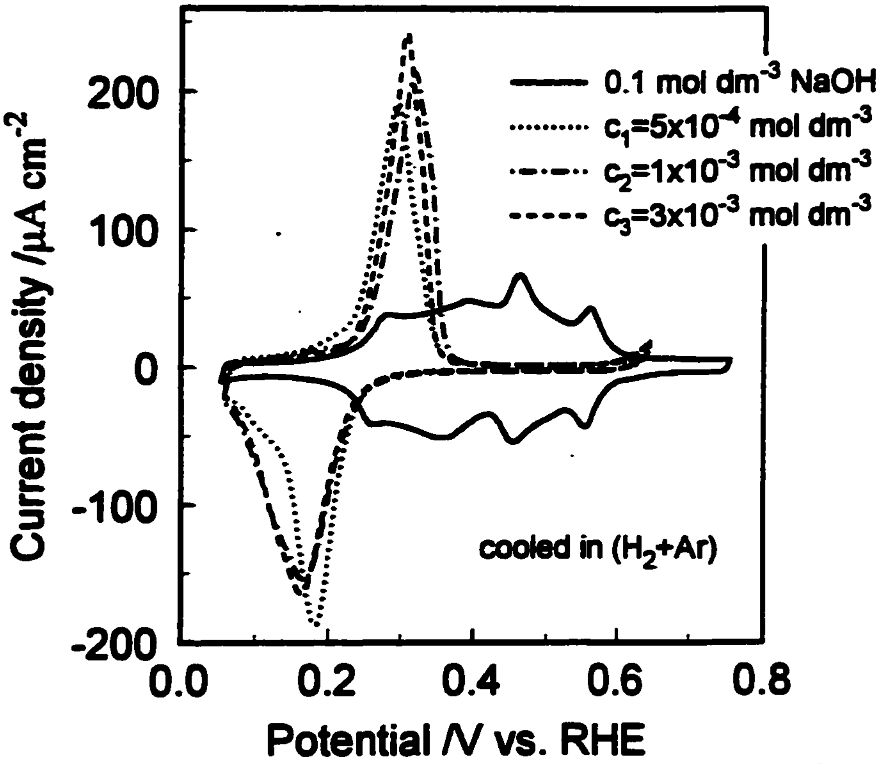

Fig. 6.28 Cyclic voltammograms for Pt(100) in 0.1 mol dm^{-3} NaOH at a sweep-rate of 0.050 V s^{-1} and in the presence of AA^{+} at the concentrations indicated; voltammograms were recorded on the third cycle.

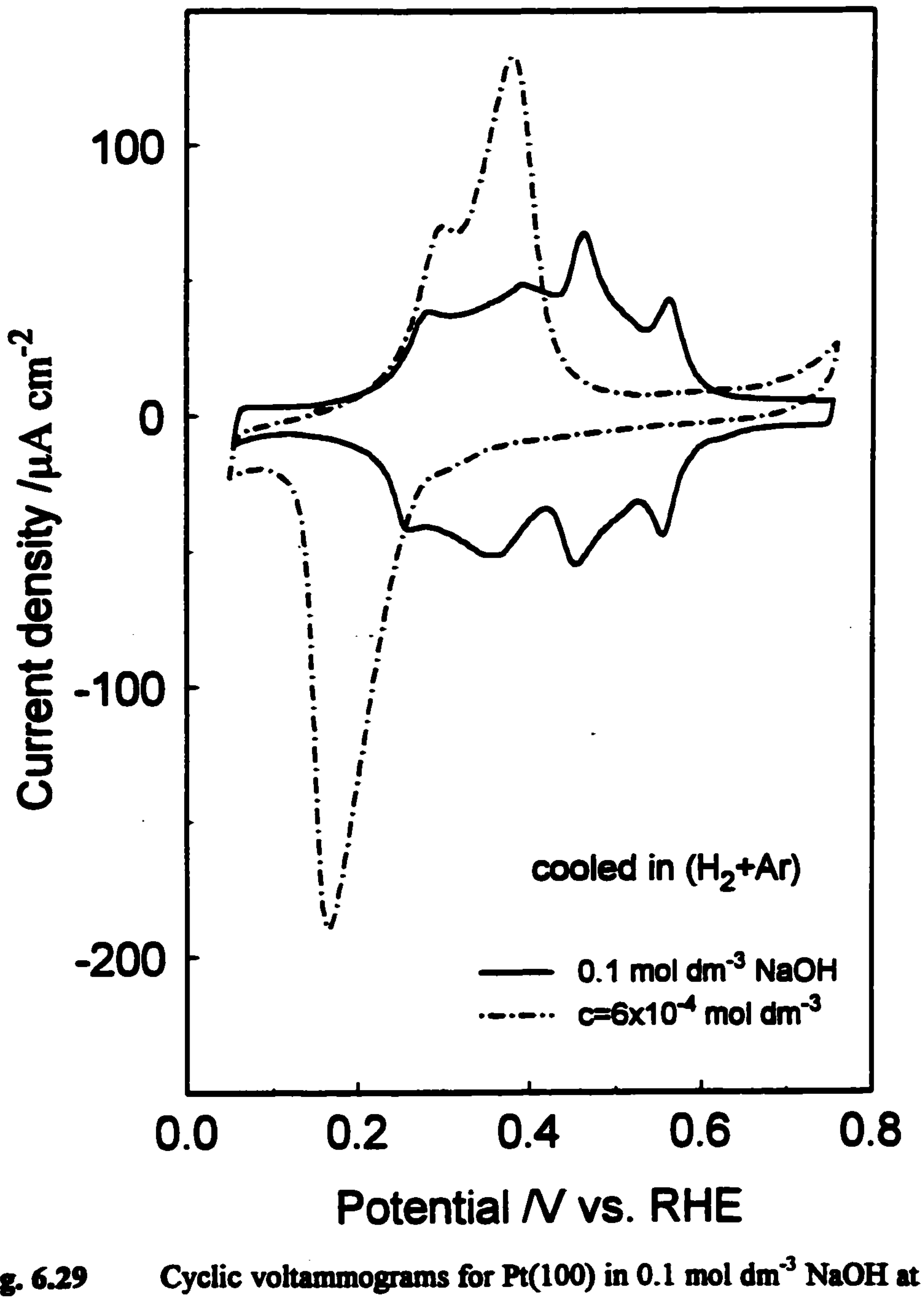

Fig. 6.29 Cyclic voltammograms for Pt(100) in 0.1 mol dm^{-3} NaOH at a sweep-rate of 0.050 V s^{-1} and in the presence of U at the concentration indicated; voltammograms were recorded on the third cycle.

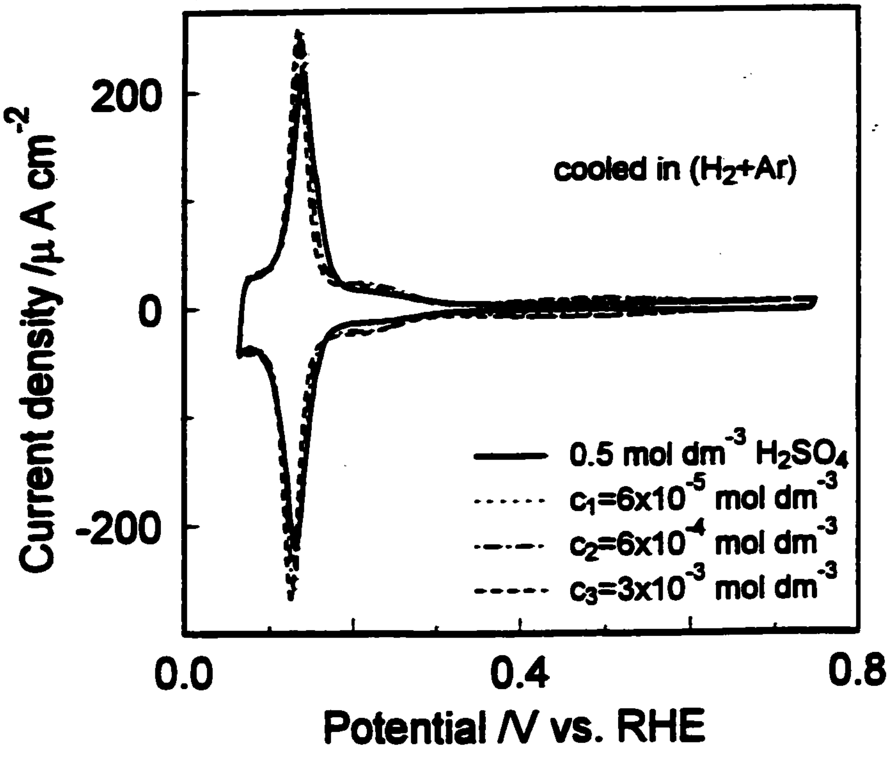

Fig. 6.30 Cyclic voltammograms for Pt(110) in 0.5 mol dm^{-3} H_2SO_4 at a sweep-rate of 0.050 V s^{-1} and in the presence of G$^+$ at the concentrations indicated; voltammograms were recorded on the third cycle.

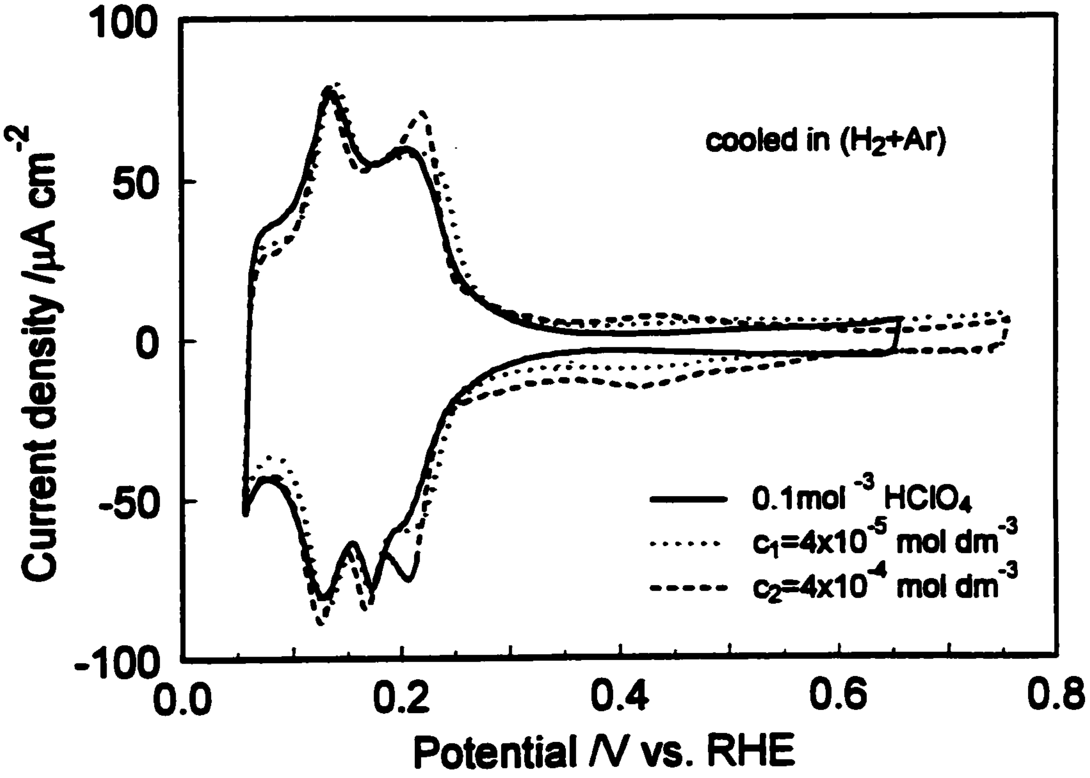

Fig. 6.31 Cyclic voltammograms for Pt(110) in 0.1 mol dm^{-3} $HClO_4$ at a sweep-rate of 0.050 V s^{-1} and in the presence of G$^+$ at the concentrations indicated; voltammograms were recorded on the third cycle.

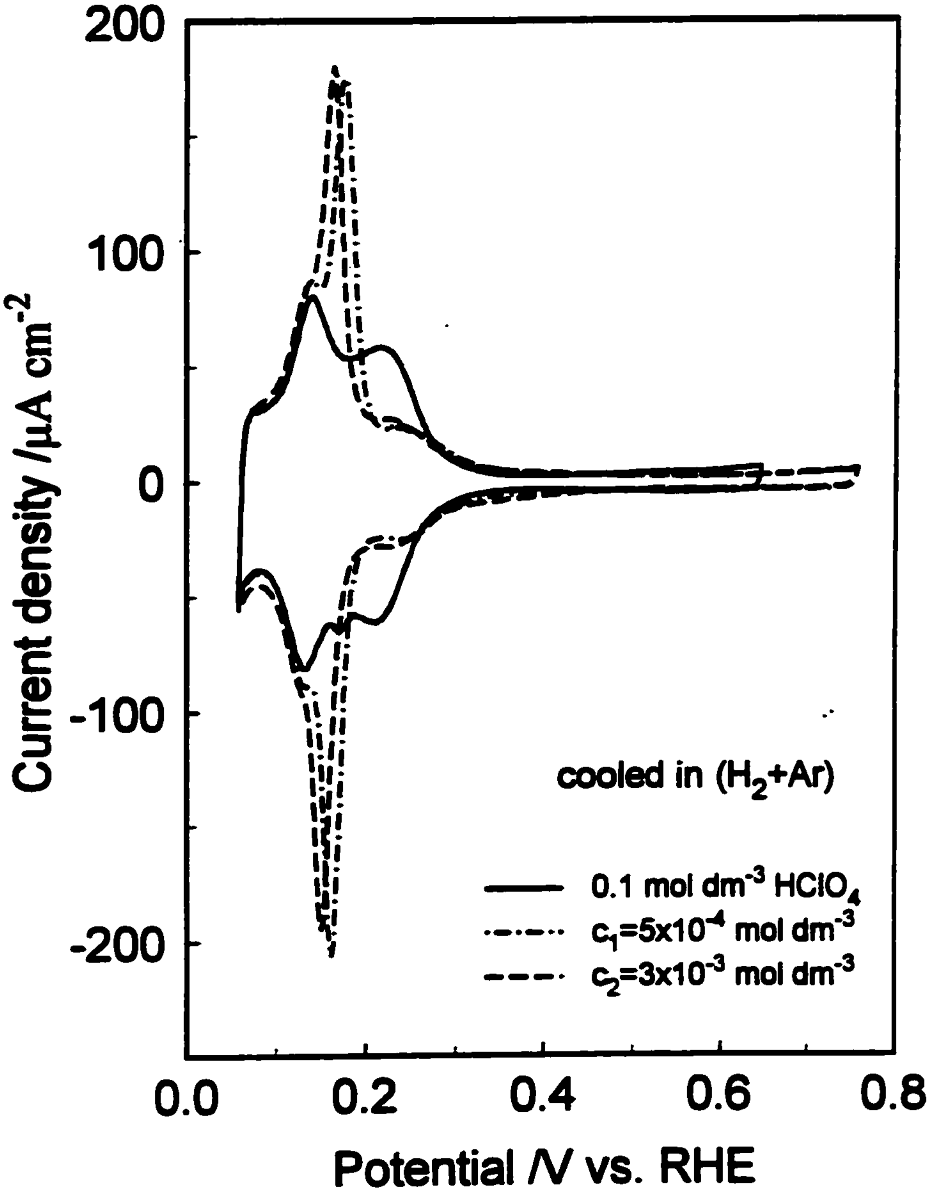

Fig. 6.32 Cyclic voltammograms for Pt(110) in 0.1 mol dm^{-3} HClO$_4$ at a sweep-rate of 0.050 V s^{-1} and in the presence of AA$^+$ at the concentrations indicated; voltammograms were recorded on the third cycle.

6.1.4 Adsorption behaviour at the Pt(110) surface

6.1.4.1 Behaviour in H_2SO_4 and $HClO_4$

At the Pt(110) surface, the effects of G^+ are quite small, with almost no changes of the anodic and cathodic peak potentials in both H_2SO_4 and $HClO_4$ electrolyte media (see Figs. 6.30 and 6.31, respectively). Thus, at the Pt(110) plane, G^+ adsorption is rather insignificant, probably owing to the particular 2[111]x[111] channelled lattice structure of this plane, where steric restrictions for accommodation of G^+ species would tend to play a key role in the adsorption process.

The behaviour of DMG^+ in H_2SO_4 and in $HClO_4$, and that of AA^+ in H_2SO_4 closely resembles that of G^+. However, the presence of AA^+ in $HClO_4$ solution leads to the "squeezing" of the voltammetric profile and increase of response current-densities, giving the voltammogram (Fig. 6.32) similar to that commonly obtained at the Pt(110) plane in 0.5 mol dm^{-3} H_2SO_4 (see also Table 6.3 for charge analysis).

6.1.4.2 Behaviour in NaOH

Unlike the behaviour in acids, in 0.1 mol dm^{-3} NaOH, the presence of G^+ leads to a substantial displacement of the current-response voltammetric profiles for the (110) plane, again to less positive potentials, by *ca.* 0.20 V (Fig. 6.33).

In NaOH, the Pt(111) plane is the only surface where the UPD H region is separated from that for adsorption of the OH anions (see Fig. 6.17) by a double-layer charging region while at Pt(110), desorption of hydrogen is immediately followed by the adsorption of oxygen-like species [15]. Hence, for the Pt(110) plane, effects due to a

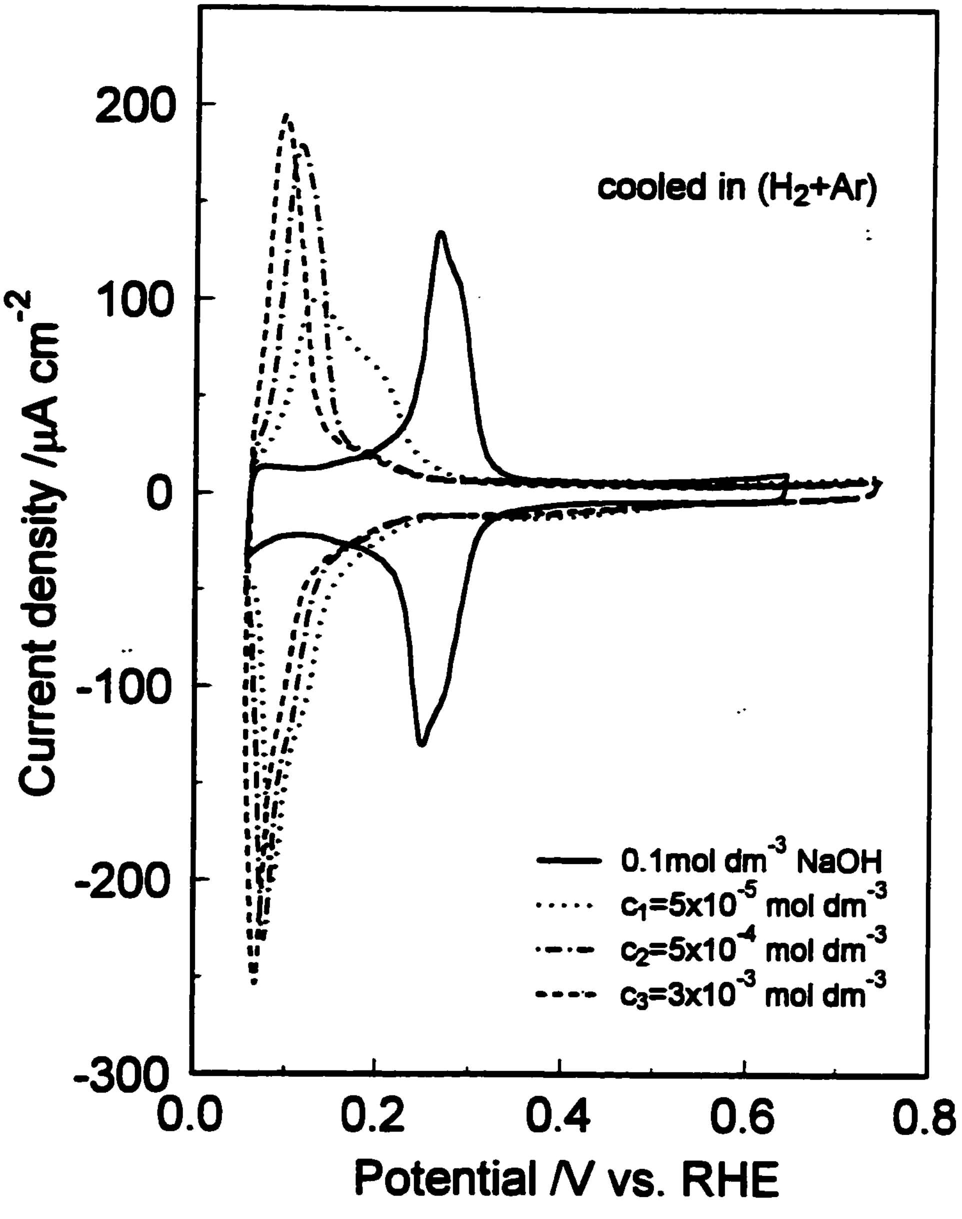

Fig. 6.33 Cyclic voltammograms for Pt(110) in 0.1 mol dm^{-3} NaOH at a sweep-rate of 0.050 V s^{-1} and in the presence of G^+ at the concentrations indicated; voltammograms were recorded on the third cycle.

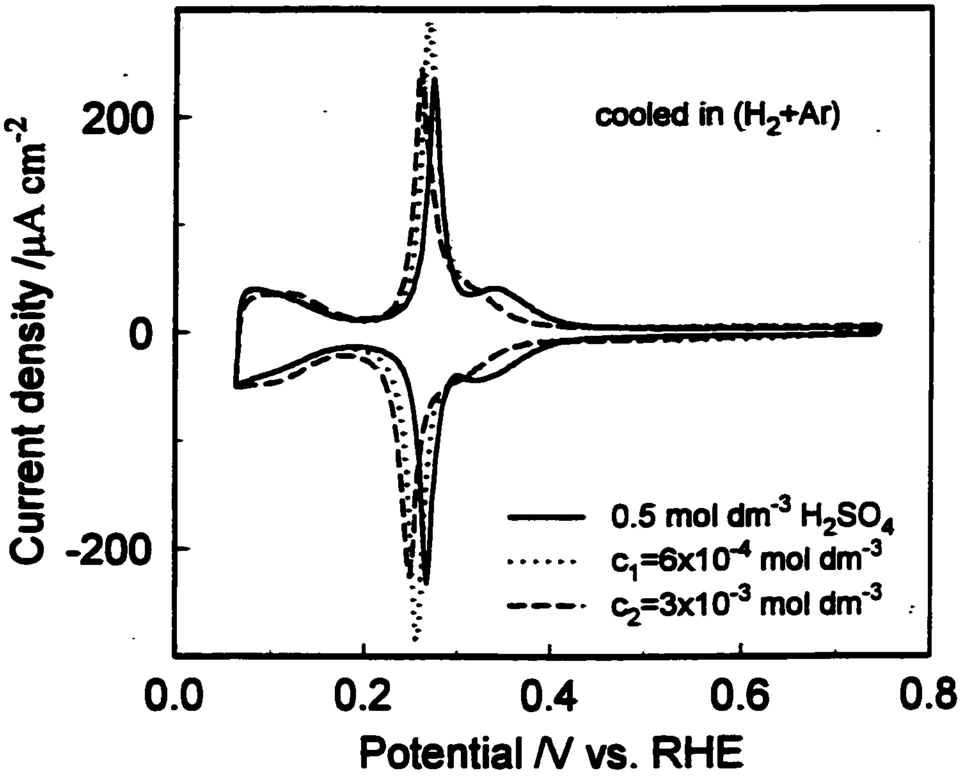

Fig. 6.34 Cyclic voltammograms for Pt(511) in 0.5 mol dm^{-3} H_2SO_4 at a sweep-rate of 0.050 V s^{-1} and in the presence of G^+ at the concentrations indicated; voltammograms were recorded on the third cycle.

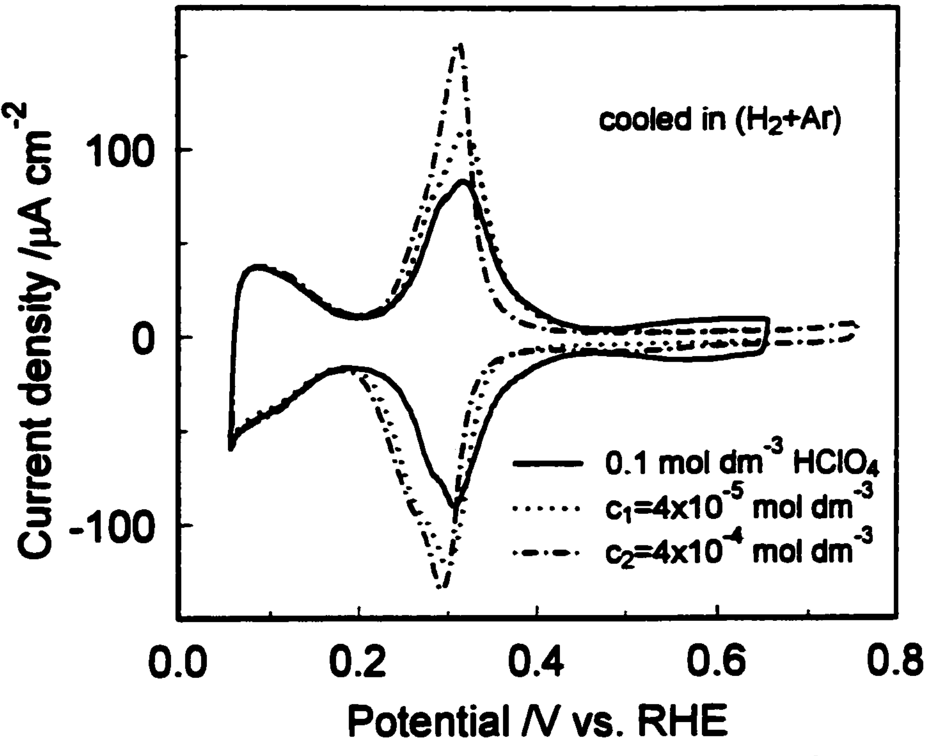

Fig. 6.35 Cyclic voltammograms for Pt(511) in 0.1 mol dm^{-3} $HClO_4$ at a sweep-rate of 0.050 V s^{-1} and in the presence of G^+ at the concentrations indicated; voltammograms were recorded on the third cycle.

significant ion-pairing between the G^+ and OH^- species can be observed. The fact that (compared with the behaviour in H_2SO_4), such a significant shift of the voltammetric charge towards the H_2 reversible electrode is observed in NaOH, reflects the respective shift of the UPD adsorption region in the latter medium towards more positive potentials, by *ca.* 130 mV. Moreover, adsorption of G^+ (as observed at the Pt(110) plane in NaOH) may also suggest that in the presence of substantially smaller anions (OH^-), accommodation of the G^+ cations on the Pt(110) plane can become enhanced.

The behaviour of DMG^+ and AA^+ is qualitatively similar to that of G^+; however, for these two species, smaller charges are passed.

6.1.5 Adsorption behaviour at the Pt(511) stepped surface

6.1.5.1 Behaviour in H_2SO_4 and $HClO_4$

The effects of G^+ are quite pronounced at the stepped Pt(511) surface, in both H_2SO_4 and $HClO_4$ solutions (see Figs. 6.34 and 6.35, respectively). In both cases, substantial changes are observed over the (100) component region (*ca.* 0.20-0.40 V) for that plane. Nonetheless, the observed shifts of the voltammetric profiles are less significant than those at the Pt(100) surface. This is probably because the (511) plane (3[100]x[111]) offers only short terraces, sterically restricting (beyond some extent) accommodation of G^+ with the HSO_4^- (or ClO_4^-) ions together on those elements of that Pt surface (see also Table 6.4 for charge analysis).

The behaviour of DMG^+ in H_2SO_4 and in $HClO_4$, and also the corresponding behaviour of AA^+ in H_2SO_4 and in $HClO_4$ (Fig. 6.36), is again qualitatively similar to that

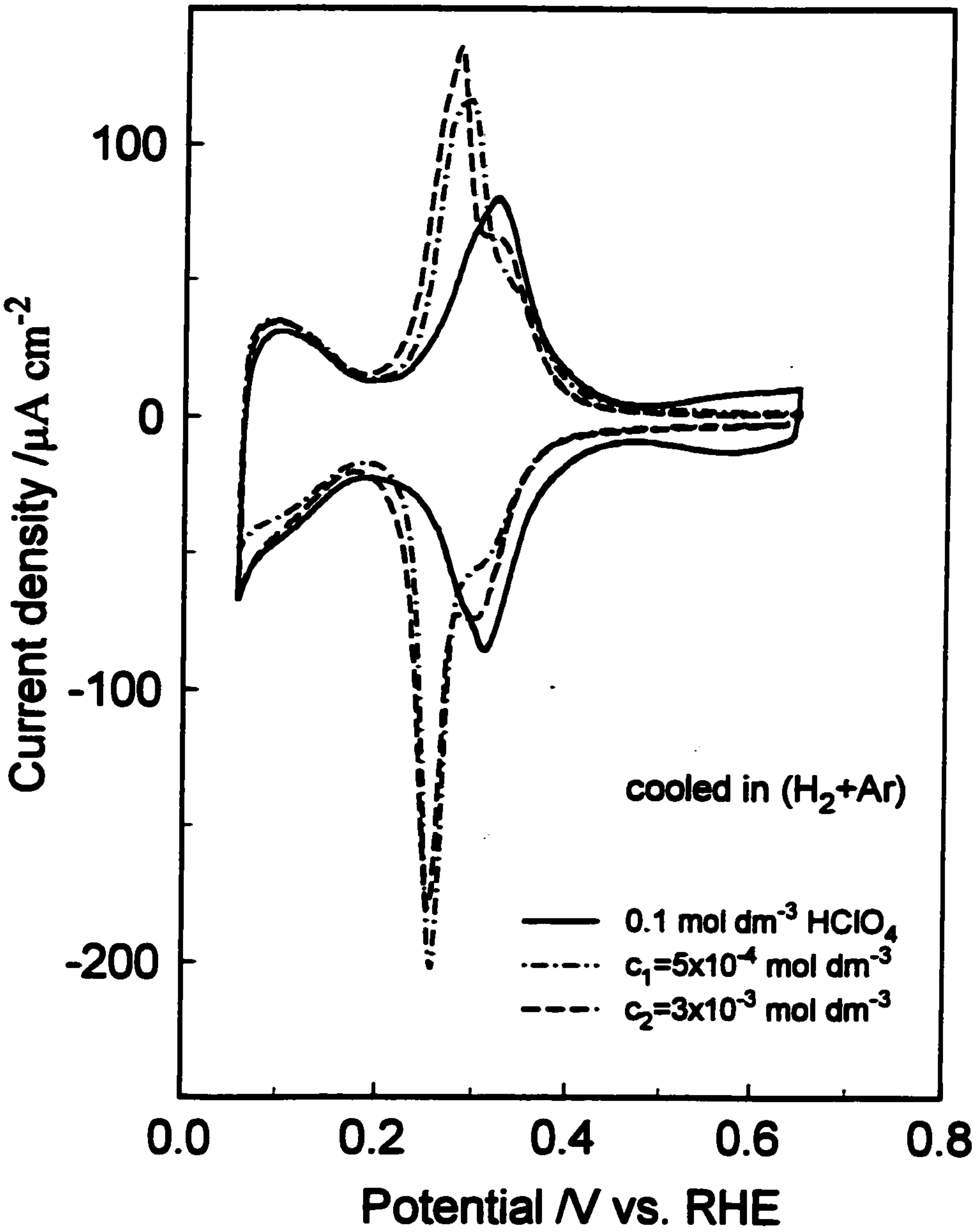

Fig. 6.36 Cyclic voltammograms for Pt(511) in 0.1 mol dm^{-3} $HClO_4$ at a sweep-rate of 0.050 V s^{-1} and in the presence of AA^+ at the concentrations indicated; voltammograms were recorded on the third cycle.

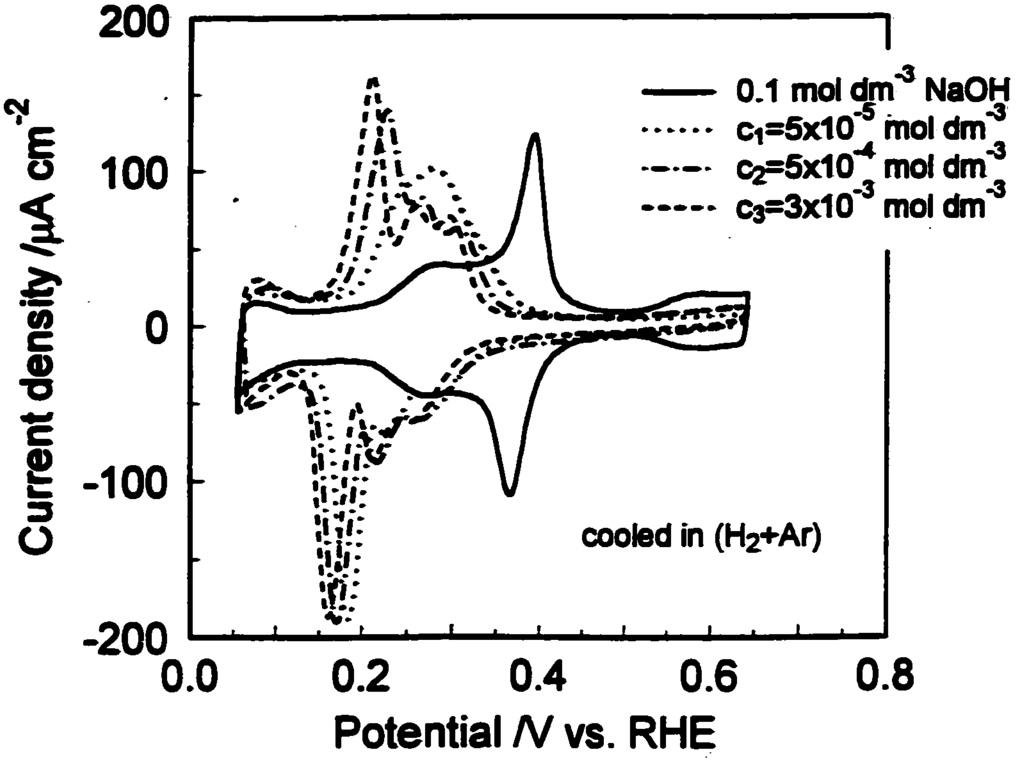

Fig. 6.37 Cyclic voltammograms for Pt(511) in 0.1 mol dm^{-3} NaOH at a sweep-rate of 0.050 V s^{-1} and in the presence of G^+ at the concentrations indicated; voltammograms were recorded on the third cycle.

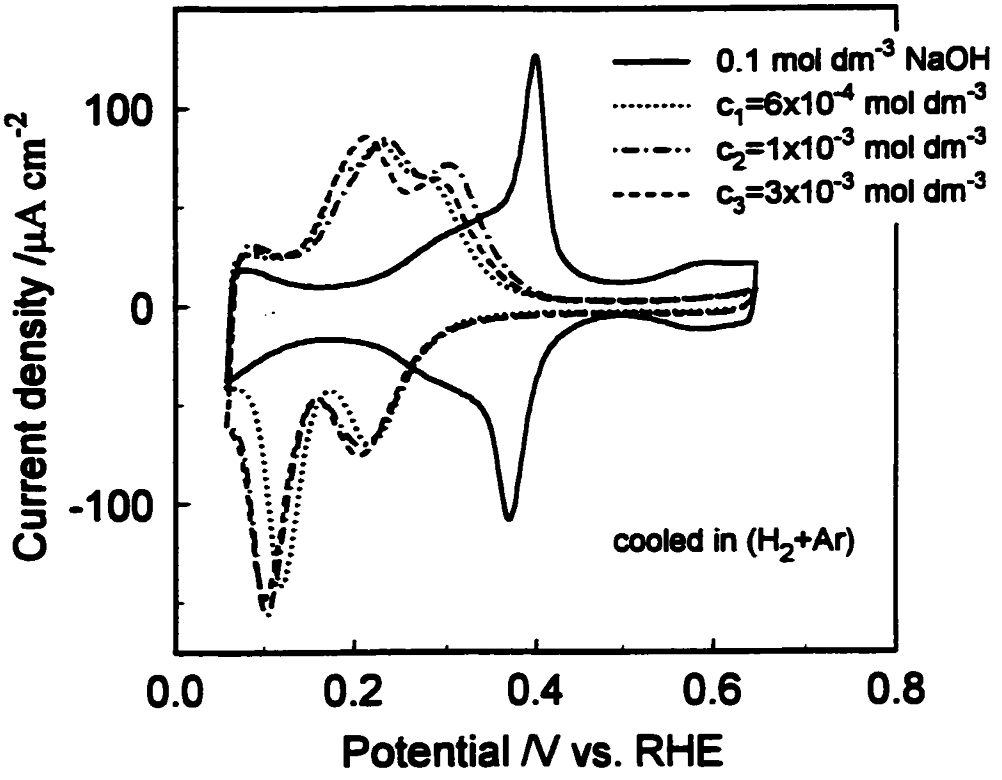

Fig. 6.38 Cyclic voltammograms for Pt(511) in 0.1 mol dm^{-3} NaOH at a sweep-rate of 0.050 V s^{-1} and in the presence of AA^+ at the concentrations indicated; voltammograms were recorded on the third cycle.

Table 6.1 Measured voltammetric charge-densities for the Pt(111) surface in 0.5 mol dm^{-3} H_2SO_4, 0.1 mol dm^{-3} $HClO_4$ and 0.1 mol dm^{-3} NaOH, and in the presence of G^+/DMG^+/AA^+ species in the solutions, at the concentrations indicated.

Total voltammetric charge densities, q$^{a)}$/μC cm^{-2} **0.5 mol dm^{-3} H_2SO_4; [G_i^+], [DMG_i^+], [AA_i^+] = mol dm^{-3}**				
0.5 mol dm^{-3} H_2SO_4	G_1^+=6x10^{-5}	G_2^+=6x10^{-4}	G_3^+=3x10^{-3}	Increase in q$^{b)}$/% G_1^+/G_2^+/G_3^+
241	252	261	226	4.5/8.3/-6.2
	DMG_1^+=6x10^{-5}	DMG_2^+=6x10^{-4}		DMG_1^+/DMG_2^+
241	261	233		8.3/-3.3
		AA_1^+=6x10^{-4}	AA_2^+=1x10^{-3}	AA_1^+/AA_2^+
241		258	238	7.0/-1.2
0.1 mol dm^{-3} $HClO_4$				
0.1 mol dm^{-3} $HClO_4$	G_1^+=4x10^{-5}	G_2^+=4x10^{-4}		Increase in q$^{b)}$/% G_1^+/G_2^+
262	258	280$^{c)}$		-1.5/6.9
		AA_1^+=5x10^{-4}	AA_2^+=3x10^{-3}	AA_1^+/AA_2^+
244		225	257	-7.8/5.3
0.1 mol dm^{-3} NaOH				
0.1 mol dm^{-3} NaOH	G_1^+=5x10^{-5}	G_2^+=5x10^{-4}	G_3^+=3x10^{-3}	Increase in q$^{b)}$/% G_1^+/G_2^+/ G_3^+
282	288	298	292$^{d)}$	2.1/5.7/3.5
	DMG_1^+=6x10^{-4}	DMG_2^+=1x10^{-3}	DMG_3^+=3x10^{-3}	DMG_1^+/DMG_2^+/DMG_3^+
282	291	294	299$^{e)}$	3.2/4.2/6.0
		AA_1^+=6x10^{-4}	AA_2^+=3x10^{-3}	AA_1^+/AA_2^+
278		290	298	4.3/7.2

a) Charges calculated after correction for the double-layer charge contribution (± 3%); general integration range 0.060-0.750 or 0.890 V vs. RHE (for the Pt(111) surface in $HClO_4$ and NaOH solutions), see also Tables 6.2 to 6.4 below.

b) Increase above the total charge in G^+, DMG^+ or AA^+-free solutions; usually third cycle was recorded for quantitative measurements (see also Tables 6.2 to 6.4 below).

c) q=115 μC cm^{-2}, as integrated from the respective voltammogram, over the potential range *ca.* 0.40-0.72 V.

d) q=170 μC cm^{-2}, as integrated from the respective voltammogram, over the potential range *ca.* 0.25-0.60 V.

e) q=122 and 55 μC cm^{-2}, as integrated from the respective voltammogram, over the potential range 0.26-0.50 V and 0.65-0.90V, respectively.

Table 6.2 Measured voltammetric charge-densities for Pt(100) surface in 0.5 mol dm^{-3} H_2SO_4, 0.1 mol dm^{-3} $HClO_4$ and 0.1 mol dm^{-3} NaOH, and in the presence of G^+/DMG^+/AA^+ species in the solutions, at the concentrations indicated.

Total voltammetric charge densities, q a)/μC cm^{-2} **0.5 mol dm^{-3} H_2SO_4; [G_i^+], [DMG_i^+], [AA_i^+] = mol dm^{-3}**				
0.5 mol dm^{-3} H_2SO_4	G_1^+=6x10^{-5}	G_2^+=6x10^{-4}	G_3^+=3x10^{-3}	Increase in q b)/% G_1^+/G_2^+/G_3^+
215	262	271	256	21.9/26.0/19.1
	DMG_1^+=6x10^{-5}	DMG_2^+=6x10^{-4}		DMG_1^+/DMG_2^+
215	241	249		12.1/15.8
		AA_1^+=6x10^{-4}	AA_2^+=1x10^{-3}	AA_1^+/AA_2^+
216		261	269	20.8/24.5
0.1 mol dm^{-3} $HClO_4$				
0.1 mol dm^{-3} $HClO_4$	G_1^+=4x10^{-5}	G_2^+=4x10^{-4}		Increase in q b)/% G_1^+/G_2^+
252	257	273		2.0/8.3
		AA_1^+=4x10^{-4}	AA_2^+=3x10^{-3}	AA_1^+/AA_2^+
248		294	302	18.5/21.8

0.1 mol dm^{-3} NaOH				
0.1 mol dm^{-3} NaOH	$G_1^+=5x10^{-5}$	$G_2^+=5x10^{-4}$	$G_3^+=3x10^{-3}$	Increase in $q^{b)}$/% $G_1^+/G_2^+/G_3^+$
273	301	329	332	10.2/20.5/21.6
		$AA_1^+=5x10^{-4}$	$AA_2^+=3x10^{-3}$	AA_1^+/AA_2^+
266		296	317	11.3/19.2

Table 6.2 Continuation.

Table 6.3 Measured voltammetric charge-densities for Pt(110) surface in 0.5 mol dm^{-3} H_2SO_4, 0.1 mol dm^{-3} $HClO_4$ and 0.1 mol dm^{-3} NaOH, and in the presence of G^+/AA^+ species in the solutions, at the concentrations indicated.

Total voltammetric charge densities, $q^{a)}$/μC cm^{-2} **0.5 mol dm^{-3} H_2SO_4; $[G_i^+]$, $[AA_i^+]$ = mol dm^{-3}**				
0.5 mol dm^{-3} H_2SO_4	$G_1^+=6x10^{-5}$	$G_2^+=6x10^{-4}$	$G_3^+=3x10^{-3}$	Increase in $q^{b)}$/% $G_1^+/G_2^+/G_3^+$
217	221	227	219	1.8/4.6/0.9
		$AA_1^+=6x10^{-4}$	$AA_2^+=1x10^{-3}$	AA_1^+/AA_2^+
214		234	251	9.3/17.3
0.1 mol dm^{-3} $HClO_4$				
0.1 mol dm^{-3} $HClO_4$	$G_1^+=4x10^{-5}$	$G_2^+=4x10^{-4}$		Increase in $q^{b)}$/% G_1^+/G_2^+
216	207	243		-4.2/12.5
		$AA_1^+=5x10^{-4}$	$AA_2^+=3x10^{-3}$	AA_1^+/AA_2^+
220		249	246	13.2/11.8
0.1 mol dm^{-3} NaOH				
0.1 mol dm^{-3} NaOH	$G_1^+=5x10^{-5}$	$G_2^+=5x10^{-4}$	$G_3^+=3x10^{-3}$	Increase in $q^{b)}$/% $G_1^+/G_2^+/G_3^+$

206	248	240	228	20.4/16.5/10.7
		$AA_1^+=6x10^{-4}$	$AA_2^+=3x10^{-3}$	AA_1^+/AA_2^+
206		142	114	-31.1/-44.7

Table 6.3 Continuation.

Table 6.4 Measured voltammetric charge-densities for Pt(511) surface in 0.5 mol dm^{-3} H_2SO_4, 0.1 mol dm^{-3} $HClO_4$ and 0.1 mol dm^{-3} NaOH, and in the presence of G^+/AA^+ species in the solutions, at the concentrations indicated.

Total voltammetric charge densities, $q^{a)}/\mu C\ cm^{-2}$ **0.5 mol dm^{-3} H_2SO_4; $[G_i^+]$, $[AA_i^+]$ = mol dm^{-3}**				
0.5 mol dm^{-3} H_2SO_4		$G_1^+=6x10^{-4}$	$G_2^+=3x10^{-3}$	Increase in $q^{b)}$/% G_1^+/G_2^+
245		246	273	0.4/11.4
		$AA_1^+=6x10^{-4}$	$AA_2^+=1x10^{-3}$	AA_1^+/AA_2^+
243		278	281	14.4/15.6
0.1 mol dm^{-3} $HClO_4$				
0.1 mol dm^{-3} $HClO_4$	$G_1^+=4x10^{-5}$	$G_2^+=4x10^{-4}$		Increase in $q^{b)}$/% G_1^+/G_2^+
220	268	272		21.8/23.6
		$AA_1^+=5x10^{-4}$	$AA_2^+=3x10^{-3}$	AA_1^+/AA_2^+
223		273	301	22.4/35.0
0.1 mol dm^{-3} NaOH				
0.1 mol dm^{-3} NaOH	$G_1^+=5x10^{-5}$	$G_2^+=5x10^{-4}$	$G_3^+=3x10^{-3}$	Increase in $q^{b)}$/% $G_1^+/G_2^+/G_3^+$
232	287	303	294	23.7/30.6/26.7
		$AA_1^+=6x10^{-4}$	$AA_2^+=3x10^{-3}$	AA_1^+/AA_2^+
222		272	294	22.5/32.4

of G^+.

6.1.5.2 Behaviour in NaOH

At the Pt(511) surface, like at the (110) plane, again substantial shifts of the current-response profiles are observed (for similar reasons to those given in section 6.1.4.2 above) in the presence of G^+ (Fig. 6.37) and qualitatively similar effects are recorded for the structure-related DMG^+ and AA^+ species (see Fig. 6.38).

6.2 G^+/HSO_4^- and related interaction models

Despite its interest as a cation of unusual electronic character, little work had been done until recently [16] on G^+ adsorption on Pt electrodes. An early work [17] on the electrochemistry of guanidine demonstrated that catalytic reduction on Pt, presumably involving adsorbed H, does not take place. Such conditions would be similar to those for which UPD H would be present. Moreover, Baugh and Parsons [18] made a thorough study of co-adsorption of the G^+ cation, co-adsorbed with other cations and anions (e.g. Cl^-, Na^+) at the Hg electrode, and derived the concentration-dependence of its specifically adsorbed charge at surface charge-densities of -8 and -10 $\mu C\ cm^{-2}$. They recognised that the special structure of the G^+ ion probably prevented it from close association with the metal's surface in the double-layer.

However, the electrocatalytic properties of Pt substrates lead guanidine (as G^+) to undergo dissociative chemisorption at the single-crystal surfaces of Pt. In H_2SO_4, the process is co-operative with adsorption of HSO_4^- ions (the ion-pairing effect) and strongly depends on the bisulphate surface coverage.

Taking into account conclusions derived from the CV behaviour of G^+ presented in the previous section, and regarding the bonding geometry for this adsorbate, the reaction for electrosorption of the G^+ cation on Pt can be represented by the process **X** below:

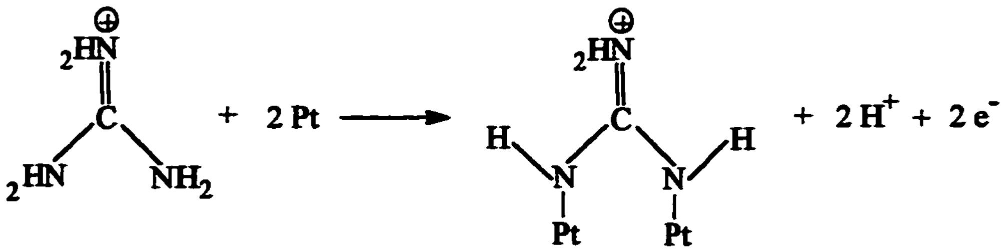

X

The G^+ cation becomes thus electrosorbed on the Pt surface in a 2-electron process, in a dissociatively chemisorbed state, i.e. with resulting electrooxidation of the dissociated H's, leading to the observed large positive charge-transients (see section 6.4 for details later).

The mechanism of ion-pairing between the G^+ and HSO_4^- at Pt(111) and the (100) plane, proposed in section 6.1, can be represented by the structures **XI** and **XII**, and the corresponding anticipated interaction between the G^+ and ClO_4^-, and OH^- anions at the Pt(111) plane by the structures **XIII** and **XIV**, respectively:

XI

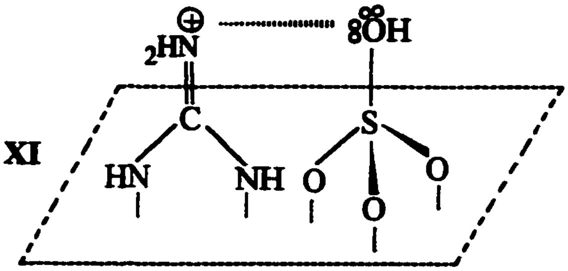

XII

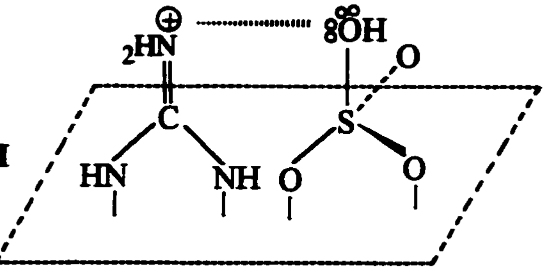

XIII

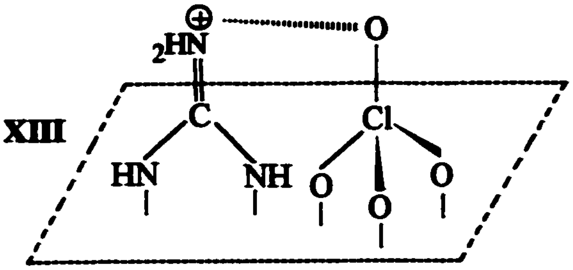

XIV

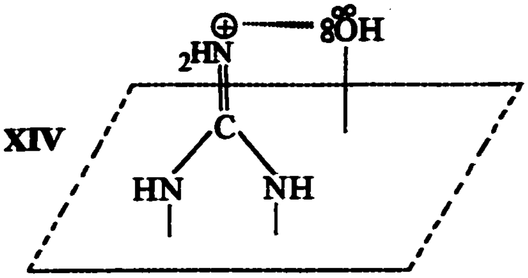

Similar interaction models can also be derived for structure-related analogues of G$^+$; namely, DMG$^+$, AA$^+$ and U, studied in this thesis. The proposed here co-operative chemisorption of DMG$^+$, AA$^+$ and U species with HSO_4^- at the Pt(111) surface is illustrated below by the structures **XV**, **XVI** and **XVII**, correspondingly:

XV

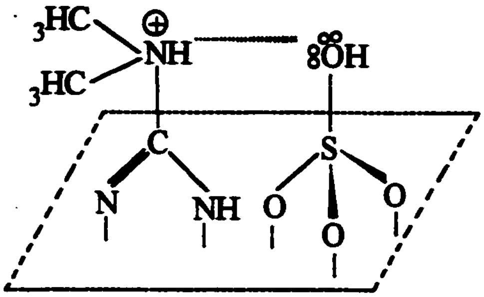

XVI

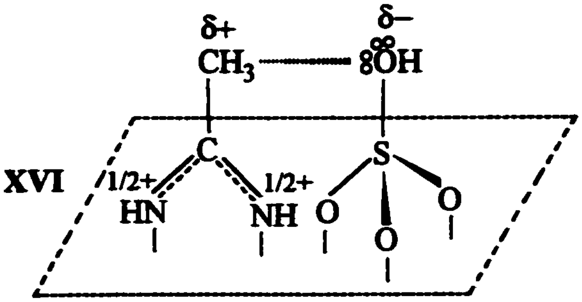

XVII

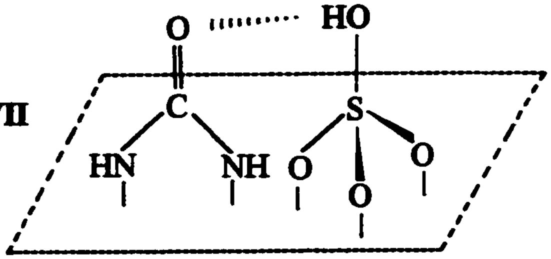

6.3 FTIR spectroscopy as a complementary procedure for characterisation of G^+/HSO_4^- and U adsorption on Pt single-crystal planes (evidence for the proposed interaction)

6.3.1 Cyclic voltammetry

Although it has not been a feature of a number of previous FTIR electrochemical spectroscopic papers, e.g. refs. 10, 11 and 19, it is regarded as desirable to show several typical voltammograms taken *in situ*, at the *actual* large-area, single-crystal electrodes used for the reflection-spectroscopy measurements. While the voltammograms are not so perfect as those separately obtained in previous works from this laboratory (cf. refs. 6, 16) using smaller, well-ordered single crystals, or in Clavilier's [20, 21], they clearly had the correct respective "signatures" for the selected single-crystal surfaces. The small deviations are due to edge effects, unavoidable when using large, commercially prepared, Pt crystals required for reflectance spectroscopy.

Cyclic voltammograms at the Pt(111) and Pt(100) single-crystal surfaces, obtained in pure 0.05 mol dm^{-3} H_2SO_4 and in the presence of guanidine, are presented in Figs. 6.39 and 6.40, respectively. Measurements were performed in the FTIR cell, in the hanging meniscus configuration. The principal features of the voltammograms for Pt(111) and (100), acquired in 0.05 mol dm^{-3} H_2SO_4 and in the presence of $3x10^{-3}$ mol dm^{-3} G^+ (Figs. 6.39 and 6.40), recorded in the FTIR cell, resemble, respectively, those previously shown in Figs. 6.11 and 6.22 for the smaller crystals prepared by Clavilier's method [22]. However, at the (111) surface, at a lower concentration of HSO_4^- anions (0.05 mol dm^{-3} acid), desorption of the latter species takes place over a relatively higher

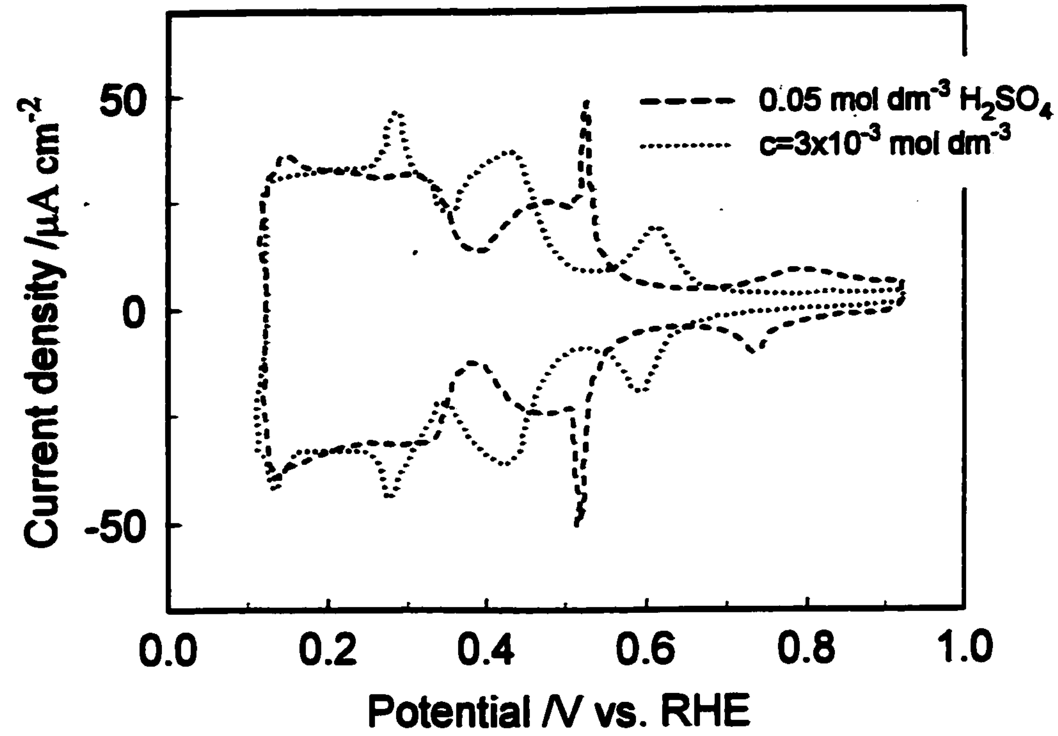

Fig. 6.39 Cyclic voltammograms for Pt(111) in 0.05 mol dm^{-3} H_2SO_4 at a sweep rate of 0.050 V s^{-1} and in the presence of G^+ at the concentration indicated, both recorded for the crystal in the FTIR cell; voltammograms were recorded on the third cycle.

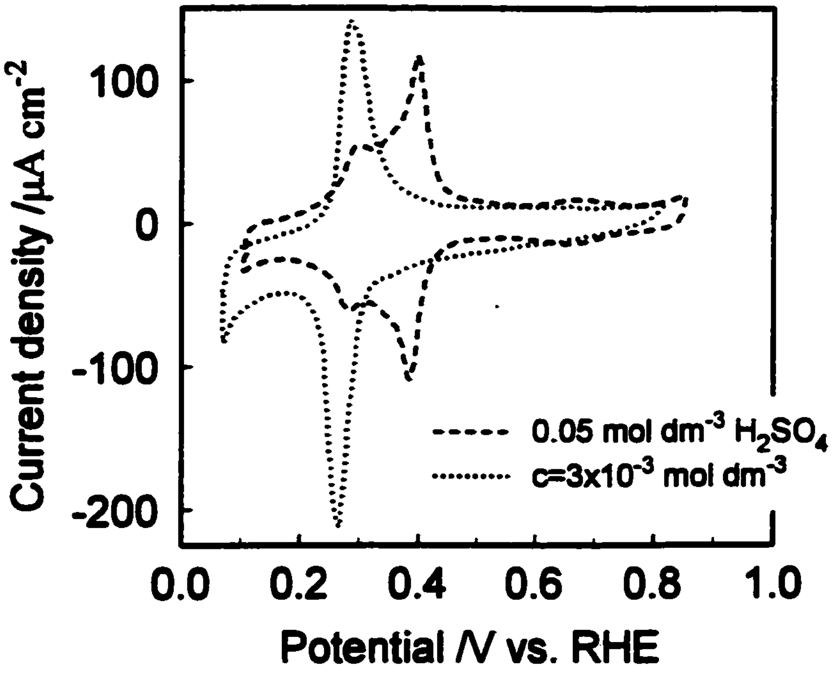

Fig. 6.40 Cyclic voltammograms for Pt(100) in 0.05 mol dm^{-3} H_2SO_4 at a sweep rate of 0.050 V s^{-1} and in the presence of G^+ at the concentration indicated, both recorded for the crystal in the FTIR cell; voltammograms were recorded on the third cycle.

positive potential range (*ca.* 0.5-0.3 V/RHE), compared with that in 0.5 mol dm^{-3} H_2SO_4 solution (see also section 6.1.2.1 above and Fig. 6.11).

6.3.2 IR spectral behaviour at the Pt(111) surface in 0.05 mol dm^{-3} H_2SO_4 and in the presence of G^+

The state of adsorption of sulphate (as bisulphate) ions on Pt(111) and other Pt single-crystal planes has been extensively studied by the FTIR technique [10, 11, 18, 23]. It is now evident that in H_2SO_4 solution, the HSO_4^- ion is the predominantly adsorbed anionic species on Pt at potentials negative to that for the initial stage of Pt oxide formation. On the Pt(111) surface, HSO_4^- is mainly adsorbed on three-fold sites and the strong IR band, observed at 1200-1300 cm^{-1}, corresponds to the asymmetric S-O HSO_4^- stretching mode [23]. In addition, in radiochemical investigations of HSO_4^- adsorption on Pt single-crystal electrodes, it was shown by Gamboa-Aldeco et al. [24], that the maximum adsorption of that anion on the (111) surface is already reached at *ca.* 0.50 V vs. Ag/AgCl. On the other hand, low coverages are reached only above 0.80 V vs. Ag/AgCl (thus beyond *ca.* 1.020 V on the RHE scale). Similarly, in another work, based on AES measurements at the Pt(111) plane, Thomas et al. [25] showed that HSO_4^- ion coverage reached its maximum value at *ca.* 0.70 V vs. Ag/AgCl, thus at about 0.92 V/RHE, almost independently of H_2SO_4 concentration. Moreover, Funtikov et al. [26] observed, by means of *in situ* STM at the Pt(111) surface in 0.05 mol dm^{-3} H_2SO_4, formation of an ordered ad-lattice of HSO_4^- in the potential range 0.50 to 0.75 V/RHE.

The first and basic aspect in this part of the present work (as in most other *in situ* FTIR studies at electrodes) was to ensure that the results refer to *surface*, not *solution* type species. This requires that only radiation having a *p*-component (i.e. parallel to the plane of incidence) experiences a finite interaction with a dynamic dipole of the adsorbed species having a component oriented normal to the surface plane. Hence the spectra for guanidine-containing 0.05 mol dm^{-3} H_2SO_4 solution, obtained with *s*- and *p*-polarised radiation, were compared at three different (low, intermediate and high) electrode potentials, as shown in Fig. 6.41. As expected, all the spectra obtained with *s*-polarised light were featureless; while significant modulation responses were seen only for *p*-polarisation.

Figures 6.42 and 6.43 show a comparative series of IR spectra for adsorbed HSO_4^- anions (6.42), and in the presence of the G^+ cations (6.43), obtained in 0.05 mol dm^{-3} H_2SO_4 at the Pt(111) surface. The spectra were obtained in *p*-polarised light and the reference potential was 140 mV/RHE. The series of spectra (Fig. 6.42) exhibit potential-dependence of a negative-going band observed in the frequency range 1200-1300 cm^{-1}. As already known [23], the predominant component of the 1200-1300 cm^{-1} band is for the trigonally co-ordinated bisulphate ion, where the frequency of the peak's centre is assigned to the asymmetric S-O stretch mode (see structure **XVIII** below):

XVIII

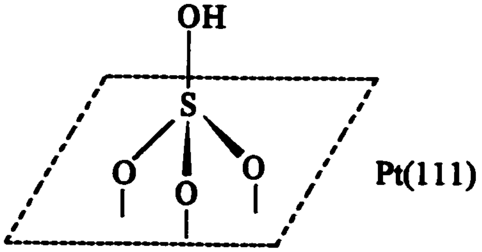

The band appears at a potential of 570 mV/RHE, which is just positive to the characteristic "butterfly" peak of the voltammogram (Fig. 6.39) of the (111) surface. As the electrode potential increases up to 970 mV/RHE, the intensity of this band increases corresponding to the continuing increase of coverage by the bisulphate ion [27] on the Pt(111) surface, behaviour which is consistent with conclusions from previous literature [10, 23-25] outlined above.

Fig. 6.43 shows a series of IR spectra obtained at the Pt(111) surface under the same conditions, but in the presence of the G^+ cations at a concentration of $3x10^{-3}$ mol dm^{-3}. At relatively low potentials (370-470 mV) only one, negative-going band is observed over the range 1200-1300 cm^{-1}. At 570 mV, however, another (broad) band appears (see section 6.3.3 below) in the IR spectrum, in the range 1500-1600 cm^{-1}. While two peaks are still observed at 620 mV, beyond that potential, however, only the broad band at 1500-1600 cm^{-1} remains which becomes intensified with increase of electrode potential.

6.3.3 *Discussion of the spectral results obtained at the Pt(111) surface in 0.05* mol dm^{-3} *H_2SO_4, in the presence of G^+*

The lower-frequency band (1200-1300 cm^{-1}), observed in Fig. 6.43, corresponds to the asymmetric stretch of the bisulphate ion chemisorbed on the Pt(111) surface, as in ref. 23 (see structure **XVIII** above). The broad band, observed in Fig. 6.43 over 1500-1600 cm^{-1}, can be assigned to the $C{=}N^+$ stretch of the guanidonium cation adsorbed on the Pt(111) surface. The characteristic vibrational group frequency for such a mode is in the range 1640-1690 cm^{-1} (aliphatic imines) [28, 29]. Moreover, Schiff's bases (RCH=NR), oximes, thiazoles, iminocarbonates and *guanidines* show a C=N stretch in the 1471-1689 cm^{-1} region [30]. Thus, assignment of the broad band in the region 1500-1600 cm^{-1} to the C=N stretching mode has a strong basis in the literature.

In the presence of G^+, a significant "bisulphate" band is already observed at 370 mV (Fig. 6.43) while, in its absence, the corresponding peak does not appear until a potential of 570 mV is reached (Fig. 6.42) but continues to be observed up to 970 mV. Thus, in the presence of G^+, the potential for HSO_4^- adsorption/desorption must have been shifted significantly (by about 200 mV) towards the H_2 reversible potential. Hence, we are dealing here with an attractive (stabilising adsorption) interaction between the chemisorbed HSO_4^- and G^+ ions on the Pt surface, as proposed above in section 6.1.2.1 on the basis of the CV results, thus confirming the latter's interpretation.

With G^+ in solution, depending on electrode potential, three adsorption stages can be distinguished, as follows: firstly, at potentials up to *ca.* 500 mV, observation of the 1200-1300 cm^{-1} band indicates that HSO_4^- ions are the preferentially adsorbed species on the Pt surface. Secondly, as progressively greater positive potentials are applied, G^+ cations become increasingly adsorbed at the surface and experience co-operative chemisorption with the already adsorbed HSO_4^- ions. In the chemisorbed state, there can then arise an electrostatic interaction between the species (cation-to-lone pair donor). The above discussion provides strong support for the mechanism proposed in section 6.1.2.1 for stabilisation of the HSO_4^- adsorption (see structure XI in section 6.2).

In the chemisorbed state, the charge on the $C=N^+$ group of G^+ will tend to become localised further from the surface (structure XI in section 6.2) providing diminished repulsion of the positive charge (carried by the G^+ ions) from the positively charged Pt surface. Additionally, the positive charge on the N atom is dispersed through the intermolecular, electrostatic ion-pairing interaction, as indicated from the spectra taken at intermediate electrode potentials (570 and 620 mV) where two peaks are then present in the spectra (Fig. 6.43). Thirdly, at high positive potentials, it appears from the experimental results observed in Fig. 6.43 that the HSO_4^- anions become replaced by adsorbed OH^- ions (see structure XIV in section 6.2).

In other words, adsorption of the HSO_4^- ions decreases as the adsorption of OH^- commences, as supposed by Iwasita et al. [11]. This is supported by disappearance of the HSO_4^- band from the spectra at 670 mV, suggesting that the HSO_4^- ions at the surface have been replaced by OH groups but to a level not detectable spectrometrically. It is rather difficult to assume that such an ion-pairing mechanism would be limited only to the HSO_4^- ion. Thus, a similar effect of stabilisation would be expected for OH^- adsorption, for which the potential of adsorption/desorption would also be shifted to less positive values by an interaction with G^+.

In addition to that, upon HSO_4^-/OH^- replacement, the coverage by chemisorbed G^+ cations increases on the Pt surface as indicated by intensification of the signal at 1500-1600 cm^{-1} (Fig. 6.43). This is because the G^+ cation can compete with the HSO_4^- and also the OH^- ion for free space sites made available after the HSO_4^- ion has become desorbed. Thus, it seems reasonable to associate the disappearance of the HSO_4^- band beyond *ca.* 620 mV (Fig. 6.43) partly with increased coverage of G^+ with increasing positive electrode potential. Eventually, at relatively high positive potentials (beyond 1.2 V, RHE), the 1500-1600 cm^{-1} band also disappears from the spectrum (not shown in Fig. 6.43), being the result of progressing surface oxidation of Pt.

In the case of the HSO_4^- band (Fig. 6.42), with increase of electrode potential, the peak's centre shifts to higher wave-numbers, e.g. from 1254 cm^{-1} at 570 mV to 1278 cm^{-1} at 970 mV. The measured slope of this electrochemical Stark effect is 64 cm^{-1} V^{-1}.

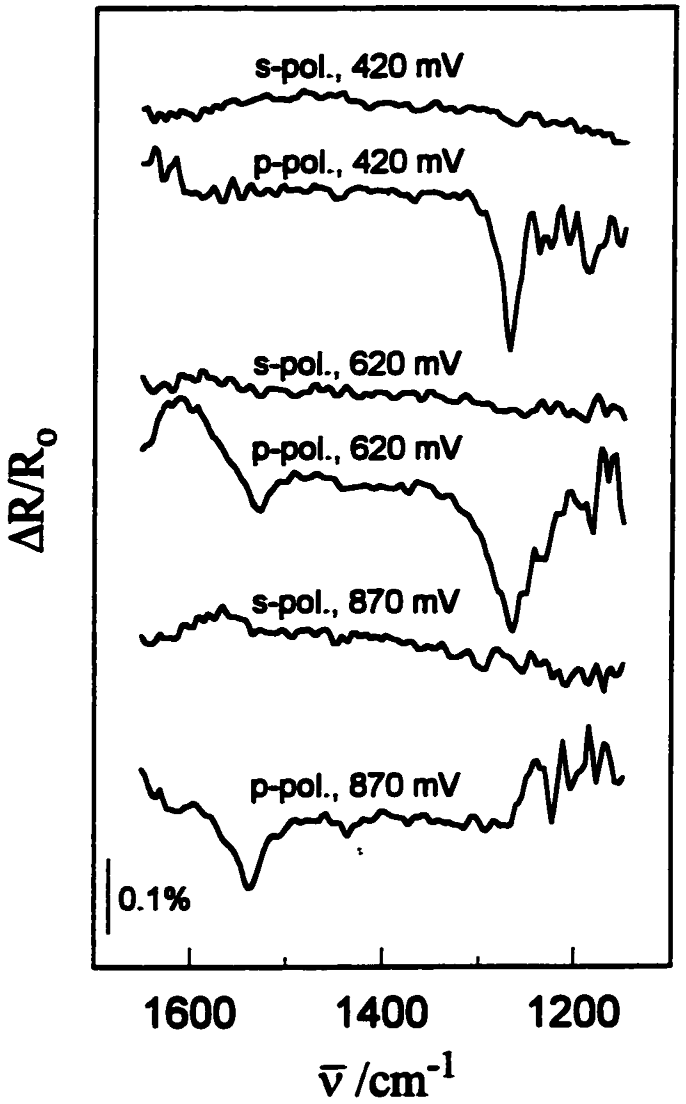

Fig. 6.41 Potential dependence, on the RHE scale, of *SNIFTIRS* spectra obtained at Pt(111) in 0.05 mol dm^{-3} H_2SO_4 and in the presence of G^+ at a concentration of 3x10^{-3} mol dm^{-3}; the reference potential was 140 mV/RHE; no. of scans 500; resolution 8 cm^{-1}; comparison of spectra obtained with *p*- and *s*-polarised mode of radiation.

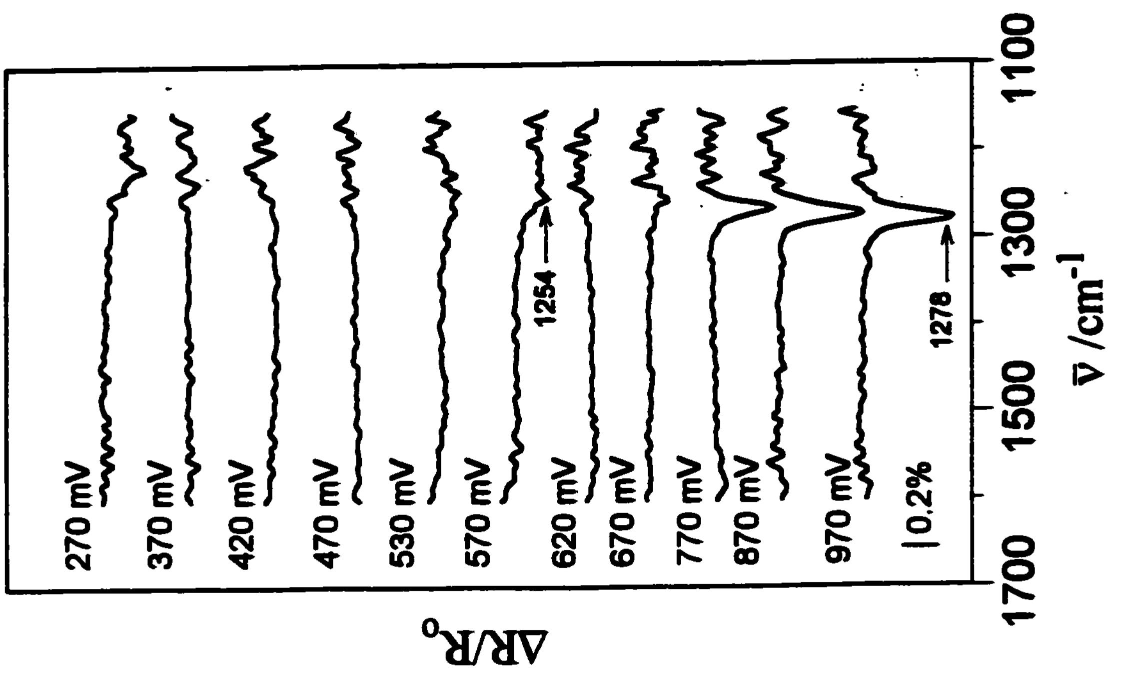

Fig. 6.42 Potential dependence, on the RHE scale, of *SNIFTIRS* spectra obtained at Pt(111) in 0.05 mol dm^{-3} H_2SO_4; the reference potential was 140 mV/RHE; no. of scans 500; resolution 8 cm^{-1}; *p*-polarised mode of radiation.

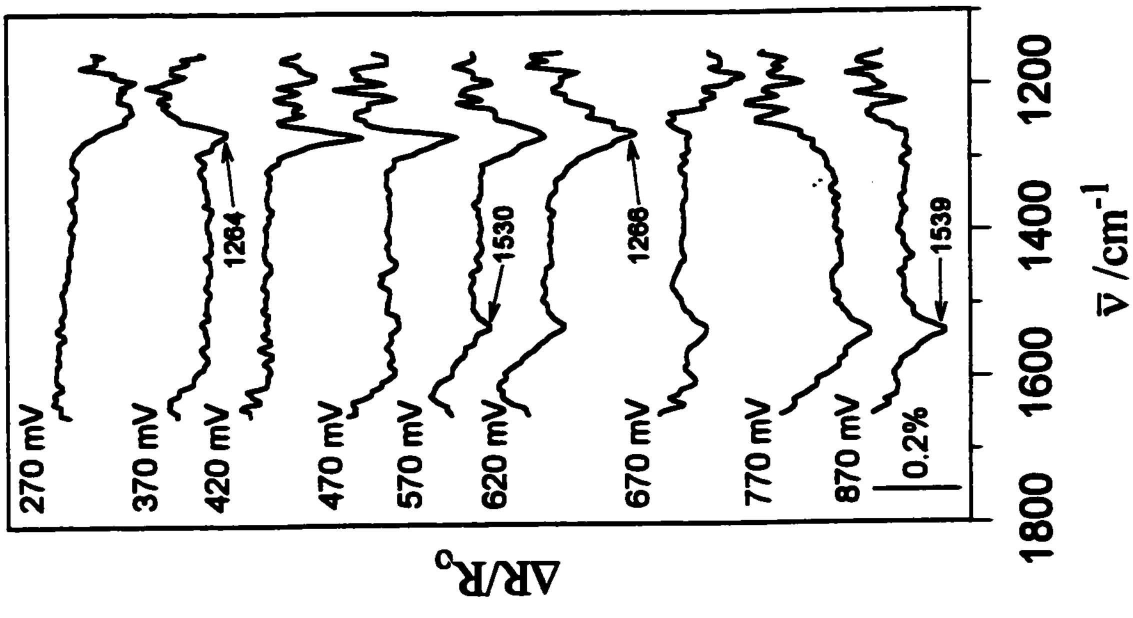

Fig. 6.43 Potential dependence, on the RHE scale, of *SNIFTIRS* spectra obtained at Pt(111) in 0.05 mol dm^{-3} H_2SO_4 and in the presence of G^+ at a concentration of $3x10^{-3}$ mol dm^{-3}; the reference potential was 140 mV/RHE; no. of scans 500; resolution 8 cm^{-1}; *p*-polarised mode of radiation.

However, when guanidine is co-adsorbed (Fig. 6.43), the position of the HSO_4^- band remains practically constant at 1267 cm^{-1} with changing potential. The virtual elimination of the Stark effect on the S-to-O bond frequency could be caused by the influence that the interaction of adsorbed G^+ with the adsorbed HSO_4^- has on the dipole moment of the S-O group, leading to its vibrational force constant remaining approximately invariant. The higher frequency band for G^+ (1500-1600 cm^{-1}) shows a small, but significant, shift of the peak's centre from 1530 cm^{-1} at 570 mV to 1539 cm^{-1} at 870 mV.

6.3.4 *IR spectral behaviour at the Pt(100) surface in 0.05 mol* dm^{-3} H_2SO_4 *and in the presence of* G^+

A similar series of spectral measurements to those at Pt(111) were conducted at the Pt(100) plane as shown in Fig. 6.44, using a reference potential of 130 mV/RHE. Generally similar behaviour to that for the Pt(111) surface is observed, although HSO_4^- ion exhibits, understandably, only two-fold co-ordination at the Pt(100) surface [11] resulting in an HSO_4^- coverage of the Pt(100) plane corresponding to only about 25% (determined by displacement by CO) of the total electric charge measured [12] from the voltammogram compared with about 34% on the Pt(111) surface, and thus to about 50% of the actual Pt(100) surface sites being covered by HSO_4^- ions (see also section 6.1.3.1 above). Hence, the intensity of the HSO_4^- band is substantially weaker at Pt(100) than that at the Pt(111) plane; it also undergoes significant diminution as the electrode potential increases (Fig. 6.44). The spectral position of the HSO_4^- peak on the Pt(100) surface differs only from that on the (111) plane by a small but significant negative shift of the HSO_4^- band by *ca.* 30 cm^{-1}.

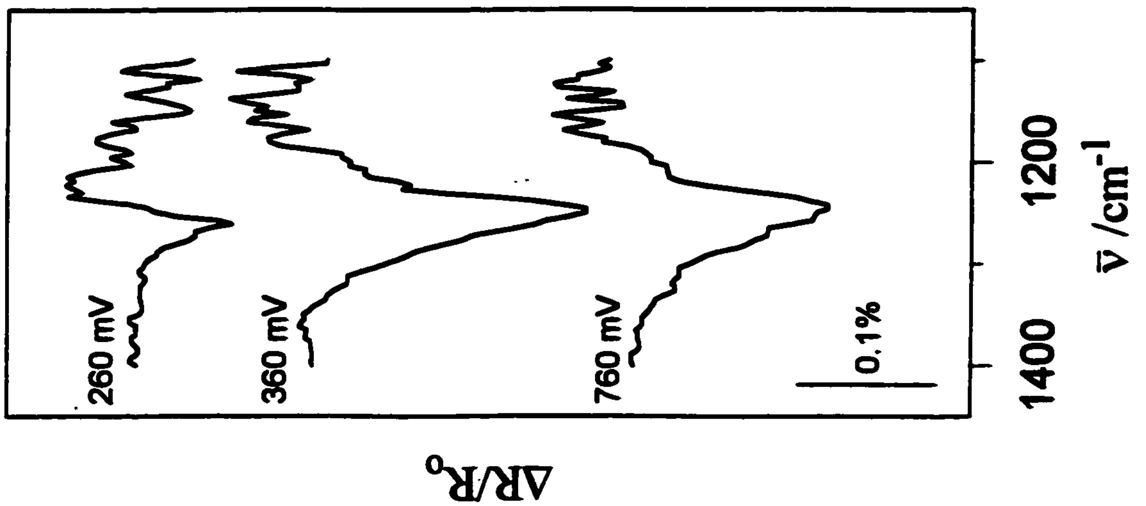

Fig. 6.44 Potential dependence, on the RHE scale, of *SNIFTIRS* spectra obtained at Pt(100) in 0.05 mol dm^{-3} H_2SO_4; the reference potential was 130 mV/RHE; no. of scans 200; resolution 8 cm^{-1}; *p*-polarised mode of radiation.

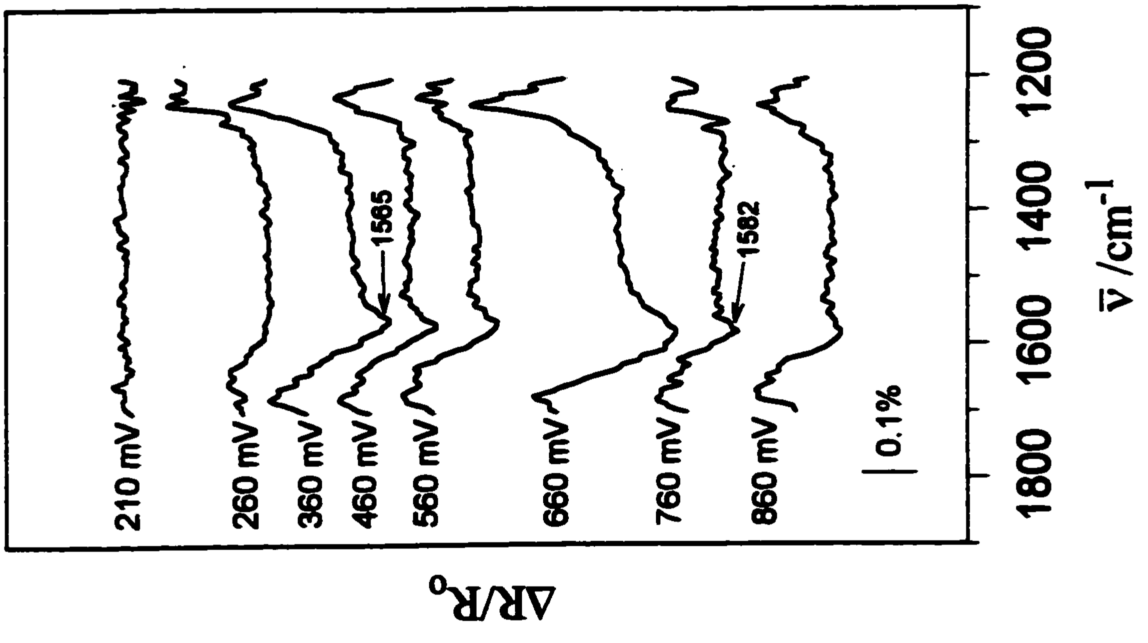

Fig. 6.45 Potential dependence, on the RHE scale, of *SNIFTIRS* spectra obtained at Pt(100) in 0.05 mol dm^{-3} H_2SO_4 and in the presence of G^+ at a concentration of 3×10^{-3} mol dm^{-3}; the reference potential was 100 mV/RHE; no. of scans 200; resolution 8 cm^{-1}; *p*-polarised mode of radiation.

Consequently, in the case of the G^+-containing solution ($3x10^{-3}$ mol dm^{-3} G^+), only the broad, higher-frequency band (1500-1600 cm^{-1}) is observable (Fig. 6.45). In comparison with the behaviour at the Pt(111) surface, the peak's centre is shifted positively by *ca.* 40 cm^{-1}. For this case, the model for interaction of G^+ cations with the Pt(100) surface and adsorbed HSO_4^- ions will be analogous to the structure **XI**, for the Pt(111) surface, but with the HSO_4^- anion being adsorbed in two-fold co-ordination [11] (see structure **XII** in section 6.2).

6.3.5 Comparative IR spectral behaviour at the Pt(100) and Pt(111) surfaces in 0.05 mol dm^{-3} H_2SO_4, in the presence of urea

Amongst the series of small organic adsorbates that have been studied at Pt, urea (U) is closest in structure to that of G or DMG. Its adsorption behaviour was therefore examined spectroscopically at Pt(100) and (111) surfaces in relation to its voltammetry response described in sections 6.1.3.1 and 6.1.2.1, respectively, and in comparison with the effects of adsorption of G^+ species.

In their recent work, Climent et al. [4] reported an *in situ* FTIR and CV study on adsorption of U from 0.1 mol dm^{-3} $HClO_4$ at the Pt(100) surface and showed that it becomes dissociatively electrosorbed on the Pt surface with release of $2H^+ + 2e^-$. Similar CV experiments on adsorption of U in $HClO_4$ at various low-index Pt surfaces were reported by Rubel et al. [31].

In the present work, two series of comparative experiments were performed with U in 0.05 mol dm^{-3} H_2SO_4 solution at both the Pt(100) and (111) surfaces. Fig. 6.46 shows three IR spectra obtained at the Pt(100) surface in 0.05 mol dm^{-3} H_2SO_4, in the

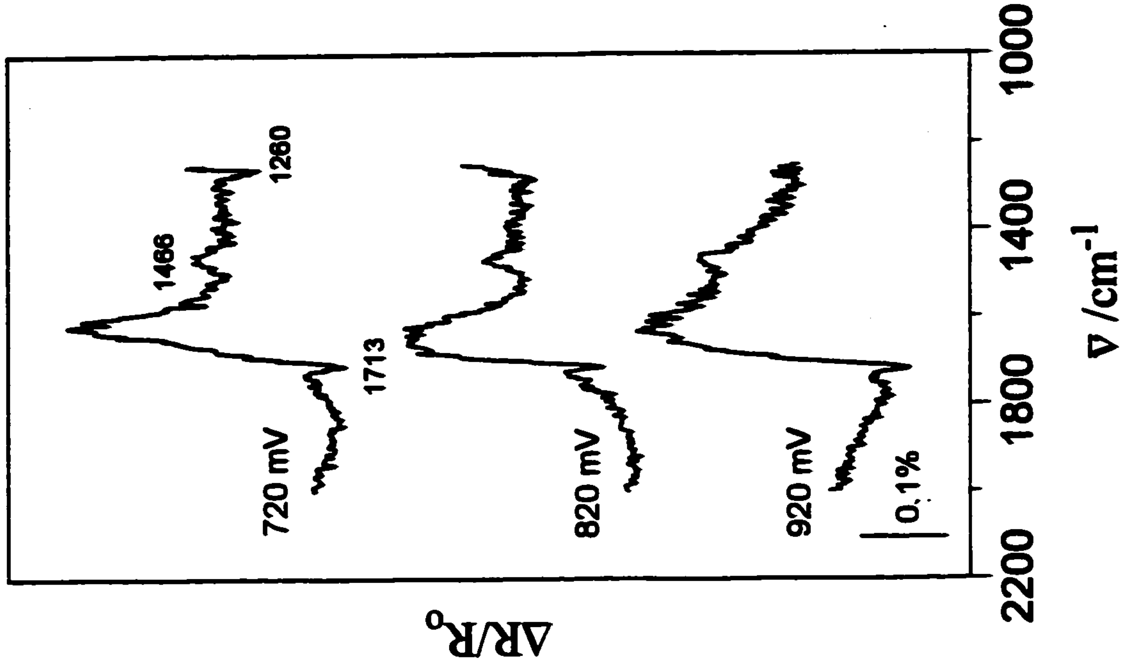

Fig. 6.46 Potential dependence, on the RHE scale, of *SNIFTIRS* spectra obtained at Pt(100) in 0.05 mol dm^{-3} H_2SO_4 in the presence of U at a concentration of 3x10^{-3} mol dm^{-3}; the reference potential was 120 mV/RHE; no. of scans 200; resolution 8 cm^{-1}; *p*-polarised mode of radiation.

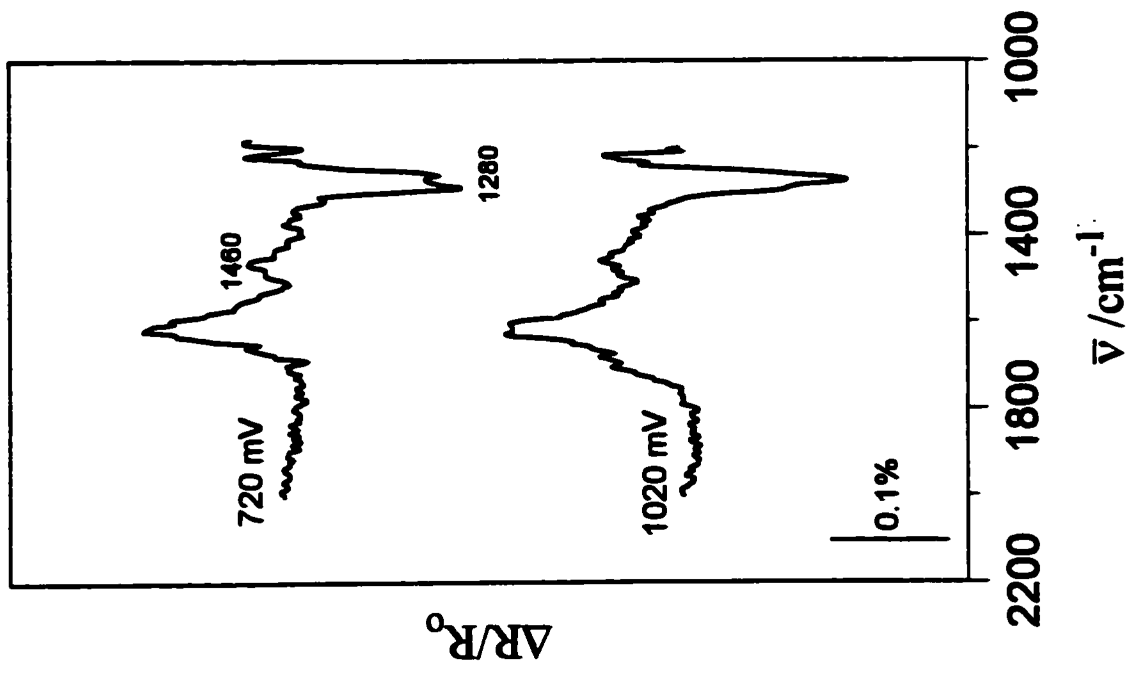

Fig. 6.47 Potential dependence, on the RHE scale, of *SNIFTIRS* spectra obtained at Pt(111) in 0.05 mol dm^{-3} H_2SO_4 in the presence of U at a concentration of 3x10^{-3} mol dm^{-3}; the reference potential was 120 mV/RHE; no. of scans 200; resolution 8 cm^{-1}; *p*-polarised mode of radiation.

presence of urea at a concentration of 3×10^{-3} mol dm^{-3}. Major features seen in these spectra (also shown in Fig. 5 of ref. 4) are a sharp, negative-going band at *ca.* 1713 cm^{-1} and a positive-going band at *ca.* 1465 cm^{-1}. The former (1713 cm^{-1}) frequency corresponds to the C=O stretching mode of adsorbed urea and the latter to the C-N stretch of urea, reflecting the supposed consumption of the species in solution when it becomes adsorbed at the sample potential [4]. Correspondingly, Fig. 6.47 shows two IR spectra obtained under the same conditions but at the Pt(111) surface. Here, an HSO_4^- peak (barely seen in Fig. 6.46) has very strong intensity, even at 1020 mV/RHE. The C=O stretching mode, on the other hand, cannot be reliably identified in either of the spectra of Fig. 6.47, implying that chemisorption of urea on the Pt(111) surface is spectrometrically undetectable (unlike that for the Pt(100) plane), presumably because of the considerably greater site-occupancy already by HSO_4^- on the Pt(111) surface.

6.4 Dissociative chemisorption of G^+ and U: charge-transients upon adsorption of, and adsorbate displacement by CO

6.4.1 Adsorption charge transients

The results obtained from *in situ* FTIR measurements indicate that both G^+ and U (detectable only on the Pt(100) surface) become chemisorbed on the Pt(111) and (100) surfaces in 0.05 mol dm^{-3} H_2SO_4. This led the author of this thesis to examine electrosorption of G^+ (or G) and U at Pt(111) by recording the adsorption charge transients in 0.1 mol dm^{-3} NaOH over a potential range where only double-layer charging is otherwise taking place, i.e. where no complicating influence from H or anionic (OH^- or

$OH^{\delta-}$) species could arise in the transients.

One-hundred μL amounts of 1% solution of urea or guanidine carbonate in 0.1 mol dm^{-3} NaOH were introduced into the initially G- or U-free 0.1 mol dm^{-3} NaOH solution, under controlled potential (0.5 V, RHE) at the Pt(111) surface. On the average, the following charge-transient densities (cf. refs. 12, 32) were obtained: +154 (±10) μC cm^{-2} for U and +152 (±8) μC cm^{-2} for G^+ (or G). Under the conditions of these experiments, the observed large anodic transient charge densities can only correspond to electrosorption of urea or of G^+ (or G) on the Pt(111) surface in a dissociatively chemisorbed state, i.e. with resulting electrooxidation of the H's dissociated from $-NH_2$ groups upon their chemisorption (as illustrated by the process **X** in section 6.2 above). The above given charge-transient densities correspond to surface coverages of $\theta_U \approx 0.63$ and $\theta_{G+} \approx 0.62$ of equivalent H monolayer coverage for U and G^+, respectively. Such values are not inconsistent with the FTIR results, referred to above, since here the transient results arose in NaOH solution where there is much less anion adsorption.

The "co-operative chemisorption" mechanism, proposed above in section 6.1.2.1, is supported by analysis of results of displacement charge-transients, previously reported in ref. 16, obtained by addition of 1% guanidonium carbonate solution to an initially G^+-free 0.5 mol dm^{-3} H_2SO_4 solution. Only very small cathodic adsorption charge-transients were observed at the potential of 80 mV (RHE). This implies that guanidine itself does not have the capability of displacing H atoms from the Pt surface (as is the case when CO is used as a charge-displacement probe, based on the effects reported in refs. 12 and 32). Thus, as previously observed in Fig. 6.8, the G^+ ions remain unadsorbed over the underpotential-H ionisation range of potential. On the other hand, at 500 mV, small but significant net anodic charge transients were observed (on the average,+14 (±2) μC cm^{-2}); the latter result is *not*, however, an indication of non-chemisorptive interaction of G^+ at the Pt(111) surface. Rather, the process of anodic adsorption of G^+ leads simultaneously to desorption of the HSO_4^- species by cathodic charge transfer. Thus, the charges associated with their electrosorption almost cancel out so that the resulting overall effect (+14 μC cm^{-2}) of guanidine injection is barely noticeable. This is particularly significant for the Pt(111) plane owing to its high coverage by HSO_4^- ions (corresponding to about 34% of the total charge [12], beyond *ca.* 0.30 V).

6.4.2 Adsorbate displacement by CO

In section 5.6 of Chapter 5, it was mentioned that the "anodic H displacement effect", discovered by Conway et al. [32-34], had been adapted by Clavilier [12, 35, 36], using CO, in order to distinguish between UPD H and HSO_4^- electrosorption. This procedure has been applied in the present work to complement the elucidation of the origin of the effects of G^+ at Pt(111) in H_2SO_4 and NaOH. The resulting integrated charge densities (μC cm^{-2}) derived from the current transients generated upon admission of O_2 -free CO at Pt(111) in 0.5 mol dm^{-3} H_2SO_4 in the presence of G^+ at a concentration of $1x10^{-3}$ mol dm^{-3}, are shown in Fig. 6.48, plotted in histogram form above the relevant voltammogram. The potentials at which the transients were initiated are indicated in the vertical bars on which are shown mean error bars based on 6-8 separate CO admission tests. Reproducibility was generally good (*ca.* ±2%). Transients were recorded at potentials ranging from 0.08 to 0.60 V, RHE. The first three potentials [two of them at the two peaks D_1 and D_2 (Fig. 6.8)] gave net anodic charge transients corresponding predominantly to H desorption as H^+ [33] while at three other, more positive potentials, net cathodic transients were observed, corresponding to HSO_4^- and G^+ desorption (cf. ref. 35).

A similar histogram for two potentials at Pt(111) in 0.1 mol dm^{-3} NaOH is shown in Fig. 6.49. In the voltammetric peak (see Figs. 6.49 and 6.17), the transient charge density is -108 μC cm^{-2} while in the H UPD region it is +107 μC cm^{-2}. Error bars are again shown on the figure.

It is of interest to show (Fig. 6.50) how the transient charge-densities for Pt(111) in 0.5 mol dm^{-3} H_2SO_4 with G^+ present compare with those derived by Clavilier et al. [12] for H_2SO_4 solution. The solid circles are Clavilier's data and the solid squares are data from the present experiments with G^+ in solution. G^+ progressively and appreciably lowers the transient charge throughout the UPD H region, as though less H would be available for desorption. Beyond 0.245 V, the negative transient charge increases due to anion and G^+ desorption over the "displaced" HSO_4^- region (Fig. 6.8). The diminished anodic H desorption charge is probably due to simultaneous desorption of HSO_4^- (and G^+) over the displaced HSO_4^- region, giving a charge component of negative sign, the observed transient charge being the algebraic sum of these two components.

The corresponding charge densities derived from the current transients generated upon introduction of CO at Pt(100) in 0.5 mol dm^{-3} H_2SO_4 and 0.1 mol dm^{-3} NaOH, in the presence of G^+ at a concentration of $1x10^{-3}$ mol dm^{-3}, are listed in Tables 6.5 and 6.6, respectively. A comparison of current transients obtained in 0.5 mol dm^{-3} H_2SO_4 with G^+ present with those derived by Clavilier [12] for such a solution is made in Table 6.5. Again, observation of significant cathodic charge transients, e.g. –65 (±1) μC cm^{-2} at

0.300 V where otherwise (in the absence of G^+) a large anodic transient of +143 μC cm^{-2} is observed [12], substantiates the appreciable shifts of current-response peaks towards

Table 6.5 Desorption transient charge-densities (μC cm^{-2}) for displacement of UPD H, HSO_4^- and G^+ ions from Pt(100) in 0.5 mol dm^{-3} H_2SO_4 [12] and in the presence of G^+ at a concentration of $1x10^{-3}$ mol dm^{-3} by the CO adsorbate displacement technique.

0.5 mol dm^{-3} H_2SO_4		0.5 mol dm^{-3} H_2SO_4 + $1x10^{-3}$ mol dm^{-3} G^+	
E/mV	$q_t(E)$/μC cm^{-2}	E/mV	$q_t(E)^{a)}$/μC cm^{-2}
100	+ 197	100	+ 195 ± 4
250	+ 164	250	+ 156 ± 5
300	+ 143	300	- 65 ± 1
450	- 57	450	- 90 ± 6

a) Given errors are based on 6-8 separate CO admission tests.

Table 6.6 Desorption transient charge-densities (μC cm^{-2}) for displacement of UPD H, OH^- and G^+ ions from Pt(100) in 0.1 mol dm^{-3} NaOH and in the presence of G^+ (G) at a concentration of $1x10^{-3}$ mol dm^{-3} by the CO adsorbate displacement technique.

0.1 mol dm^{-3} NaOH		0.1 mol dm^{-3} NaOH + $1x10^{-3}$ mol dm^{-3} G^+	
E/mV	$q_t(E)^{a)}$/μC cm^{-2}	E/mV	$q_t(E)^{a)}$/μC cm^{-2}
100	+ 169 ± 5	100	+ 171 ± 11
300	+ 120 ± 11	300	- 117 ± 12

a) Given errors are based on 6-8 separate CO admission tests.

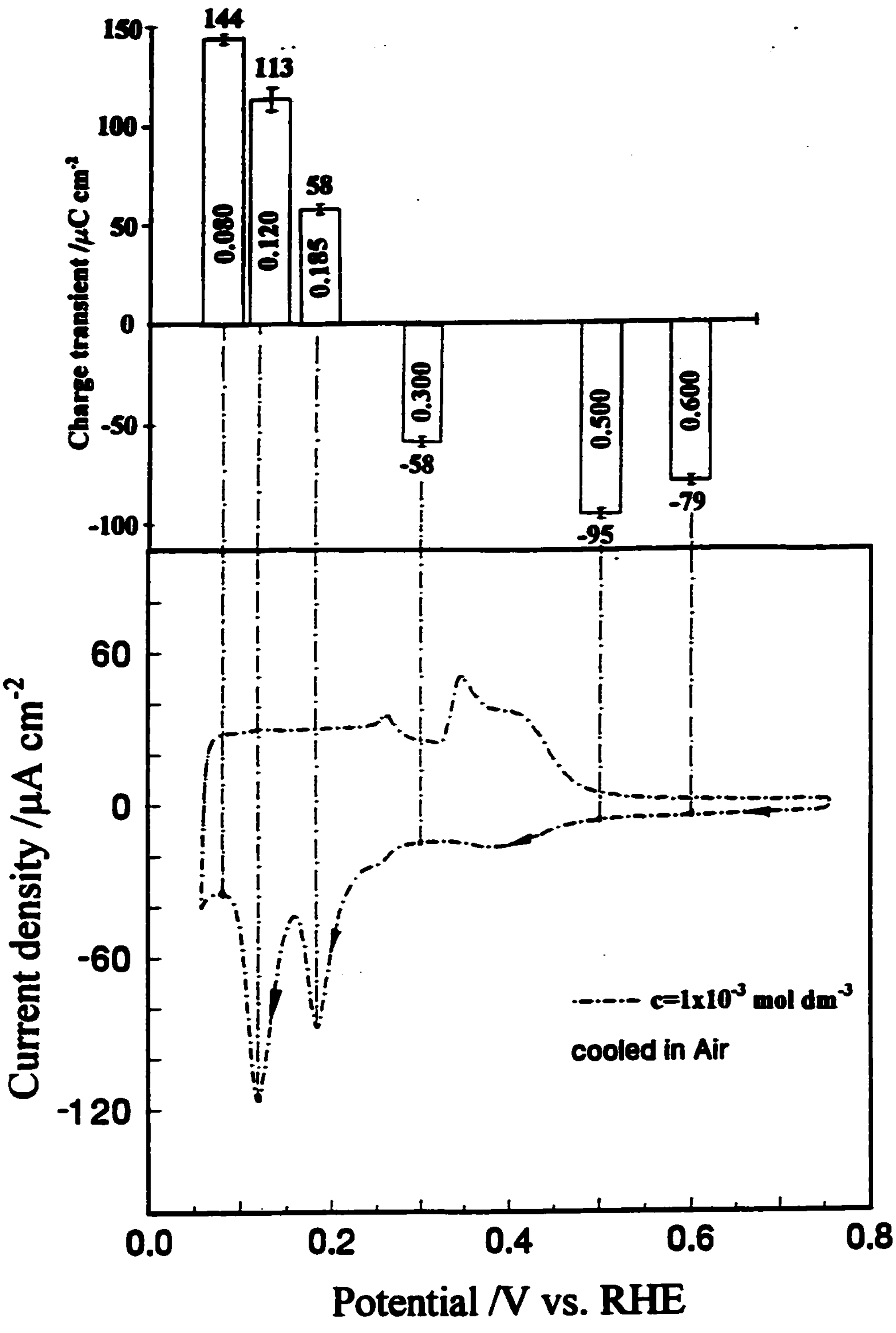

Fig. 6.48 Desorption transient charge-densities (μC cm^{-2}) for displacement of UPD H, HSO_4^- and G^+ ions from Pt(111) in 0.5 mol dm^{-3} H_2SO_4 containing $1x10^{-3}$ mol dm^{-3} G^+ by CO represented in a histogram plot vis-à-vis the voltammogram.

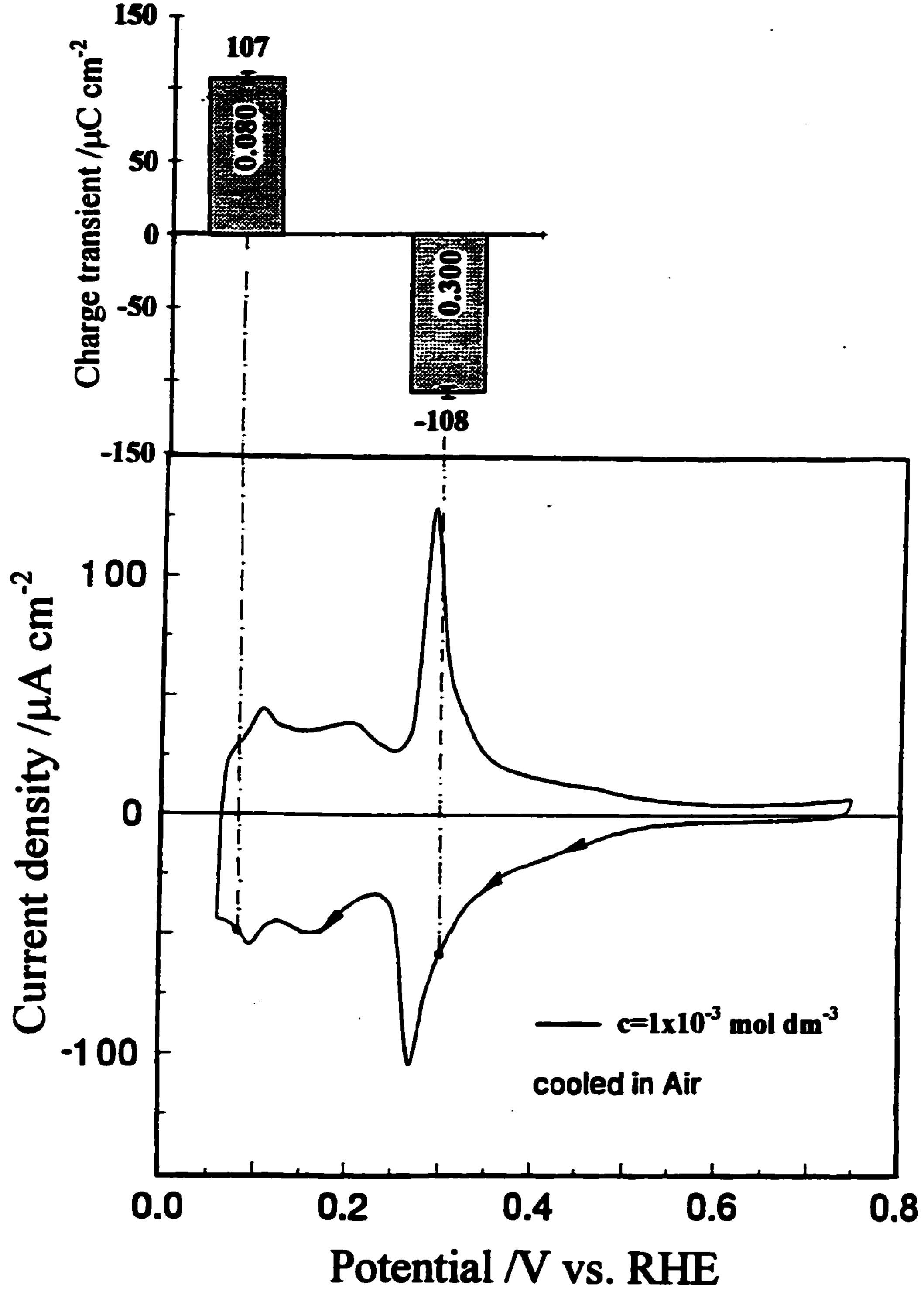

Fig. 6.49 Desorption transient charge-densities (μC cm^{-2}) for displacement of UPD H and G^+ ions from Pt(111) in 0.1 mol dm^{-3} NaOH containing $1x10^{-3}$ mol dm^{-3} G (as G^+ plus some equilibrium concentration of G) by CO represented in a histogram plot vis-à-vis the voltammogram.

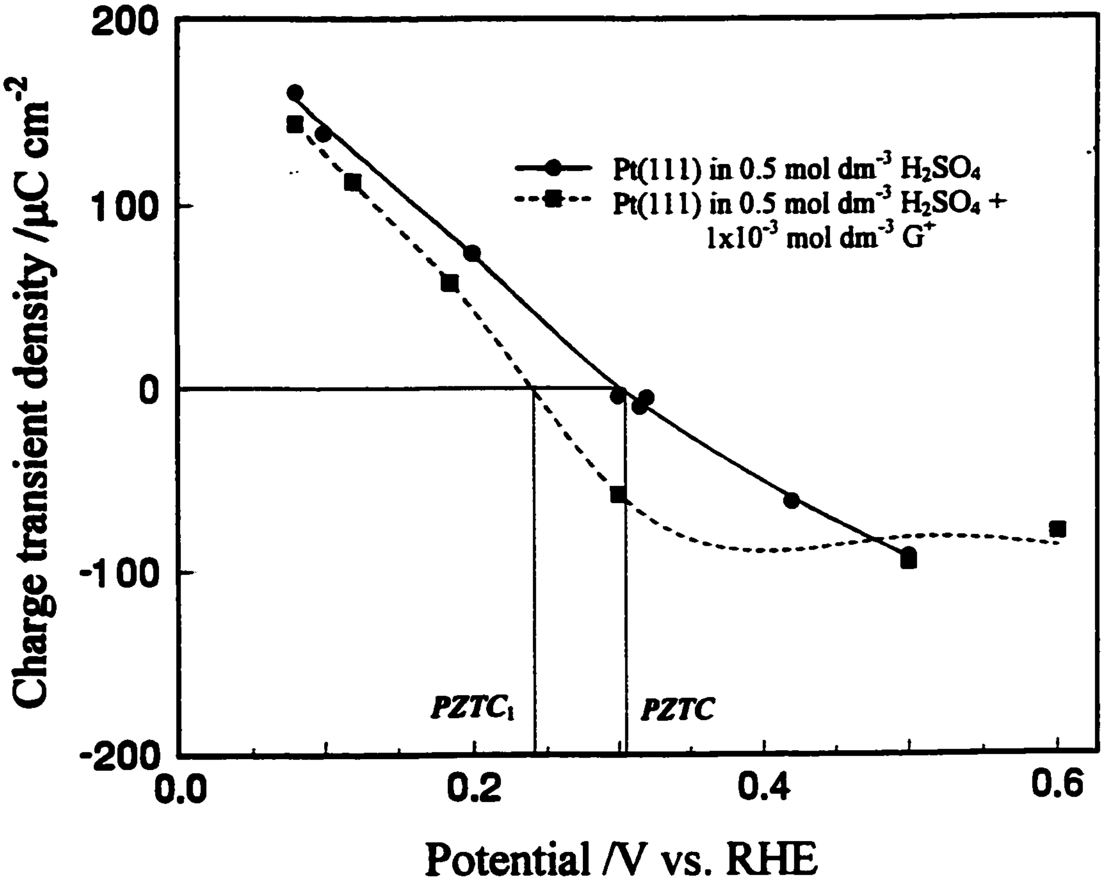

Fig. 6.50 Plots of desorption transient charge-densities at Pt(111) as a function of electrode potential (vs. RHE) in the absence [12] and in the presence of G^+ at 1×10^{-3} mol dm^{-3} concentration in 0.5 mol dm^{-3} H_2SO_4.

the H_2 reversible potential, originating from the proposed ion-pairing effects in the double-layer.

A similar behaviour arises in NaOH solution, where in the presence of G^+, the cathodic charge transient obtained at 0.300 V is almost equal but opposite in sign to that acquired in the absence of G^+ in solution. However, charge densities derived from the current transient obtained at 0.100 V in the absence and presence of G^+ are practically superimposable and correspond entirely to desorption of UPD H from the Pt surface (see Table 6.6).

6.5 Absence of diffusion-controlled processes

As was noted in ref. 16, upon interruption of a voltammetric sweep in the H UPD potential region in the presence of G^+, currents returned immediately to the zero-current line and no continuous residual Faradaic currents could be observed in well deoxygenated solutions. Similar behaviour was also observed in the presence of the DMG^+ ion.

Also, experiments conducted [16] at various sweep-rates, s, in 0.5 mol dm^{-3} H_2SO_4, 0.1 mol dm^{-3} $HClO_4$ and 0.1 mol dm^{-3} NaOH electrolytes, gave in almost all cases, response currents that were almost *linear* with s. As examples, Figs. 6.51a and 6.51b show the anodic and cathodic peak-current responses as a function of s at the Pt(111) surface in 0.5 mol dm^{-3} H_2SO_4, in the presence of G^+ at concentrations of 6×10^{-5} and 6×10^{-4} mol dm^{-3}. The observed, almost purely capacitive response indicates absence of significant diffusion-control of the recorded response-currents, so that the latter are directly associated with surface electrochemical processes. For comparison, Figs. 6.52a and 6.52b show the corresponding peak-current responses plotted as a function of $s^{1/2}$,

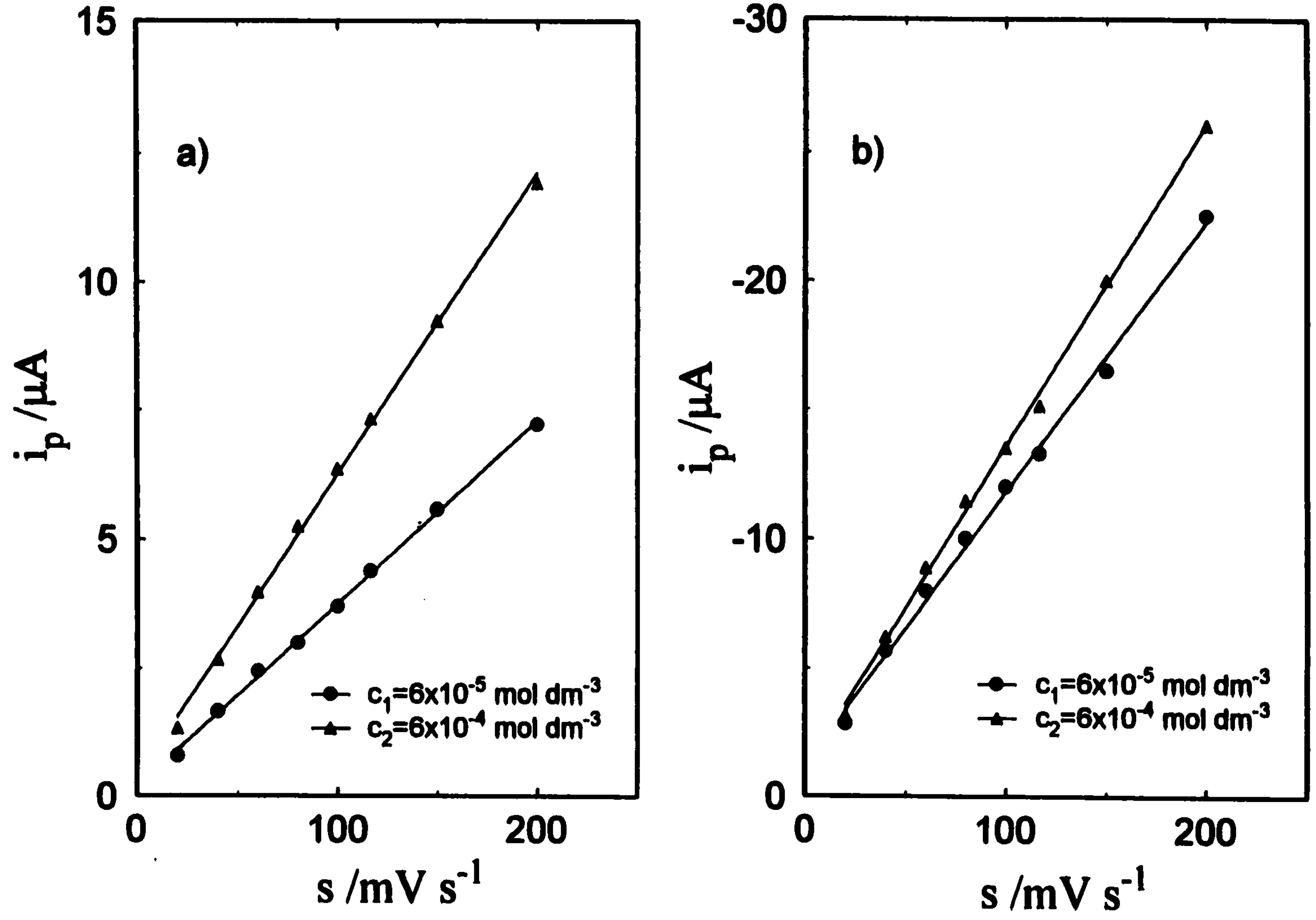

Fig. 6.51 a) Peak anodic current vs. sweep rate for Pt(111) in 0.5 mol dm^{-3} H_2SO_4 and in the presence of G^+ at the two concentrations indicated; b) As in (a), but peak cathodic current.

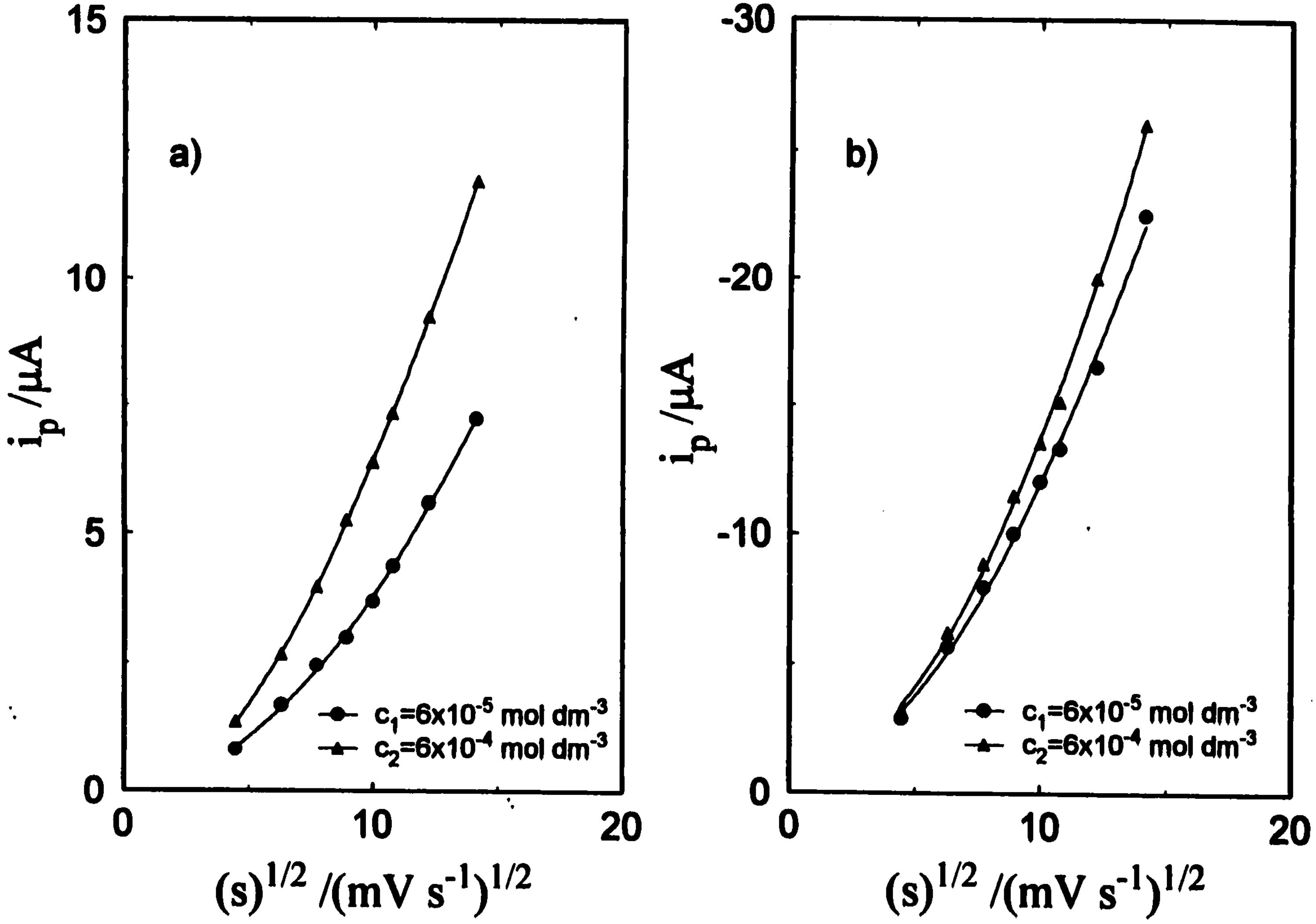

Fig. 6.52 a) Peak anodic current vs. square-root of sweep rate for Pt(111) in 0.5 mol dm^{-3} H_2SO_4 and in the presence of G^+ at the two concentrations indicated; b) As in (a), but peak cathodic current.

rather than s^1; then the deviations from linearity are quite significant indicating that the sweep-rate response behaviour is not mainly associated with diffusion control.

6.6 Comparison with oxime adsorption and Faradaic reaction at Pt single-crystal surfaces

Oximes are tautomeric with nitroso compounds. Depending on the source from which they are derived, oximes can be divided into two groups: *aldoximes* and *ketoximes*. Aldoximes are obtained in reactions of aldehydes (RCHO) with hydroxylamine (NH_2OH) and ketoximes may be prepared in reactions of NH_2OH with ketones (R_2CO or RR'CO) [37, 38]. Both formamidoxime (F_{NOH}) and acetaldehyde oxime (A_{NOH}), studied in the present work (see their chemical formulae as structures **VIII** and **IX** in Fig. 4.6 of Chapter 4, respectively), can be formally regarded as belonging to the group of aldoximes.

As already mentioned in Chapter 4, generally, in acidic and neutral solutions, both aliphatic and aromatic oximes undergo electrolytic reduction to amines [37-41]. The process may occur by e^- and H^+ transfer at metals such as Hg or Pb (at which H chemisorption is undetectable), or otherwise it can proceed through an electrochemical hydrogenation reaction with adsorbed H [39] (Raney nickel) or with UPD H at Pt; see the reduction process **XIX** below, written for acidic solutions:

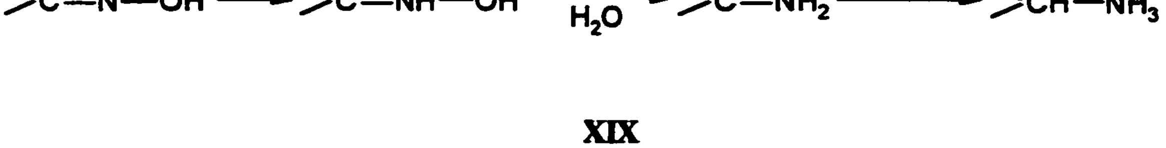

$$>C=N-OH \xrightarrow{H^+} >C=\overset{+}{N}H-OH \xrightarrow[H_2O]{\overset{2H\cdot}{(2H^++2e^-)}} >C=\overset{+}{N}H_2 \xrightarrow{\overset{2H\cdot}{(2H^++2e^-)}} >CH-\overset{+}{N}H_3$$

XIX

The overall reaction is formally a four-electron process and has several steps.

Firstly (in acidic solution), the oxime is preferably protonated at N, rather than O, because of the more basic character of the former. The protonated species then undergoes reduction with initial cleavage of the N-O bond, producing an unstable intermediate *imine* [39, 41]. Finally, the >C=N- double bond becomes hydrogenated to generate an amine.

The major purpose of the present part of the thesis is to report how the reactivity of two small aliphatic oximes (F_{NOH} and A_{NOH}) at the Pt surface can be influenced by differences of Pt surface geometry and corresponding [42] electronic properties. In addition, the effect of appreciable change in pH of solution on their reactivity at two principal [(111) and (100)] Pt single-crystal planes has been examined.

6.6.1 Electrochemical behaviour of F_{NOH} at Pt(111) and (100) single-crystal surfaces in 0.5 mol dm^{-3} H_2SO_4

The electrochemical behaviour of formamidoxime (F_{NOH}) at a concentration of 3×10^{-4} mol dm^{-3} at the Pt(111) surface in 0.5 mol dm^{-3} H_2SO_4 is shown in the cyclic voltammograms of Fig. 6.53. The most significant feature (second cycle) is the presence of two, well-pronounced, cathodic current peaks (denoted **a** and **b**), over the potential range 0.20-0.50 V, vs. RHE, that arise both on the positive- *and the* negative-going sweeps, a feature indicating involvement of a Faradaic reduction process. They appear over a considerable fraction of the potential range for UPD of H, although the remaining range (0.06-0.20 V) remains substantially unaltered. At the same time, the two peaks, characteristic [43] of electrosorption of HSO_4^- anions on the (111) plane, that are normally observed in 0.5 mol dm^{-3} H_2SO_4 at *ca.* 0.45V, disappear from the voltammetric profile.

The role of a continuous Faradaic reduction process is indicated by the observation that, upon interruptions of a voltammetric sweep at the potential of the peak cathodic current at Pt(111), substantial residual continuous currents, e.g. 87 µA cm^{-2} at 0.33 V are recordable, the conditions being as for Fig. 6.53. This current dropped by only 2% after 60 s of holding at the latter potential. Such behaviour is quite different from that observed with G^+ and DMG^+ (ref. 16) at Pt(111) where no residual currents pass on interruptions of sweeps, thus indicating in the usual way that only non-continuous, 2-dimensional surface processes are taking place.

The electrochemical behaviour of F_{NOH} at the Pt(111) surface (Fig. 6.53) involving a continuous type of Faradaic process, coupled with changes of electrosorption of H, reflects a process of electrochemical reductive scission of the protonated F_{NOH} at the N-to-O bond (cf. refs. 39 and 41) which commences upon adsorption of the $(F_{NOH})^+$ molecule-ion on the Pt surface, as represented by the sequence of reaction steps XX-XXIV below:

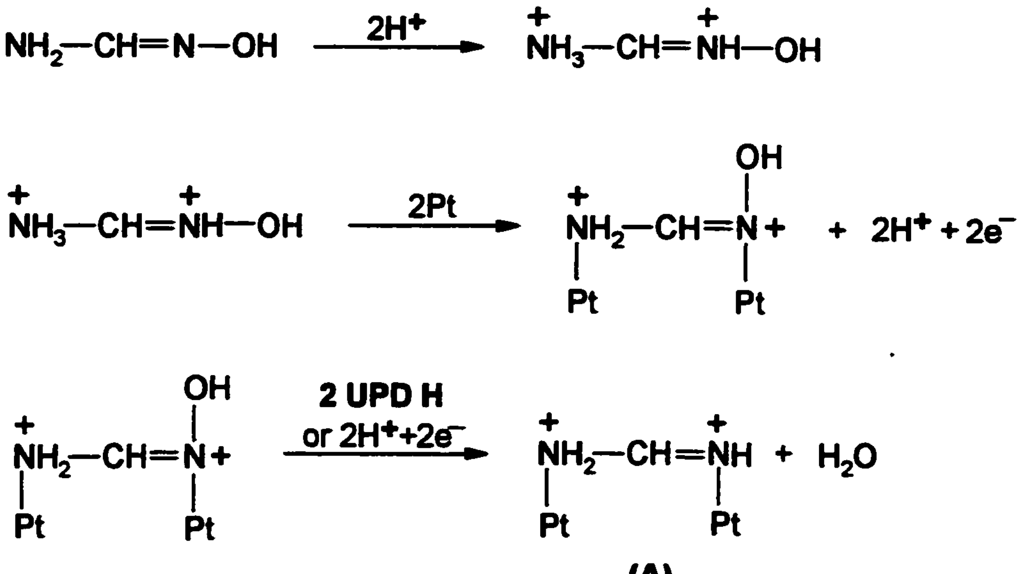

XX $NH_2-CH=N-OH \xrightarrow{2H^+} \overset{+}{N}H_3-CH=\overset{+}{N}H-OH$

XXI $\overset{+}{N}H_3-CH=\overset{+}{N}H-OH \xrightarrow{2Pt} \underset{Pt}{\overset{+}{N}H_2}-CH=\underset{Pt}{\overset{OH}{N}}+ \quad + 2H^+ + 2e^-$

XXII $\underset{Pt}{\overset{+}{N}H_2}-CH=\underset{Pt}{\overset{OH}{N}}+ \xrightarrow[\text{or } 2H^+ + 2e^-]{\text{2 UPD H}} \underset{Pt}{\overset{+}{N}H_2}-CH=\underset{Pt}{\overset{+}{N}H} + H_2O$

(A)

XXIII

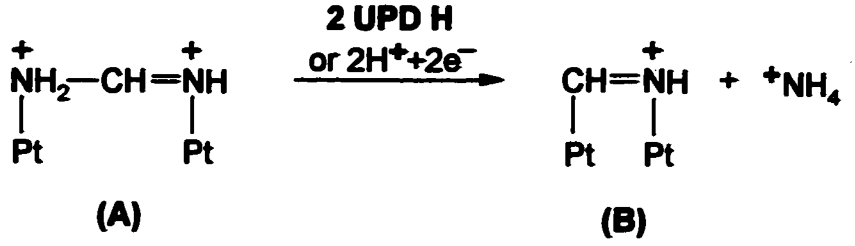

XXIV

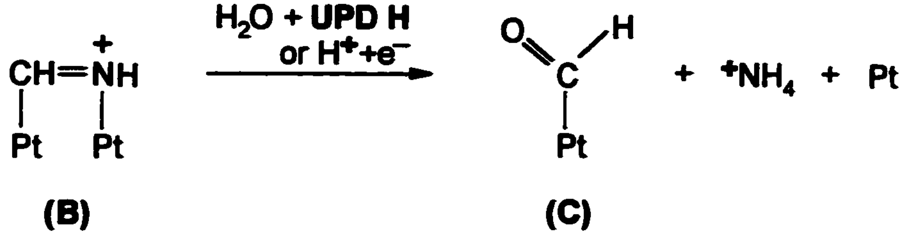

Reaction steps such as **XXII**, **XXIII** and **XXIV** could proceed by electrochemical discharge [39] involving $2H^+ + 2e^-$ ($H^+ + e^-$ for the step **XXIV**); however, since the reduction peaks in Fig. 6.53 arise over the H UPD region at a Pt surface, here (111), it seems that the preferred mechanism (cf. ref. 39, p.865) would be through electrocatalytic uptake of 2 UPD H's, as in the steps **XXII** and **XXIII**, and 1 UPD H in the step **XXIV**. For such a mechanism it has to be explained that the observed Faradaic currents passed over the controlled-UPD potential range would then arise from the requirement of maintenance of coverage by UPD H at a given potential, matching that lost from the surface by electrocatalytic consumption of adsorbed H in steps such as **XXII**, **XXIII** and **XXIV**.

As with most heterogeneous reactions involving chemisorption, it is difficult to characterise the molecular structures of the adsorbed intermediates involved in reaction sequences. The above sequence of steps, and that postulated later for the case of A_{NOH}, has to be based on known types of chemistry, supported by the voltammetry response behaviour and that derived from complementary charge-transient measurements. Some speculative proposals are unavoidable but it is believed they are chemically rational. With simpler adsorbates such as guanidine or urea co-adsorbed with HSO_4^- ion, discussed in previous sections of this Chapter, it was possible to obtain complementary information by *in situ* IR reflectance spectroscopy (see section 6.3 of this Chapter) but here, owing to involvement of time-dependent Faradaic reactions, that approach, which would require potential modulation, is unproductive.

Here, the F_{NOH} molecules are probably protonated on both N atoms as they are separated by one –CH= group. The charge-transient data indicate that they are adsorbed on the Pt surface (step **XXI**) so that the following steps (**XXII-XXIV**) proceed in the chemisorbed state on the Pt surface, as for the case of CH_3CN [6]. The reduction steps (**XXII**, **XXIII** and **XXIV**) in the sequence **XX-XXIV** are represented as preferred electrolytic hydrogenation reactions (cf. ref. 39). On the negative-going sweep, reduction commences and progresses through H UP-deposition, and then becomes reactivated on the following positive-going sweep over the H UP-ionisation range of potential.

Reaction **XXII** leads to the formation of an unstable formamidine species (**A**), by analogy with the known mechanism (reaction **XIX**) for oximes, in general, in which (**A**) would not undergo reduction to amine. However, this intermediate could undergo further dissociation in step **XXIII** to form a methylene-imine intermediate (**B**) and an NH_4^+ ion. The former can then become reductively hydrolysed in step **XXIV** to adsorbed formaldehyde (**C**) and another NH_4^+ ion. All the intermediate products of $(F_{NOH})^+$ reduction formed here will tend to exist in protonated forms in the 0.5 mol dm^{-3} acidic electrolyte.

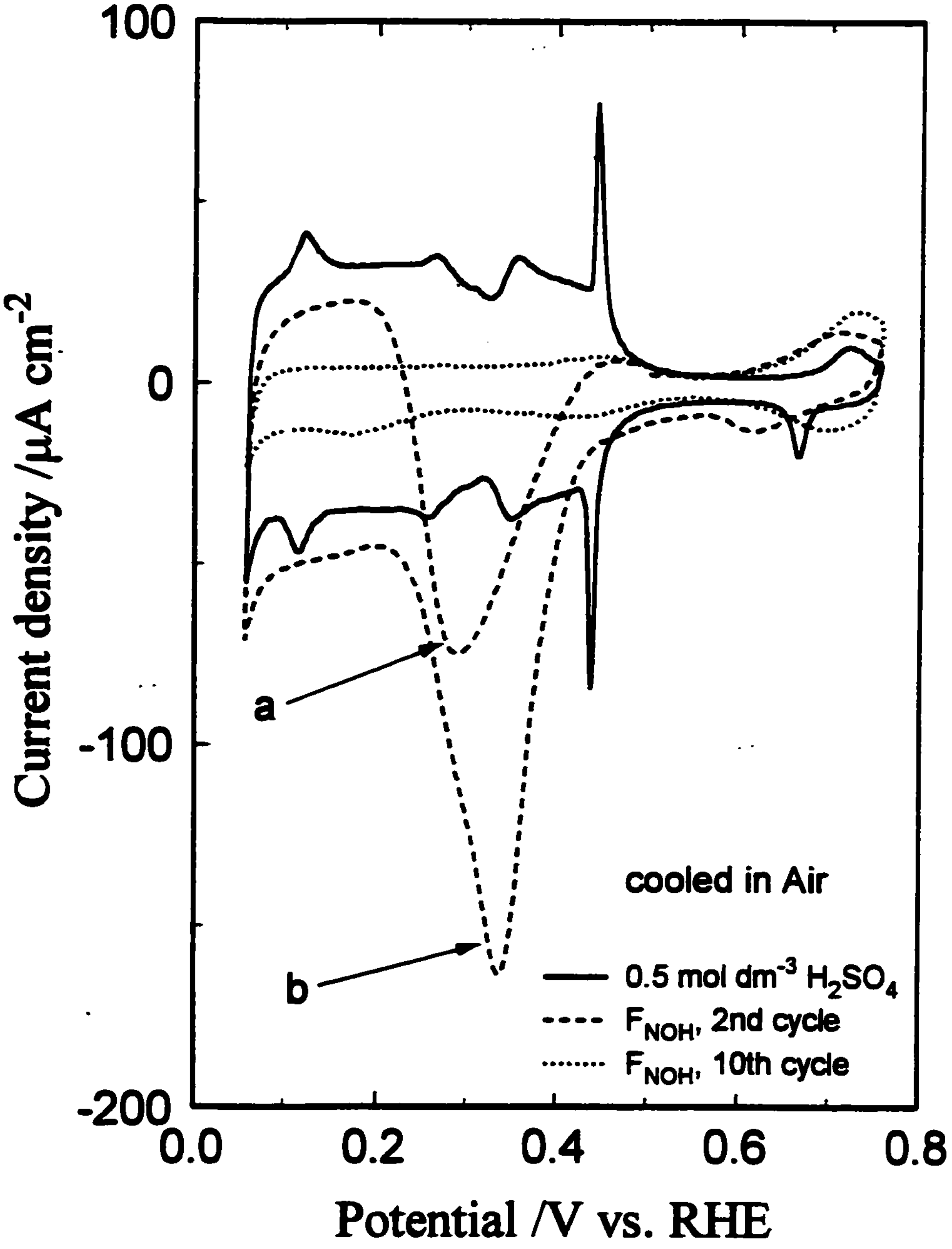

Fig. 6.53 Cyclic voltammograms for Pt(111) in 0.5 mol dm^{-3} H_2SO_4 at a sweep rate of 0.050 V s^{-1}, in the presence of F_{NOH} at a concentration of 3x10^{-4} mol dm^{-3}; second and tenth cycles were recorded.

By analogy with the mechanism of oxidation of HCOOH on Pt(111) [44], forming CO_{ads}, a similar process has been suggested, e.g. in refs. 45 and 46, for formation of CO_{ads} from HCHO (see also section 2.6.2 of Chapter 2).

There is strong enough evidence in the literature [44-49] to propose that, under these conditions, PtCHO formed in the above (XX-XXIV) sequence of reactions can become dissociatively oxidised on the Pt surface, forming adsorbed carbon monoxide (CO_{ads}), leading to poisoning of the Pt surfaces which is well-known in the literature [12, 35, 36]. Thus, refs. 45-47 indicate that HCHO can become oxidised on a Pt surface through a dissociative catalytic pathway, first to form adsorbed Pt-CHO, then with further anodic dissociation of H to form strongly bound CO species [50, 51], linearly or bridge-bonded to the surface. Furthermore, chemisorbed CO can act as a self-inhibiting species in the electrosorption of HCHO on the Pt surface [45]. The process of HCHO oxidation on the Pt(111) plane can be written according to the surface reaction **XXV** below:

XXV

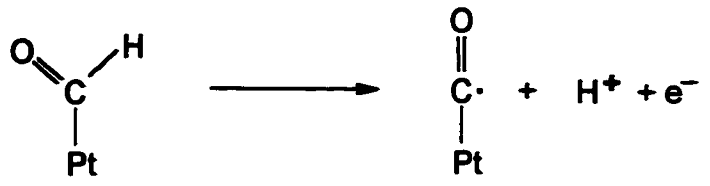

(C)

The fact that almost complete blocking of the Pt(111) surface arises after only a few cycles (Fig. 6.53), suggesting ultimate adsorption of CO, supports retention of the double-bond in steps **XX** to **XXIV**, otherwise formation of HCHO, leading to CO_{ads} (step **XXV**) would be difficult to envisage. The aspect of the presence of the CO_{ads} species as a final, but indirect, product of F_{NOH} reduction on the Pt(111) surface is important and helps to distinguish the mechanism of reduction of F_{NOH} on the Pt(111) surface from the corresponding process for acetaldehyde oxime (A_{NOH}); see Fig. 6.56 later.

The behaviour of F_{NOH} at a concentration of $3x10^{-4}$ mol dm^{-3} at the Pt(100) surface in 0.5 mol dm^{-3} H_2SO_4 is shown in Fig. 6.54. Here, unlike at the Pt(111) surface, the usual [43] characteristic voltammetric features of the (100) plane observed in 0.5 mol dm^{-3} H_2SO_4 are still substantially maintained in the presence of F_{NOH}. Thus *both* cathodic and anodic current-response peaks still arise in this case, but are broadened and considerably shifted towards the H_2 reversible potential (Fig. 6.54), as was similarly found in our work [16] on adsorption of guanidonium ion, G^+. Also, on interruption of a negative-going sweep, the current diminishes rapidly, becoming only 4 μA cm^{-2} after 60 s, a behaviour characteristic of electrosorption rather than continuous Faradaic reduction of the type observed at Pt(111) in Fig. 6.53. Additionally, the effect of surface self-poisoning by the products of F_{NOH} reduction is far less significant at Pt(100) than at the Pt(111) plane (compare the voltammograms for F_{NOH} at Pt(111) with those at the (100) plane after the second or first, and the tenth, cycles in Figs. 6.53 and 6.54).

The above behaviour at Pt(100) resembles that of guanidonium ions (G^+) in 0.5 mol dm^{-3} H_2SO_4 (see ref. 16 and section 6.1.3 above) in the sense that interaction of F_{NOH} with the Pt(100) surface seems to be dominated by co-operative chemisorption of $(F_{NOH})^+$ ions with adsorbed anionic species (HSO_4^-), similarly to that originally proposed in section 6.1.2 for the adsorption of G^+ species on the Pt(111) surface (see structure **XXVI** below). This leads to stabilisation of the HSO_4^- ion adsorption as explained in section 6.1.2 and supported by the results reported therein, corresponding to the current-response profile being displaced towards the H_2 reversible potential (Fig. 6.54).

However, comparison of the cathodic voltammetric charge with that accumulated

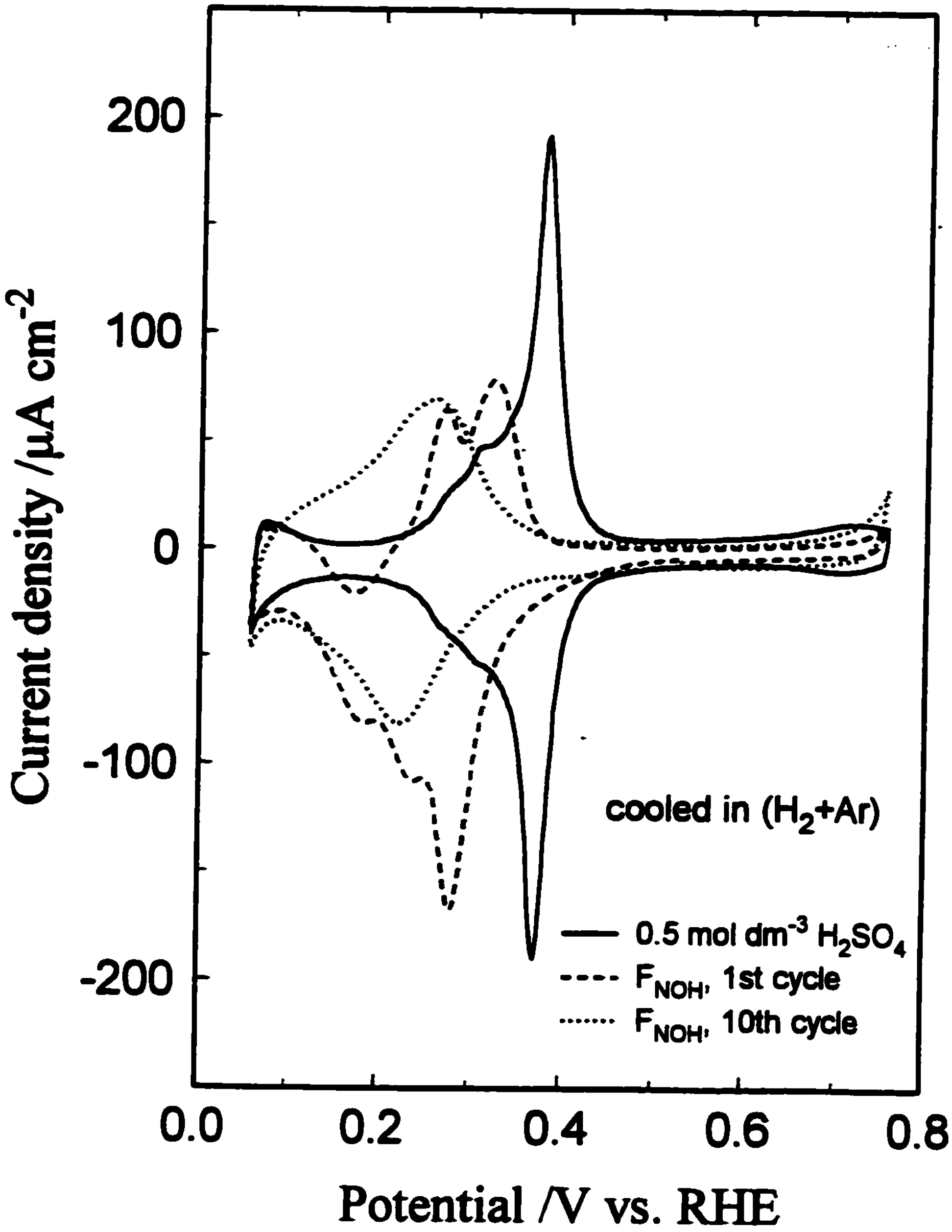

Fig. 6.54 Cyclic voltammograms for Pt(100) in 0.5 mol dm^{-3} H_2SO_4 at a sweep rate of 0.050 V s^{-1}, in the presence of F_{NOH} at a concentration of 3x10^{-4} mol dm^{-3}; first and tenth cycles were recorded.

on the anodic sweep (integrated from the voltammogram in Fig. 6.54, first cycle) after appropriate corrections for the double-layer charge contributions, shows an appreciable cathodic/anodic charge ratio of 2.6/1. The latter implies that, on the Pt(100) surface, in addition to the mechanism of co-operative chemisorption of F_{NOH} with adsorbed HSO_4^-, there must also be involved a non-continuous electrochemical reduction process, progressing through the steps **XXII**, **XXIII** and **XXIV**, which leads (as in the case of the (111) plane) ultimately to formation of the CO_{ads} species on the Pt(100) surface with eventual current inhibition, but much more slowly than at Pt(111).

XXVI

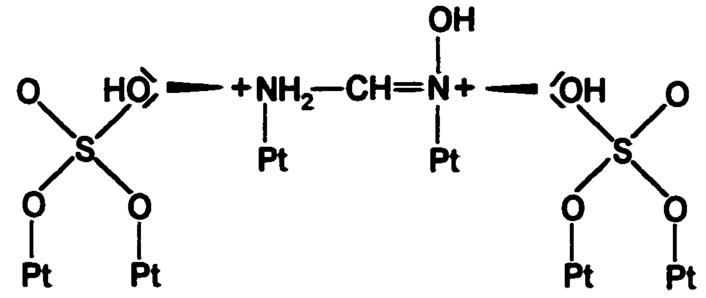

Pt(100)

Thus, summarising the behaviour at the Pt(100) surface, the overall mechanism seems to be a combination of two parallel processes, where chemisorption of F_{NOH} on the Pt surface (not involving the chain of reactions **XXII-XXIV**) is indicated as the dominant process. The strong distinction between the behaviour of F_{NOH} at the two Pt single-crystal surfaces provides a clear example of reaction specificity due to differences in surface co-ordination geometry and electronic properties, manifested as differences in their electro-catalytic behaviour.

As noted above, for F_{NOH} at the Pt(111) plane, upon interruptions of the voltammetric sweep in the H UPD potential region, significant residual Faradaic currents

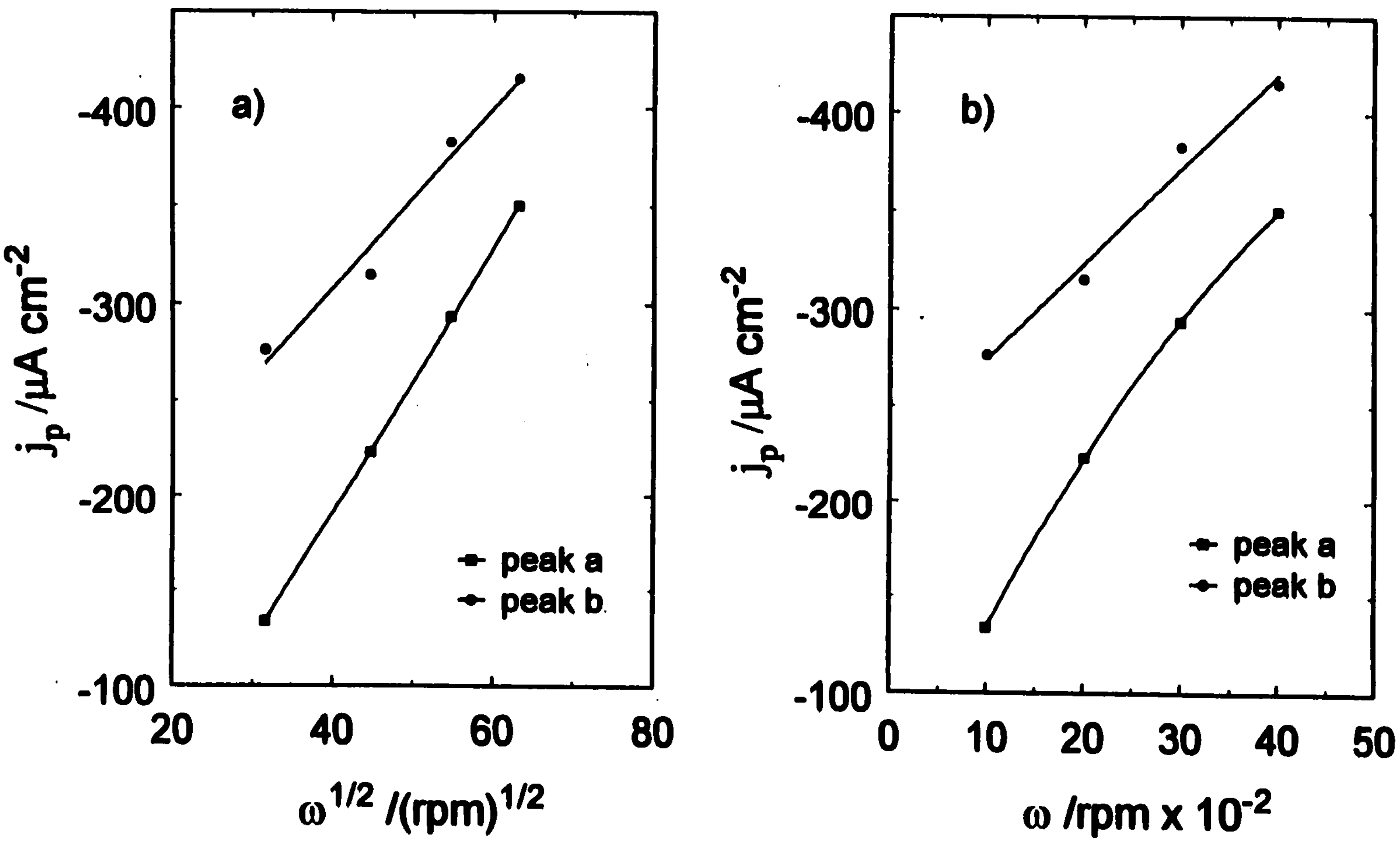

Fig. 6.55 a) Levich plots, $j_p = f(\omega^{1/2})$, for the process of reduction of formamidoxime on Pt(111) in 0.5 mol dm^{-3} H_2SO_4, at a concentration of 4x10^{-4} mol dm^{-3} F_{NOH}, recorded for peak reduction current densities upon both positive- (peak a) and negative-going (peak b) sweeps; b) As in (a), but plotted as $j_p = f(\omega)$.

were observed, implying the role of diffusion control. Hence, experiments at a rotating Pt(111) disk electrode in 0.5 mol dm^{-3} H_2SO_4 in the presence of $4x10^{-4}$ mol dm^{-3} F_{NOH} were conducted, giving the Levich plots [15] shown in Fig. 6.55a for the peak reduction current densities, j_p, annotated **a** and **b** in Fig. 6.53. For both anodic and cathodic sweeps, j_p is linearly dependent on the *square-root* of rotation rate, $\omega^{1/2}$; however, a precise fit is only obtained for "peak **a**", arising on the positive-going sweep. On the other hand, a plot against ω^1 is discernably curved (see the corresponding curve for "peak a" in Fig. 6.55b), confirming, in a negative way, involvement of diffusion.

Conversely, at the Pt(100) plane under the same conditions, practically *no* effect of rotation was observable, giving good support for the mechanism proposed above for the interaction of F_{NOH} with this surface; so that the reaction sequence **XXII-XXIV**, applicable to Pt(111), is not predominant at the (100) plane.

It has also to be noted that comparative behaviour at the Pt(110) plane was in most cases featureless, on account of blocking of the H adsorption sites by adsorption of the oxime (F_{NOH} and A_{NOH}) molecules.

6.6.2 *Comparative behaviour of acetaldehyde oxime (A_{NOH}) at the Pt(111) single-crystal surface in 0.5 mol dm^{-3} H_2SO_4*

The reactivity of A_{NOH} at a concentration of $5x10^{-4}$ mol dm^{-3} on the Pt(111) surface in 0.5 mol dm^{-3} H_2SO_4, shown in Fig. 6.56, is quite similar to that of F_{NOH} (compare Fig. 6.53). Thus, well pronounced cathodic current peaks arise over the potential range 0.10-0.50 V in *both directions* of the potential sweep. Upon interruption of the negative-going voltammetric sweep at 0.25 V, a residual current-density of 25 μA

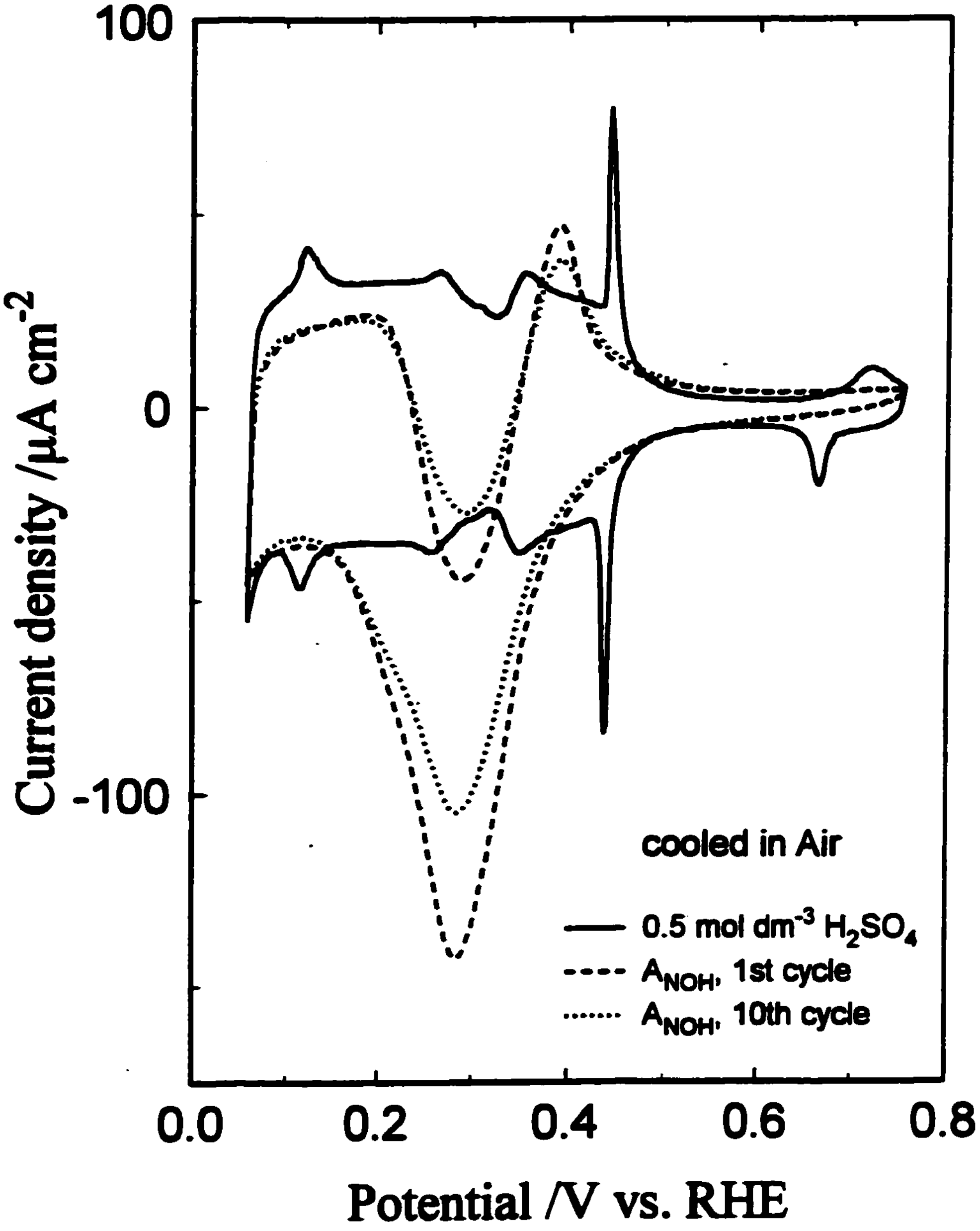

Fig. 6.56 Cyclic voltammograms for Pt(111) in 0.5 mol dm^{-3} H_2SO_4 at a sweep rate of 0.050 V s^{-1}, in the presence of A_{NOH} at a concentration of $5x10^{-4}$ mol dm^{-3}; first and tenth cycles were recorded.

cm^{-2} is detectable and declines after 60 s by about 16 per cent, indicating the role of a significant, but time-dependent, residual Faradaic current, as with F_{NOH} at the Pt(111) surface.

The most important difference between the behaviour of F_{NOH} and A_{NOH} at the Pt(111) plane is, however, that with the latter adsorbate, no significant accumulation of a surface-blocking reaction product (cf. Figs. 6.53, 6.56) is observed during repetitive cycling within the 0.06-0.76 V potential range, e.g., after ten cycles, the Pt surface remains still largely unblocked (see Fig. 6.56).

The mechanism for interaction of A_{NOH} with the Pt(111) surface can again be based on electrocatalytic reduction of the oxime group but, in this case, to primary amine [37, 39-41], as represented by the reaction sequence **XXVII-XXX** below:

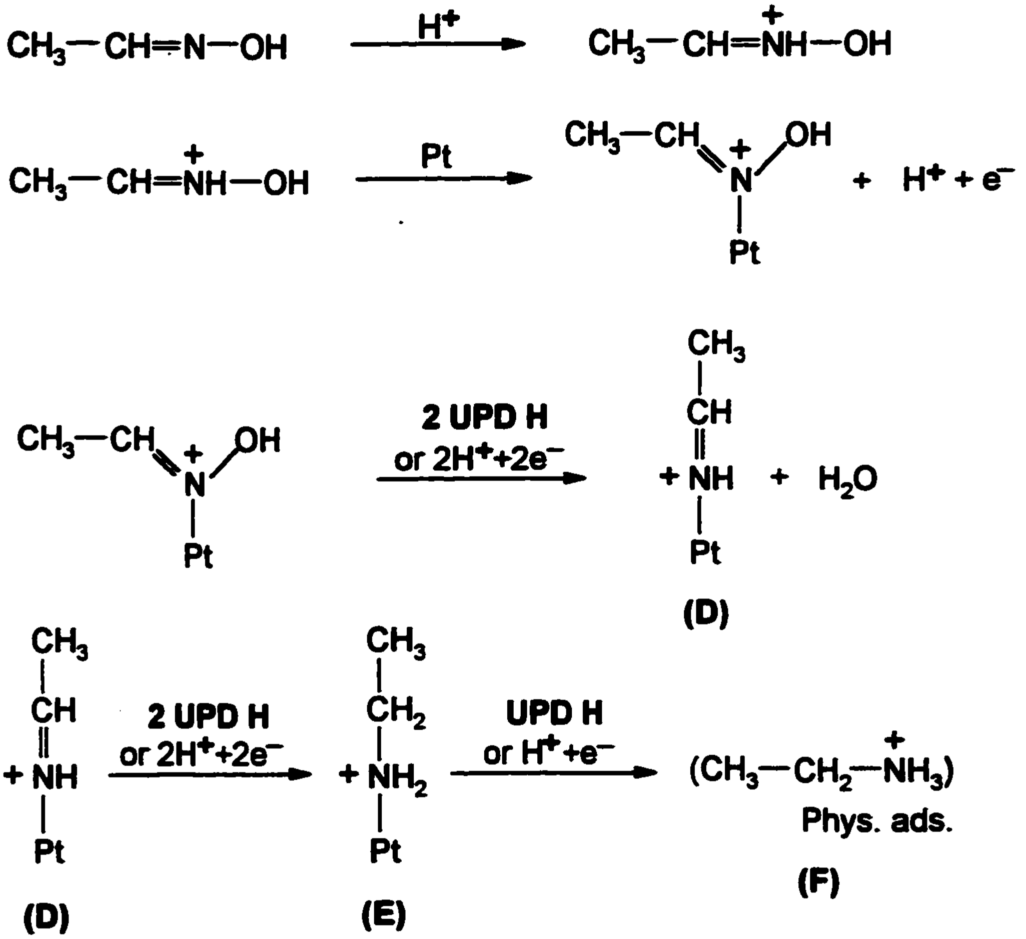

XXVII $CH_3-CH=N-OH \xrightarrow{H^+} CH_3-CH=\overset{+}{N}H-OH$

XXVIII $CH_3-CH=\overset{+}{N}H-OH \xrightarrow{Pt} CH_3-CH=\overset{+}{N}(-OH)-Pt + H^+ + e^-$

XXIX $CH_3-CH=\overset{+}{N}(-OH)-Pt \xrightarrow{2\ \text{UPD H or } 2H^++2e^-} CH_3-CH=\overset{+}{N}H-Pt + H_2O$ **(D)**

XXX $\underset{\textbf{(D)}}{CH_3-CH=\overset{+}{N}H-Pt} \xrightarrow{2\ \text{UPD H or } 2H^++2e^-} \underset{\textbf{(E)}}{CH_3-CH_2-\overset{+}{N}H_2-Pt} \xrightarrow{\text{UPD H or } H^++e^-} \underset{\textbf{(F)}}{(CH_3-CH_2-\overset{+}{N}H_3)\ \text{Phys. ads.}}$

After adsorption, the protonated A_{NOH} molecule undergoes reductive cleavage of the N to OH bond, forming an intermediate ethylimine species (**D**) [39] in reaction **XXIX**. Since such a species is unstable, the process continues and the >C=NH double bond becomes catalytically hydrogenated over the H UPD region to generate ethylamine (**E**) in reaction **XXX**. In order to generate the latter species (**E**), the overall reduction scheme **XXVII** to **XXX**, following the initial anodic electrosorption **XXVIII**, would be expected (cf. ref. 39) to proceed by the preferred electrochemical hydrogenation pathway involving the indicated chemisorbed species but formally requiring $4H^+ + 4e^-$ for provision of 4 UPD H's. Ethylamine seems to be only weakly adsorbed on the Pt surface (see **F** in step **XXX**), so that blocking of the Pt surface by adsorbed product molecules, such as CO in the case of F_{NOH}, is insignificant; then reduction of A_{NOH} is not self-inhibited, in the way observed with reduction of F_{NOH} on Pt(111) (compare Fig. 6.53 with Fig. 6.56).

6.6.3 *Charge transients associated with electrosorption of F_{NOH} on Pt(111) in 0.1 mol dm^{-3} NaOH, in the potential range for double-layer charging*

In addition to cyclic voltammetric studies, potentiostatic charge-transient experiments were also conducted by injecting F_{NOH} at the Pt(111) surface in 0.1 mol dm^{-3} NaOH, as explained in section 4.1.2 of Chapter 4. With 100 μL of 1% F_{NOH} injected at a controlled potential (0.53 V, RHE), an average anodic charge transient of +76 (±2) μC cm^{-2} was recorded.

These experiments were conducted over the potential range for double-layer charging, in order that no interfering displacement (see also section 4.1.2 of Chapter 4) of previously adsorbed H or OH^- species could arise. The observed anodic charge-densities then can only correspond to electrosorption of F_{NOH} on the Pt(111) surface with resulting electrooxidation of dissociated H's, represented by the process **XXXI** below, which is similar to that proposed before for acidic solution (see reaction **XXI** above):

XXXI

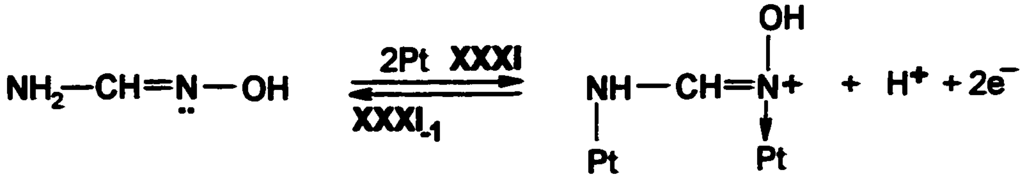

$$NH_2{-}CH{=}\ddot{N}{-}OH \underset{XXXI_{-1}}{\overset{2Pt\ XXXI}{\rightleftharpoons}} \underset{\underset{Pt}{|}}{NH}{-}CH{=}\underset{\underset{Pt}{\downarrow}}{\overset{\overset{OH}{|}}{N^{+}}} + H^{+} + 2e^{-}$$

It can be noted, however, that **XXXI** could involve partial charge transfer at the N centre like in the case of "electrosorption valency" in anion chemisorption.

Thus, electrosorption of F_{NOH} does not involve *associative adsorption*, which would take place without a transient passage of charge from oxidation of dissociated H's, as for the case of CH_3CN in ref. 6 but rather the dissociative electrosorption step **XXXI** is indicated. The electrosorption reactions **XXI**, **XXVIII** and **XXXI** supposedly involve dissociation of H's from N atoms, thus resulting in chemisorption to the Pt surface through the N atoms. This mechanism would be preferred to that from C atoms as the bond energy of N-H compared with that of C-H would favour dissociation of the former bond [52, 53] by *ca.* 8-21 kJ mol^{-1}.

6.6.4 Comparison of behaviour of adsorbed F_{NOH} with A_{NOH} at Pt(111) and with that of F_{NOH} at Pt(100) surfaces in 0.1 mol dm^{-3} NaOH

In alkaline solution the conditions for chemisorption of F_{NOH} and A_{NOH} are importantly different from those in H_2SO_4 solutions, owing to the absence of strongly bound HSO_4^- ions.

The behaviour of F_{NOH} at a concentration of $3x10^{-4}$ mol dm^{-3} at the Pt(111) surface in 0.1 mol dm^{-3} NaOH is shown in Fig. 6.57. Here, as in Figs. 6.53 and 6.54, substantial changes in the voltammetric profile are also observed; the familiar "butterfly" region [B(A), B(C), Fig. 6.57] at *ca.* 0.60-0.90 V, RHE, observed in alkaline solution, is almost completely suppressed and a new, sharp cathodic current peak (C_2) appears on the negative-going sweep in the H UPD region at *ca.* 0.15-0.30 V. Also, at the beginning (≥ *ca.* 0.35 V) of the potential range for double-layer charging, two peaks (A_1, C_1), fairly reversible with respect to total anodic/cathodic charges passed, are observed, respectively, on the positive- and negative-going sweeps. These results suggest that F_{NOH} becomes reactively electrosorbed on the Pt surface on the positive-going sweep (step XXXI) but only after H has been desorbed. However, the details of the process and its interpretation are complex.

The total charge-density of +73 (±2) μC cm^{-2}, measured under the conjugate negative-going peak, observed (Fig. 6.57) between *ca.* 0.55-0.30 V, is in good agreement with the adsorption transient charge of +76 (±2) μC cm^{-2} recorded at 0.53 V (section 6.6.3).

On the other hand, the charge-density of +59 (±2) μC cm^{-2}, measured under the apparently corresponding positive-going current peak (A_1) between *ca.* 0.35-0.55 V is in less good agreement with the transient charge of +76 (±2) μC cm^{-2}, probably since some blocking of the surface by the products of reduction arises under the conditions of cycling. Taking into account the fact that the potential in the voltammetric sweep, commenced at 0.55 V, is progressing towards the H_2 reversible potential, the seemingly conjugate cathodic and anodic peaks, C_1 and A_1, would actually correspond to the same electrosorption process but reduction within the range *ca.* 0.55-0.30 V does not lead to desorption of a product from the surface, as is also the case for CH_3CN at Pt [6]. This was demonstrated by reversing the negatively-going sweep at *ca.* 0.30 V so that the H UPD region was not traversed. Then the apparently conjugate anodic peak, A_I in Fig. 6.57, was no longer observed, indicating that the F_{NOH} species had remained in the adsorbed state. The A_I peak can only be observed again if the next negatively-going sweep is extended to 0.06 V and then reversed positively, exhibiting cathodic peak C_2 (Fig. 6.57).

The maximum coverage of the Pt(111) surface by the F_{NOH} molecules (based on the potentiostatic charge transient experiments reported in section 6.6.3) can be evaluated as *ca.* 0.3 of an equivalent monolayer of H, where the calculated charge for an ideal (111) plane with a coverage of one H atom per Pt surface atom, is [12] 243 $\mu C\ cm^{-2}$. The reduction steps **XXIII** and **XXIV** (see the sequence of reactions **XX-XXIV** above) lead to significant diminution of the surface coverage by the products of the above reactions, compared with the initial coverage by the F_{NOH} species. For this reason, on the first positive-going sweep, the charge passed in the potential range for UPD of H is comparable with that passed in F_{NOH} – free, 0.1 mol dm^{-3} NaOH solution.

Note that the above type of behaviour *does not arise* in the case of adsorption of G^+ on Pt(111) in aq. NaOH (see Fig. 6.18 in section 6.1 of this Chapter). There, reversal of the sweep at onset of UPD of H gives rise directly to an anodic/cathodic pair of peaks, *reversibly generatable*, and no other reduction peak arises over the H UPD region, nor do any continuous Faradaic currents pass in that case. The reactivity behaviour of F_{NOH} is therefore quite different from that of G^+ (see section 6.1.2.3 above).

The anodic electrosorption reaction is as shown above for process **XXXI** and the corresponding reduction would be its reverse, **$XXXI_1$**, in which associative chemisorp-

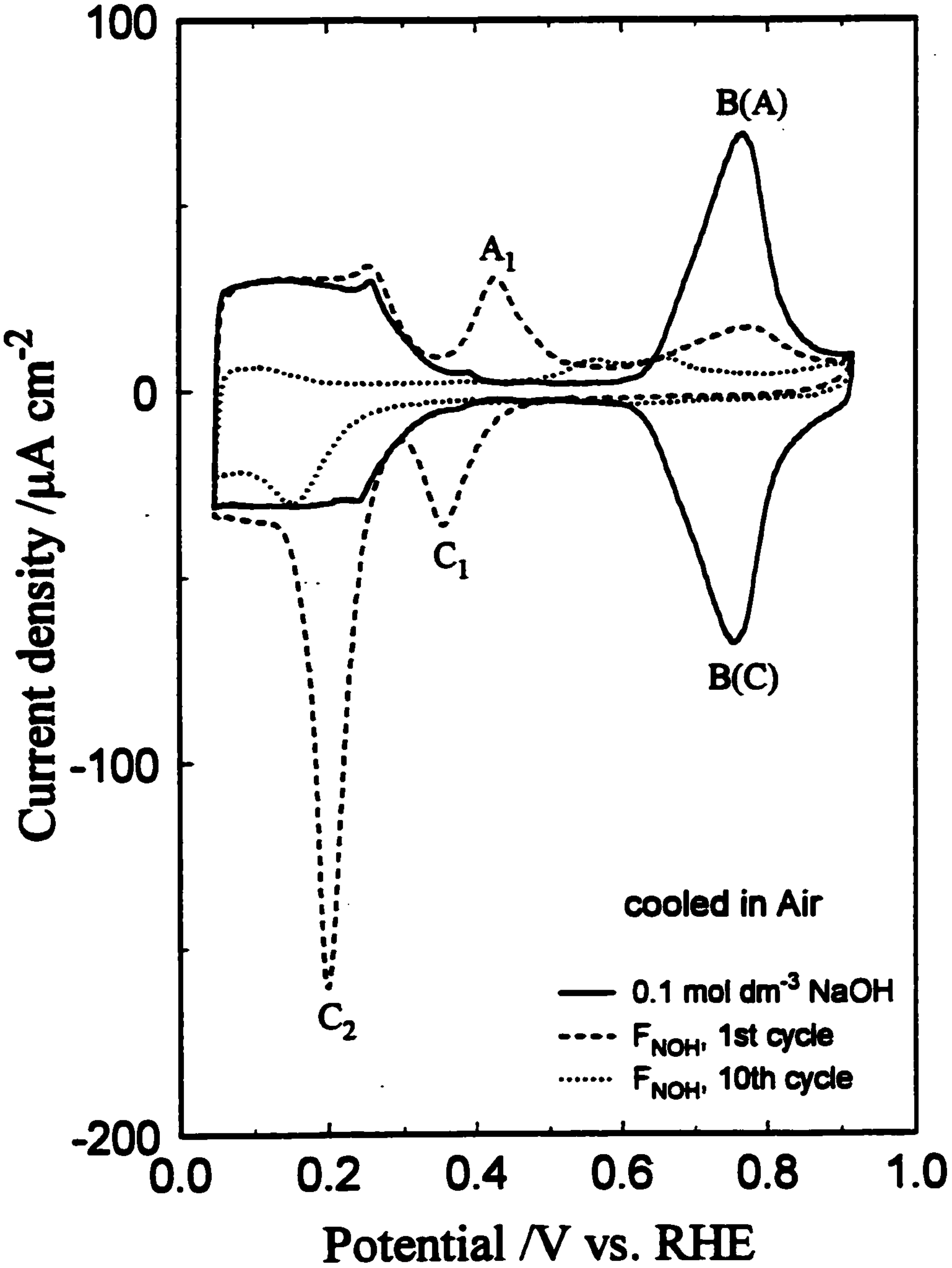

Fig. 6.57 Cyclic voltammograms for Pt(111) in 0.1 mol dm^{-3} NaOH at a sweep rate of 0.050 V s^{-1}, in the presence of F_{NOH} at a concentration of 3x10^{-4} mol dm^{-3}; first and tenth cycles were recorded.

tion of the oxime species could eventually arise with the Pt surface through opening of the double bond. However, such a process would not give rise to a Faradaic charge transient. Further, if the voltammetric sweep is interrupted at the cathodic peak C_2 (*ca.* 0.20 V, RHE), no significant *continuous current* is detectable, which is consistent with the electrochemical reduction current being that for pre-adsorbed rather than for diffusing F_{NOH} molecules.

The reaction goes through the cycle XXI-XXIV (although, in NaOH, with unprotonated F_{NOH}) and HCHO generated in step XXIV can become oxidised on the Pt surface, probably over the potential range 0.50-0.90 V, finally to form strongly adsorbed CO_{ads} species [44, 51], as proposed in section 6.6.1, reaction step XXV. Such CO species formed will tend to become oxidatively desorbed over the range 0.80-1.00 V, exhibiting the anodic current observed at *ca.* 0.90 V [51, 54]. Thus, it can be assumed here that after the reversal of the positive-going sweep at 0.92 V, a significant fraction of CO formed remains still adsorbed on the Pt surface. The effect of progressive accumulation of CO on the surface can be observed in Fig. 6.57 [compare the voltammograms recorded after the first and the tenth (dotted line) cycles].

The behaviour of A_{NOH} at a concentration of 1×10^{-3} mol dm^{-3} at the Pt(111) surface in 0.1 mol dm^{-3} NaOH is shown in Fig. 6.58. It is similar in important ways to that of F_{NOH}. Here, as for F_{NOH}, two, seemingly almost reversible, anodic and cathodic current peaks are observed in the potential range that would otherwise correspond to double-layer charging, although relatively much greater charge is accumulated. However, unlike the behaviour of G^+ at Pt(111), again, if the negative-going sweep is reversed at 0.30 V, *no* conjugate anodic peak is observed: it is only generated after traversal through

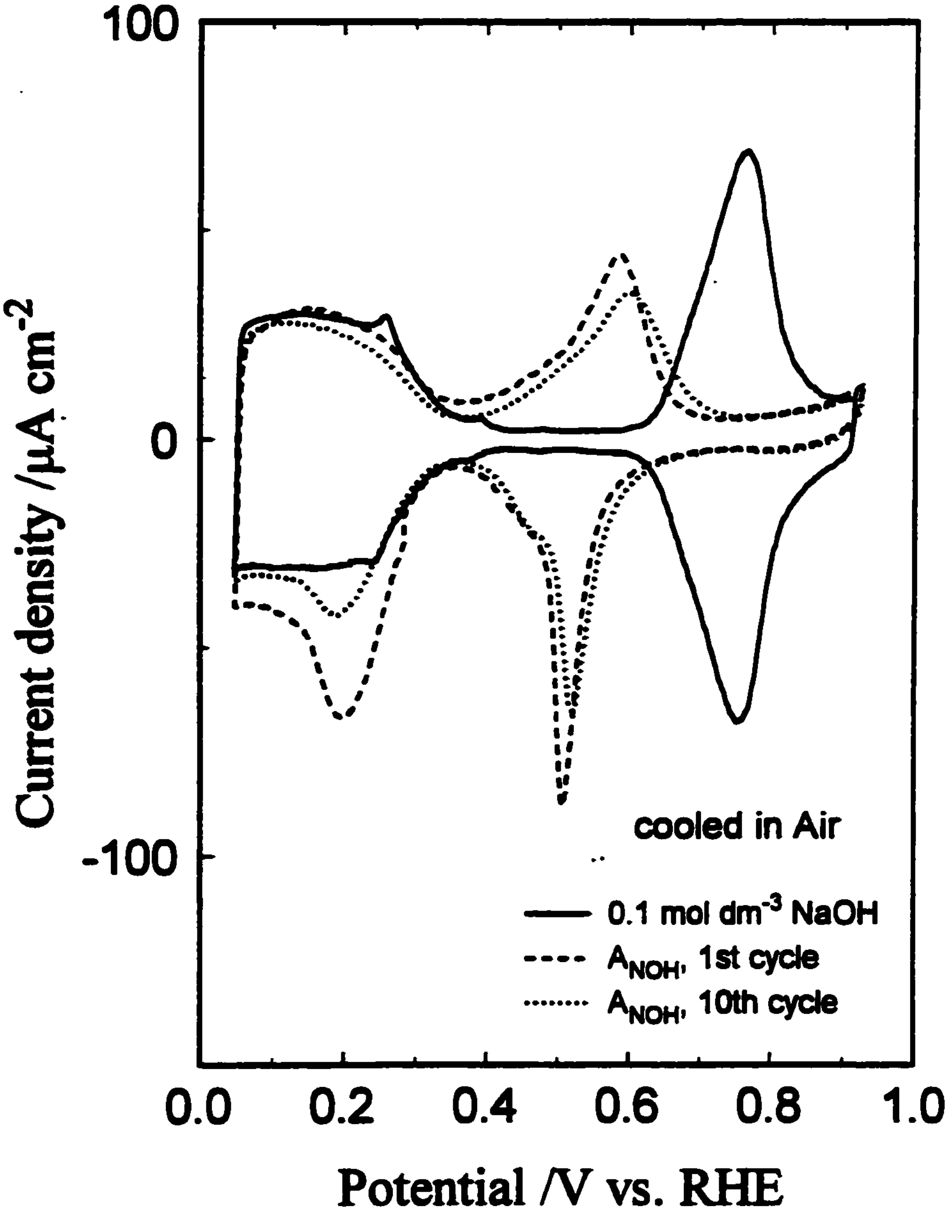

Fig. 6.58 Cyclic voltammograms for Pt(111) in 0.1 mol dm^{-3} NaOH at a sweep rate of 0.050 V s^{-1}, in the presence of A_{NOH} at a concentration of 1×10^{-3} mol dm^{-3}; first and tenth cycles were recorded.

the UPD H region in which a substantial cathodic reduction peak arises between *ca.* 0.30-0.10 V, as seen in Fig. 6.58. Then this anodic peak is seemingly conjugate to the cathodic one up to *ca.* 0.30 V, as for F_{NOH} in Fig. 6.57. Over this following positive-going sweep, an approximately doubled charge-density (compared with that in the presence of F_{NOH}) of +127 (±4) μC cm^{-2} is passed, including the double-layer charge; it would correspond to an oxidative electrosorption reaction proposed as **XXXII** below:

XXXII

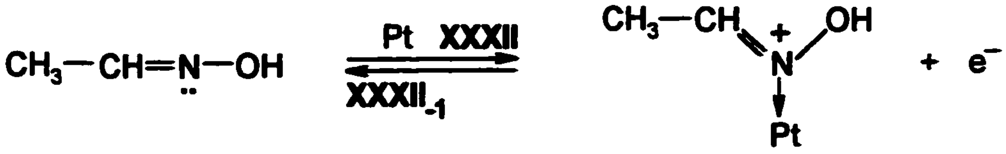

Again, as for process **XXXI**, chemisorption at the N, through partial charge transfer could be involved.

The significant differences in anodic electrosorption charges for F_{NOH} and A_{NOH} species are presumably related to their bonding geometries upon adsorption. Here, the A_{NOH} molecule probably binds to the Pt surface through only the N atom, a configuration that would allow larger coverage and correspondingly greater charge-density for electrosorption. The total charge integrated over the negative-going sweep (between 0.37-0.73 V) is +149 (±4) μC cm^{-2} which implies, again, that the cathodic process can be represented by the reverse of the anodic electrosorption, i.e. process **XXXII**$_1$ above, in which the reduced species remains adsorbed on the surface.

As UPD of H begins, A_{NOH} can undergo electrocatalytic reductive scission [39] to ethylamine (steps **XXIX** and **XXX** above). An important feature of Fig. 6.58, in contrast to Figs. 6.53 and 6.57, is the absence of significant surface contamination by a reaction product, such as CO_{ads}, upon prolonged cycling within the 0.06-0.93 V potential range;

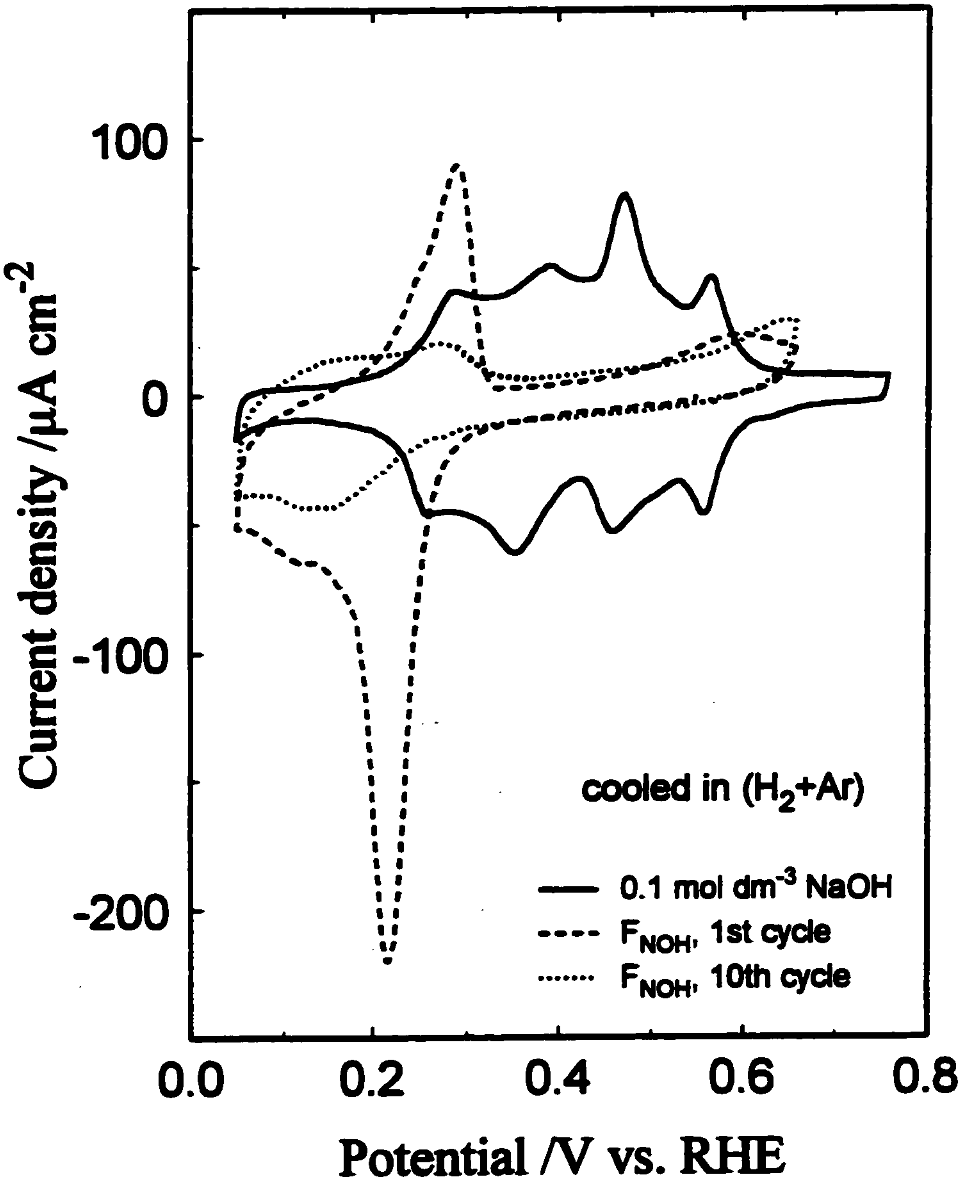

Fig. 6.59 Cyclic voltammograms for Pt(100) in 0.1 mol dm^{-3} NaOH at a sweep rate of 0.050 V s^{-1}, in the presence of F$_{NOH}$ at a concentration of 6x10^{-4} mol dm^{-3}; first and tenth cycles were recorded.

see also Fig. 6.56 for comparison with the behaviour at Pt(111) in H_2SO_4.

The electrochemical behaviour of F_{NOH} at a concentration of $6x10^{-4}$ mol dm^{-3} at Pt(100) in 0.1 mol dm^{-3} NaOH is shown in Fig. 6.59. Qualitatively, the direction of effects compares well with those observed in H_2SO_4. A mechanism of co-operative chemisorption is based here on interaction between the F_{NOH} molecules with adsorbed hydroxyl (OH^-) anions, as with HSO_4^- in the acidic solution case (see also sections 6.1 and 6.3 above for comparison with G^+).

In this case, interaction between adsorbed F_{NOH} and OH^- leads to stabilisation of the adsorption of OH^- causing (cf. ref. 16) the voltammetric profile to be appreciably shifted towards the H_2 reversible potential. However, the charge accumulated on the negative-going sweep is substantially greater than that on the positive-going one (see Fig. 6.59), which implies that considerable reductive scission on the Pt(100) surface is involved, leading indirectly to surface poisoning by CO which arises upon prolonged cycling. The effect of surface poisoning is more noticeable here than that in H_2SO_4 (see Fig. 6.54), thus supporting the proposed mechanism.

The major difference between the adsorption behaviour in 0.1 mol dm^{-3} NaOH at the Pt(111) and (100) surfaces originates because, in NaOH, the Pt(111) plane is the only principal-index plane where the UPD H region is widely separated from that [15] for adsorption of OH^- anions by a double-layer charging zone (see sections 2.4 of Chapter 2 and 6.1.4.2 in this Chapter). Conversely, on the Pt(100) plane, desorption of H is immediately followed by an almost overlapping process of adsorption of oxygen-like species [15] (Fig. 6.59).

6.7 A.c. impedance behaviour of processes involving adsorption of G^+, DMG^+, F_{NOH} and A_{NOH} at Pt single-crystal surfaces

A.c. impedance spectroscopy (see Chapter 2) was employed in the course of this work as a technique complementary to cyclic voltammetry and *in situ* FTIR spectroscopy, which led to the results described earlier in sections 6.1 and 6.3 of this Chapter. Various details about the a.c. impedance equipment, the design of the electrochemical cell used and the impedance measurements were given in sections 4.1.3 and 4.2 of Chapter 4.

Impedance measurements over a wide frequency range enable quantitative distinctions to be made between capacitive, Faradaic kinetic, electrosorptive and purely ohmic components of the response of the overall interfacial electrode process to time- dependent voltage modulation. The interpretation of the resulting data is then usually made by examining which of several rationally selected equivalent circuits, involving series/parallel arrangements of C and R components (sometimes also L), quantitatively leads to best fitting of the data set with respect to the range of frequencies covered in the experiments and also to electrode-potential dependence of such results. Such procedures have been applied in analysis of the experimental results reported in this section of the thesis.

It should be emphasised that the "data fitting" is not simply an empirical polynomial curve-fitting procedure but rather one based on the frequency-response functions generated for the respective selected equivalent-circuit configurations having appropriately valued C and R components, each having defined physical significance.

6.7.1 Impedance behaviour at Pt(100) and (111) single-crystal surfaces in 0.5 mol dm^{-3} H$_2$SO$_4$

First we present the impedance behaviour of Pt(100) and (111) surfaces in 0.5 mol dm^{-3} aq. H_2SO_4 in the absence of the organic adsorbates.

UPD of H at Pt and several other noble or semi-noble metals (see also section 2.2 of Chapter 2) leads to well-ordered, 2-dimensional arrays of H atoms before bulk-phase deposition (OPD of H) commences beyond the H_2 reversible potential. In acidic medium, the process of UPD of H at Pt can be represented by equation 2.50 given in Chapter 2, where an underpotentially deposited array of H is formed by the proton discharge reaction.

For the process of UPD of H, which involves a single adsorbate, the electrical equivalent circuit [55] is as shown in Fig. 2.6a in Chapter 2. The admittance, Y, of that circuit is represented by the equation:

$$Y = \frac{1}{Z_{R_H} + Z_{C_{pH}}} + \frac{1}{Z_{C_{dl}}} = \frac{1}{R_H + \dfrac{1}{j\omega C_{pH}}} + j\omega C_{dl}$$

$$= \frac{\omega C_{pH}}{R_H \omega C_{pH} - j} + j\omega C_{dl} \qquad (6.1)$$

where R_H and C_{pH} are the Faradaic charge-transfer resistance and adsorption pseudocapacitance [55] for UPD of H, respectively, and Z_{RH} and Z_{CpH} are the corresponding impedances of those two components. Equation 6.1, after separating the real and imaginary components, takes the form of equation 2.41 in Chapter 2.

The above-described equivalent circuit gives rise to a semicircle observable throughout the high and intermediate frequency regions of the Nyquist plot and a vertical line characterising a purely capacitive behaviour at sufficiently low frequencies.

The first kinetic study of the process of UPD of H (in 0.5 mol dm^{-3} H_2SO_4), at several Pt single-crystal surfaces by means of a.c. impedance spectroscopy was reported by Morin et al. [56]. These authors examined the dependence of the kinetics of the charge transfer involved in UPD of H at Pt(100) and (311) planes through evaluation of the corresponding charge-transfer resistance [56]. Note, however, that the earliest impedance study of adsorbed H at Pt, but at polycrystalline surfaces, was that of Dolin and Ershler [57].

In the present work, impedance experiments similar to those of ref. 56 were performed at the Pt(100) and (111) electrodes in 0.5 mol dm^{-3} H_2SO_4. The results shown in Table 6.7 below follow, in general, those reported in ref. 56. Thus, over the potential range 0.100 to 0.300 V, the double-layer capacitance values, C_{dl}, for Pt(100) are almost constant with an average value of 24 (±1) μF cm^{-2}. The H adsorption pseudocapacitance, C_{pH}, varies with potential in a similar way to the current-density changes in the CV profiles (see Fig. 4 in ref. 56). The corresponding charge-transfer resistance, R_H, is proportional to the inverse of the exchange rate for the process of UPD of H and remains approximately invariant over the potential range 0.100 to 0.380 V with an average value of 0.274 (±0.004) Ω cm^2. A following rapid increase of R_H, observed at potentials positive to that of the maximum C_{pH} (0.380 V), is probably related to significant interaction from co-adsorbed HSO_4^- on the Pt surface [56]. Furthermore, C_{pH} and C_{dl} reach their maxima at the potential of 0.380 V, beyond which C_{pH} dramatically declines to finally reach a comparatively small value at 0.500 V, and C_{dl} approaches constant value over the potential range for double-layer charging (see Table 6.7). Presumably, for potentials positive to 0.300 V, the double-layer capacitance contains a significant contribution from electrosorption of HSO_4^-. Examples of complex-plane impedance (Nyquist) and Bode phase-angle plots for two values of electrode potential are shown in Figs. 6.60 and 6.61, respectively.

It should be noted that cyclic voltammograms of the Pt(100) surface were recor-

Table 6.7 Parameters for UPD of H at the Pt(100) surface in contact with 0.5 mol dm^{-3} H_2SO_4 (at 293 K), obtained by fitting the equivalent circuit shown in Fig. 2.6a in Chapter 2[2] to the impedance data.

E/mV	R_H/Ω cm^2	x10^5 C_{pH}/F cm^{-2}	x10^6 C_{dl}/F cm^{-2}
100	0.203 ± 0.006	19.70 ± 0.25	21.95 ± 1.62
150	0.151 ± 0.005	14.26 ± 0.19	27.31 ± 1.78
200	0.391 ± 0.006	21.10 ± 0.13	18.64 ± 0.96
250	0.206 ± 0.004	31.88 ± 0.31	26.96 ± 1.15
300	0.258 ± 0.002	78.89 ± 1.18	24.97 ± 0.59
350	0.390 ± 0.003	123.1 ± 0.4	93.80 ± 2.10
380	0.317 ± 0.002	245.0 ± 1.2	193.4 ± 4.2
400	0.568 ± 0.005	64.24 ± 0.28	161.7 ± 2.6
450	5.595 ± 0.545	2.08 ± 0.09	111.1 ± 0.9
500	9.553 ± 3.136	1.17 ± 0.16	104.7 ± 1.8

---

[2] The errors given in the Table above (and in following Tables) correspond to the standard deviations from the fits.

ded before and after each impedance measurement, in order to ensure that no significant surface poisoning or modification had occurred, either during the process of surface preparation or during the time of the a.c. data acquisition. Moreover, after each potentiostatic impedance measurement, the Pt(100) electrode was flame-annealed or prepared by the "fast cycling" electrochemical procedure (see section 5.3.4 of Chapter 5) to match the CV profile shown e.g. in Fig. 6.22 in the present Chapter.

As pointed out by Morin et al. in ref. 56, the rate of the process of UPD of H on the Pt(111) surface was much greater than the corresponding rate on the Pt(100) plane, and, for this reason, was not accessible for frequencies below 3×10^5 Hz. Thus, only a purely capacitive (90° angle) impedance behaviour was observable within the studied frequency range. This observation was confirmed through experiments performed by the present author and will be referred to in more detail later in section 6.7.3, which describes the impedance behaviour of F_{NOH} and A_{NOH} oxime molecules at the Pt(111) surface.

6.7.2 *Impedance behaviour in 0.5 mol dm^{-3} H_2SO_4 at Pt(100) and (111) single-crystal surfaces in the presence of G^+ and DMG^+ in solution*

The a.c. impedance behaviour of the guanidonium cation, at a concentration of 1×10^{-3} mol dm^{-3} G^+, in 0.5 mol dm^{-3} H_2SO_4 at the Pt(100) surface, is shown in Figs. 6.62 and 6.63 over frequency range 2×10^5 to *ca.* 0.1 Hz and 2×10^5 to *ca.* 100 Hz, respectively, below. Here, at potentials close to that of the capacitive "peak" in Fig. 6.22 (270 and 280 mV), the impedance spectra exhibit two semicircles and a capacitive line but at an angle to the Z′ axis different from 90°. The smaller partial semicircle (see Fig. 6.63), observed only at high frequencies, corresponds to the process of UPD of H (compare with Fig.

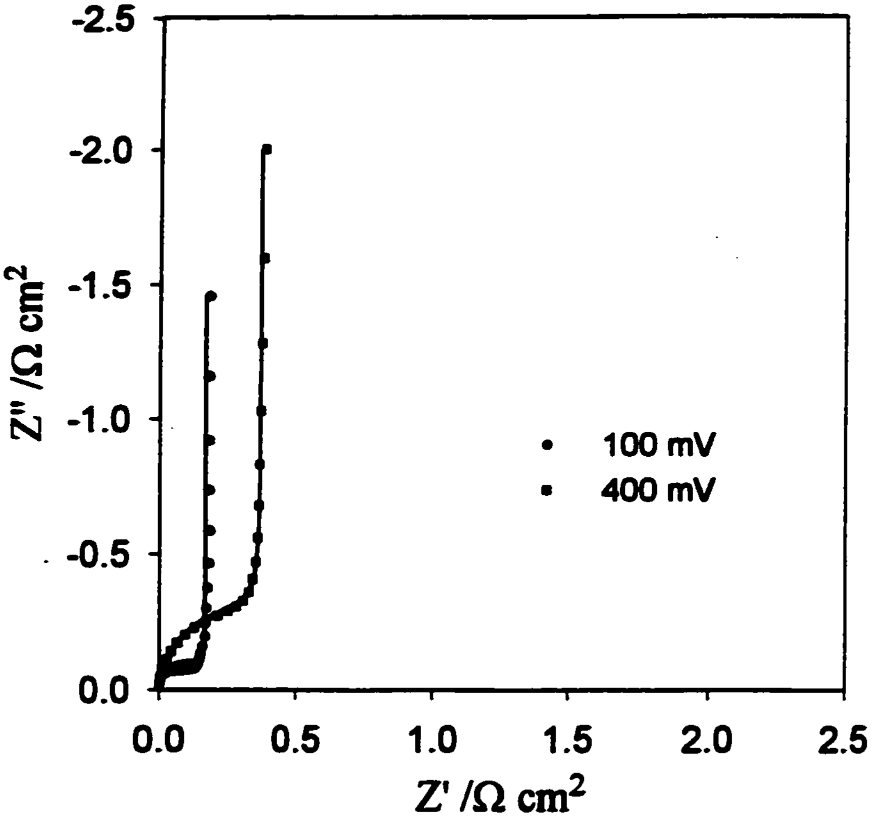

Fig. 6.60 Complex-plane impedance plots for Pt(100) in contact with 0.5 mol dm^{-3} H_2SO_4, recorded at 293 K for the two stated potential values. The solid lines correspond to representation of the data according to the equivalent circuit shown as Fig. 2.6a in Chapter 2. For reasons of clarity, the significant solution resistance component was compensated out from the plots.

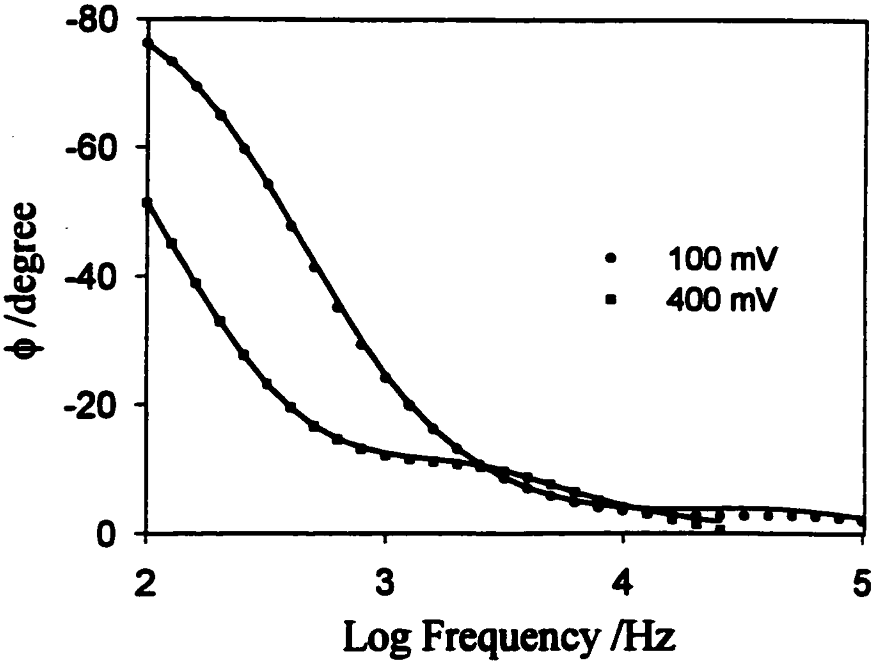

Fig. 6.61 Bode phase-angle plots for the conditions given in Fig. 6.60 above.

6.60), and the part of a large-diameter semicircle (see Fig. 6.63 again), observed throughout the intermediate frequency range (at 270 mV), is probably associated with the charge-transfer process accompanying electrosorption of the G^+ cation on the Pt surface (as previously shown in the process **X**, section 6.2 of this Chapter). Existence of two maxima (at potentials of 270 and 280 mV) is clearly demonstrated in the Bode phase-angle plots in Fig. 6.64. Furthermore, diffusion-control behaviour was not observed in the complex-plane impedance spectra.

A deviation from the purely capacitive (90° phase-angle) behaviour corresponds to distribution (dispersion) of capacitance and can be associated with slow ion adsorption -desorption processes, as recently suggested by Pajkossy [58]. Thus, dispersion of capacitance observed in Fig. 6.62 could be caused by adsorption of G^+ ions on the Pt(100) surface. However, the dispersion effect could also be partly associated with increasing surface inhomogeneity [58] (but was not indicated experimentally), being a result of a prolonged potentiostatic impedance measurement.

For the potential range 0.100-0.200 V, only one semicircle, at high frequencies, is observed in the spectra, which corresponds to the process of UPD of H (see spectrum obtained at 200 mV in Fig. 6.63). However, at potentials positive to 0.350 V, only regular capacitive behaviour (with some dispersion of C) is recorded.

Parameters of the equivalent circuit shown in Fig. 2.6a in Chapter 2 or that presented in Fig. 6.65, comprising the CPE component (see section 2.1.2 of Chapter 2), depending on measurement potential, were then fitted to the experimentally obtained impedance data. All calculated parameters are shown in Table 6.8 below. Analysing the above results, one can observe (at potentials adjacent to that of the capacitive peak in Fig.

6.22) the appearance of significant adsorption pseudocapacitance, C_{pG+}, and charge-transfer resistance, R_{G+}, corresponding to the process of adsorption of G^+ ions on the Pt surface. The R_{G+} parameter increases as potential becomes more positive and its large values (*ca.* 100x greater than R_{H}'s) indicate that kinetics of adsorption of G^+ on Pt(100) is much slower than that of UPD of H on this surface. Conversely, C_{pG+} rapidly declines at potentials positive to the capacitive spike. The slope of the capacitive line is approximately constant over the 0.270-0.300 V potential range and the average value of the φ parameter is 0.749 ± 0.004 (see p. 34 and Fig. 2.8 in Chapter 2). A significant increase of R_H beyond the potential of 0.300 V (compared with that observed in G^+-free H_2SO_4, see Table 6.7), can be explained in terms of the ion-pairing mechanism, proposed earlier in this thesis, where the presence of surface-adsorbed HSO_4^- at significantly lower electrode potentials, as well as co-adsorbed G^+ ions, appreciably influences the kinetics of UPD of H on this surface.

The impedance behaviour of DMG^+ closely resembles that of the G^+ molecule-ion. Thus, over the potential range where the capacitive peak is observed in the CV profile (see Fig. 6.23), significant adsorption pseudocapacitance, C_{pDMG+} and charge-transfer resistance, R_{DMG+}, can be detected (see Table 6.9 below). However, within the narrow potential range over which the capacitive peak is observed in the CV profiles, the process of adsorption of DMG^+ is characterised by significantly ***larger*** R_{DMG+} and substantially ***smaller*** C_{pDMG+} parameter values, compared with the respective parameters for adsorption of the G^+ ion (contrast the results in Table 6.8 with those in 6.9). The above trend reflects differences in adsorption behaviour of G^+ and DMG^+ molecule-ions at Pt where (based on the CV results discussed in section 6.1 of this Chapter) in the

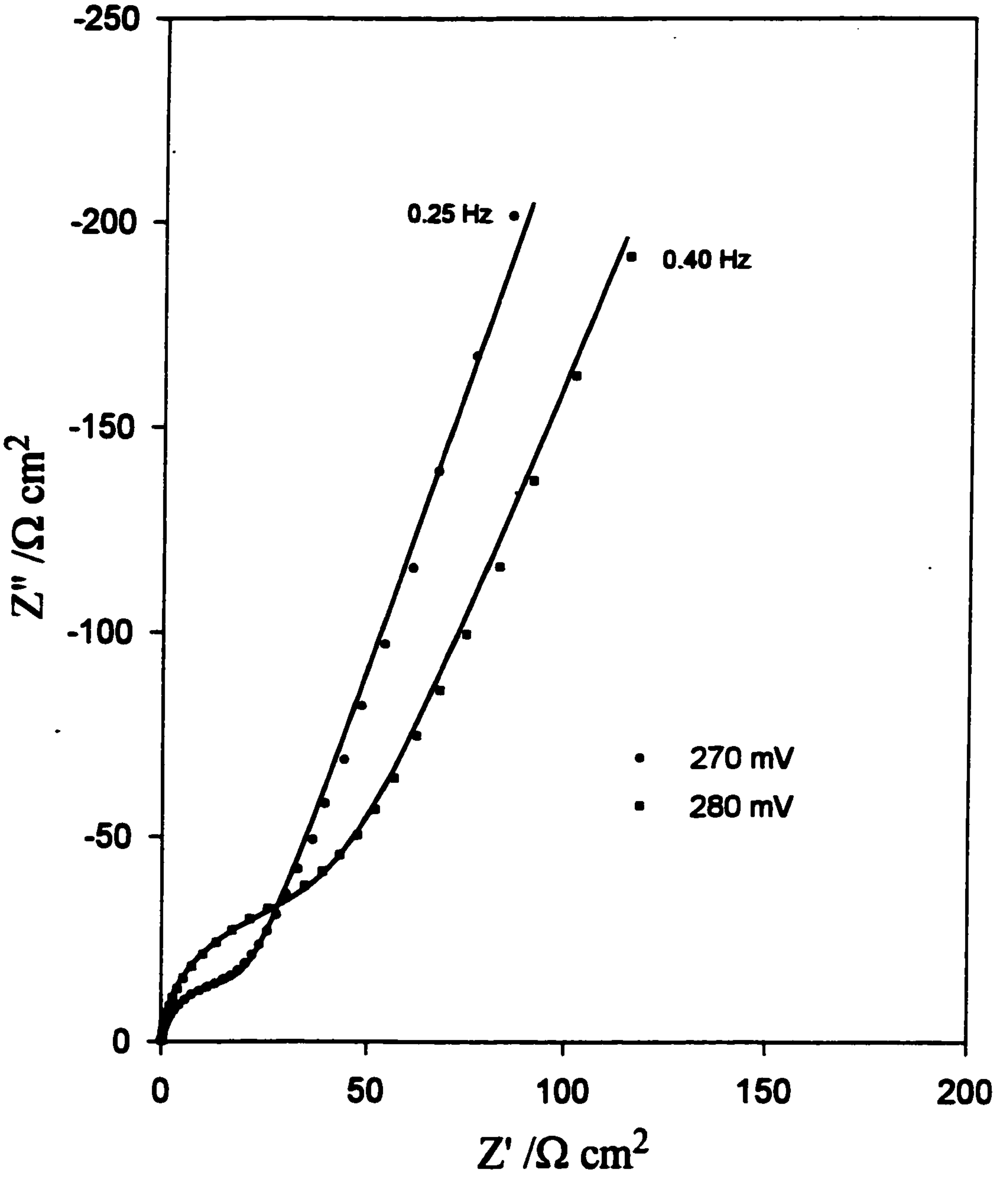

Fig. 6.62 Complex-plane impedance plots for Pt(100) in contact with 0.5 mol dm^{-3} H_2SO_4 in the presence of 1x10^{-3} mol dm^{-3} G^+, recorded at 293 K for the two stated potential values. The solid lines correspond to representation of the data according to the equivalent circuit shown in Fig. 6.65. The solution resistance component was compensated out from the plots.

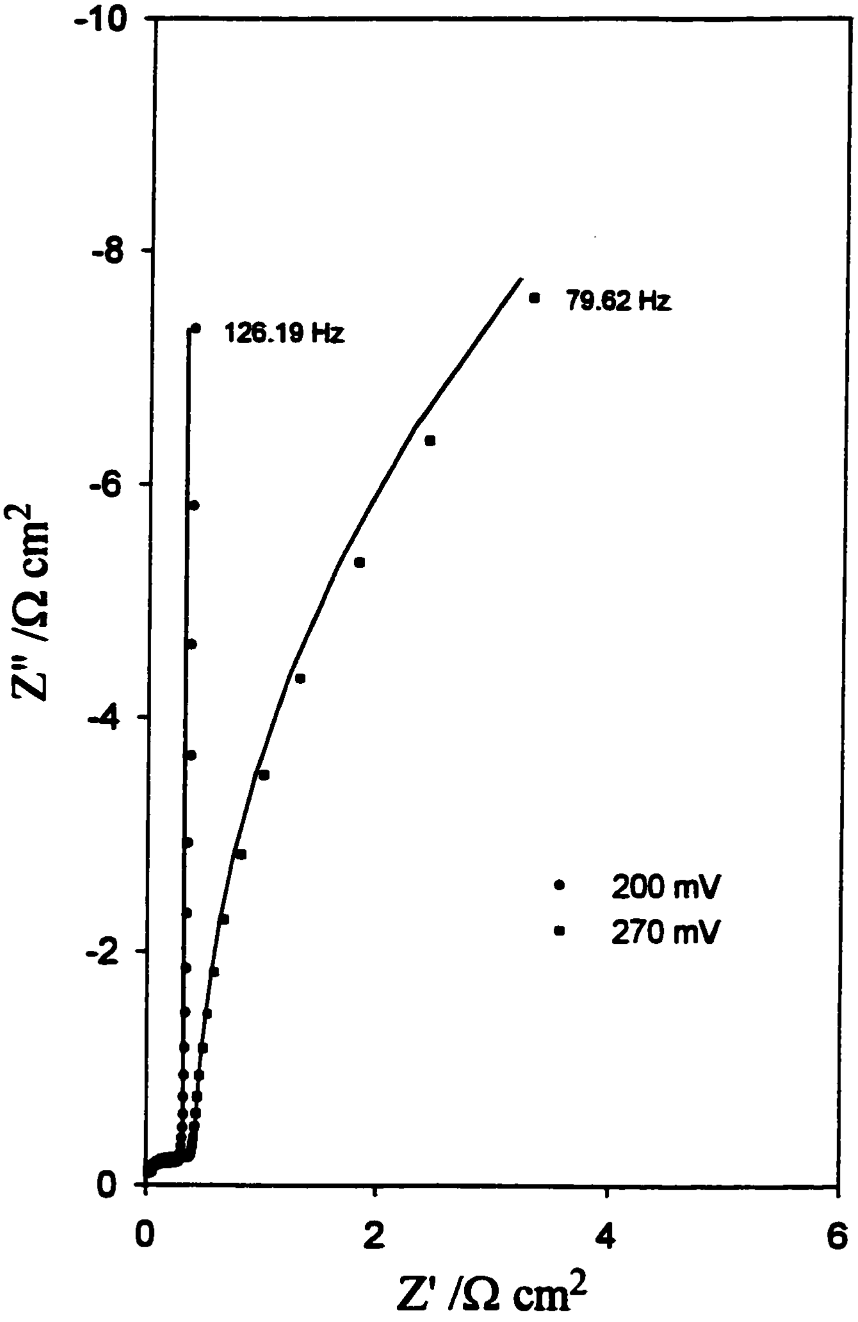

Fig. 6.63 Comparison of complex-plane impedance plots (over the high frequency range) with and without the observable effect of adsorption of G^+ ions at Pt(100), in contact with 0.5 mol dm^{-3} H_2SO_4 and in the presence of 1×10^{-3} mol dm^{-3} G^+, recorded at 293 K for the two stated potential values. The solid lines correspond to representation of the data according to the two above-described equivalent circuits. The solution resistance component was compensated out from the plots.

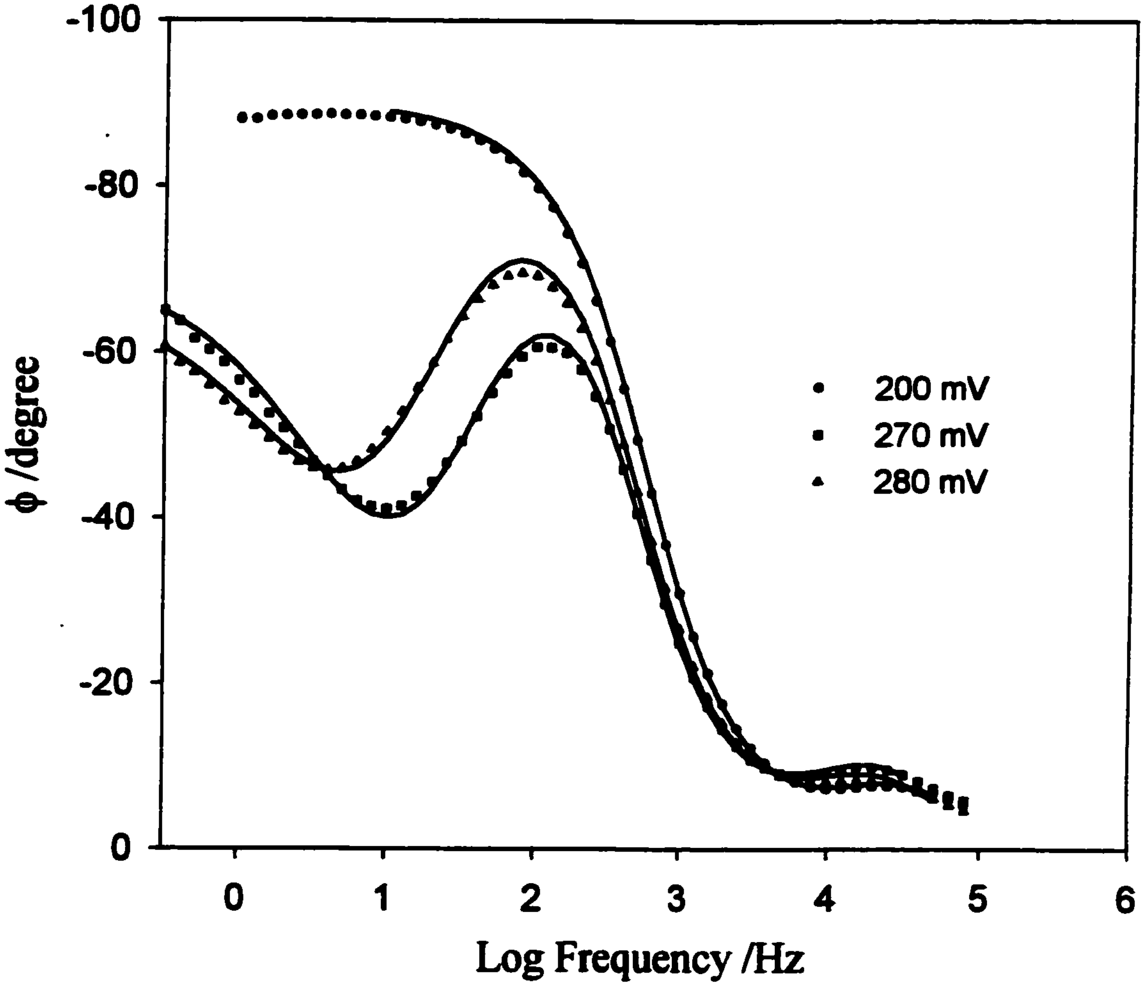

Fig. 6.64 Comparison of Bode phase-angle plots with and without the observable effect of adsorption of G^+, for the conditions given in Figs. 6.62 and 6.63 above.

presence of DMG^+, a substantially weaker chemisorptive interaction (ion-pairing with anionic species) than that for G^+ is observed.

Surprisingly, at the Pt(111) surface, in the presence of 1×10^{-3} mol dm^{-3} G^+, purely capacitive behaviour was observed and no charge-transfer resistance due to adsorption of the G^+ ions could be detected over the potential range 0.100-0.600 V/RHE. This purely capacitive behaviour indicates that kinetics for the process of adsorption of G^+ at the Pt(111) surface is substantially faster (as is also UPD of H) than the corresponding process at the (100) plane. Some small but significant dispersion of capacitance (which was not observed in G^+-free H_2SO_4) was recorded at potentials positive to 0.350 V. The

Table 6.8 Parameters for UPD of H and the process of adsorption of G^+ cation (at a concentration of 1×10^{-3} mol dm^{-3}) at Pt(100) in 0.5 mol dm^{-3} H_2SO_4 (at 293 K), obtained by finding the equivalent circuits which best fitted the impedance data, as shown in Fig. 2.6a in Chapter 2[a] and that shown in Fig. 6.65[b].

E/ mV	R_H/ Ω cm^2	$\times10^5$ C_{pH}/ F cm^{-2}	$\times10^6$ C_{dl}/ F cm^{-2}	R_{G+}/ Ω cm^2	$\times10^5$ C_{pG+}/ F cm^{-2}
100[a]	0.368 ± 0.009	19.57 ± 0.14	16.41 ± 1.18		
150[a]	0.368 ± 0.006	11.67 ± 0.05	15.35 ± 0.44		
200[a]	0.393 ± 0.004	15.47 ± 0.06	17.23 ± 0.54		
270[b]	0.515 ± 0.011	19.22 ± 0.14	19.46 ± 1.06	23.73 ± 0.23	303.6 ± 1.7
280[b]	0.434 ± 0.008	19.22 ± 0.12	22.86 ± 1.07	51.05 ± 0.51	221.5 ± 1.1
300[b]	0.531 ± 0.024	13.36 ± 0.23	32.47 ± 1.91	60.88 ± 4.01	126.6 ± 0.9
350	1.578 ± 0.048	9.26 ± 0.13	35.16 ± 0.43		

Table 6.9 Parameters for UPD of H and the process of adsorption of DMG$^+$ cation (at a concentration of 1x10^{-3} mol dm^{-3}) at Pt(100) in 0.5 mol dm^{-3} H_2SO_4 (at 293 K), obtained by finding the equivalent circuits which best fitted the impedance data, as shown in Fig. 2.6a in Chapter 2^a and that shown in Fig. 6.65^b.

E/ mV	R_H/ Ω cm^2	x10^5 C_{pH}/ F cm^{-2}	x10^6 C_{dl}/ F cm^{-2}	R_{DMG+}/ Ω cm^2	x10^5 C_{pDMG+}/ F cm^{-2}
100^a	0.415 ± 0.010	14.88 ± 0.12	16.41 ± 1.20		
150^a	0.396 ± 0.012	15.24 ± 0.15	16.17 ± 1.50		
200^a	0.573 ± 0.010	11.37 ± 0.08	16.17 ± 0.78		
265^b	0.431 ± 0.007	34.93 ± 0.15	22.03 ± 1.03	31.93 ± 0.38	154.7 ± 1.7
300^b	0.750 ± 0.009	24.61 ± 0.12	38.92 ± 1.01	117.9 ± 3.7	99.64 ± 1.29
380^a	2.103 ± 0.155	4.22 ± 0.14	56.97 ± 1.48		

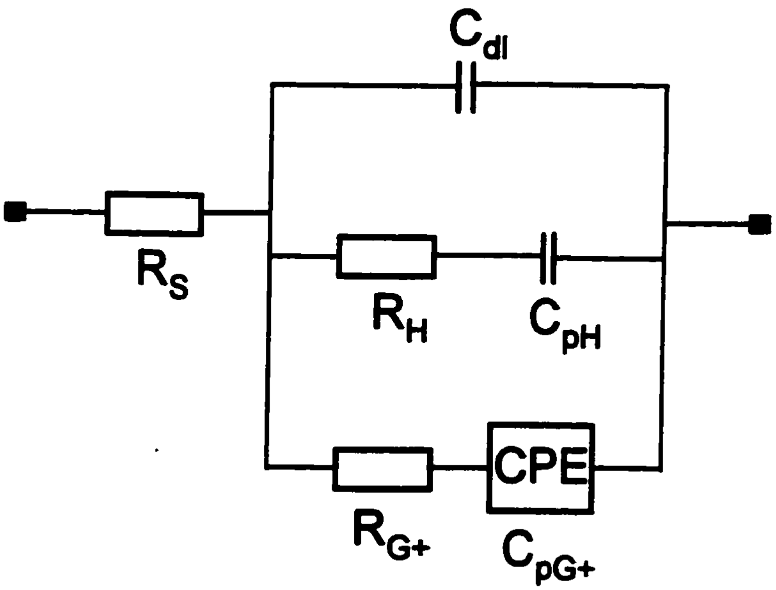

Fig. 6.65 Equivalent circuit for UPD of H in the presence of co-adsorption of G$^+$ ions, comprising the constant phase element (CPE) for distributed capacitance.

impedance behaviour of DMG^+ at the Pt(111) surface was also purely capacitive.

6.7.3 Impedance behaviour in 0.5 mol dm^{-3} H_2SO_4 at Pt(111) single-crystal surface in the presence of A_{NOH} and F_{NOH} in solution

It will be recalled from the cyclic voltammograms of Figs. 6.53 and 6.56 that the current-responses for F_{NOH} and A_{NOH} differ from those of G^+ or DMG^+ by the appearance of cathodic Faradaic current peaks on both the positive and negative-going directions of sweeps.

The impedance behaviour of $(A_{NOH})^+$ at a concentration of 1x10^{-3} mol dm^{-3}, in 0.5 mol dm^{-3} H_2SO_4, at the Pt(111) surface, is shown in Figs. 6.66 and 6.67. The complex-plane Nyquist spectra of A_{NOH}, within the potential region corresponding to the reduction of the molecule on the Pt surface (see Fig. 6.56 in section 6.6.2 of this Chapter), are characterised by the presence of two semicircles. The first, small semicircle, observable only over the high-frequency range (Fig. 6.67), is reminiscent of the reduction process represented by the sequence of reactions **XXIX** and **XXX**, previously shown in section 6.6.2. Understandably, the reduction process becomes facilitated as potential progresses from 0.300 to 0.250 V, towards the H_2 reversible potential (the charge-transfer resistance for the process of reduction of A_{NOH}, R_1, becomes smaller, see Table 6.10 below). It has to pointed out here that, at potentials less positive than 0.250 V, only purely capacitive behaviour was observed; thus, the process of UPD of H on the Pt(111) plane (as in pure 0.5 mol dm^{-3} H_2SO_4), could not be resolved in the presence of A_{NOH} (see Fig. 6.67).

A second, large-diameter partial semicircle (Fig. 6.66), observed over intermediate and low frequencies, probably corresponds to the process of adsorption of A_{NOH} on the

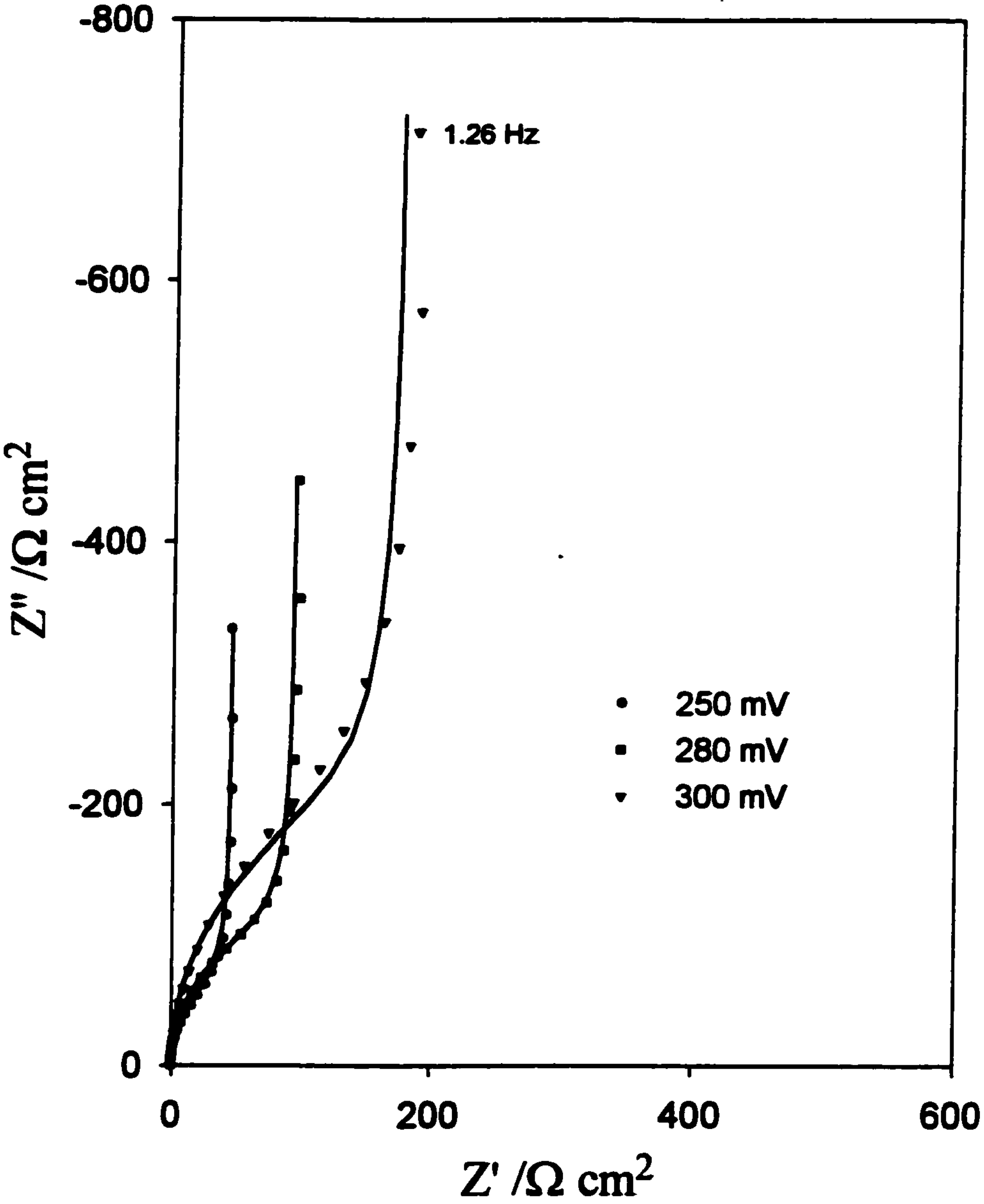

Fig. 6.66 Complex-plane impedance plots for Pt(111) in contact with 0.5 mol dm^{-3} H_2SO_4 in the presence of 1x10^{-3} mol dm^{-3} $(A_{NOH})^+$, recorded at 293 K for the three stated potential values. The solid lines correspond to representation of the data according to the equivalent circuit as shown in Fig. 6.72. The solution resistance component was compensated out from the plots.

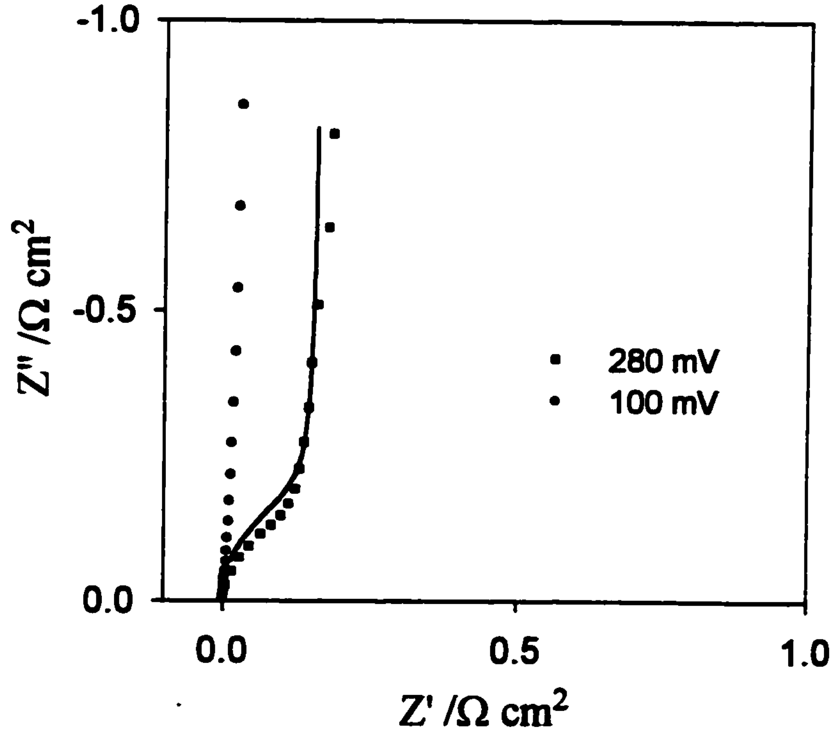

Fig. 6.67 Comparison of complex-plane impedance plots (over the high frequency range) with and without the observable effect of adsorption and reactivity of $(A_{NOH})^+$ at Pt(111), in contact with 0.5 mol dm^{-3} H_2SO_4 and in the presence of $1x10^{-3}$ mol dm^{-3} $(A_{NOH})^+$, recorded at 293 K for the two stated potential values. The solid line corresponds to representation of the data according to the equivalent circuit shown in Fig. 6.72. The solution resistance component was compensated out from the plots.

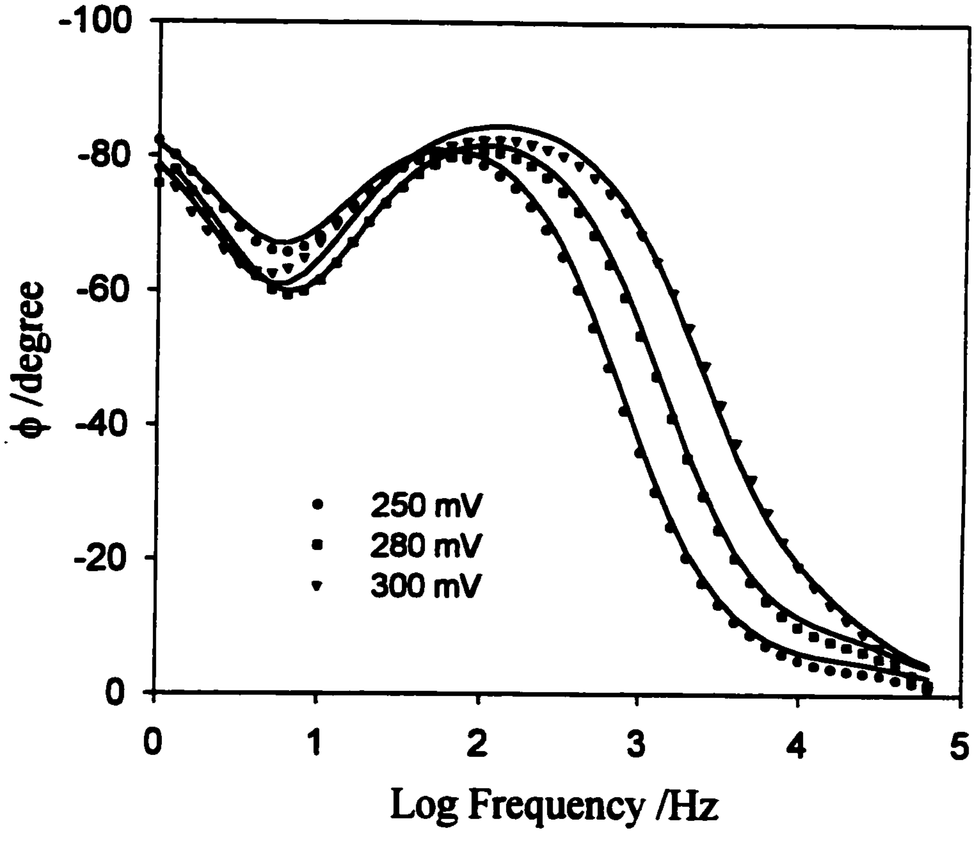

Fig. 6.68 Showing how adsorption and reactivity of A_{NOH} at the Pt(111) surface, for the conditions as in Fig. 6.66, affect the Bode phase-angle plots.

Pt surface (see reaction XXVIII). At 0.250 V, the charge-transfer resistance, R_2, for this process is approximately 1000x greater than that corresponding to the reduction process (R_1). Increase of R_2 (along with decrease of the corresponding adsorption pseudocapacitance, C_{p2}) upon augmentation of the electrode potential, may be related to the influence of co-adsorption from HSO_4^- anions, the onset of which is observed at *ca.* 0.350 V in 0.5 mol dm^{-3} H_2SO_4. However, one cannot exclude a possibility of some ion-pairing between $(A_{NOH})^+$ cations and the HSO_4^- anions on the Pt surface, which would stabilise the adsorption process of the bisulphate ions towards less positive potentials (as was found in the case of G^+ and its analogues). The above-discussed potential-dependence of the charge-transfer resistance for adsorption of A_{NOH} is clearly demonstrated in Fig. 6.66 (see also the Bode phase-angle plots for respective potentials in Fig. 6.68).

At potentials positive to 0.350 V, only capacitive behaviour, with some dispersion of the total capacitance (unlike that purely capacitive behaviour recorded at 0.100 V), is observed in the spectra. All parameters for A_{NOH} shown in Table 6.10 were obtained by fitting the equivalent circuit shown in Fig. 6.72 to the experimental impedance data as a function of frequency at several potentials.

The impedance behaviour of $(F_{NOH})^+$ at a concentration of $1x10^{-3}$ mol dm^{-3}, in 0.5 mol dm^{-3} H_2SO_4, at the Pt(111) surface, is shown in Figs. 6.69 and 6.70. Here, only the low frequency semicircle, related to the process of adsorption of F_{NOH}, is observed in the Nyquist spectra. The semicircle present over the high frequency range for A_{NOH} is not resolvable in the case of F_{NOH}. However, it has to be noted again that no charge-transfer resistance was detectable at potentials below 0.300 V (see, as an example, the purely capacitive line which arises at 0.250 V in Fig. 6.70).

Considerably smaller values of R_2 parameter (compared with those for A_{NOH}) suggest that the kinetics of the process of adsorption of formamidoxime on Pt(111) is significantly faster than the corresponding process for acetaldehyde oxime (see Table 6.10 below). A dramatic increase of the double-layer capacitance over the region where the reductive peak is observed in the CV profile (see Fig. 6.53), could be associated with influence from electrosorption of HSO_4^- anions, as the presence of F_{NOH} on the Pt surface may lead to a shift of the potential of zero charge (*PZC*) for this interface to less positive values. The kinetic parameters for potentials of 0.300 and 0.320 V (as recorded in Table 6.10) were obtained by fitting a circuit (comprising the CPE component) similar to that of Fig. 6.65 but simplified for the case of only one adsorption process taking place, to the experimental impedance data.

In contrast to the behaviour of A_{NOH}, the process of adsorption of F_{NOH} becomes diffusion-controlled around a potential of 0.350 V (see again Fig. 6.69 and the Bode plot for 0.350 V in Fig. 6.71). A phase angle close to 45° is exhibited at low frequencies at this potential, corresponding to diffusion control. The resulting diffusional Warburg parameters (Table 6.10) were obtained by fitting the equivalent circuit shown in Fig. 6.73 to the impedance data.

The diffusional resistance, R_D, the time constant, T, and other parameters obtained from the fit allow calculation to be made of the diffusion coefficient, D_F, for F_{NOH}, the diffusion layer thickness, L, and the diffusional capacitance, C_D. Calculation of the latter parameter is based on equation 6.2 below [59], where for the time constant T«3:

$$C_D = \frac{T}{3R_D} \tag{6.2}$$

Thus, the calculated $C_D = 534 \pm 52$ μF cm^{-2}.

Since, as observed in Fig. 6.69 (at 350 mV), a Faradaic part of the Nyquist spectrum is largely obscured by the diffusional part already at high frequencies, the extrapolated Z' intercept of the diffusional 45° line is negative (-13.44 Ω cm^2). Therefore, further calculations of the diffusion coefficient, D_F, and the diffusion-layer thickness, L, do not lead to meaningful values. However, if such calculations are performed (see Fig. 2.7 and equation 2.43 in Chapter 2), values of the diffusion coefficient, $D_F \approx 1 \times 10^{-8}$ cm^2 s^{-1} and the diffusion layer thickness, $L \approx 8 \times 10^{-5}$ cm, result.

Table 6.10 Parameters for the process of surface adsorption and reduction of $(A_{NOH})^+$ and $(F_{NOH})^+$ molecule-ions (at concentrations of 1×10^{-3} mol dm^{-3}), at Pt(111), in 0.5 mol dm^{-3} H_2SO_4 (at 293 K), obtained by finding the equivalent circuits which best fitted the impedance data, as shown in Figs. 6.72^a and 6.73^b below.

E/ mV	R_1/ Ω cm^2	x10^5 C_{p1}/ F cm^{-2}	x10^6 C_{dl}/ F cm^{-2}	R_2/ Ω cm^2	x10^5 C_{p2}/ F cm^{-2}
			A_{NOH}		
250^a	0.152 ± 0.013	16.48 ± 0.57	59.16 ± 5.79	149.0 ± 2.5	27.58 ± 0.35
280^a	0.356 ± 0.022	6.56 ± 0.17	34.05 ± 1.70	213.3 ± 2.3	19.56 ± 0.19
300^a	0.884 ± 0.031	2.40 ± 0.10	38.52 ± 0.96	420.9 ± 8.4	11.71 ± 0.22
			F_{NOH}		
300			343.6 ± 1.1	48.91 ± 1.67	36.20 ± 1.09
320			300.4 ± 1.3	44.18 ± 0.92	44.37 ± 0.85
	T/s	**R_D/Ω cm^2**			
350^b	0.666 ± 0.056	415.8 ± 20.3	171.0 ± 0.6	59.14 ± 2.12	

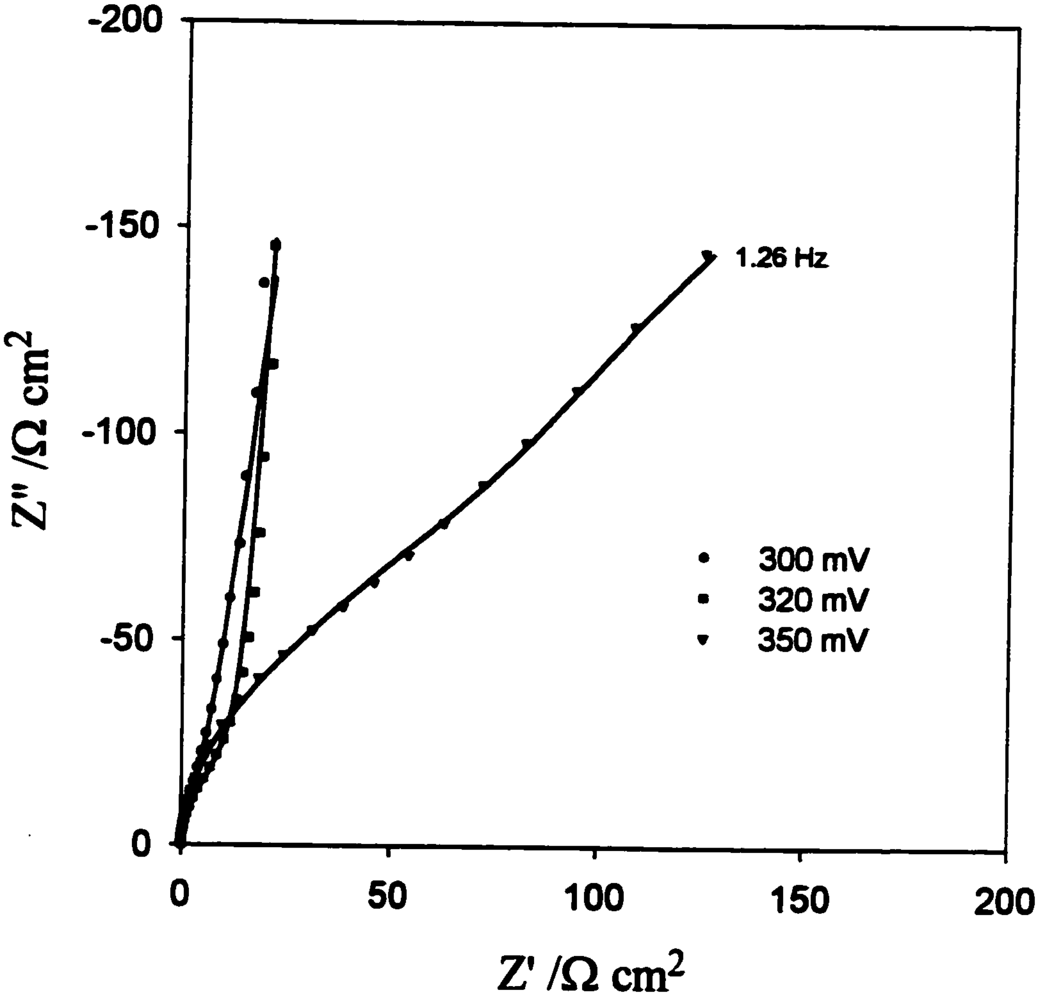

Fig. 6.69 Complex-plane impedance plots for Pt(111) in contact with 0.5 mol dm^{-3} H_2SO_4 in the presence of 1x10^{-3} mol dm^{-3} $(F_{NOH})^+$, recorded at 293 K for the three stated potential values. The solid lines correspond to representation of the data according to the equivalent circuits, as discussed above. The solution resistance component was compensated out from the plots.

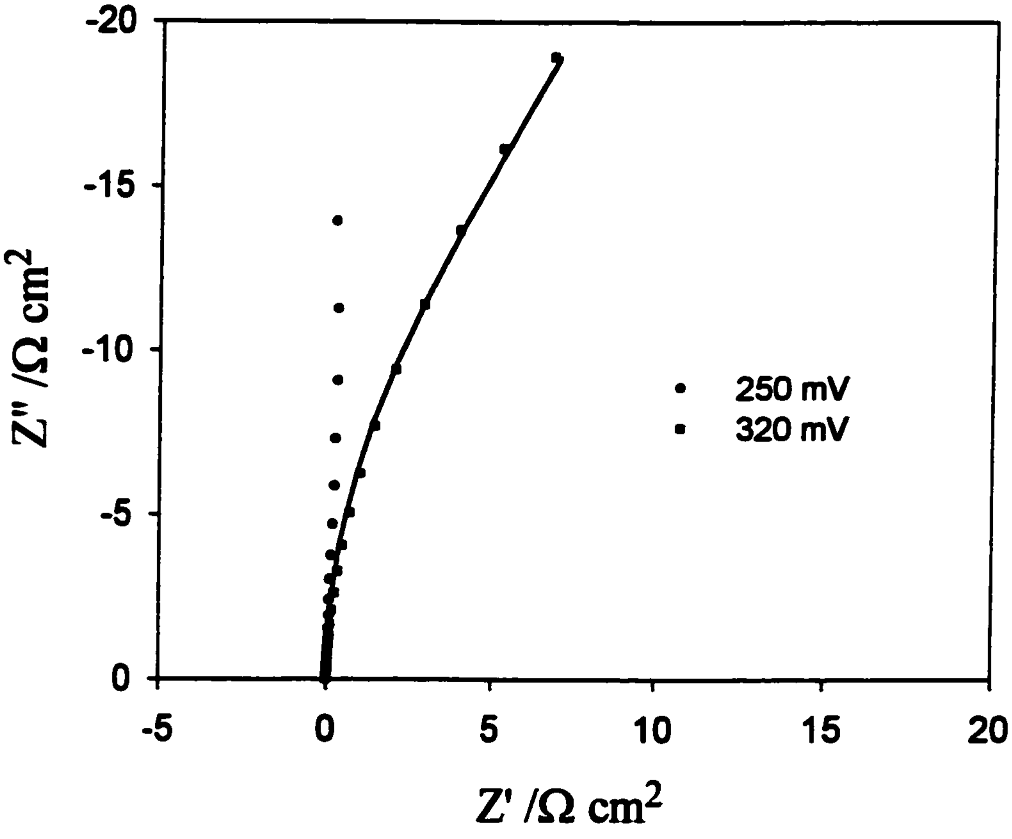

Fig. 6.70 Comparison of complex-plane impedance plots (over the high frequency range) with and without the observable effect of adsorption of $(F_{NOH})^+$ at Pt(111), in contact with 0.5 mol dm^{-3} H_2SO_4 and in the presence of 1x10^{-3} mol dm^{-3} $(F_{NOH})^+$, recorded at 293 K for the two stated potential values. The solid line corresponds to representation of the data according to the equivalent circuit, as discussed above. The solution resistance component was compensated out from the plots.

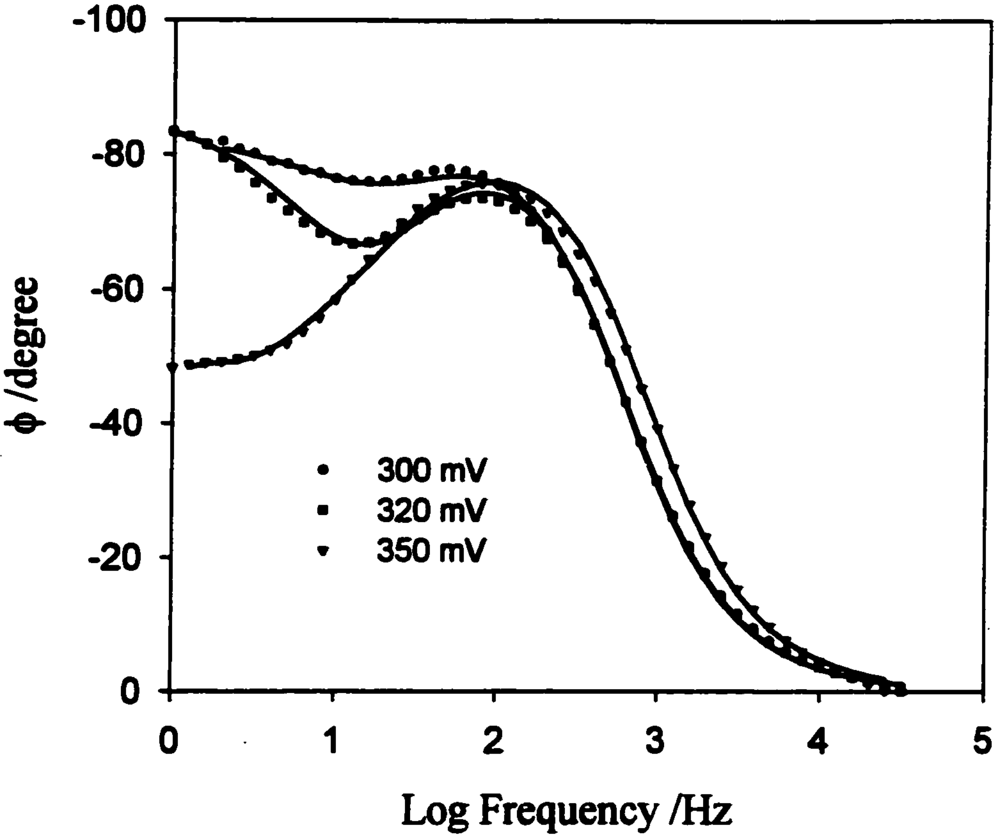

Fig. 6.71 Showing how the Bode phase-angle plots are affected by adsorption and diffusion of F_{NOH} to the Pt(111) surface, for the conditions as in Fig. 6.69.

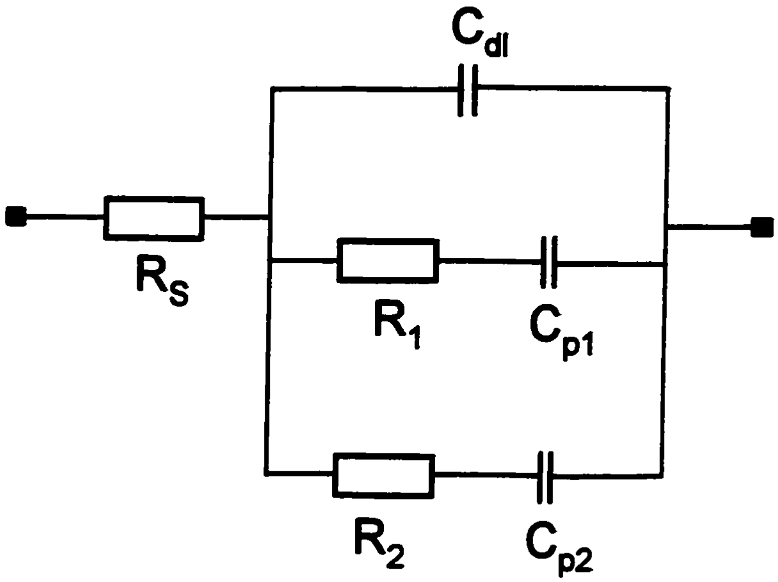

Fig. 6.72 Equivalent circuit for the case when two parallel charge-transfer surface processes take place (adsorption coupled with reduction of A_{NOH} at the Pt(111) plane).

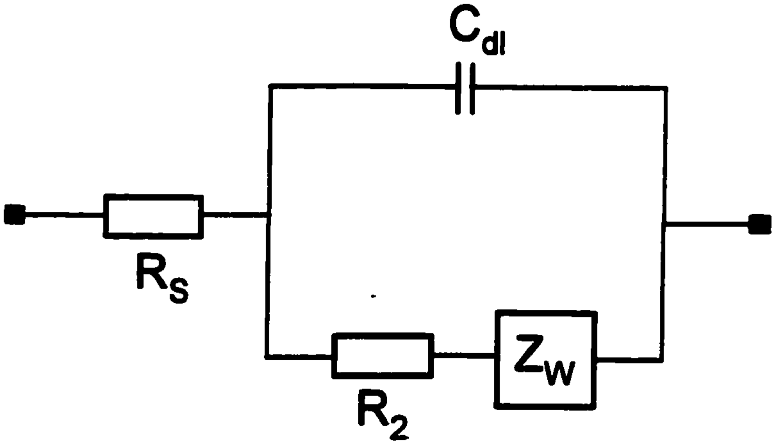

Fig. 6.73 Equivalent circuit for the charge-transfer surface process (adsorption of F_{NOH} at the Pt(111) plane) coupled with diffusion of the species (F_{NOH}) to the Pt surface.

6.8 References

1. J.D. Roberts and M.C. Caserio, *"Basic Principles of Organic Chemistry"*, second edition, W.A. Benjamin, Inc., Menlo Park, 1977, **23**.
2. D.M. Novak and B.E. Conway, *J. Chem. Soc., Faraday Trans.* I, 1981, 77, 2341.
3. B.E. Conway, Y. Phillips and S.Y. Qian, *J. Chem. Soc., Faraday Trans.*, 1995, **91(2)**, 283.
4. V. Climent, A. Rodes, J.M. Orts, J.M. Feliu, J.M. Perez and A. Aldaz, *Langmuir*, 1997, **13**, 2380.
5. J. Clavilier, K.El Achi and A. Rodes, *Chem. Phys.*, 1990, **141**, 1.
6. S. Morin and B.E. Conway, *J. Electroanal. Chem.*, 1994, **376**, 135.
7. S.Ye, H. Kita and A. Aramata, *J. Electroanal. Chem.*, 1992, **333**, 299.
8. E. Morallon, J.L. Vasquez and A. Aldaz, *J. Electroanal. Chem.*, 1992, **334**, 323.
9. H. Kita, S. Ye, A. Aramata and N. Furuya, *J. Electroanal. Chem.*, 1990, **295**, 317.
10. F.C. Nart, T. Iwasita and M. Weber, *Electrochim. Acta*, 1994, **39, No.7**, 961.
11. T. Iwasita, F.C. Nart, A. Rodes, E. Pastor and M. Weber, *Electrochim. Acta*, 1995, **40, No.1**, 53.
12. J. Clavilier, J.M. Orts, R. Gomez, J.M. Feliu and A. Aldaz, *Proc. Symp. on Electrochemistry and Materials Science of Cathodic H Absorption and Adsorption*, B.E. Conway and G. Jerkiewicz (Eds.), The Electrochemical Society, N.J., 1995, **94-21**, 167.
13. E. Morallon, J.L. Vasquez and A. Aldaz, *J. Electroanal. Chem.*, 1990, **288**, 217.
14. N.S. Marinkovic, N.M. Markovic and R.R. Adzic, *J. Electrochem. Soc.*, 1992, **330**, 433.

15. N.M. Markovic, S.T. Sarraf, H.A. Gasteiger and P.N. Ross, Jr., *J. Chem. Soc., Faraday Trans.*, 1996, **92**, 3719.

16. B. Pierozynski, S. Morin and B.E. Conway, *J. Electroanal. Chem.*, 1999, **467**, 30.

17. T.L. Davies, W.E. Yelland and C.C. Ma, *J. Am. Chem. Soc.*, 1937, **59**, 1993.

18. L.M. Baugh and R. Parsons, *J. Electroanal. Chem.*, 1975, **58**, 229.

19. T. Iwasita and F.C. Nart, *J. Electroanal. Chem.*, 1990, **295**, 215.

20. J. Clavilier, *J. Electroanal. Chem.*, 1980, **107**, 211.

21. J. Clavilier, R. Faure, D. Guinet and R. Durand, *J. Electroanal. Chem.*, 1980, **107**, 205.

22. J. Clavilier and R. Pineaux, *C.R. Acad. Sci., Paris*, 1965, **260**, 891.

23. P.W. Faguy, N. Markovic, R.R. Adzic, C.A. Fierro and E.B. Yeager, *J. Electroanal. Chem.*, 1990, **289**, 245.

24. M.E. Gamboa-Aldeco, E. Herrero, P.S. Zelenay and A. Wieckowski, *J. Electroanal. Chem.*, 1993, **348**, 451.

25. S. Thomas, Y.E. Sung, H.S. Kim and A. Wieckowski, *J. Phys. Chem.*, 1996, **100**, 11726.

26. A.M. Funtikov, U. Stimming and R. Vogel, *J. Electroanal. Chem.*, 1997, **428**, 147.

27. A. Wieckowski, P. Zelenay and K. Varga, *J. Chim. Phys.*, 1991, **88**, 1247.

28. R.T. Conley, *Infrared Spectroscopy*, Allyn and Bacon, Inc., Boston, 1966.

29. J.B. Lambert, H.F. Shurvell, L. Verbit, R.G. Cooks and G.H. Stout, *Organic Structural Analysis*, Macmillan Publishing Co., Inc., New York, 1976.

30. R. M. Silverstein and F. X. Webster, *Spectrometric Identification of Organic*

Compounds, John Wiley & Sons, Inc., 6th edition, New York, 1998.

31. M. Rubel, C.K. Rhee, A. Wieckowski and P.A. Rikvold, *J. Electroanal. Chem.*, 1991, **315**, 301.

32. H.A. Kozlowska , B.R. MacDougall and B.E. Conway, *J. Electroanal. Chem.*, 1972, **39**, 287.

33. B.E. Conway, B. MacDougall and H.A. Kozlowska, *J. Chem. Soc., Faraday Trans. I*, 1972, **68**, 1566.

34. B. MacDougall, B.E. Conway and H.A. Kozlowska, *J. Electroanal. Chem.*, 1971, **32**, App. 15.

35. J. Clavilier, R. Albalat, R. Gomez, J.M. Orts, J.M. Feliu and A. Aldaz, *J. Electroanal. Chem.*, 1992, **330**, 489.

36. J. Clavilier, R. Albalat, R. Gomez, J.M. Orts and J.M. Feliu, *J. Electroanal. Chem.*, 1993, **360**, 325.

37. D.S. Kemp and F. Vellaccio, *Organic Chemistry*, Worth Publisher, Inc., New York, 1980.

38. A. Streitweiser Jr. and C.H. Heathcock, *Introduction to Organic Chemistry,* Macmillan Publisher, New York, 1976.

39. M.M. Baizer and H. Lund, *Organic Electrochemistry. An Introduction and a Guide*, Marcel Dekker, Inc., New York, 1983.

40. R.M. Elofson and J.G. Atkinson, *Can. J. Chem.*, 1956, **34**, 4.

41. A.J. Fry, *Synthetic Organic Electrochemistry*, John Wiley & Sons, Inc., New York, 1999.

42. A. Hamelin, in *Modern Aspects of Electrochemistry*, B.E. Conway, J.O'M.

Bockris and R.E. White (Eds.), Plenum Press, New York, 1985, **16**, Chapter1.

43. J. Clavilier, A. Rodes, K. El Achi and M.A. Zamakhchari, *J. Chim., Phys.*, 1991, **88**, 1291.

44. R.R. Adzic, W.E. O'Grady and S. Srinivasan, *Surf. Sci.*, 1980, **94**, L.191.

45. B.E. Conway and B.V. Tilak, *Adv. Cat.*, 1992, **38**, 1.

46. A. Bewick, *J. Electroanal. Chem.*, 1983, **150**, 481.

47. R.R. Adzic, W.E. O'Grady and S. Srinivasan, *J. Electrochem. Soc.*, 1981, **128**, 1913.

48. H. Angerstein-Kozlowska, B. MacDougall and B.E. Conway, *J. Electrochem. Soc.*, 1973, **120, No.6**, 756.

49. M.W. Breiter, *Electrochim. Acta*, 1963, **8**, 457.

50. A. Hamnett, in *Interfacial Electrochemistry, Theory, Experiment and Applications*, A. Wieckowski (Ed.), Marcel Dekker, Inc., New York, 1999, **47**, 843.

51. G.Q. Lu, A. Crown and A. Wieckowski, *J. Phys. Chem. B*, 1999, **103**, 9700.

52. A.G. Gaydon, *Dissociation Energies and Spectra of Diatomic Molecules*, Chapman and Hall Ltd., 3rd edition, London, 1968.

53. S.G. Lias, J.E. Bartness, J.F. Liebman, J.L. Holmes, R.D. Levia and W.G. Mallard, *J. Phys. Chem. Ref. Data*, 1988, **17**, suppl.1.

54. W. Vielstich, *Fuel Cells: Modern Processes for the Electrochemical Production of Energy*, (translation from German by D.J.G. Ives), Chichester, Wiley-Interscience, New York, 1970.

55. D.A. Harrington and B.E. Conway, *Electrochim. Acta*, 1987, **32**, 1703.

56. S. Morin, H. Dumont and B.E. Conway, *J. Electroanal. Chem.*, 1996, **412**, 39.

57. P. Dolin and B. Ershler, *Acta Physicochim. URSS*, 1940, **13**, 747.

58. T. Pajkossy, *J. Electroanal. Chem.*, 1994, **364**, 111.

59. J. Ross Macdonald (Ed.), *"Impedance Spectroscopy. Emphasizing Solid Materials and Systems"*, John Wiley and Sons, New York, 1987.

Chapter 7

Conclusions and Claims to Original Work

General conclusions

During the course of this work, two electrochemical surface processes were investigated: the process of adsorption of guanidonium (and structurally-related) molecule-ions and the reactivity of two aliphatic oximes, formamidoxime and acetaldehyde oxime, at Pt single-crystal surfaces.

The present electrochemical studies on the guanidonium cation (G^+) as an adsorbate on various Pt single-crystal planes, have been conducted by means of cyclic voltammetry in three different electrolyte media. The results revealed remarkable surface specificities upon adsorption, accompanied by usually small but, for some cases, appreciable increases in the total electric charges measured within the range of UPD of H. The shifts of current-response peaks towards the H_2 reversible potential and "squeezing" of the UPD H CV profiles that have been observed, are explained in terms of co-operative chemisorption (an ion-pairing effect in the chemisorbed state) between the G^+ cations and co-adsorbed anions (HSO_4^-, ClO_4^- or OH^-), leading to stabilisation of adsorption of the anionic species.

The most striking effects in voltammetry are found at the Pt(111) plane in H_2SO_4 where, in the presence of G^+, the potential for HSO_4^- desorption becomes shifted appreciably (by about 200 mV) towards the RHE potential. The only surface at which the process of adsorption of G^+ occurs in the relative absence of adsorbed anionic species is the Pt(111) plane, where this behaviour is observed in NaOH and $HClO_4$ solutions.

Overall, the effects of G^+ are, surprisingly, qualitatively similar to those of adsorbed *anions*, such as Cl^-, Br^- or I^- at Pt, i.e. "anion mimetic" effects arise on account of adsorption of *a cation*. No significant diffusion control accompanies the process of adsorption of G^+ on the Pt surface.

In terms of charge effects, the most remarkable effects of G^+ adsorption are found for the Pt(100) plane and its derivative surface, the Pt(511) stepped plane, where the increases of the total charge are up to 30% above those for the G^+-free solutions (26% at Pt(100) in 0.5 mol dm^{-3} H_2SO_4). These effects are the result of chemisorption of the G^+ cations themselves on the Pt surface. It has to be noted that due to the significantly smaller coverage by HSO_4^- ions on the Pt(100) surface, compared with that on the (111) plane, substantially more sites are available for adsorption of the G^+ cations on the former surface.

For the three molecules structurally-related to G^+, namely, N,N-dimethylguanidonium (DMG^+) and acetamidonium (AA^+) cations, and urea (U), the observed differences in voltammetric behaviour from that recorded for G^+ are explained in terms of the ion-pairing between the G-analogues and surface-adsorbed HSO_4^- (ClO_4^-, OH^-) anions being substantially weaker than that for the corresponding effect of the G^+ cation. For DMG^+, the latter difference is assigned to steric effects that are introduced by the presence of the two *gem*-methyl groups on one of the N atoms. For AA^+, less significant interaction of this cation with e.g. the HSO_4^- anion, is related to the fact that a dipole-dipole rather than a cation-dipole (as indicated for the G^+ cation) interaction between the AA^+ species and the HSO_4^- anion is indicated. Finally, in the case of urea, an analogous effect of weakening the ion-pairing is attributed to urea's low basicity and thus much lower tendency for urea to exist in a protonated form compared with that for G (thus, only *ca.* 10% of U molecules exist as U^+ at pH≈1 compared with *ca.* 99% of G^+ under the same pH conditions).

In situ FTIR spectroscopy was employed to provide complementary information to that obtained by means of voltammetry for studying the adsorption behaviour of the selected small molecules at Pt surfaces. In the present work, the process of adsorption of G^+ cations on Pt(111) and Pt(100) single-crystal surfaces, and their effects on UPD of H, were examined. *In situ* FTIR spectroscopy enabled the mechanism of these effects, proposed on the basis of the CV results, to be better understood in terms of the observable influence, at the molecular level, of co-adsorbed G^+ on the state of adsorbed HSO_4^- ions. From previous literature, it seemed unlikely that G^+ ions could undergo catalytic reduction (by hydrogenation) or be chemisorbed at an Hg electrode. However, as confirmed by the FTIR measurements, the electrocatalytic properties of Pt substrates lead to guanidine undergoing dissociative chemisorption at the (111) and (100) surfaces. The process is co-operative with adsorption of HSO_4^- ions (the ion-pairing effect) and strongly depends on the bisulphate surface coverage. The dissociative electrosorption of G^+ on the Pt surface is a 2-electron anodic process, in which $2H^+ + 2e^-$ are released. The above process was supported by making appropriate comparisons with the behaviour of urea, which was also shown to be chemisorbed under the same conditions. However, compared with G^+ at the Pt(111) surface, a significantly weaker strength of the interaction between U and HSO_4^- is indicated. Again, the latter effect is related to the considerably lower tendency for urea to be protonated in acidic media.

The broad band observed in the IR spectra over the 1500-1600 cm^{-1} range corresponds to the $C=N^+$ stretch of G^+. The characteristic vibrational group frequency for this mode is about 1640-1690 cm^{-1} and its negative shift in frequency (to *ca.* 1540 cm^{-1} for the G^+ cation) can be largely attributed to the effect of diminution of the force constant of the $C=N^+$ group upon adsorption of the G^+ species on the Pt surface. The effects involved in this behaviour are attributed to electrostatic (ion/lone-pair donor) interaction between the G^+ and the HSO_4^- species, associated with the presence of a localised positive charge on the N atom of the G^+ ion when it becomes adsorbed.

On the other hand, the positive shift in frequency of the $C=N^+$ stretch mode in the case of the Pt(100)/G^+ system, by *ca.* 40 cm^{-1}, is attributed to the relative increase of the force constant, influenced to some degree by dispersal of the positive charge on $C=N^+$ interacting with adsorbed HSO_4^-, related to change of strength of the interphasial ion-pairing interaction.

The bisulphate band (1200-1300 cm^{-1}), characteristic of HSO_4^- adsorption at the Pt(111) surface, appears in the spectra at significantly less positive potentials (*ca.* 200 mV) when G^+ is present than in its absence in G^+-free, 0.05 mol dm^{-3} H_2SO_4 solution. This provides a molecular basis for the substantial voltammetric shift of potential for HSO_4^- desorption (and possibly also OH^-) towards the H_2 reversible potential that arises in the presence of the G^+ ions and thus supports the proposed interfacial ion-pairing effect.

Employment of a.c. impedance spectroscopy provided further complementary information on the interfacial processes involving adsorption of G^+, DMG^+ at the Pt single-crystal surfaces, and the coupled electrosorptive reduction processes that take place with A_{NOH} and F_{NOH}. In particular, Faradaic charge-transfer processes are distinguishable from purely capacitive ones and the role of diffusion control can be characterised from phase-angle measurements over a wide range of frequencies.

The contributions to original research are the following:

For the first time, thorough investigations have been made of the process of adsorption of G^+ and its three structurally close analogues at various Pt single-crystal surfaces, in conjunction with supporting electrolytes containing three different anions.

1. The process of adsorption of G^+ was shown to exhibit a high degree of specificity to four different Pt surface geometries examined, providing a new example of surface-specific adsorption of a small organic molecule at single-crystal Pt surfaces (compare with previous results reported from this laboratory for CH_3CN electrosorption).
2. The effects of G^+ on the cyclic voltammetric profiles are explained in terms of co-operative chemisorption (the ion-pairing effect) of the latter cation with the three different anionic species, adsorbed in the interphase.
3. Observable differences in adsorption behaviour of G-analogues are conveniently explained in terms of weakening of the ion-pairing interaction between the latter G-analogues and co-adsorbed anions on the Pt surface.
4. CO adsorbate displacement measurements in the presence of G^+ in 0.5 mol dm^{-3} H_2SO_4 and 0.1 mol dm^{-3} NaOH solutions at Pt(111) and (100) surfaces strongly supported the above-proposed mechanism of interaction of G^+ (and its analogues) with the surface adsorbed anions. Moreover, adsorbate displacement by CO in NaOH has been reported for the first time.

5. Evaluations of transient charges upon adsorption of G^+ and U in 0.5 mol dm^{-3} H_2SO_4 and 0.1 mol dm^{-3} NaOH were made; the results obtained at Pt(111) in the latter electrolyte (over the potential range for the double-layer charging), proved that G^+ (and U) become electrosorbed in an anodic charge-transfer process, thus corresponding to dissociative electrooxidation of H from these adsorbates. Based on the above results, coverages of the Pt(111) surface by the G^+ and U species in NaOH were evaluated at $\theta_{G+} = 0.62$ and $\theta_U = 0.63$ of an equivalent H monolayer.
6. FTIR spectroscopic characterisation of the process of co-operative chemisorption of G^+ with HSO_4^- anion provided molecular evidence for the ion-pairing interaction mechanism that had been proposed, based on the CV results.
7. The effects of G^+ were found to be surprisingly similar to those of specifically adsorbed anions, e.g. Cl^-, Br^- or I^-, but were shown to be quite different in origin.
8. A.c. impedance spectroscopy provided confirmation of the role of electrosorption of G^+ and DMG^+ through evaluation of the associated charge-transfer resistances. Also the impedance results provided support for the ion-pairing mechanism based on the voltammetric and spectroscopic results.

The necessity and importance of using the several procedures referred to above, in a complementary way, was demonstrated as a requirement for full understanding of the complex processes that arise in the present work.

Electrochemical cyclic voltammetric experiments on reactivity of formamidoxime (F_{NOH}) and acetaldehyde oxime (A_{NOH}) at Pt(111) and (100) surfaces were also conducted and again revealed remarkable specificities to surface geometry upon adsorption. The most striking effects were found for the Pt(111) plane in H_2SO_4 solution where potential-dependent Faradaic reduction currents arise, unlike the behaviour with G^+, DMG^+ and AA^+.

In 0.5 mol dm^{-3} H_2SO_4, both the $(F_{NOH})^+$ and $(A_{NOH})^+$ molecule-ions undergo preferred electrocatalytic reductive scission in the chemisorbed state on the Pt(111) surface, involving UPD H. The $(A_{NOH})^+$ adsorbate becomes reduced to ethylamine but, in the process of $(F_{NOH})^+$ reduction, the eventual product is strongly adsorbed CO_{ads} which progressively poisons the Pt surface. Although UPD H is actively involved in both reduction processes, diffusion–control of the overall (Faradaic) currents arises only at the (111) plane. Reduction on the Pt(100) plane in H_2SO_4 is substantially different: a) the observed rapid relaxation of response current to zero upon interruption of a sweep indicates that the reduction is mainly of a pre-adsorbed F_{NOH} species, confirmed b) by the relative absence of diffusion-control (indicated by electrode rotation experiments), in comparison with that involved at the (111) surface. Thus, the mechanism suggested for interaction of F_{NOH} with the Pt(100) plane in H_2SO_4 is a combination of two parallel processes in which co-operative chemisorption of $(F_{NOH})^+$ with HSO_4^- ions on the Pt surface is complemented by reductive scission in the adsorbed state.

In alkaline solution, because the N atom is no longer protonated, direct cleavage of the oxime N-O bond is significantly suppressed. However, following adsorption of F_{NOH} (or A_{NOH}) on Pt(111) over the potential range for double-layer charging, electrocatalytic reductive scission by UPD H can take place giving rise to the reductive current peak (C_2, in Fig. 6.57, for the F_{NOH} adsorbate). At the Pt(100) plane, the electrochemical behaviour of F_{NOH} resembles that observed in H_2SO_4, where co-operative chemisorption of the F_{NOH} molecules with adsorbed OH^- ions is complemented by the process of reductive scission of electrosorbed F_{NOH} species on the Pt surface.

For the above section of the work, the contributions to original research are the following:

1. Study of oximes at Pt single-crystal surfaces has been done for the first time.
2. Faradaic reduction of both F_{NOH} and A_{NOH} molecules is coupled with surface adsorption processes. Based on the CV characterisation in H_2SO_4 and NaOH, adsorption charge transient results in NaOH, and on information from the relevant literature, mechanisms and structures of adsorbed intermediates were proposed.
3. The appearance of the Faradaic reduction process (reductive scission) is highly specific to the Pt surface geometry and pH of the electrolyte. The Faradaic reaction alone is observed at the Pt(111) plane in H_2SO_4, whereas, in alkaline solution (also including Pt(100) in H_2SO_4), a mixed mechanism is observed where the principal process of co-operative chemisorption (similar to the effect found with G^+) is complemented by Faradaic reductive scission.
4. The mechanism of the Faradaic reduction goes through preferred electrolytic hydrogenation steps, involving UPD H. The process of reduction of F_{NOH} on the Pt(111) surface is diffusion-controlled, as was indicated by electrode rotation experiments.
5. The results obtained from application of a.c. impedance spectroscopy provided complementary confirmation of concepts introduced for interpretation of the voltammetry results for processes involving reductive chemisorption of A_{NOH} and

F_{NOH}. The roles of Faradaic reduction coupled with electrosorption, including participation of diffusion control, were clearly distinguishable.